1-1-1980

Studies of melt crystallized poly(vinylidene fluoride)/poly(methyl methacrylate) blends.

Bruce Steven Morra
University of Massachusetts Amherst

STUDIES OF MELT CRYSTALLIZED POLY(VINYLIDENE FLUORIDE)/ POLY(METHYL METHACRYLATE) BLENDS

A Dissertation Presented

By

BRUCE STEVEN MORRA

Submitted to the Graduate School of the
University of Massachusetts in partial fulfillment
of the requirements for the degree of

DOCTOR OF PHILOSOPHY

September 1980

Polymer Science and Engineering

STUDIES OF MELT CRYSTALLIZED POLY(VINYLIDENE FLUORIDE)/ POLY(METHYL METHACRYLATE) BLENDS

A Dissertation Presented

By

BRUCE STEVEN MORRA

Approved as to style and content by:

Richard S. Stein, Co-chairperson of Committee

William J. MacKnight, Co-chairperson of Committee

Frank E. Karasz, Member

Robert L. Laurence, Member

William J. MacKnight, Department Head
Polymer Science and Engineering

Dedicated to my wife

Cathy

without whose support, understanding, and love

this work would not have been possible

ACKNOWLEDGMENTS

I would like to express my sincerest appreciation to my principal advisor Dr. Richard S. Stein, for his guidance, patience, thoughtfulness, endurance and stimulating discussions throughout the course of this work. It has been a tremendously rewarding experience to work with and know this man.

I am also grateful for the advice and assistance of my other advisor Dr. William J. MacKnight, as well as the other members of my dissertation committee; Dr. Frank E. Karasz and Dr. Robert L. Laurence.

A special thanks is extended to Dr. Garth L. Wilkes whose guidance and friendship throughout my undergraduate and graduate years has been of great help in both my professional and personal life.

The assistance of Drs. E. Sherman, E. Roche and E. Thomas, and L. Raboin in electron microscopy techniques and interpretations, as well as R. Nathhorst and J. Minter in setting up the light microscopy equipment, is greatly appreciated.

I want to acknowledge Dr. I. Sanchez for his helpful comments on polymer blend thermodynamics, and Dr. T. Hashimoto for his pertinent communications regarding light

scattering interpretations. The numerous invaluable discussions and communications with Drs. W. Prest and A. Lovinger dealing with the many intricacies of PVF_2 were also of great aid in this endeavor.

The fellowship support of IBM during a portion of my graduate career is gratefully appreciated.

I am thankful for the many stimulating discussions with and technical assistance from Drs. T. Russell and J. Koberstein, and D. Anderson and M. Wai regarding scattering analysis and techniques. I would also like to thank the many other members of Dr. Stein's research group, past and present, and all of the people associated with the Polymer Science and Engineering Department, for their support and friendship over the years, as well as the many other friends outside the PSE Department who brought me back to reality.

Lastly, I am indebted to my parents for their endless support and for putting up with me all these years.

ABSTRACT

Studies of Melt Crystallized Poly(vinylidene fluoride)/
Poly(methyl methacrylate) Blends

(September 1980)

Bruce Steven Morra, B.S.E., Princeton University,
M.S., M.B.A., Ph.D., University of Massachusetts

Directed by: Professors Richard S. Stein
and William J. MacKnight

Banded, non-banded and mixed spherulites, axialite- and platelet-like morphologies are grown from melt crystallized blends of poly(vinylidene fluoride)/poly(methyl methacrylate), PVF_2/PMMA, at low undercoolings. Interfibrillar amorphous regions, most likely containing larger than equilibrium amounts of PMMA, are seen in the banded spherulites. There were two crystal forms melting in three distinct temperature ranges. The banded α spherulites melted at the lowest temperature. The remaining were γ crystals with the highest melting species, referred to as γ', resulting solely from a solid-solid phase transition from the α crystals.

The extinction spacing, p, of the bands in the α spherulites increased with temperature and PMMA content. At low crystallization temperatures, T_c, p approaches a

lower limit, which increased with PMMA content. At higher T_c's all the data fell on one line when plotted as ln(p) vs. $1/(T_m^o - T_c)$. STEM μ,μ diffraction from these spherulites determined that the crystal unit cell twisted about the radially oriented b axis. Rod-like light scattering patterns arising from the staggered arrays of twisting and branching lamellae were seen at large angles.

Hoffman-Weeks plots of T_m vs. T_c showed a change in the slope of the α crystals which was explained by having different amounts of head-to-head PVF_2 units being included in the crystals at different temperatures. Extrapolated T_m^o's from the γ and high T_c α crystals showed a melting point depression, from which a concentration dependent interaction energy density varying from -5.40×10^6 to -2.96×10^7 j/m^3 as the composition was changed from 40.1 to 100 volume % PVF_2 was found.

SAXS intensities were analyzed from samples crystallized at 418 K (where only α crystals were grown) using the Hosemann paracrystalline and Vonk correlation function models, Vonk diameter distribution function approach and Bragg's law. The liquid scattering, crystalline-amorphous boundary zone thickness, long period and invariant increased with PMMA content. It was concluded that the PMMA was included, in equilibrium amounts, in the interlamellar amorphous regions.

Initial growth rates for both the α and γ spherulites decreased with PMMA content and as T_c was raised from 424 to 434 K. Compositional changes in T_g and T_m^o could not fully account for this. Analyses using two variations of the Turnbull-Fisher growth rate equation encountered difficulties due to a changing regime of kinetics. However, the surface energies of γ crystals were higher than the α crystals and both appeared to decline as more PMMA was added.

The growth rates of the blends decreased with time due to partial exclusion of PMMA from the spherulites. This phenomenon was more apparent at higher T_c's. A general model for diffusion controlled growth of a sphere was developed.

The PMMA in these blends can therefore be located either between lamellae, between fibrils, or excluded from the spherulite. The largest amount is in the first region, but at higher temperatures, significant concentrations of PMMA are also observed in the other regions. In conjunction with results on other semicrystalline blends, this suggests that the location of the amorphous component is a function of interactions between the components, as well as temperature and molecular weight.

TABLE OF CONTENTS

LIST OF TABLES

LIST OF FIGURES

C H A P T E R I

INTRODUCTION

A. Poly(vinylidene fluoride)

Poly(vinylidene fluoride), PVF_2, has attracted much attention in recent years for a variety of reasons. It has long been known to be a tough, corrosive resistant thermoplastic. Because of its piezoelectric and pyroelectric properties, it has been widely used as a transducer. It is also one of the few polymers known to exist in multiple crystal forms.

Being a fluoro-polymer it is inert to many solvents that would normally swell or dissolve most other polymers. Combining this attribute with its mechanical properties and processability by conventional techniques makes PVF_2 an attractive structural material. Thus, it has found applications as solid and lined pipes, valves, pumps, seals and gaskets, as well as in packaging and architectural finishes (1).

Its structural qualifications are also important in applications where PVF_2 is utilized as a transducer material (2-4). A transducer is a material capable of transforming one type of energy to another. Piezoelectricity is the ability to interconvert mechanical and

electrical energy, and pyroelectricity involves the conversion between thermal and electrical energy. In 1969, Kawai (5) found extraordinarily large piezoelectric activity in PVF_2 and soon after, Bergman (6) et al., revealed the material's pyroelectricity. In light of these findings, the uses for PVF_2 have been greatly expanded.

In the audio field, PVF_2 is finding uses in both microphones and speakers, as well as underwater hydrophones (2,4). Because PVF_2 can maintain an electric charge placed on it after the applied field is removed, it can be used as an electret (7). Additional unconventional applications include blood flow sensors (4), low mass accelerometers, and inexpensive seismometers (8). Undoubtably, there still exists many commercial applications for a material combining such unusual properties.

Others have been more interested in PVF_2 because of its multiple crystal forms. Gal'perin, et al. (9) in 1965 noted extra reflections developing in x-ray diffraction patterns when PVF_2 was stretched. Lando, et al. (10) found similar results using nuclear magnetic resonance as well as x-ray diffraction measurements. The new form, generated by elongating the samples, was designated β or Phase I, while the original form was α or Phase II. In 1968, Doll and Lando (11) showed that a third form, γ or Phase III could be induced if crystallization

occurred under hydrostatic pressure. Since that time, numerous other works (12-26) have looked at these three crystalline forms and recently, a fourth form, which is a polar α phase, has been proposed (27).

The crystal structures of the α and β forms have been fairly well established. The α form is composed of chains in approximately a trans-gauche-trans-gauche' (TGTG') backbone (15). The unit cell is monoclinic (pseudo-orthorhombic) (15) having dimensions a = 0.496 nm, b = 0.964 nm and c(chain direction) = 0.462 nm (14,15), with all unit cell angles equal to 90°. The β form consists of nearly planar zig-zag chains packed in an orthorhombic unit cell having dimensions a = 0.858 nm, b = 0.491 nm, and c = 0.256 nm (10,15).

There has been much controversy, though, over the structure of the γ form. Hasegawa et al. (15) concluded that this form is almost identical to the β form, having an all trans backbone in a monoclinic unit cell with dimensions a = 0.866 nm, b = 0.493 nm, and c = 0.258 nm and the monoclinic angle equal to 97°. Bartenev et al. (17) describes a different γ phase, prepared at 200 atm., in which the chains are in a helix, but have a similar unit cell to the β phase with dimensions a = 0.488 nm, b = 0.875 nm and c = 0.614 nm. Recently, Weinhold et al. (21) have proposed a new structure for the γ form which has

been verified by Lovinger and Keith (22). The unit cell is orthorhombic with dimensions a = 0.497 nm, b = 0.966 nm and c = 0.918 nm. From Tripathy et al. (20) the chain conformations appear to be TTTGTTTG'.

X-ray diffraction studies of polar α phase, labelled δ(27) have been reported by several authors (27-30). Since there were no changes in the d-spacings between the α and δ phases, it was concluded that the two unit cells were similar. However, significant changes in the relative intensities of the reflections from the two phases were noted (27). Specifically, the hkO reflections for h = k + 2n + 1 were much weaker in the δ phase, implying an n-glide plane perpendicular to the c axis. It was also noted that this phase exhibited some piezoelectric activity indicating a net dipole moment, unlike the α phase which has no net dipole moment.

The different crystal forms have been shown to give rise to various morphologies (22-24,26) which melt at different temperatures (11,17,24,25). Using optical microscopy with crossed polars above and below the sample, two populations of spherulites have been observed at low degrees of undercooling (22-26). One population consisted of small coarse spherulites which were sometimes banded, while the others were large and very distinctly banded.

When the temperature of these samples was slowly raised, three melting regions were seen (24,26). The majority of the large banded spherulites were the first to melt, though some remained in part or whole. Prest and Luca (24) noted that this partial melting left structures which they called wagon wheels because the rim and hub portion of the spherulites remained, but the area where the spokes of a wagon wheel would have been had melted. At temperatures approximately 5-7 K higher, the small coarse spherulites melted. The last crystals to melt were the remaining portions of the large banded spherulites. These disappeared approximately 10-15 K higher than the first melting region.

Lovinger and Keith observed only two melting regions in their samples (22). The large banded spherulites, which melted completely, comprised the first melting region. The remaining structures, which all melted at the temperature of the second melting region described above, had a variety of morphologies. There were wagon-wheel spherulites resembling those of Prest and Luca (24), spherulites which appeared to constitute a collection of lobes, some which had very coarse speckling or poorly coordinated zigzag extinction bands, as well as the typical non-banded spherulites. Some of these structures had very little birefringence as a result

of the lamellae being almost parallel to the film surfaces. From x-ray diffraction and infra-red analysis, Prest and Luca (24) found the lowest melting species to be α phase, the second melting species to be β, and the highest melting species to be γ crystals. Gianotti, et al. (26), utilizing the same techniques, had the β and γ assignments reversed. Selected area electron diffraction studies by Lovinger (23) agreed with Gianotti's interpretation, showing the first melting species to be comprised of α crystals while the structures which melted in the second melting region were γ phase with small amounts of α crystals imbedded in them. Lovinger did not observe β phase crystals in any of his samples.

The development of the crystals melting in the highest temperature region seen by Prest and Luca (24) and Gianotti, et al. (26), was attributed by both groups to a solid-solid phase transition from the α form. This transition only took place in samples held for long periods of time at low undercoolings. It was not possible to determine how much of a given spherulite had undergone this transition without melting, since no morphological changes were observed.

In another study, Prest and Luca (25) demonstrated that the γ crystals can also be obtained from either the α or β crystals as a result of a slow melting and recrystallization process, and that the rate of this

process can be greatly accelerated by certain siloxane-oxyalkylene copolymer surfactants.

A number of authors (24,25,26,31-34) have attempted to determine the equilibrium melting point, $T_m°$, of PVF_2 by using a Hoffman-Weeks (35) plot, where the observed melting points, T_m, of isothermally crystallized samples are plotted as a function of crystallization temperature, T_c. According to the theory, which is discussed in more detail in Chapter IV, this plot should give a straight line which can be extrapolated to the $T_m = T_c$ line. The intersection of this is at $T_m°$. Values of 446.3 (24), 447 (34), 450.7 (31), 455 (26), 461 (33), and 483 K (32) were obtained by this method for the α crystal phase.

For the second melting species, Gianotti, et al. (26) found a $T_m°$ of 467 K. Osaki and Ishida (33) reported that both the second and third melting species extrapolated to 491 K, while Prest and Luca (25) did not find any $T_m°$'s for either the second or third melting species since the data ran almost parallel to the $T_m = T_c$ line. This last group also noted that at the higher crystallization temperatures the data for the α crystals deviated upwards from the straight line fit to the data at low T_c's.

Other techniques for determining $T_m°$ of the α crystal phase have also been utilized. By crystallizing in the presence of various amounts of solvent, and extrapolating the observed T_m's to zero diluent, Welch and Miller (31) found a $T_m°$ of 451 K. Nakagawa and Ishida (32) measured average lamellar thicknesses from electron micrographs of isothermally crystallized samples and plotted this data as T_m vs. $(\text{thickness})^{-1}$. Extrapolation to infinitely thick lamellae gave $T_m°$ = 483 K.

It should be noted that the same PVF_2 was not used in all of the studies described above. Variation of polymerization techniques and conditions can alter many aspects of the polymer produced, including, among other characteristics, the amount of head to head linkages present. This could account in part for the different $T_m°$'s reported.

The growth kinetics of the α phase PVF_2 crystals have also been studied (23,26,37). Mancarella and Martuscelli (36) applied the Avrami equation (38) to differential scanning calorimetry data obtaining an average Avrami exponent of 3.94. From the heat of fusion the lateral surface free energy, σ, was estimated as 9.7 erg/cm^2 and the end surface free energy, σ_e, was found to be 65 erg/cm^2 if $T_m°$ = 451 K and 239 erg/cm^2

for T_m° = 483 K. Nishi and Wang (37) determined σ_e to be 47.5 erg/cm^2 from analysis of spherulitic growth rates. Lovinger (23) showed that the growth rates of the small coarse spherulites seen only at low undercoolings, were less temperature dependent than the α spherulites.

Further interest has been generated in PVF_2 since it has been found to be compatible with a number of other polymers. Using various techniques, a homogeneous amorphous phase was found when PVF_2 was blended with poly(methyl methacrylate) (33,39-44), poly(ethyl methacrylate) (39,44,45,46), poly(methyl acrylate) and poly(ethyl acrylate) (47), poly(vinyl acetate) (48), poly(vinyl methyl ketone) (49) and in a ternary system with poly(methyl methacrylate) and poly(ethyl methacrylate) (50).

B. Polymer Mixtures

Physical mixtures of polymers is an area of interest to a number of researchers and industrialists and has received much attention in the literature (51-57). The addition of one polymer to another will cause modifications in the properties of the two homopolymers. An understanding of these modifications will enable one to tailor-make a product with the desired properties using

materials which are currently available. Obviously this route is much more economic than attempts to develop chemical modifications and synthesizing new polymers from them.

The actual properties attained from a mixture of this kind will depend upon the relative miscibility of the two materials. Polymers that are incompatible will form a phase separated system where each phase contains only pure homopolymer. If the polymers are miscible and form a homogeneous, molecularly dispersed system, they are said to be compatible. There will also be partially compatible systems in which phase separation does exist, but the phases do not contain pure homopolymer.

There is a large variety of methods used to verify polymer compatibility. The most widely used is the appearance of a single glass transition temperature, T_g, between the T_g's of the two homopolymers (51,58,59). If the molecules of the different materials are not sufficiently compatible, individual phases will form, resulting in multiple T_g's. A compatible blend has one T_g which can be related to the composition and the T_g's of the components. Obviously, this criteria becomes useless if the T_g's of the two homopolymers are close to one another.

Visual inspection is a very quick and simple method

for determining compatibility. A homogeneous amorphous system will be transparent, whereas a phase separated system will often scatter light (56). This criterion is based upon the assumption that the refractive indicies of the two homopolymers are different, therefore giving a transparent blend only if one homogeneous phase exists. A few precautions are necessary, however, when evaluating compatibility with this technique. If the refractive indices are close to each other, phase separation can occur but the sample will not scatter light. The blend will also be transparent if the phases are very small, even if the refractive indices are widely disparate. One might then think the system to be homogeneous when it is not (60,61). The styrene-butadiene-styrene block copolymer system, though optically transparent, is comprised of many small distinct phase regions (62-64). On the other hand, a single amorphous phase may be present, but a crystalline phase formed from one or both of the homopolymers would make the sample opaque, even though the polymers are compatible.

If the phases are very small it is possible to use the electron microscope to view fracture surfaces and distinguish one and two phase systems (64-66). Small angle x-ray scattering, SAXS, can also be used for phases below a few hundred nm, if there is enough difference in

the electron density of the phases.

Besides information on phase sizes, which may or may not be present, scattering techniques also provide insight into conformations and configurations of individual polymer chains. These will vary with the compatibility of the system being examined. Zimm (67) has demonstrated that using the concentration and angular dependence of light scattering from dilute polymer solutions, the molecular weight, radius of gyration and second virial coefficient can be calculated. These parameters are related to interactions occurring between the polymer chain and the solvent. Using the same type of analysis, Kratky (68-70) has shown that x-ray scattering from solutions can also give this information. These same ideas can be applied to blends if another polymer is used in place of the solvent. Krigbaum and Godwin (71) and Hayashi, et al. (72) using dilute amounts of iodinated chains, and Russell (73) using various blend systems, performed this experiment on bulk samples.

The development of small angle neutron scattering has expanded the possibilities for studies of this nature. Heavy atoms, necessary for x-ray contrast, but which distort the chains, can be avoided by this technique. Contrast is obtained by selective deuteration

of certain chains, which can then be studied in the bulk (74-79). This technique has been recently used to investigate various polymer blends (79-81).

Other methods which show alterations of one polymer due to the presence of another have also been employed to study blends. Coleman, et al. (82,83), from Fourier transform infra-red spectroscopic studies, has shown that certain absorbance bands of compatible blends cannot be reproduced by adding the absorbance bands of the two homopolymers. However, with an incompatible mixture, the spectrum can be entirely reconstructed from the spectra of the constituents. Therefore, there are sufficient interactions between the two species in the compatible system to alter the chains from their states in a pure homopolymer.

Quantitative assessment of this interaction can be obtained from measurement of the Flory-Huggins (84) interaction parameter between the two polymers. From vapor sorption measurements on polymer solutions, ternary solution theory (84-86) allows one to determine the degree of polymer-polymer compatibility. Kwei et al. (90) have found negative values of χ in compatible blends of polystyrene and poly(vinyl methyl ether) by this method. This technique has also been employed by Jaques and Hopfenberg (87) to show that blends of

polystyrene and poly(phenylene oxide) form a homogeneous amorphous phase. For a variety of polymer-polymer mixtures, Tager, et al. (88,89) calculated the change in free energy upon mixing and related this to the compatibility of the systems. In addition to these studies, Olabisi (91) has utilized the gas-liquid chromatography method of Guillet (92,93) to analyze the interactions in poly(ε-caprolactone)/poly(vinyl chloride) blends.

For semi-crystalline blends, where one polymer crystallizes out of the homogeneous amorphous matrix, melting point depression of the crystals has been observed (10,11,12,16,62,63,65,66). The amount of this depression can be related to the interaction between the two components (10,12,64,65,66). This approach, along with precautions one must consider will be discussed in detail in Chapter IV.

C. PVF_2/PMMA Blends

A large amount of the work on blends has involved the PVF_2/PMMA system. In fact, much of the literature cited above deals with these polymers. From thermal (34, 39-42,94), dynamic mechanical (40,41) and dilatometric (39,40) analysis, compatibility has been determined by the observance of a continually varying glass transition temperature, and depression of the melting point of the

PVF_2 as additional PMMA is added. Thermal analysis has also been performed on blends in which the tacticity of the PMMA was varied (42).

Measurement of the amount of melting point depression as a function of composition enabled the calculation of the interaction energy density, B, of the PVF_2/PMMA pair. Values of B equal to -2.98 and -3.85 cal/(cm^3 of PMMA) were computed by Nishi and Wang (34), and Paul et al. (95) respectively. Roerdink and Challa (42) found that B varied from 0 to -1.21 for syndiotactic PMMA and -1.26 to -2.20 for isotactic PMMA when the relative undercooling, $(T_m^\circ - T_c)/T_m^\circ$, was changed from 0.06 to 0.10.

In addition to melting point depression measurements, Wendorff (94) has calculated the Flory-Huggins (84) interaction energy parameter, χ_{12}, from small angle x-ray data by following changes in the absolute value of the strucure factor extrapolated to zero scattering angle. The two interaction parameters are related by $\chi_{12} = BV_{1u}/RT$ where V_{1u} is the molar volume of the PMMA. His findings resulted in an interaction parameter which was always negative, but varied with the composition of the blend. χ ranged from -0.49 to -0.7 at 90 wt. % PVF_2 and -0.04 to -0.12 at 10 wt. % PVF_2. This was in close agreement with the results presented in Chapter IV.

The Fourier transform infra-red studies cited previously (82,83) postulate that this interaction is in some way related to the carbonyl group of the PMMA. The absorbance band for this group is very strong and was affected most by the addition of PVF_2. By examining a series of blends of PVF_2 and various oxygen containing polymers, the interaction parameters for these systems have also been related to both the dipole moments of the polymers and the lower critical solution temperature, LCST (95). The LCST is the point at which phase separation of a compatible system is first seen as the temperature is raised. This was shown to increase as B decreased, implying that the instability was more influenced by enthalpic than entropic factors.

In addition to the above, other novel techniques in the analysis of polymer blends have been used with this system. Measurements of longitudinal sonic velocity (41) suggest that in samples having between 30 and 60 volume percent of PMMA, two continuous phases exist, one being crystalline PVF_2 and the other an amorphous mixture of the two polymers. Above 60% PMMA, only the latter is continuous, while below 30% the former is continuous. Changes in the Brillouin scattering from this blend (43) have been used to follow melting and glass transition temperature variations, verifying the existence of a single

homogenous amorphous phase. Assuming that cross relaxation effects imply near-neighbor dipolar interactions between protons and fluorine nuclei, the transient Overhauser effect studied by pulsed nuclear magnetic resonance, has indicated that these two components are intimately mixed in the amorphous regions (44).

Besides lowering the melting points, the addition of PMMA alters other properties of the PVF_2 crystals. A monotonic decrease in the pyroelectric coefficient of PVF_2 has been observed as more PMMA was added (96). This coefficient became zero when 50 wt. percent was reached. The growth rates of α form spherulites have been observed to decrease dramatically with the addition of PMMA (97). This was analyzed as a function of crystallization temperature to derive surface energies of the crystals. Studies of the growth rates of the α form as well as γ form crystals in a higher temperature range will be discussed in Chapter VI.

The purpose of the present investigation is to evaluate how the PMMA affects the PVF_2 crystals in blends of the two polymers. Changes in morphology of the crystals, the type of crystals grown and the growth rates will be explored. The melting temperatures of the different crystal forms as a function of composition will be used to calculate polymer-polymer interaction parameters.

These studies will not only shed additional light on the very complex nature of crystalline PVF_2, but will also add to the understanding of polymer-polymer compatibility.

C H A P T E R I I

EXPERIMENTAL

A. Polymer Characterization

Chemical structures for PVF_2 and PMMA are given in Figure 1.

The PVF_2, Kynar 881, was supplied in powder form by the Pennwalt Corp. The American Cyanamid Company provided the PMMA, Acrylite H-12, in pellet form. Molecular weights were obtained from gel permeation chromatography of the homopolymers in N, N-Dimethyl-formade using polystyrene as the calibration. This was performed at Bell Labs in Murray Hill, New Jersey. The weight average and number average molecular weights, $\bar{M}_w$ and $\bar{M}_n$ respectively, along with the heterogeneity index are given in Table 1.

B. Blend Preparation

Weighted amounts of the homopolymers were dissolved in N, N-dimethylacetamide containing 1% acetic anhydride. The latter was added to act as a scavenging agent for free amines, thereby helping to prevent

Poly (vinylidene fluoride)

PVF_2

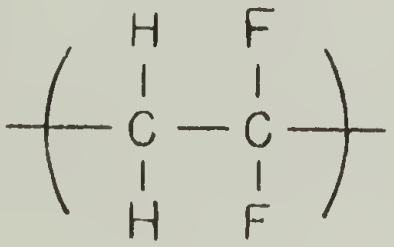

Poly (methyl methacrylate)

PMMA

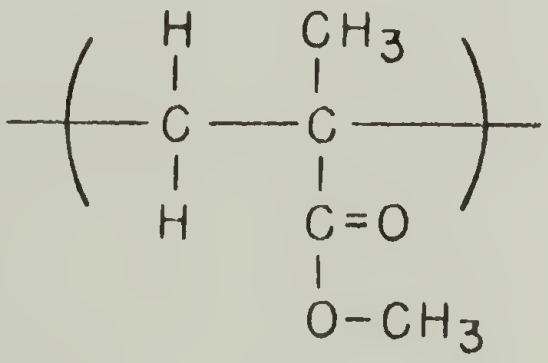

Figure 1. Chemical structures of PVF_2 and PMMA.

TABLE 1

MOLECULAR WEIGHTS AND HETEROGENEITY INDICES OF MATERIALS USED

	PVF_2 (Kynar 881)	PMMA (Acrylite H-12)
$\bar{M}w$	555,000	91,500
$\bar{M}n$	375,000	36,600
$\bar{M}w/\bar{M}n$	1.48	2.50

degradation of the polymer. The total concentration of polymer was 3.0 g/cc of solvent in all cases except in preparation of samples for the electron microscope, where the concentration was 0.2 to 0.4 g/cc. The PVF_2 powder dissolved within a few minutes when placed into the stirred solvent. Continuous stirring at room temperature for 1 to 2 days was necessary to completely dissolve the PMMA pellets.

The 3.0 g/cc solutions were poured into specially made flat bottom glass dishes to a liquid level of about 2-5 mm. Cheesecloth was placed over the dishes to prevent dust and foreign particles from getting into the solutions. These were then allowed to sit for 2 to 3 days in a hood until dry films remained. The films were stripped from the glass dishes and placed in a vacuum oven at 40°C for three days to facilitate the removal of any excess solvent. Sometimes the films would adhere to the glass dishes. If this occurred, about 10 cc of methanol was poured onto the film. The methanol would float the film free in 10 to 15 minutes after which it was placed in the vacuum oven. Periodic weighing of a certain number of the films during this period verified that no further weight loss was occurring after three days. Films approximately 3 to 7 x 10^{-2} mm thick were thus obtained.

All of the as cast films had small spherulitic structures composed of α form PVF_2 crystals. From DSC and hot stage microscopy, the melting points were found to be in the 435 to 440°K range.

To prepare samples isothermally crystallized, it was first necessary to remove any effects due to the as cast morphology and start from an amorphous blend. This was accomplished by melting all samples at 485 K for 10 minutes as will be described in more detail in the following section. Polarizing hot stage microscopy confirmed that there was a total loss of birefringence in the as cast films at this temperature.

For the electron microscopy, very thin films, 100 nm or less, are needed. Since it was not possible to remove films from a glass substrate without seriously damaging them, they were cast on freshly cleaved mica. After being cleaved, the mica was dried for one day in a vacuum oven at 475 K. This served to remove any water present in the mica which would increase adhesion of the film to the surface. Two to three drops of the 0.2 to 0.4 g/cc solutions were deposited on the cleaved surface of the mica and this was immediately put in another vacuum oven at 315 K for three days.

Composition of the blends is reported as both weight and volume fractions. The latter were calculated

assuming volume additivity of the components and using densities of 1.20 and 1.78 (1) g/cc for PMMA and PVF_2 respectively.

C. Sample Preparation

1. DSC. Two microscope slides were set on a hot stage at 485 ± 2 K for approximately ten minutes. A stack of cast films, 7 - 12 layers high, obtained from the flat bottom glass dishes, was placed on one slide. The other slide was then set on top of the stack and slight pressure was applied with a tweezer to fuse the stack of films together. The samples of polymer thus formed were wrapped in aluminum foil and attached to a wire hook. To crystallize these, the whole assembly was heated in an oven at 485 ± 2 K for 10 minutes and then the wrapped samples were immediately suspended in either a silicone oil bath maintained at the desired temperature to ± 0.5 K or a sand bath set to ± 1.0 K. After a predetermined amount of time in the crystallization baths, the samples were quenched in ice water. Weighing of the oil crystallized samples before and after crystallization verified that no oil was absorbed. No differences between the oil crystallized and sand crystallized samples were observed in any of the experiments.

During the quench, some of the samples would

undergo additional crystallization. These crystals melted at a lower temperature than the others and usually amounted to small percentages of the total crystallinity.

2. WAXD. Sections of the DSC samples after being crystallized were used for WAXD. Often, several pieces of the sample were stacked together to increase the thickness.

3. SAXS. Strips approximately 1.5 cm wide and 3.0 cm long were cut from the as cast films. These were placed in a slot of a stainless steel mold specifically designed for a Kratky SAXS camera. The slot was 0.75 cm wide, 3.5 cm long, .085 cm deep, and had beveled edges to facilitate removal of the sample. Two pieces of teflon coated aluminum foil, with the teflon side facing away from the sample, were placed on either side of the mold with the strips of polymer being in the slot. This assembly was put between the platens of a Carver press heated to 485 K so that the upper platen was just touching the foil. Allowing the sample to melt for 5 minutes, the assembly was removed from the press and more polymer was added to the slot. After another 5 minutes between the platens, pressure was applied in a cyclical fashion from 0 to 10,000 psi over a period of about 2 minutes. The sample was then removed and examined for voids. If any existed, additional strips were placed in the slot.

These were allowed to melt for 5 minutes in the press and cyclical pressure was again applied. If voids were still present, the sample was discarded. Otherwise, the teflon foil was crimped around the mold, and the sample saved for crystallization.

After attaching these samples to wire hooks, they were crystallized, as were the DSC samples, by melting in an oven at 485 ± 2 K for 10 minutes and suspending in a silicone oil bath. All of the SAXS samples were crystallized at 418 ± 0.5 K for 24 hours. At this temperature only α spherulites are formed. Samples crystallized at higher temperatures would contain other crystal forms, resulting in distribution of lamellar thicknesses which would make interpretation of SAXS data much more ambiguous.

Once they were crystallized, thickness variations in the samples were corrected by filing to an even thickness, and the sample surfaces were smoothed with a fine file.

4. Optical microscopy and light scattering. A piece of film cast from the glass dishes was placed between cover slips and melted on a hot stage at 485 ± 2 K for 10 minutes. The whole sandwich was then lightly squeezed together with a pair of tweezers to get the desired adhesion between the film and cover clips. This was done to eliminate any surface effects.

Crystallization of some of these samples was followed under the microscope. They were melted again on the hot stage at 485 ± 2 K for 10 minutes and placed immediately in a Mettler FP2 hot stage which had previously been aligned in the microscope and equilibrated to the desired temperature ± 0.5 K. Additional samples were crystallized along with samples for x-ray scattering and DSC studies in order to verify consistency of temperatures and methods used.

5. Electron microscopy. The samples, cast on the mica, were melted on a hot stage at 485 ± 2 K for 10 minutes and placed in either the Mettler hot stage, or an oven preset to the desired temperature. Once crystallized, the films were floated off the mica onto distilled water. The water was in a large Buchner funnel in which a wire mesh, with several microscope grids on it, was submerged. With the film floating on the surface, the water was slowly removed through the bottom of the funnel as the film was positioned over the microscope grids with forceps. In this manner the film came to rest on top of the grids. It was then allowed to dry and the excess film was cut away from the perimeter of the grids.

Thin coatings of gold, about 20 Å, were evaporated onto some of the samples to use as a calibration standard for the diffraction patterns.

beam travelled about 1 cm in air before the sample. The scattered radiation after traversing another 1 cm in air entered a home built vacuum chamber to which a one dimensional position sensitive detector was attached. A mylar® sheet was used as a window in the front of the vacuum chamber and the detector had a beryllium window. The Tennelec® PSD 1100 position sensitive detector was operated at +2600 volts using P - 10 (90% argon + 10% ethane) flow gas at 100 psi. The tungsten wire had a point to point spatial resolution of 200 μm and was 53 cm from the sample. The x-ray tube, camera and detector were all in a constant temperature box at 31°C. EG&G's Ortec electronics were used for energy discrimination, position encoding and transfer of the data to an Ino-Tech (Norland Corp.) IT-5200 multichannel analyzer where they were stored and simultaneously displayed on an oscilloscope screen. Once the run was complete, the stored data was transferred to magnetic tape cassettes via a Datacassette 8410 (Techtran Ind. Inc.).

Calibration of the scattering angle was performed using a dry uranyl acetate stained duck tendon which had a known repeat distance of 64.0 nm. This sample produced 11 sharp scattered intensity peaks in the small angle region. The detector wire sensitivity was calibrated at each channel using ^{55}Fe as a constant, angularly independent

source of radiation.

4. Optical microscopy. A Zeiss standard polarizing microscope equipped with long focal length objectives and a Leica 35 mm camera back was used in conjunction with a Mettler FP2 optical hot stage to follow crystallization and melting of the blends. A 1 mm stage micrometer, divided into 100 units, was used to calibrate all photographs.

5. Light scattering. Two types of solid state light scattering experiments were performed. The more conventional method employed a Spectra Physics He Ne laser (λ = 632.8 nm) with 1 mm pinhole collimation. The sample was on a stage situated between a rotatable polarizer and analyzer. Polaroid film was used to record the pattern. Sample to film distance could be varied and was calibrated with diffraction gratings. The patterns observed were an average of the scattering from a number of spherulites.

It was also desirable to obtain light scattering patterns from different regions within a given spherulite. To accomplish this a Zeiss standard WL polarizing microscope with POL objectives was equipped for selected area light scattering. A pinhole, roughly 20 μm in diameter, made in 5 mil aluminum shim stock, was placed in the focal plane of the condenser lens on the side nearest the light

source. A monocular tube containing a removable Bertrand lens and an iris diaphragm above it was inserted below the eyepiece. The iris diaphragms on the collector lens and above the Bertrand lens were aligned and fully stopped down. A 60 W, 12 V light source was used with a wide band pass green filter added when photographing the scattering patterns. Photographs of both the scattering patterns and the images were recorded on Polaroid film with a conical camera attachment. With the Bertrand lens removed, areas of the sample about 50 μm in diameter could be viewed and an image photographed. The light scattering pattern corresponding to that particular area could then be recorded by simply replacing the Bertrand lens. The scattering patterns covered the wide angle region up to approximately 45° and were very weak. Even using ASA 3000 film required approximately 10 minute exposure times. Calibration was performed with diffraction gratings and a stage micrometer.

6. Electron microscopy. Both transmission and scanning transmission electron microscopy (STEM) were performed on a Jeol Temscan 100 CX at 100 Kv. Because the samples were extremely beam sensitive a current of 60 μA was used. Electron diffraction patterns were taken in both the selected area transmission mode and μ,μ stem mode.

The advantage of the μ,μ STEM diffraction is that

the area surrounding the diffracting region is not damaged by the beam. This enabled the recording of adjacent diffraction patterns along the radius of a spherulite. This was performed by first recording a STEM image of the sample on polaroid film. This image was taken through the smallest condenser lens aperture and with a very short exposure time (normally 25 seconds) to avoid damage of the specimen. The large selected area diffraction (SAD) aperture was also inserted to increase contrast. This picture was used to determine from which areas diffraction patterns would be taken. Using the free lens control to set the current in condenser lens 2, a beam approximately 670 nm in diameter could be applied in the spot mode. Without moving the sample, the beam was positioned with the current off. The current was then turned on for a set amount of time, which had been previously determined, and the diffraction pattern was recorded. At the conclusion of this set time period, the current was shut off and the beam repositioned, using the STEM image as a guide, to the next area from which a diffraction pattern would be taken. Another Polaroid STEM image was taken after recording all the diffraction patterns so that a visual check of the regions from which the patterns came could be made.

C H A P T E R I I I

MORPHOLOGY

Since PVF_2 is known to exist in a variety of crystal forms and morphologies, it was desirable to study the effects the addition of PMMA would have on this already complicated polymer. Variations in types of spherulites and crystals grown isothermally from the melt were followed for samples ranging from 40.1 volume % to pure PVF_2. Blends having concentrations below 40 volume % PVF_2 took prohibitively long times to develop appreciable amounts of crystallinity at the high range of temperatures of interest and therefore were not studied. However, it is believed that the results can be extended to these blends if long enough crystallization times are used.

A. General Morphology

1. Pure PVF_2. At crystallization temperatures (T_c) below 424 K, α form spherulites were always obtained. These nucleated more profusely as T_c was lowered. Above this temperature, however, two separate populations of spherulites grew; large, distinctly banded spherulites and smaller, coarser ones. When T_c was between 424 and 434K the smaller spherulites had a bandwidth about twice

that of the larger ones, but above these temperatures they were non-banded. Figure 2 is an electron micrograph of the two different types of spherulites impinging on one another.

Upon melting, these samples exhibited three melting regions in both the optical microscope and DSC studies. A detailed analysis of the melting points as a function of crystallization temperature and blend composition will be presented in the following chapter. Relation of the melting regions to the different crystal forms is desired though, and a preliminary discussion of the complex melting behavior follows.

Figure 3 shows a sample volume filled with both the large and small spherulites. As the temperature was raised from 298 to 448 K, note that almost all of the large spherulites disappeared except for the parts closest to the small spherulites. When the temperature had reached 456 K, the small spherulites were also lost, leaving only the remnants from the large ones. Finally, at 461 K, all of the crystals had melted. As mentioned in the introduction, Prest and Luca (24), using the 400 to 900 cm^{-1} infrared absorbance region and WAXD assigned these, in order of melting, to the α, β and γ phases, respectively, while Gianotti (26), using the 2853-2925 cm^{-1} infrared region found the second melting species to be the γ phase

Figure 2. Electron micrograph of PVF_2 showing two different spherulites impinging, T_c = 436 K, 165 hours.

2μm

Figure 3. Optical micrographs of PVF_2 crystallized at 438.2 K for 70 hours and then slowly melted, (a) 298 K, (b) 448 K, (c) 456 K.

a

b

100μm

c

and the β phase the last to melt. Lovinger and Keith (22) have shown that platelets which melt at the same time as the small, coarse spherulites give electron diffraction patterns consistent with Weinhold's et al. (21) γ form. We will call the three crystals, in order of melting, the α, γ and γ' forms, respectively. The reasons for this nomenclature will be discussed later.

Both types of spherulites nucleate homogeneously as well as heterogeneously. Often the γ spherulites nucleate the α ones on their surface as can be seen in the center part of the pictures in Figure 3. This is also what Lovinger and Wang (98) observed in directionally solidified samples. The highest melting species, γ', arises only from a solid-solid transition from the α phase. This transition was almost always seen to nucleate at the point where an α spherulite was in contact with a γ spherulite, as shown in Figure 3. The transition would then spread back along the α lamellae. Upon close inspection of the upper right part of the pictures in Figure 3, it will be noticed that at the center of each group of γ' lamellae is a tiny γ spherulite.

The α form must be favored kinetically, and the γ' form favored thermodynamically since, over time, at a constant temperature, more and more γ' is formed at the expense of α but the γ' never nucleates and grows on its

own. In Figure 4, two DSC traces of identical samples show how the area under the high temperature γ' peak grows while the α peak, predominant at 72 hours, shrinks with time. The γ peak remains roughly the same size since this sample is volume filled by 72 hours and therefore few new crystals can grow. The α to γ' transition via melting and recrystallization during the heating, mentioned by Prest and Luca (25) did not seem to occur in this study because even in their work, this process only proceeded at an appreciable rate when a surfactant was added.

Low temperature endothermic responses seen in Figure 4 as shoulders on the α peak as well as separate, broad peaks, were due to crystals formed during the quenching of the samples. Variations of the heating rates caused shifts in these low temperature responses but did not alter the α, γ or γ' peaks. The optical microscopy melting studies also verified this.

2. PVF_2/PMMA blends. The addition of PMMA to the PVF_2 increases the bandwidths or periodicity and generally causes the spherulites to appear more open and disordered. The α spherulites are affected much more than the γ spherulites in this manner. The electron micrograph of Figure 5 is from a portion of an α spherulite grown at 423.2 K in a 50.1 volume % PVF_2 sample. The amount of undercooling is roughly the same as for the pure PVF_2

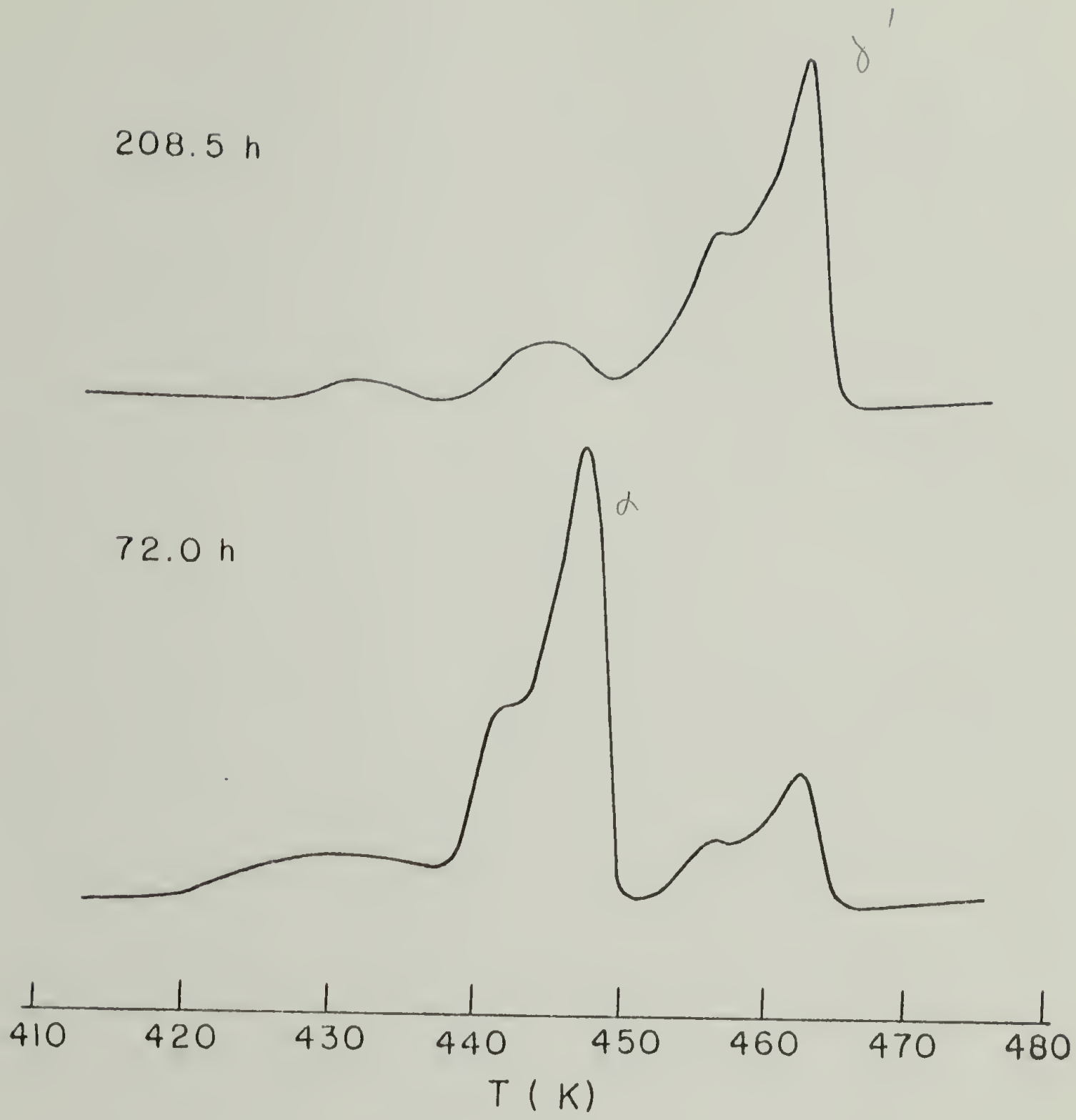

Figure 4. DSC traces of PVF_2 crystallized at 432.7 K for various times.

Figure 5. Electron micrograph of 50.1 vol. % PVF_2 blend crystallized at 428.2 K for 93 hours.

Figure 6. Optical micrographs of (a) PVF_2 crystallized at 435 K and (b) a 50.1 vol. % PVF_2 blend crystallized at 428.2 K.

Fig. 5

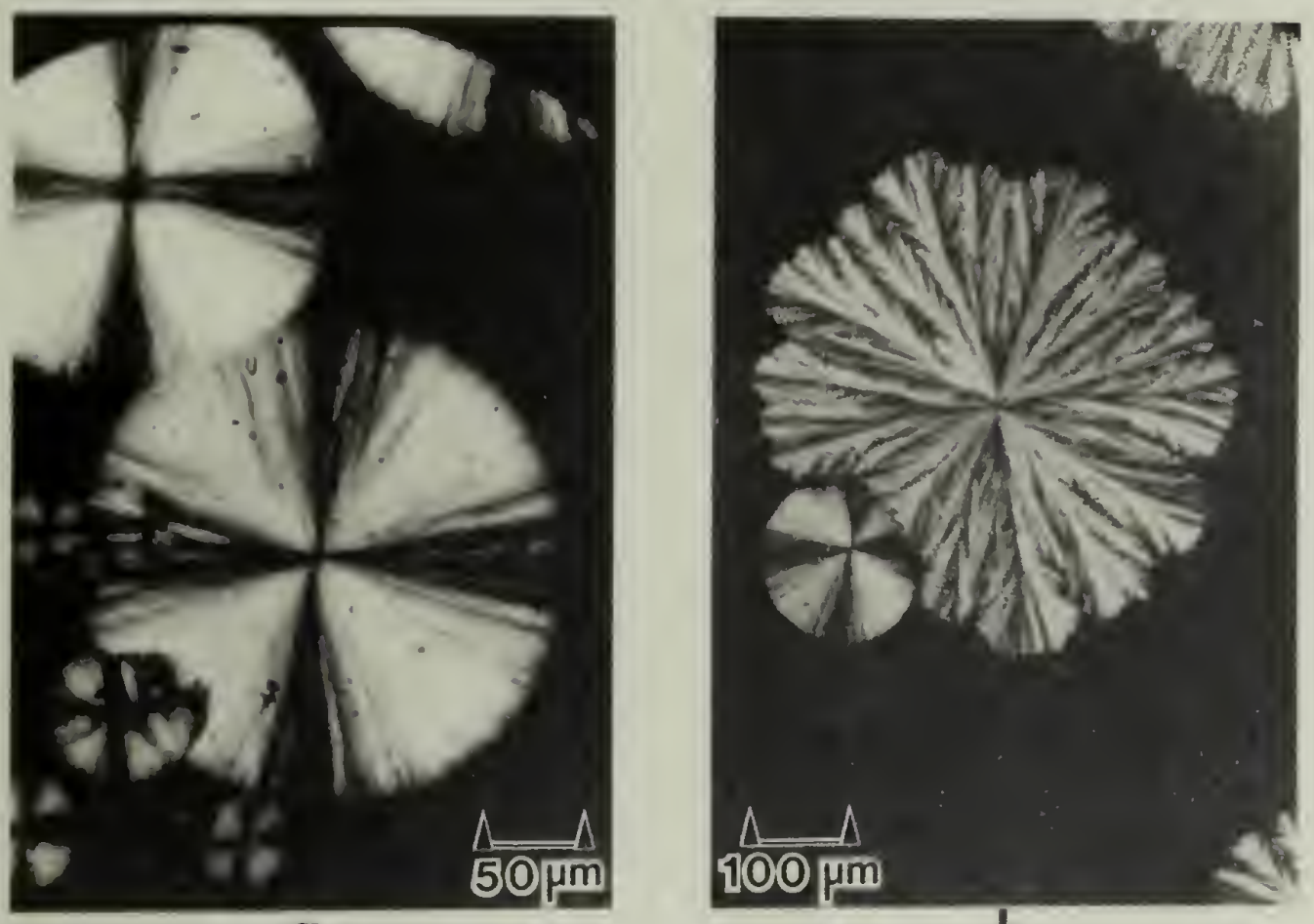

a b

Fig. 6

shown in Figure 2. Note the many regions of pure amorphous material trapped within the spherulite between the bundles of lamellae. This type of morphology was occasionally seen near the growth fronts of α spherulites in pure PVF_2, but only at very low undercoolings in extremely thin films (less than a few hundred angstroms thick). For samples such as the one shown in Figure 2, at undercoolings comparable to that for the blend of Figure 5, this type of morphology was never seen. Therefore the amorphous regions in the interior portion of the blend spherulites are believed to contain large amounts of PMMA.

In the blend it appears as if bundles of lamellae grow out into the amorphous melt. These bundles grow in almost all directions, though there is a generally preferred orientation, as seen in Figure 5. When two or more of these bundles come together they often entrap an amorphous region which is somewhat depleted of PVF_2. Since diffusion of additional PVF_2 through the crystalline lamellae to this region is unlikely, these areas remain isolated inside the spherulite.

Radiation damage was a problem with many of the samples studied due to the high beam sensitivity of the PVF_2. The black streaks running perpendicular to the general growth direction in Figure 5 are artifacts from

this type of damage. These streaks are tears and buckles in the sample caused by the incident electron beam. Radiation damage would eventually destroy the sample, but at low doses, as in Figure 5, only very small distortions from the original morphology were observed.

As the spherulites grow larger, the randomness of the lamellae seen in Figure 5 within the spherulite causes the loss of the traditional maltese cross pattern normally seen in the optical microscope. Figure 6 compares optical micrographs taken through crossed polars of pure PVF_2 and a 50.1 volume percent blend at similar undercoolings to those of Figures 2 and 5. The small γ spherulites appear fairly similar, but the large α spherulites of the blend are much more disordered. When the lamellae lose their radial orientation, the individual chains are no longer arranged tangential to the spherulite radius and the usual extinction at 0° and 90° to the polarizers is not seen.

The randomness of the lamellae is also related to their relative size. Comparing Figure 5 to the α spherulite in Figure 2, it is apparent that the addition of PMMA results in much shorter lamellae in the growth direction. A new nucleation event seems to occur before the lamellae can grow very far. This may be due to the depletion of PVF_2 from the immediate area of lamellae

growth which would therefore terminate that lamellae. Diffusion of more PVF_2 to this area would now bring the level up to the point where another nucleation event can take place and growth continues.

The addition of PMMA also seems to increase the ratio of γ to α spherulites. These γ spherulites have less banding character as more PMMA is added. The 60.9 volume % PVF_2 sample only has twisted lamellae below 423 K, while samples with less PVF_2 never show banding in the γ spherulites. These often cease to grow as spherulites and develop an axialite-like character. Figure 7 shows a γ spherulite on the right in a 50.1 volume % PVF_2 blend starting this type of growth. An α type spherulite and a mixed spherulite are also seen in this picture. Often quite a variety of crystal structures grew in one sample. A detailed discussion of the mixed spherulite will be presented later.

Figure 8 is an optical micrograph of a 60.9 volume % PVF_2 blend grown at 433 K. All of the various morphologies discussed are visible. There is a large banded and a large non-banded spherulite, as well as axialite growths that have been fully developed. The tiny, partially formed spherulites in the upper right section grew after the sample was quenched to room temperature. The lack of these crystals in the areas immediately surrounding

Figure 7. Optical micrograph of a 50.1 vol. % PVF_2 blend crystallized at 432.7 K for 210 hours.

Figure 8. Optical micrograph of a 60.9 vol. % PVF_2 blend crystallized at 433.2 K for 72 hours.

Fig. 7

Fig. 8

the large spherulites and axialites is evidence of the depletion of PVF_2 in these regions. The center rib, as well as many other parts of the axialites seen in Figure 8 are almost totally non-birefringent. These are made of platelet-like growths of γ crystals with the lamellae surface oriented almost parallel (and their optic axis roughly perpendicular) to the plane of the polymer film. Therefore there is little or no birefringence. An example of this rib structure viewed with the electron microscope is shown in Figure 9 for a 72.8 volume % PVF_2 blend.

The pure PVF_2 did not display the rib-like structure but did contain large crystalline areas of low birefringence, as in the lower left portion of Figure 8, when grown at temperatures above 436 K. Pictures of these types of crystals viewed under the electron microscope are shown in Figure 10. Lovinger and Keith (22,23) have performed an excellent crystallographic study of this morphology in pure PVF_2. The interested reader is referred to their work for a more detailed discussion of the crystal unit cells.

Prest and Luca (24) describe spherulites of PVF_2 containing interior speckled regions of low birefringence, which they call "wagon wheel spherulites." In their case, these spherulites were banded. The highly birefringent

Figure 9. Electron micrograph of a 72.8 vol. % PVF_2 blend crystallized at 438 K for 330 hours.

Figure 10. Electron micrographs at two magnifications of PVF_2 grown at 438.2 K for 330 hours.

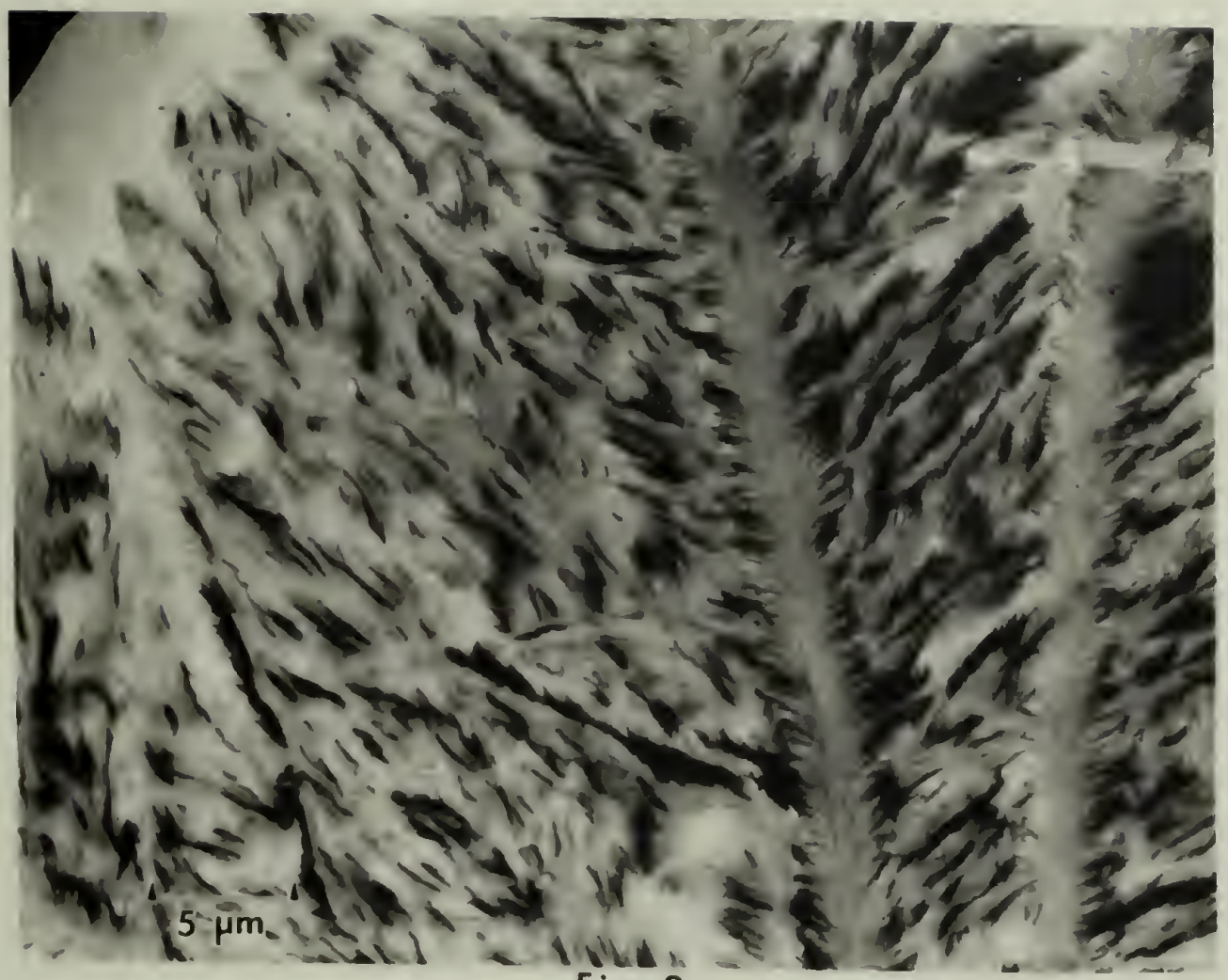

Fig. 9

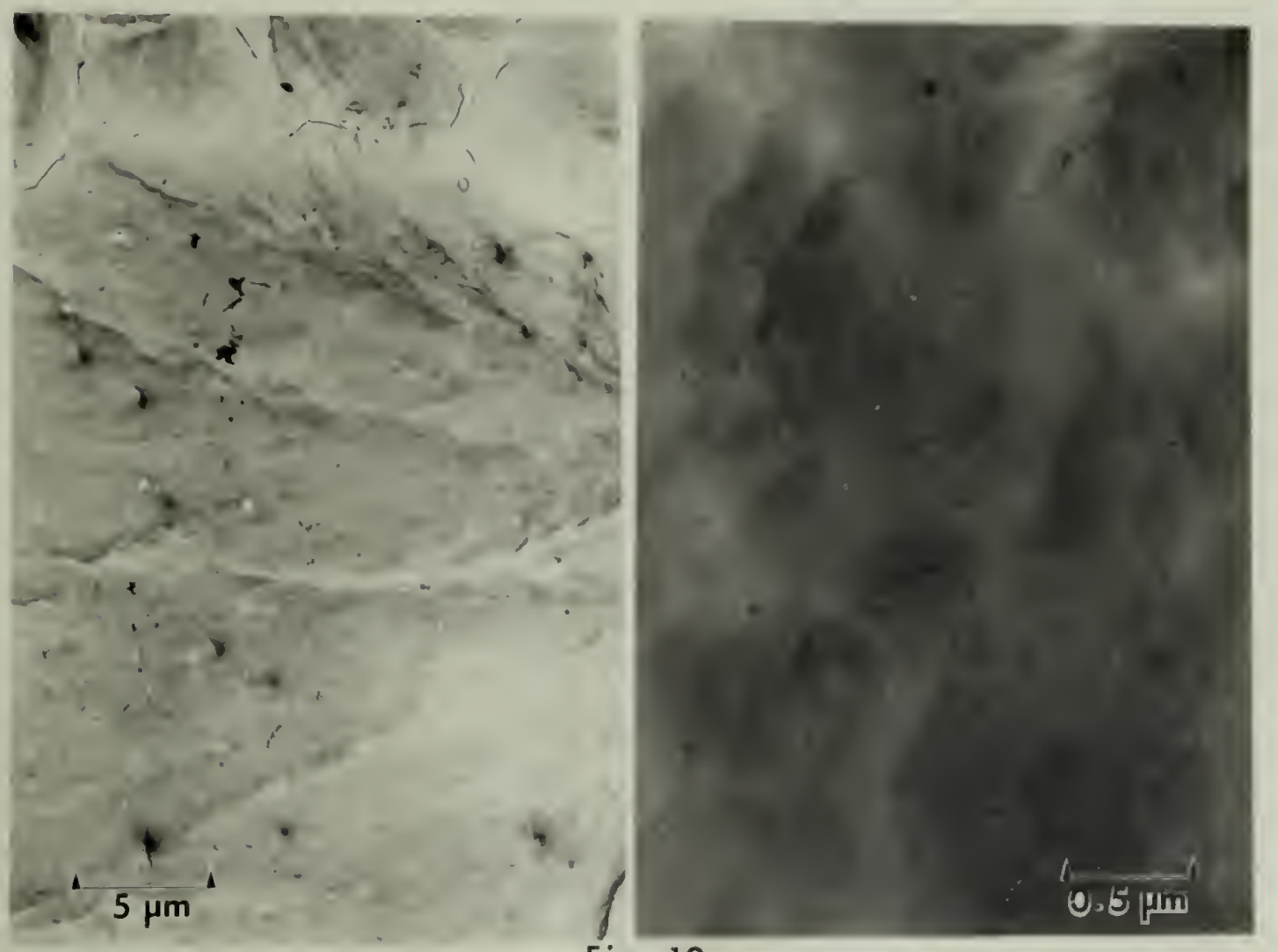

Fig. 10

portions melted with the highest melting species and the low birefringent sections melted at or slightly above the second melting temperature. In both Lovinger and Keith's (22,23) as well as the present work, the non-birefringent regions appeared in the coarse, non-banded spherulites, and melted, as did the rest of the spherulite, with the second melting species.

The mixed spherulite of Figure 7, in which the center banded portion is surrounded by a non-banded perimeter, is actually a result of the α to γ' transition in the blends. These spherulites were never seen in pure PVF_2. The increased number of γ spherulites in the blends, resulting in more impingements on α spherulites, caused the transition to be initiated more often. In the event the transition started when the α spherulite was small, a mixed spherulite would result. The series of micrographs shown in Figure 11 helps to explain how these developed.

Following the melting of this sample, most of the large banded spherulites were seen to melt first, the non-banded regions next, and finally the interior of the combined spherulites along with the portion of the banded one adjacent to the non-banded one. These are again attributed to α, γ and γ', respectively. The combined spherulite developed when a γ spherulite impinged on an α

Figure 11. Optical micrographs of 50.1 vol. % PVF_2 blend crystallized at 432.7 K for 209 hours and slowly melted, (a) 298 K, (b) 446 K, (c) 453 K.

a b c

50μm

spherulite. This is seen in Figure 11 where the edge of a γ spherulite is impinging on the center banded part of the combined spherulite. This impingement initiated the α to γ' transition which preceded back along the lamellae of the banded spherulite. (This process was also occurring in the other banded spherulite.) When the transition front reached the growth front the spherulite began growing with γ form crystals, causing a non-banded rim to develop.

Figure 12 is an electron micrograph of a spherulite immediately after the α to γ' transition caught up to the growth front. The lamellae grown at the tips are now γ type and do not have the periodic banding of the earlier grown lamellae. Prest and Luca (24) postulated a similar formation for their wagon wheel spherulites, but no wagon wheel spherulites of their type were observed in the samples used in the present work.

In both the 60.9 and 72.8 volume % PVF_2 blends another interesting phenomenon was noted at 424 K. These samples are shown in Figure 13. The spherulites were initially very weakly birefringent, but over time the core began to become more birefringent. This front of increased birefringence followed the growth front at approximately the same rate, however, in the 60.9% sample, the second front often lagged much farther behind the growth front, while in the 72.8% sample there was much less

Figure 12. Electron micrograph of a 50.1 vol. % PVF_2 blend crystallized at 423.3 K, for 45 hours showing the development of a mixed spherulite, i.e., a banded spherulite converting to the non-banded morphology at the growth front.

Figure 13. Optical micrographs of blends crystallized at 424 K: (a) 60.9 and (b) 72.8 vol. % PVF_2.

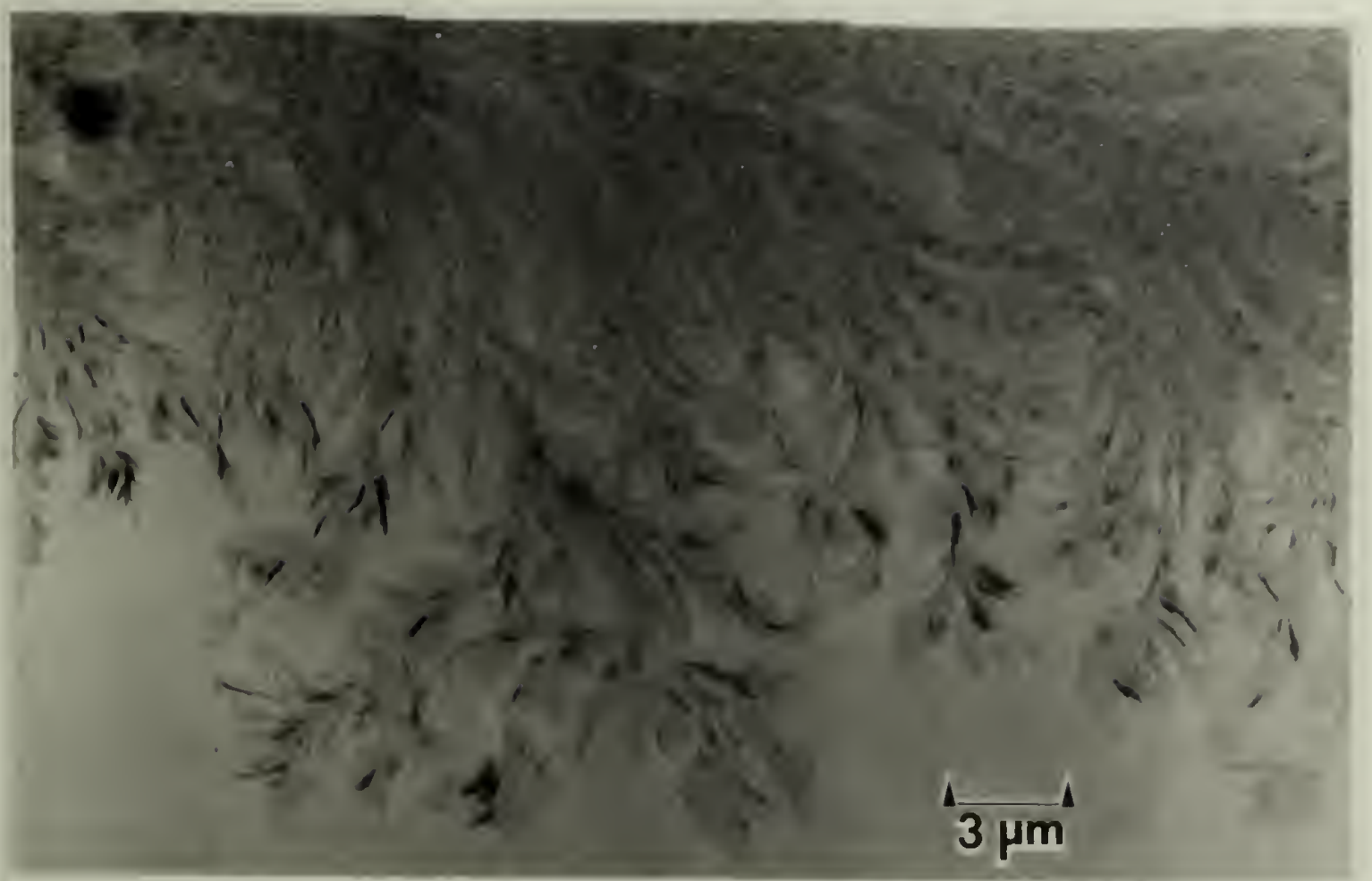

Fig. 12

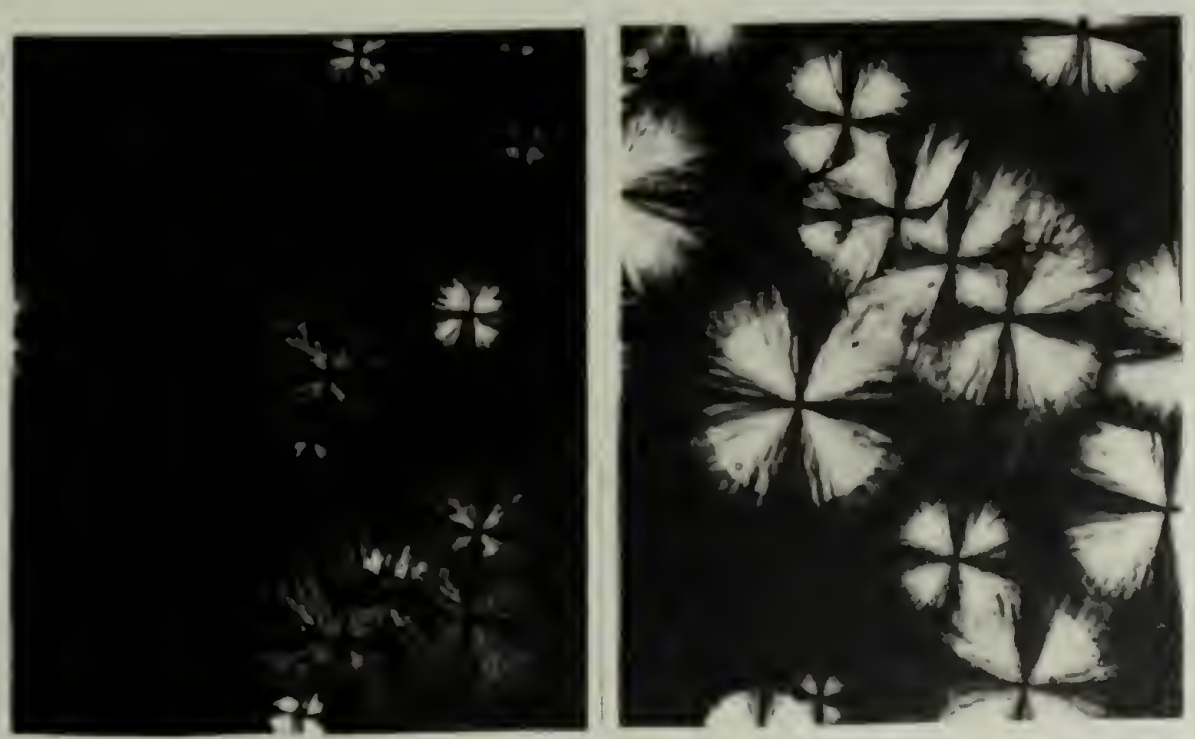

Fig. 13

of a delay. 50.1 % samples only had the weakly birefringent spherulites. 85.8 % samples did not show two fronts in one spherulite but had a population of the banded spherulites which were slightly less birefringent than the rest. All the spherulites in the pure PVF_2 were the same. In all cases, the entire spherulite melted at the same temperature and was all of the α type. It is difficult to postulate this as being due to secondary crystallization since it occurs in such a well-defined movement. At present, however, no satisfactory explanation for this phenomenon can be offered.

3. Selected area electron diffraction and WAXD. Electron diffraction and WAXD were used to elucidate the types of crystals present in the samples. Figure 14 is a selected area electron diffraction pattern from a banded spherulite which can be indexed to the α crystalline form. Note that there are three sets of diffuse reflections represented by thick lines and indexed with parentheses in the diagram. These reflections belong to small β crystals embedded in the α spherulite. These could have resulted from small strain put on the sample during preparation, which would convert α to β crystals. The only place β crystals were seen in any of the samples was the small crystallite regions imbedded in large α spherulites. No β

Figure 14. Electron diffraction pattern of PVF_2 grown at 436 K, α form (and some β form indexed with parentheses).

Figure 15. γ form electron diffraction pattern taken from a coarse, non-banded spherulite in a 72.8 vol. % PVF_2 blend.

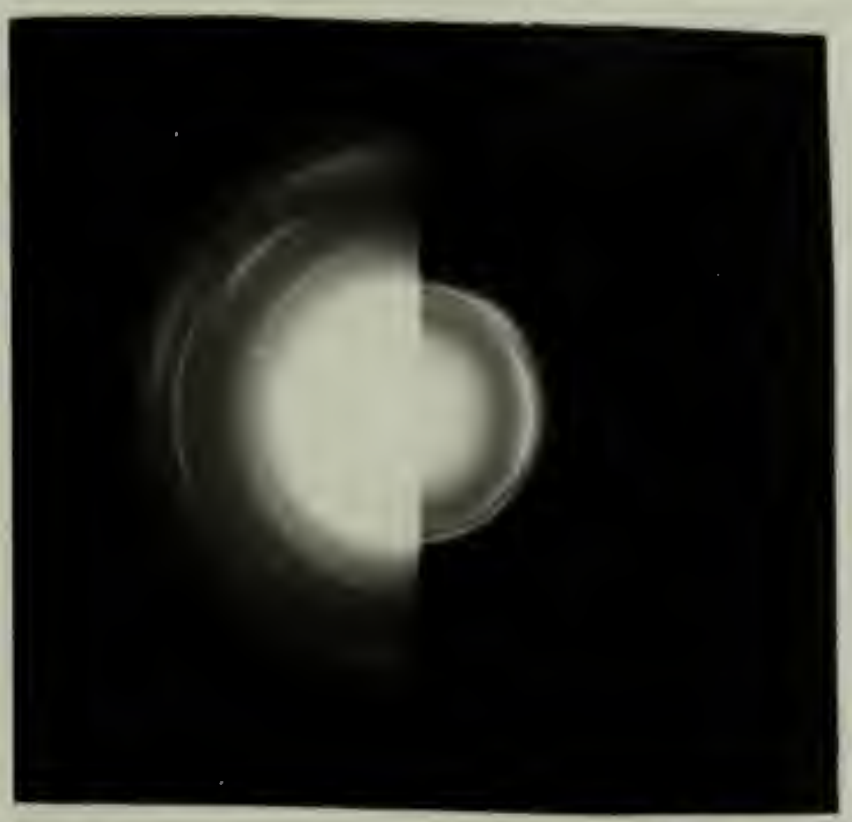
221,230
112
002
200
121
111
(001)
110
(111,201)
020
040
(200)
100
021
120

Fig. 14


111
gold
131
111
110
020

Fig. 15

form spherulites were observed.

First attempts to obtain electron diffraction patterns from the coarse non-banded spherulites were unsuccessful. The patterns were orders of magnitude weaker than the α patterns and disappeared rapidly under the electron beam. By using very low current densities, the pattern shown in Figure 15 was finally obtained. This pattern fits the latest γ form of Weinhold et al. (21) which agrees with Lovinger and Keith's (22) findings. It definitely does not fit the β crystal structure. As discussed above, these spherulites often had non-birefringent regions of platelet-like growth. Figure 16 is an electron micrograph showing the platelet-like structure in the central part of the spherulite, eventually giving way to a more typical spherulitic growth. Both regions of these types of spherulites melt simultaneously at the temperature of the second melting species. The diffraction pattern of Figure 17 is from the center portion of the spherulite in Figure 16. Here we see a spot pattern, which is indexed to the γ form, identical to that seen by Lovinger and Keith (22). In this region all the crystals are in register, therefore resulting in the much stronger scattering. Proceeding to the outside part of the spherulite, the pattern again became very weak and resembled the one in Figure 15. Often, only the first two

Figure 16. Electron micrograph of PVF_2 grown at 438.2 K for 330 hours.

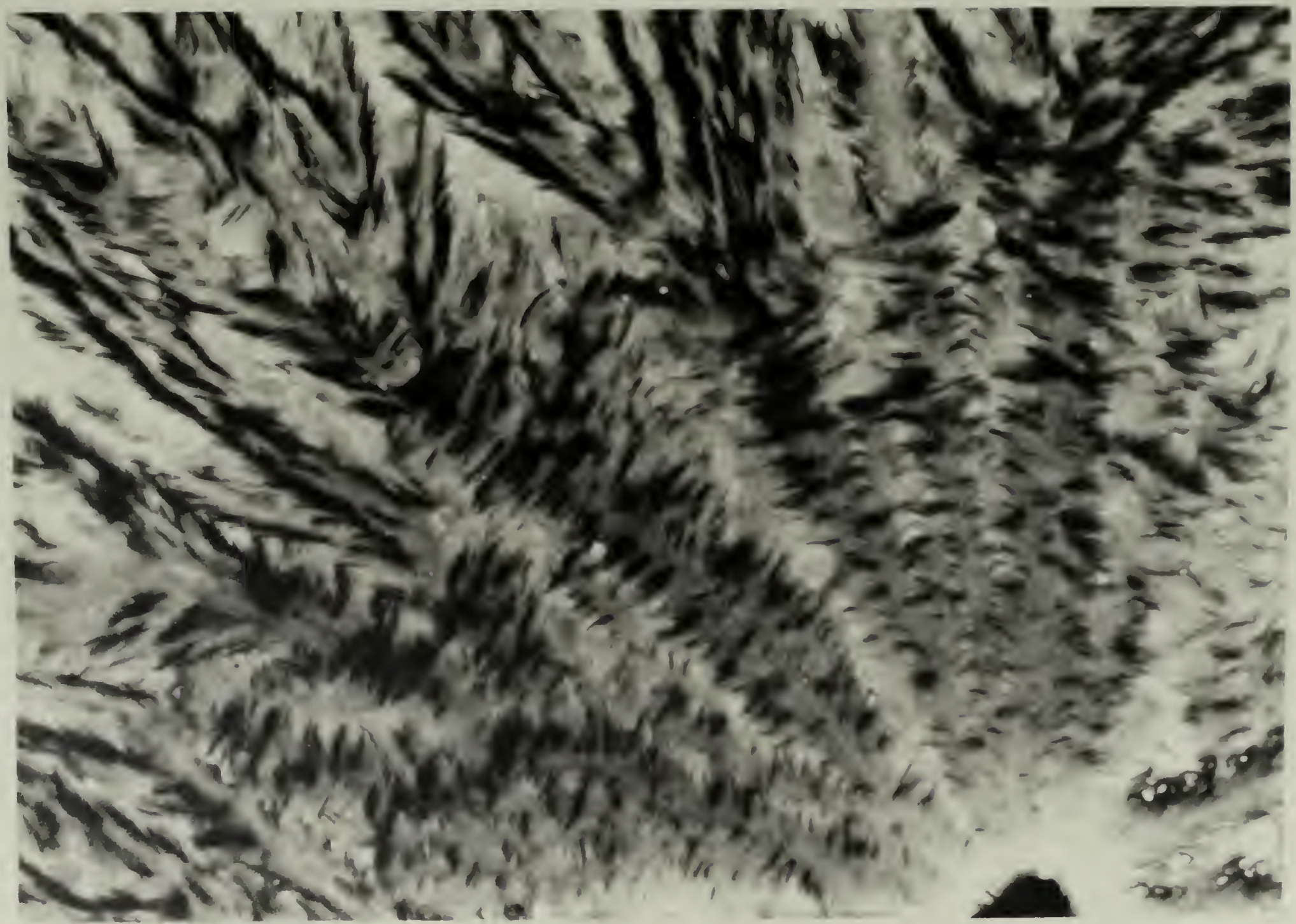
2 μm

Figure 17. γ form electron diffraction pattern from platelet like structures shown at the center of the spherulite in Figure 16.

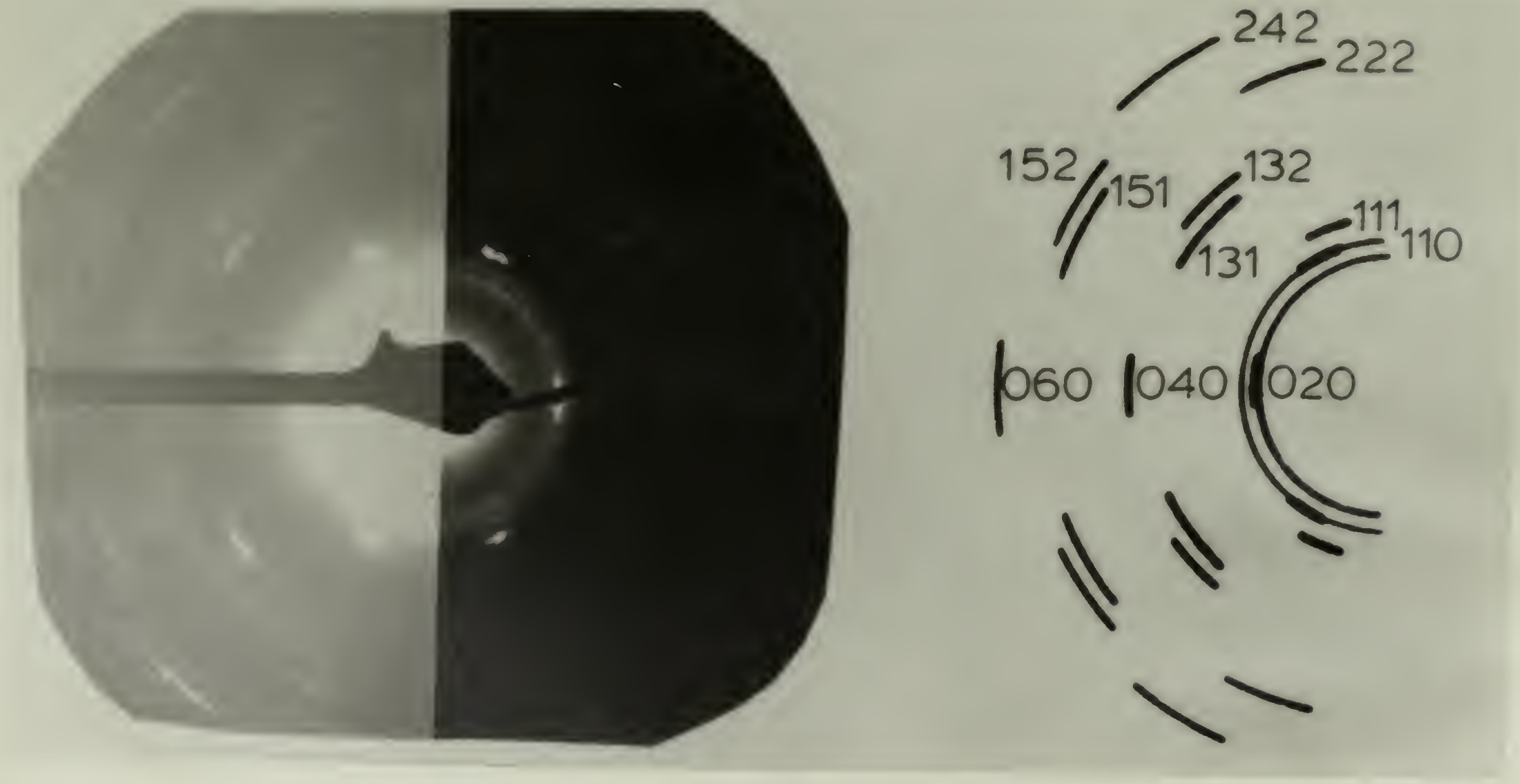
242
222
152
151
132
131
111
110
060
040
020

reflections could be seen. WAXD patterns from samples containing predominantly these types of spherulites were also very weak. Since the DSC traces did not show appreciably smaller peaks for the γ form in samples containing roughly equal amounts of α and γ crystals, it is assumed the weak pattern is due to slight disorder in the crystal and not low degrees of crystallinity.

The reason for referring to the highest melting species as the γ' form is because it too has a diffraction pattern that fits the γ unit crystal of Weinhold et al. (21), but morphologically it is totally different from the γ type spherulites which grow on their own. The γ' form, as discussed above, looks morphologically identical to the α form, and results only from a solid-solid transition from the α form. Diffraction patterns were used to distinguish α from γ' without melting.

The intensity of the γ' diffraction pattern is roughly the same order of magnitude as the α crystal form. Figure 18 shows WAXD patterns of a pure PVF_2 which is all α crystals and an 85.8% blend containing predominantly γ' crystals. Because an n-glide perpendicular to the c axis is present, hkO reflections for which h + k = odd are absent (21). The main criteria used to distinguish the transformed γ' lamellae from the α lamellae was therefore: (1) loss in the γ' form of the 100 reflection, (2) moving

Figure 18. WAXD patterns of α crystals in pure PVF_2 and an 85.8 vol. % PVF_2 blend containing predominantly γ' $_2$ crystals.

PVF_2

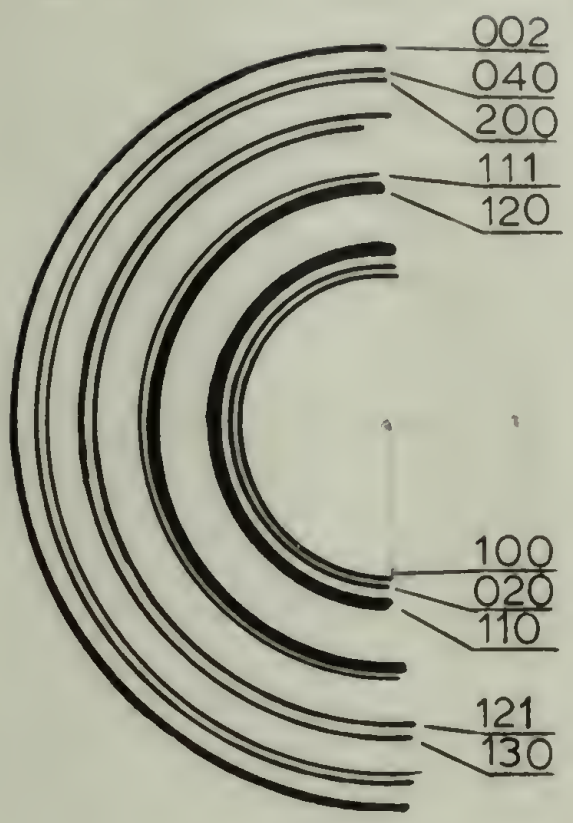

α form

85.8 VOL. % PVF_2

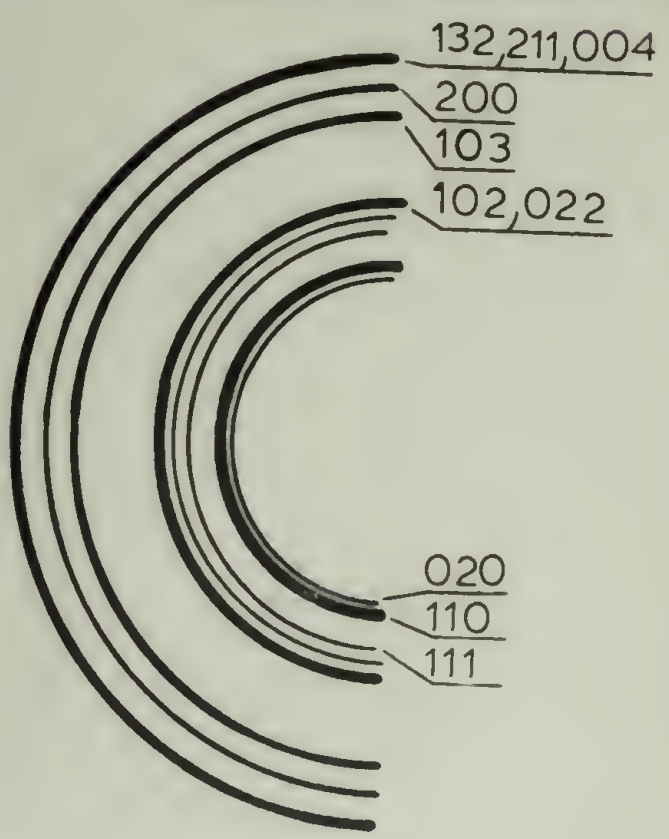

γ′ form

Fig. 18

of the 111 reflection from 0.317 nm to 0.395 nm, and (3) loss of the 121 peak at 0.277 nm in γ' crystals.

In certain samples, an unexplained reflection is observed at 0.358 nm. This occurred in both γ and γ' diffraction patterns but with no noticeable regularity. Lando (99) has also seen this reflection, as well as higher order reflections of this spacing in pure PVF_2. It does not fit any of the proposed γ unit cells and at present its appearance is not understood.

4. Conclusions. There is a wide variety of morphologies observed in PVF_2 and blends of PVF_2 with PMMA when they are crystallized at small undercoolings. Two populations of spherulites as well as axialite-like growths occur. The addition of PMMA causes the large banded spherulites to be much more disordered. Amorphous regions, probably rich in PMMA are trapped between bundles of lamellae at these crystallization temperatures. Increasing dilution of the PVF_2 also causes the small, coarse spherulites to lose their banding, increase in relative proportion to the large banded ones, and develop more axialite character. Structures which contain lamellae lying almost parallel to the film surface, thus having very low birefringence, are grown at low undercoolings.

Three melting temperature regions are observed, the highest being portions of the large banded spherulites

which have undergone a solid-solid transition, usually initiated by the coarse spherulites. In the blends, when this solid-solid transition overtook the growth front, the spherulite began growing as a non-banded spherulite and axialites thus forming mixed spherulites. The portions of the large banded spherulites not transformed were the first to melt. The small coarse spherulites (usually non-banded), axialite and low birefringence structures all melted in the second melting region.

Diffraction patterns of these structures enabled the first melting regions to be assigned to the α crystal form, and the second and third melting regions to the γ form. The highest melting species was named γ' since morphologically it was totally different from the other structures, and only resulted from solid-solid transition from the α form.

B. Lamellae in the Banded Spherulites

1. Background. Spherulites having a concentric banded structure when viewed through crossed polars have been observed in many polymeric systems. Some of the early theoretical analysis of this morphology explained the appearance of the bands as due to helical twisting of the crystalline lamellae as they grew radially outward (100-104). A schematic representation of this type of twisting is shown in Figure 19. Two hypothesis were originally

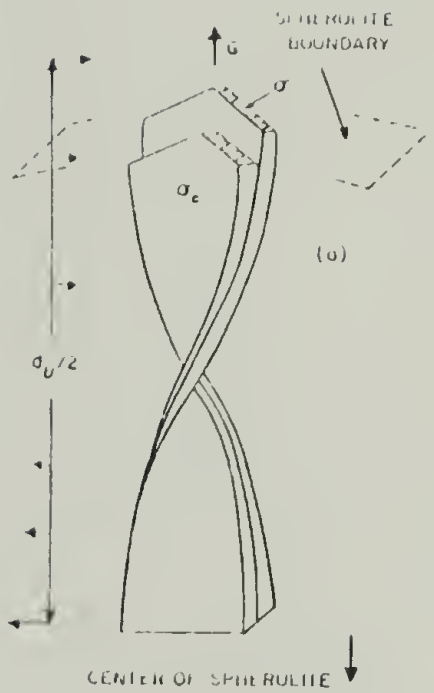

Figure 19. Schematic representation of lamellar twist (from ref. 103).

proferred to explain this phenomenon. Hoffman and Lauritzen (103) attributed the twist to the buildup of stresses on the surfaces of the crystalline lamellae from the packing of the molecular folds. The other proposal, from Keith and Padden (102), was that rejection of impurities and entanglements by the growing crystals would cause strain in the outer edges of the lamellae, which could be relieved by twisting. The latter work also suggested that the band periodicity would be proportional to a parameter $\delta = D/G$, where D is the diffusion coefficient of noncrystallizable impurities in the melt, and G is the radial growth rate of the spherulite. An additional mechanism was later proposed by Burns (105) which depended entirely on the requirements of fitting together regular, crystallographic, fold surfaces.

More recently, new schools of thought have developed which question the full twisting helical model. Breedon et al. (106), based on scanning electron microscopic studies of polyethylene spherulites, offer a model in which the lamellae consist of alternating right and left handed half twists. Kanig (107) and Low et al. (108) are skeptical that lamellar twisting is actually the cause of the observed extinction bands. As in Breedon's (106) work, Low et al. (108) studied polyethylene spherulites in a scanning-transmission electron microscope but concluded that the banded contrast is due to the occurrence of different lamellar morphologies in the light and dark bands.

Still another model has been offered by Bassett and Hodge (109) from studies utilizing the same polymer and similar techniques. They believe that the lamellae do spiral about the spherulite radius, but that this is achieved by interleaving sequences of curved lamellar units, which themselves are substantially untwisted. Each of these units is proposed to have a slightly different azimuthal orientation about the radius and a length of 1/4 to 1/3 of the band period.

Attempts to relate the periodicity of the twisting to the temperature of crystallization have also been made. Naono (110) found that a plot of extinction spacing, or band periodicity, p, vs. $1/\Delta T$ (where $\Delta T = T_m^o - T_c$) was linear with a positive slope in low density polyethylene spherulites while Lindenmeyer and Holland (111) only found linear relations in plots of ln (G·S) vs. $1/T\Delta T$ for high density polyethylene. In both studies, p increased with T_c. Lovinger (23) has also found a larger extinction spacing at higher crystallization temperatures for spherulites of PVF_2.

The extinction periodicity of polymer spherulites can also be varied by blending the crystallizable polymer with an amorphous polymer. Using samples of poly(ε-caprolactone), PCL, blended with poly(vinyl chloride), PVC, isothermically crystallized at 30°C, Khambatta et al. (112) found a linear decrease in the extinction spacing of the PCL spherulites as more of the amorphous PVC was added.

In this section, the banded spherulites of PVF_2 in blends of PVF_2 and PMMA will be examined. Changes in p as a function of both temperature and composition will be followed. Using electron diffraction, orientation changes of the crystals will be viewed as a function of radial position in the spherulite. The larger scale branching of the lamellae will also be shown to result in some very interesting light scattering patterns.

2. Results and discussion. As discussed in the previous section on morphology, banding can be seen in both α and γ spherulites of PVF_2 over a certain temperature and composition range. Since the γ spherulites are not banded at high crystallization temperatures, and the range for which the γ spherulites are large enough to show consistent banding is rather small, the α spherulites were utilized for this study. It should be mentioned that many of these spherulites have undoubtedly undergone some transformation to γ' crystals in the sample studied. This transformation, however, involves no changes in the observable morphology and therefore will not alter the results.

Lamellar orientation within these spherulites will be viewed from both a smaller scale, giving rise to the extinction bands, as well as a larger scale, causing branching of groups of lamellae.

a. Banding periodicity. The average periodicities

of the extinction bands in the spherulites were measured both in the optical microscope between crossed polars and by wide angle light scattering. For the optical microscope studies averages over several spherulites were taken. In the light scattering technique an average spacing is obtained by applying Bragg's law (113) to the diffraction rings observed. Diffraction rings typical of the samples studied can be seen in the wide angle light scattering patterns of Figure 33c and d. Bragg's law states that the average spacing between scattering entities, d, is related to the angle of the scattering maxima θ_m by

$$d = n\lambda/2 \sin \theta_m \qquad (1)$$

for radiation with wavelength λ, where n is the order of the reflection. Therefore the angle of the diffraction ring will give p. Further discussion of other features in the light scattering patterns will be presented in a later section.

The change in p as a function of the volume fraction of PVF_2, v_2, is shown in Figure 20 for the crystallization temperatures. Contrary to the PVC/PCL case, the banding periodicity increases as more of the amorphous polymer is added, and the change is certainly not linear with composition. Raising the crystallization temperature is also seen to result in larger extinction spacings.

Since there is little known about these extinction

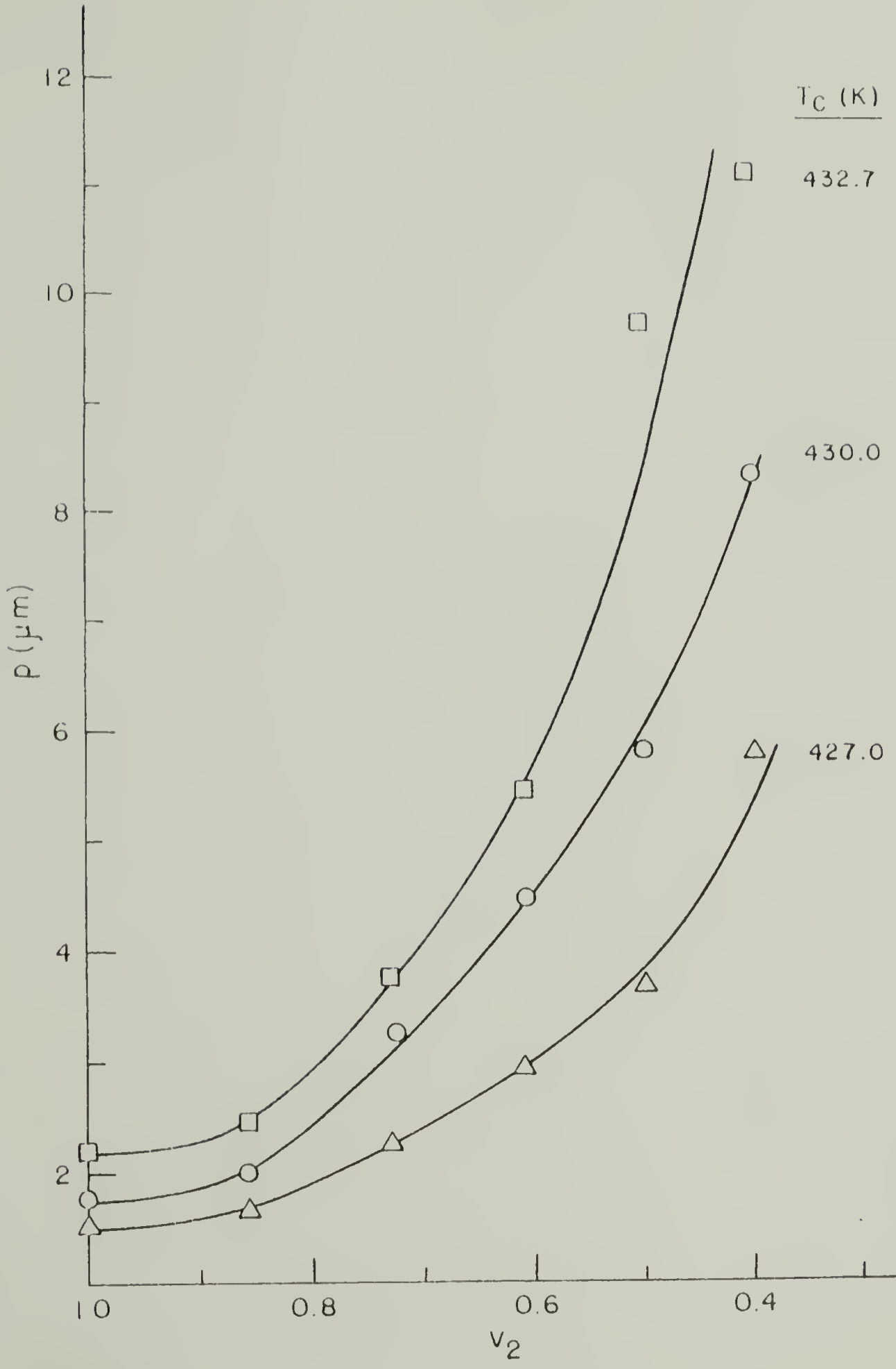

Figure 20. Extinction spacing p, as a function of volume fraction PVF_2, v_2, at three crystallization temperatures.

bands, and much controversy over what has been observed, an attempt to find some kind of correlation between p, T_c, and composition was made. Plots of the value of p measured vs. T_c are shown in Figures 21-26 for all six samples. There was very good agreement between the measurements from light scattering and optical microscopy. As can be seen from these plots, the basic shapes of the curves are similar, though the actual values of p vary widely. It was noted that as T_c was lowered, the values of p appeared to approach a lower limit. This was more obvious for the blends containing higher percentages of PMMA. For example, the plots for the 50.1 and 40.1 volume % PVF_2 samples seem to become independent of T_c and are very flat in the low temperature range. Though it is difficult to determine the lower limit of p in the PVF_2 rich systems, it appears that this limiting value increases as more PMMA is added. This would imply that the PMMA within the spherulites is either (1) interfering with the lamellae so that they cannot reorient as much as they normally might; or (2) that, acting somewhat like a lubricant, it is reducing the stresses and helping the fit of the lamellae so that the driving force for reorientation is not as great.

Following suggestions of some of the studies cited above, plots of p and ln(p) vs. $1/T_c$, $1/\Delta T$ and $1/T_c\Delta T$ were prepared for each sample. The values for T_m^o were determined from Hoffman-Weeks (114) plots using samples with

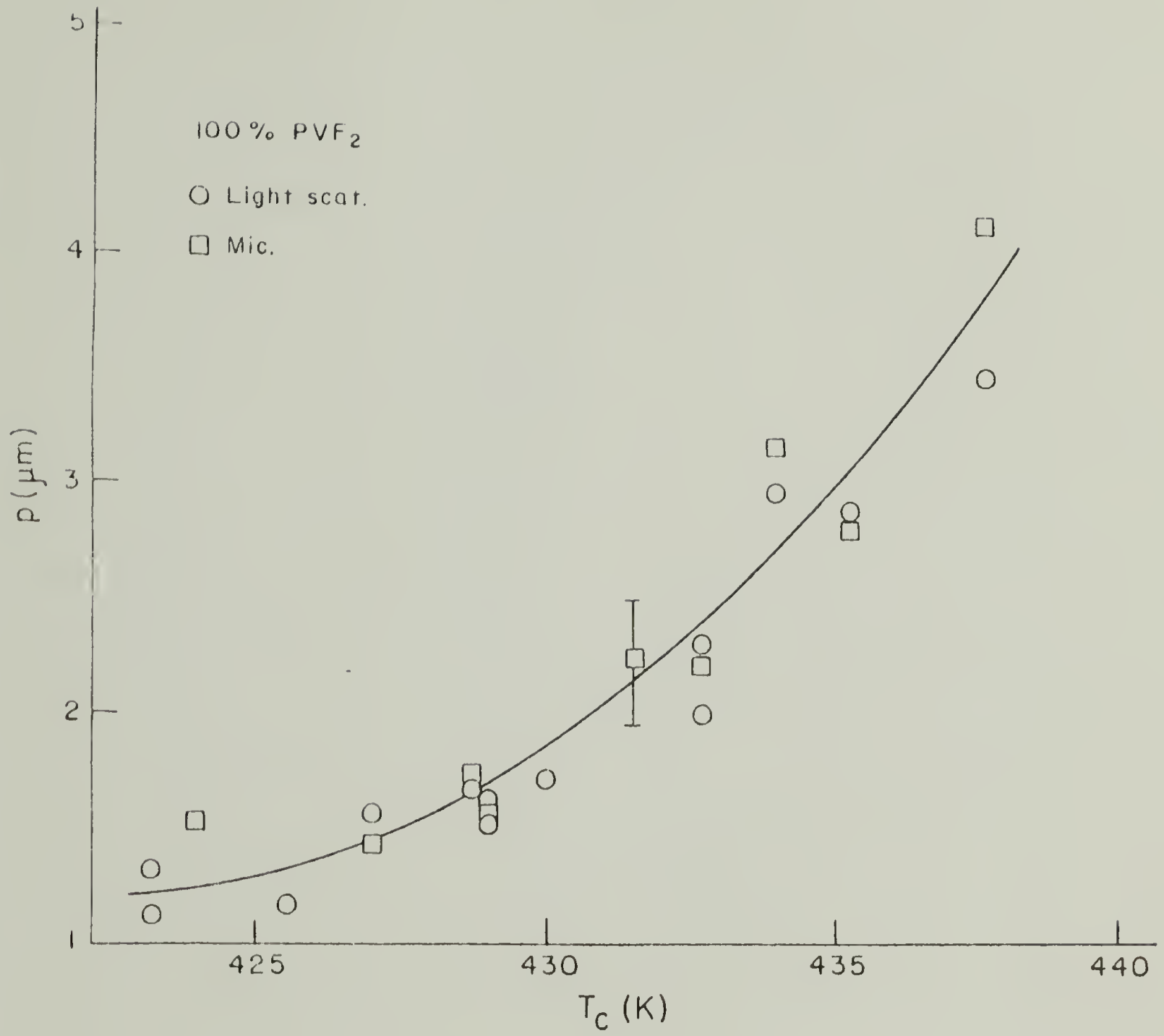

Figure 21. Extinction spacing p, vs. crystallization temperature for 100% PVF_2.

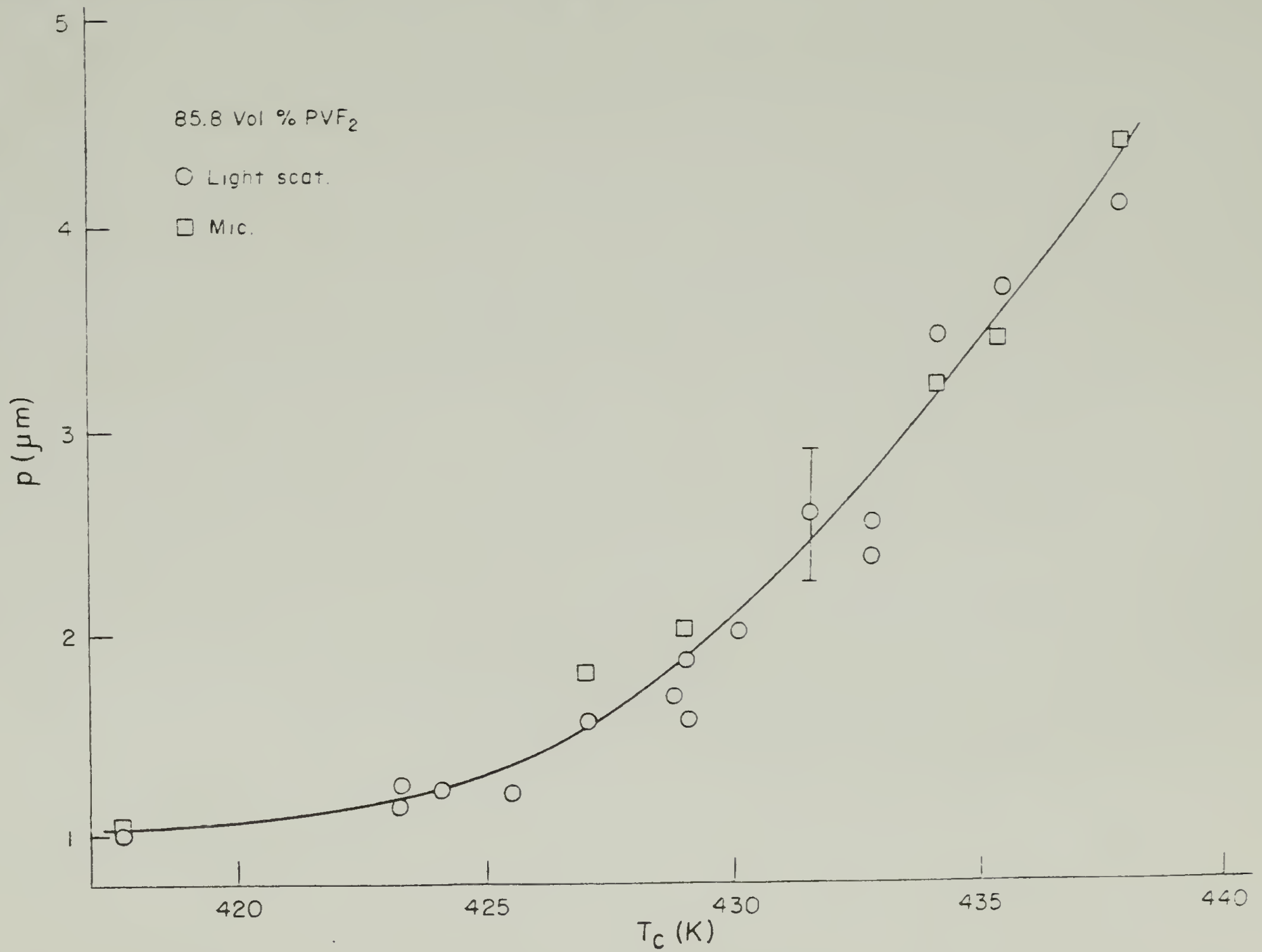

Figure 22. Extinction spacing p, vs. crystallization temperature for 85.8 vol. % PVF_2 blends.

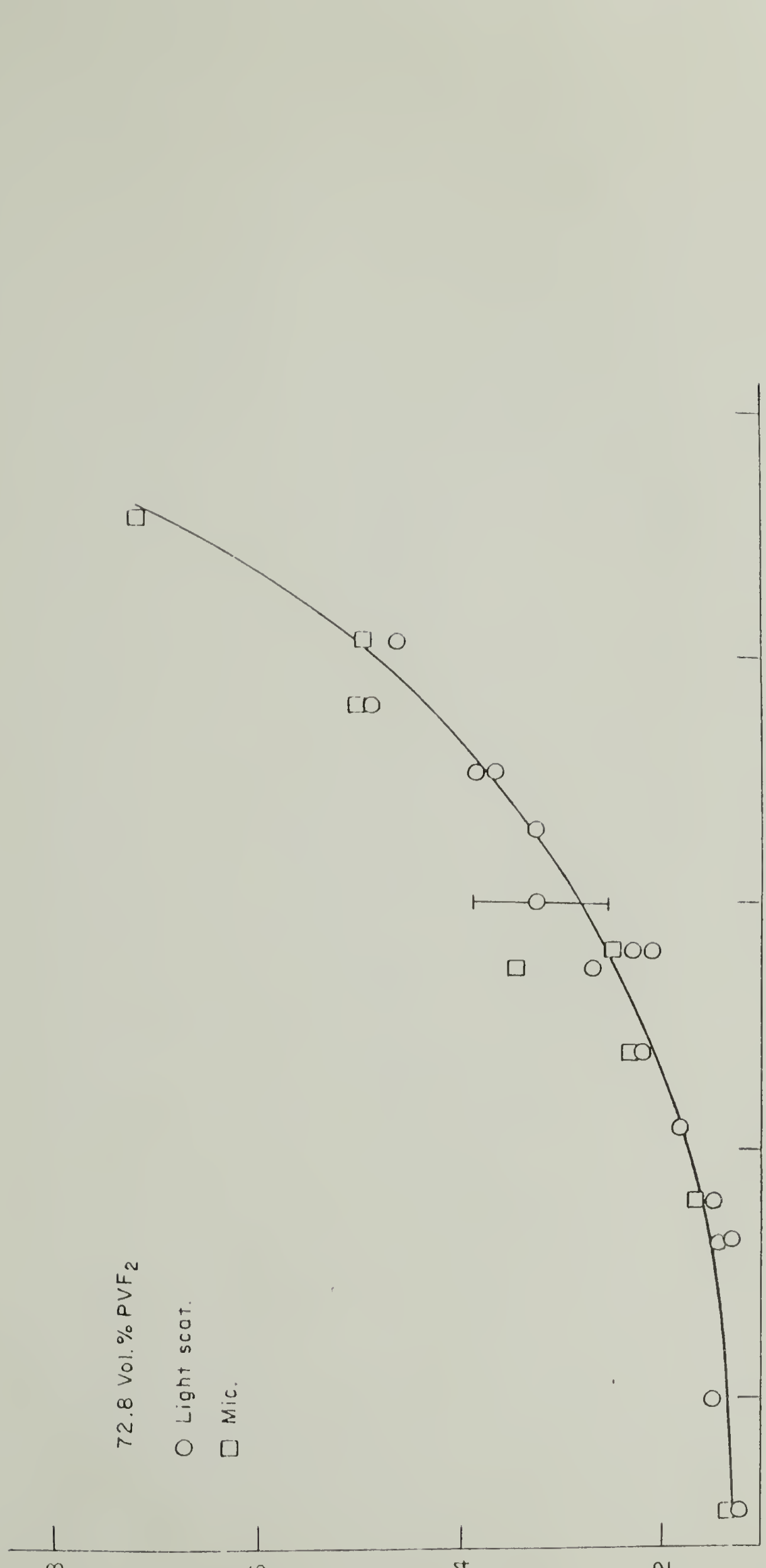

Figure 23. Extinction spacing p, vs. crystallization temperature for 72.8 vol. % PVF_2 blends.

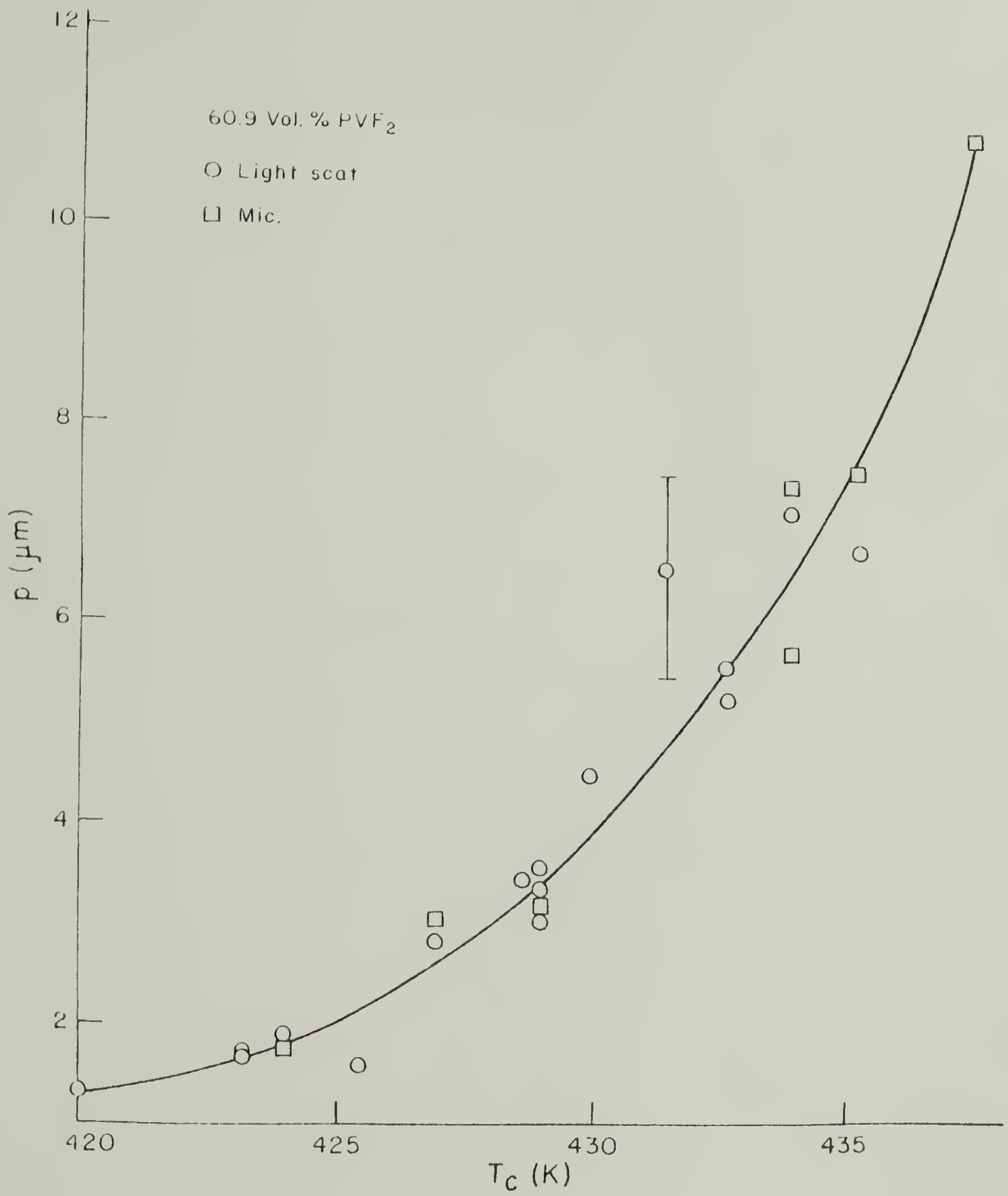

Figure 24. Extinction spacing p, vs. crystallization temperature for 60.9 vol. % PVF_2 blends.

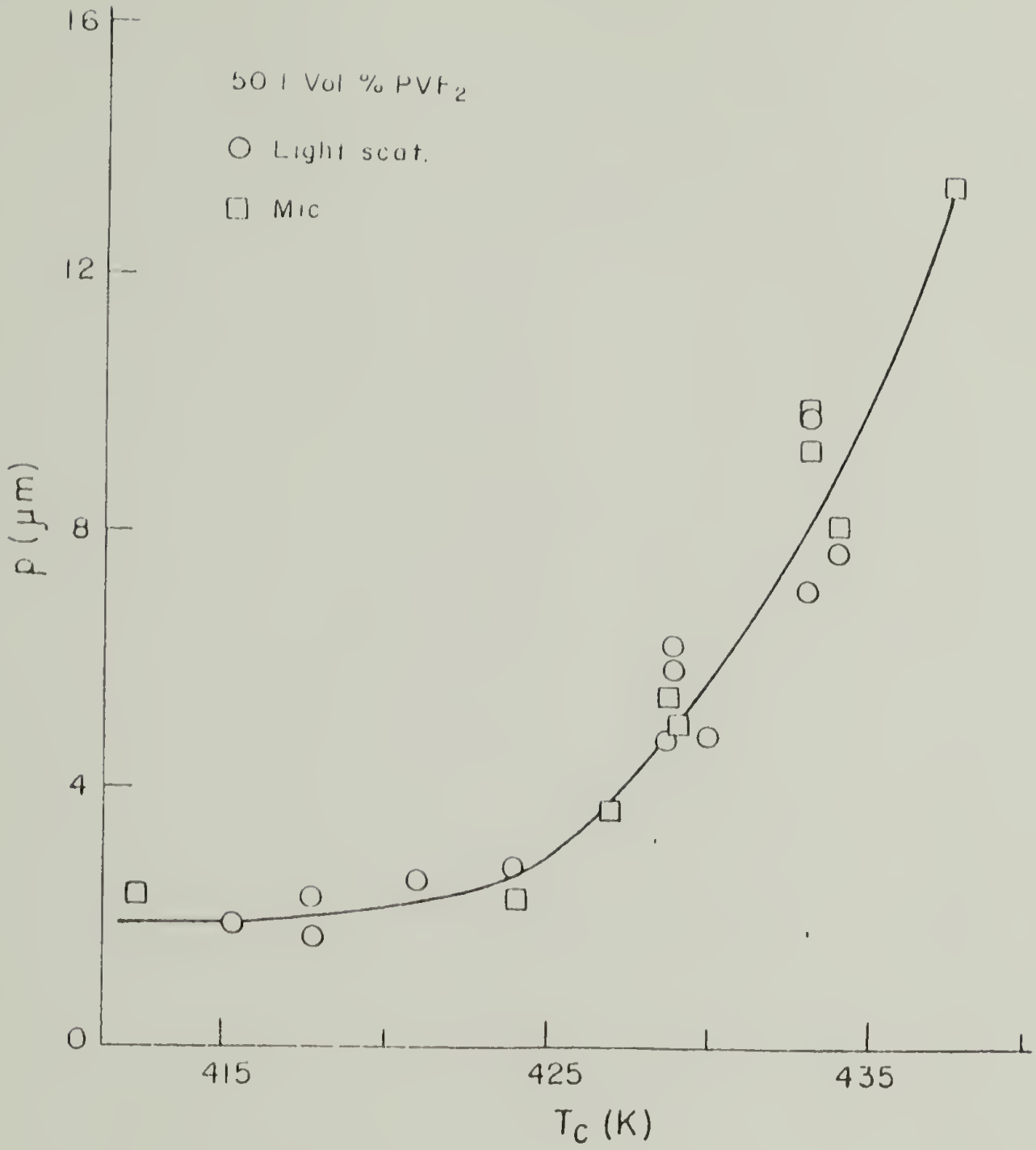

Figure 25. Extinction spacing p, vs. crystallization temperature for 50.1 vol. % PVF_2 blends.

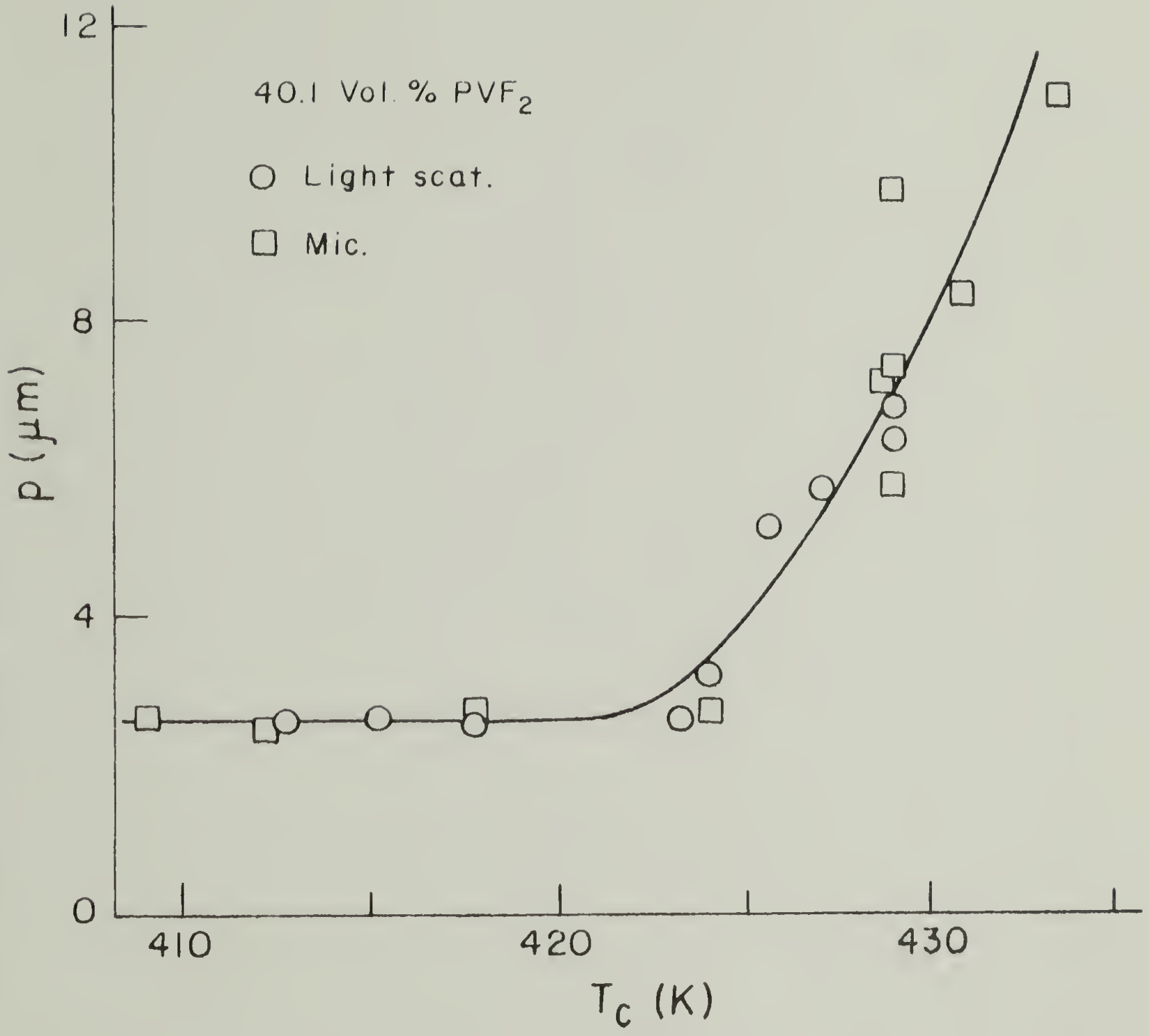

Figure 26. Extinction spacing p, vs. crystallization temperature for 40.1 vol. % PVF_2 blends.

high crystallization temperatures. This data is presented in Table 2, and will be discussed in detail in the following chapter. Plots of ln(p) vs. $1/T_c\Delta T$ were S shaped for most samples. Plots of ln(p) vs. $1/T_c$ or $1/\Delta T$ were linear in the high T_c region. Deviations from linearity were observed in both the $1/T_c$ and $1/\Delta T$ plots as p approached its lower limiting value discussed above. However, these deviations were slightly larger for the ln(p) vs. $1/T_c$ plots. It was also noted that when the data for all the samples was plotted together, the ln(p) vs. $1/\Delta T$ plots superimposed rather well to give what might be called a master curve. This is shown in Figure 27. As can be seen, the lower temperature data, especially for the more dilute blends, was not in good agreement. This is where p seemed to approach the lower limiting value. Without counting these points, a straight line can be drawn through the remainder of the data. The exact meaning of this type of plot is unclear at present, but it is noteworthy that p seems to be a function of only the undercooling, and not the composition at high crystallization temperatures, while the limiting value of p at low crystallization temperatures becomes independent of T_c but does vary with composition.

In an attempt to quantify Figure 27, one can view it as an activation energy plot. In this regard, the relationship between p and ΔT might be given as

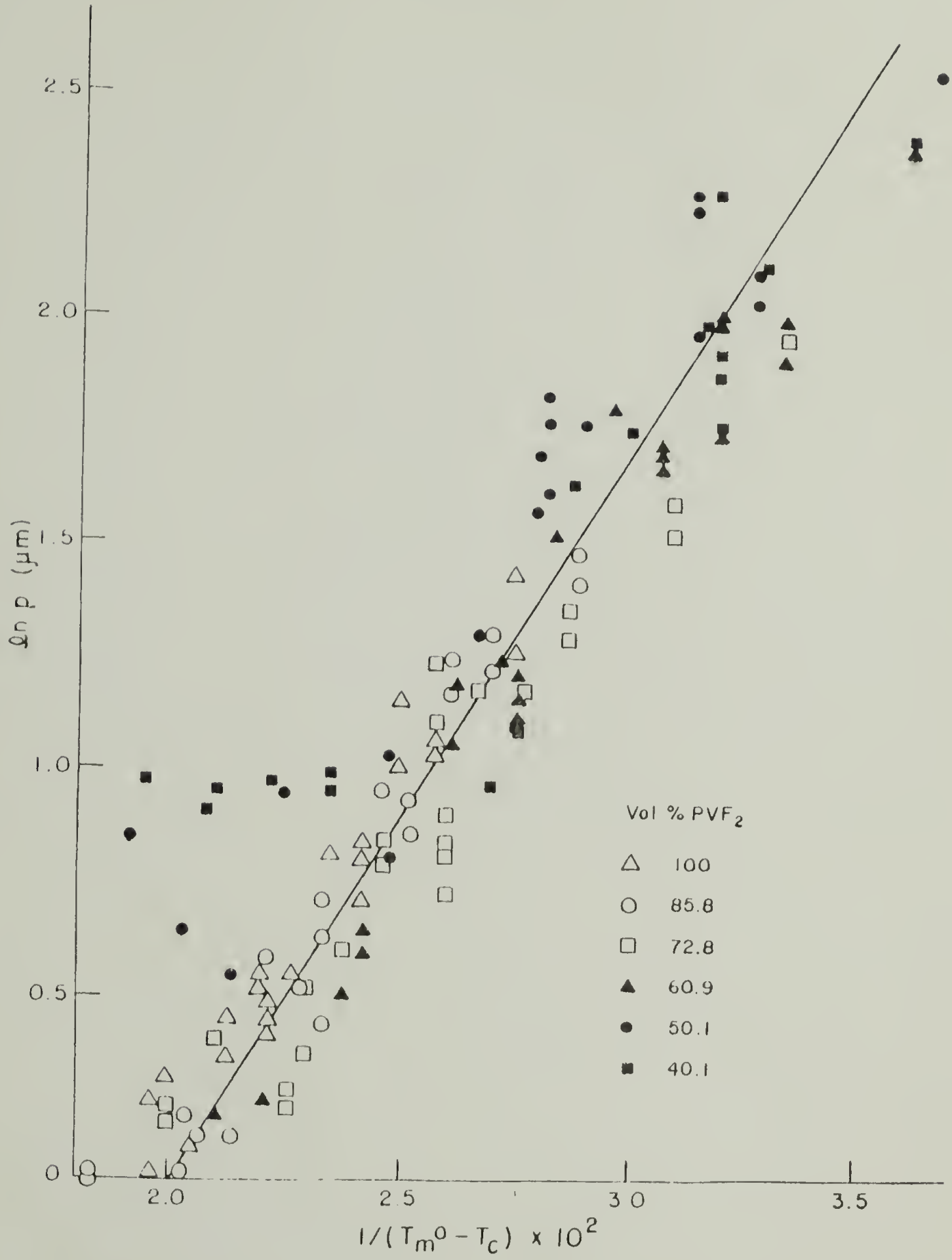

Figure 27. Master curve of ln (p) vs. 1/ΔT.

$$p = p_0 \exp\left(\frac{E}{R\Delta T}\right) \qquad (2)$$

where E is an activation energy. The straight line fit in Figure 27 has a slope of 162 and an intercept of -3.13. Analyzing this in terms of equation 2 would give values for E and p_0 of 322 cal/mole and 0.0438 μm respectively. A possible interpretation of E might be the amount of energy that is relieved by having the lamellae reorient. The value of p_0 could be the extinction spacing a spherulite would have if it were crystallized at T_m^o.

b. μ, μ diffraction. Using the μ, μ diffraction technique and controlling the beam with the free lens control, diffraction patterns as a function of radius in a banded α spherulite were taken on the STEM. Each pattern was taken from a circular area about 670 nm in diameter without damaging the surrounding regions. Figure 28 is an electron micrograph of one of the regions from which a series of patterns was taken. This sample was 72.8 volume % PVF_2 crystallized at 431 K. The line of connected circles running across the picture horizontally is the area damaged by the beam when a diffraction pattern was taken. Each circle represents the area for one pattern. These circles are in a line along the radius of the spherulite. They cover approximately one and a half band periods, as can be seen by the alternating light and dark regions they

Figure 28. STEM micrograph of 72.8 vol. % PVF_2 sample crystallized at 431 K for 165 hours. The circles are the areas from which diffraction patterns were taken.

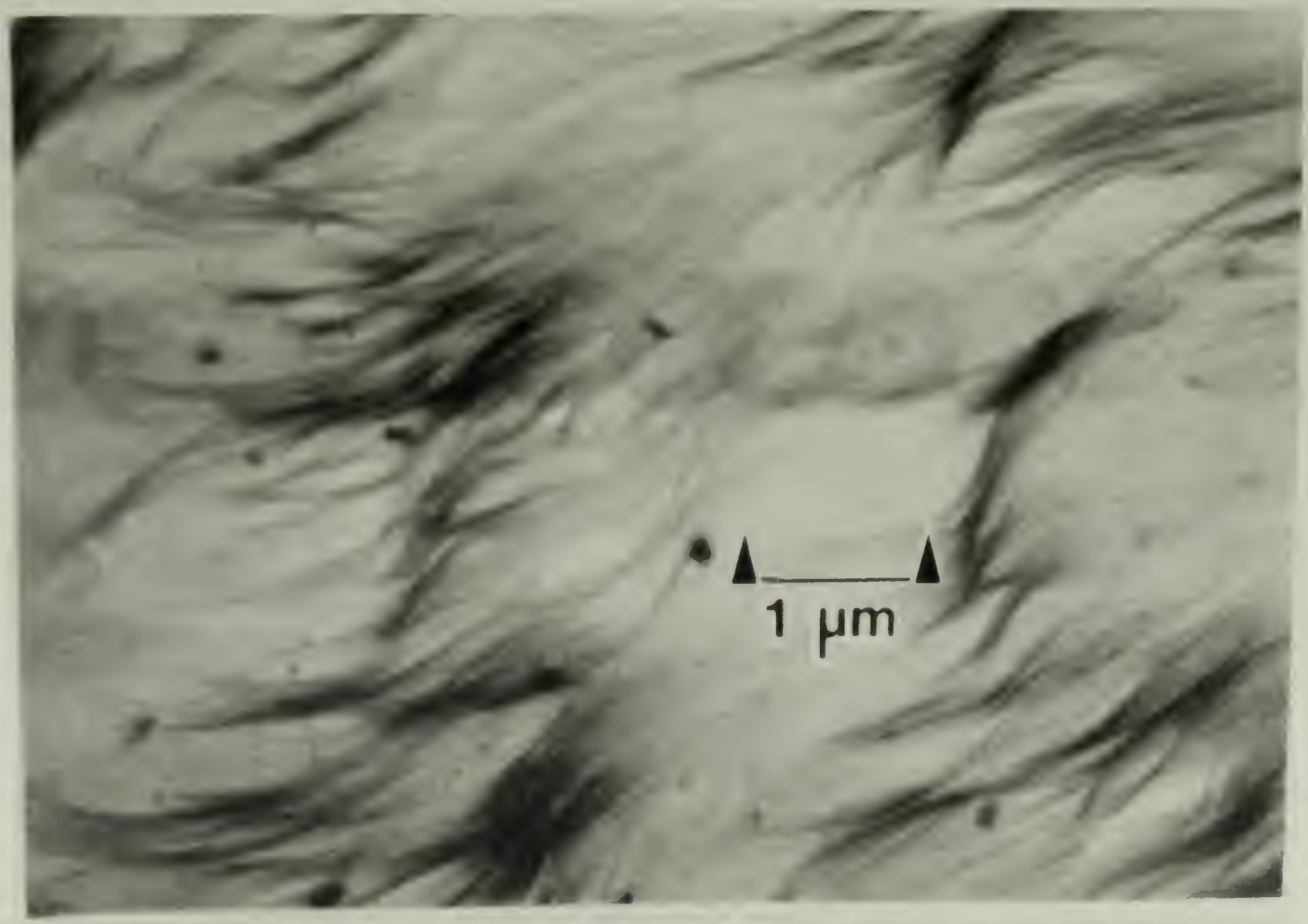

Fig. 28

traverse.

Since the diffraction patterns are taken from such a small area containing relatively few crystals, the beam flux must be very high. However, this higher intensity causes a rapid loss of the pattern due to radiation damage. Therefore the patterns were very weak as compared to the selected area diffraction patterns of these spherulites, presented in an earlier section, which were taken over much larger regions. The thickness of the sample was also an important parameter. Because there was a larger volume diffracting, thicker samples gave a stronger pattern. This was only true up to the limit at which the sample became so thick (usually greater than a few hundred nm) that transmission of the beam was severely retarded. On the other hand, the quality of the image was usually better in the thinner samples. Therefore there was a trade-off between the image and the diffraction pattern. For this reason, the diffraction patterns from the thin area used for Figure 28 were poor, though it is a good image with which to illustrate the technique. Better patterns were obtained from a sample prepared identically, but with a thickness two to three times that shown in Figure 28. An image of this sample along with representative diffraction patterns is shown in Figure 29.

The circles representing the regions from which diffraction patterns were obtained are more difficult to

Figure 29. STEM micrograph of a 72.8 vol. % PVF_2 sample crystallized at 431 K for 165 hours. Diffraction patterns were taken from the numbered circular regions. Representative patterns are shown.

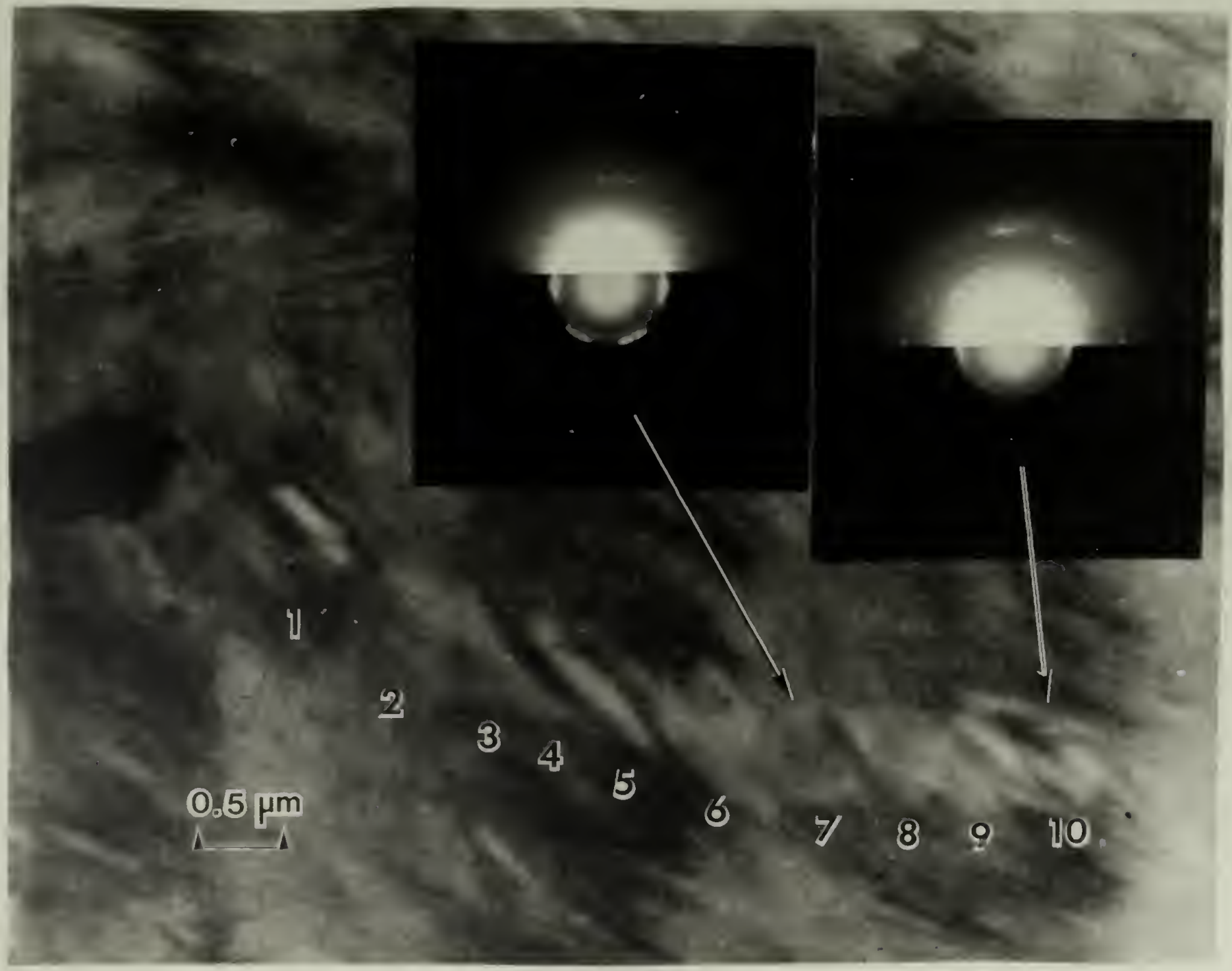

Fig. 29

see in this picture and were therefore numbered from 1 to 10. As before, these were taken along the radius of the spherulite. The patterns recorded from this sample are still very weak, but were the best obtainable using the μ, μ conditions. The two patterns shown in Figure 29 are representative of those from the center of a light band, region 7, and dark band, region 10, separated by approximately a half band period. An obvious change can be seen.

A schematic of the diffraction patterns from each of the ten regions is presented in Figure 30. All of these patterns can be indexed to the α crystal all with different orientations. The 020 and 040 reflections, which appear in all patterns, indicate that the b axis of the unit cell is oriented radially, and that the crystals twist about this axis. The alternation between strong 110 and strong 021 reflections corresponds to the c axis and a axis respectively, being oriented perpendicular to the plane of the figure. The patterns where either one or both of these appear as weaker reflections along with several other reflections can be related to various degrees of tilt of the unit cell. Figure 31 shows a representation of how the c and a axis of the unit all would appear for each area of Figure 29 if one were to view it along the radius of the spherulite. From Figure 31 it can be seen that the unit cell twists about the radius. It cannot be determined, though, whether it is a full twist or two opposite half

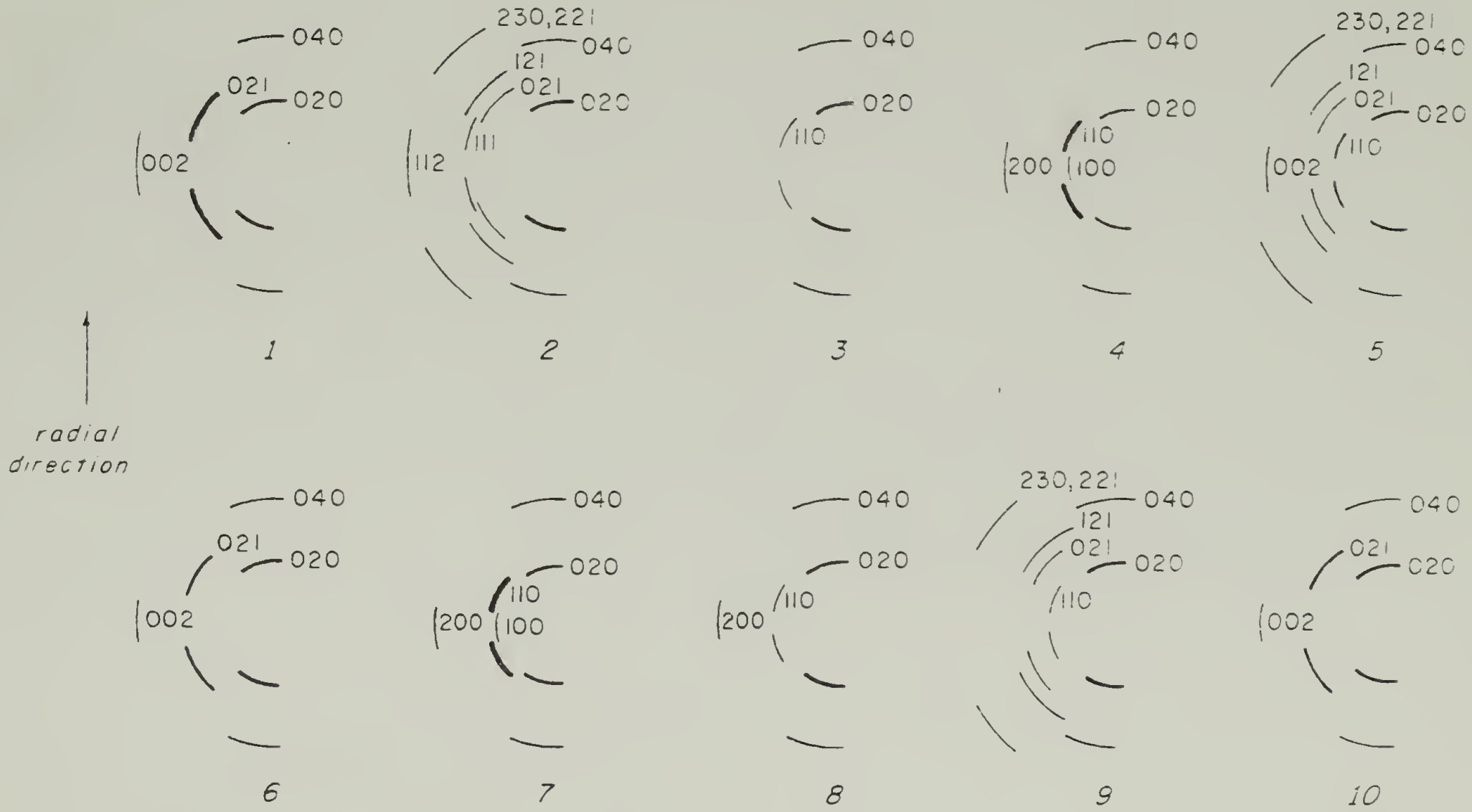

Figure 30. Schematic diagrams of the diffraction patterns from the circular regions labelled 1 to 10 in Figure 29.

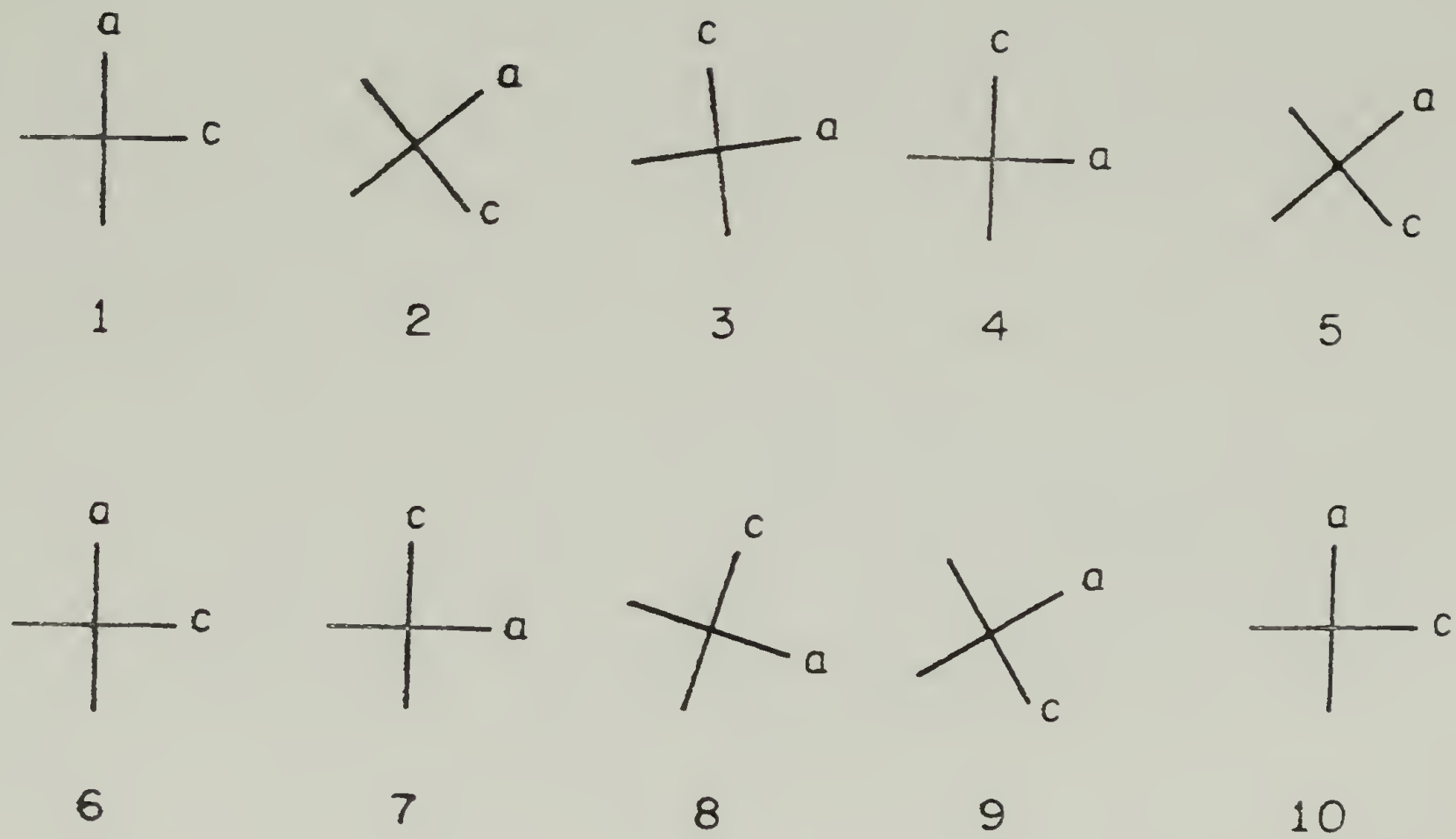

Figure 31. Representation of the a and c crystal axis orientation as viewed along the spherulite radius. The numbers correspond to those in Figure 30 and the number regions in Figure 29.

twists. This twisting can be related to alterations in lamellar orientation. The light and dark bands in the STEM images represent the lamellae being viewed lying parallel and perpendicular to the surface respectively. Changes in the lamellar orientation from the images agree with changes in the orientation of the unit cell from the diffraction patterns. This is to be expected if the unit cell is assumed fixed in the lamellae. Therefore, the lamellae themselves must twist about the spherulite radius.

c. Light scattering. The experimental arrangement for solid state light scattering of thin films is shown in Figure 32. The incident beam s_0 passes through a polarizer and impinges upon the sample. The scattered beam s_1, coming off the sample at the scattering angle θ and an azimuthal angle μ, passes through an analyzer and is then recorded on a photographic plate. For vertical polarization in both the incident and scattered beams, the scattering pattern is designated V_V, while for horizontal polarization of the scattered beam and vertical polarization of the incident beam, it is designated H_V. Both wide angle and small angle patterns for H_V and V_V polarizations were recorded using a laser source. Examples of these for a 72.8 volume % PVF_2 blend crystallized at 429 K are shown in Figure 33.

The small angle H_V scattering gives a four leaf

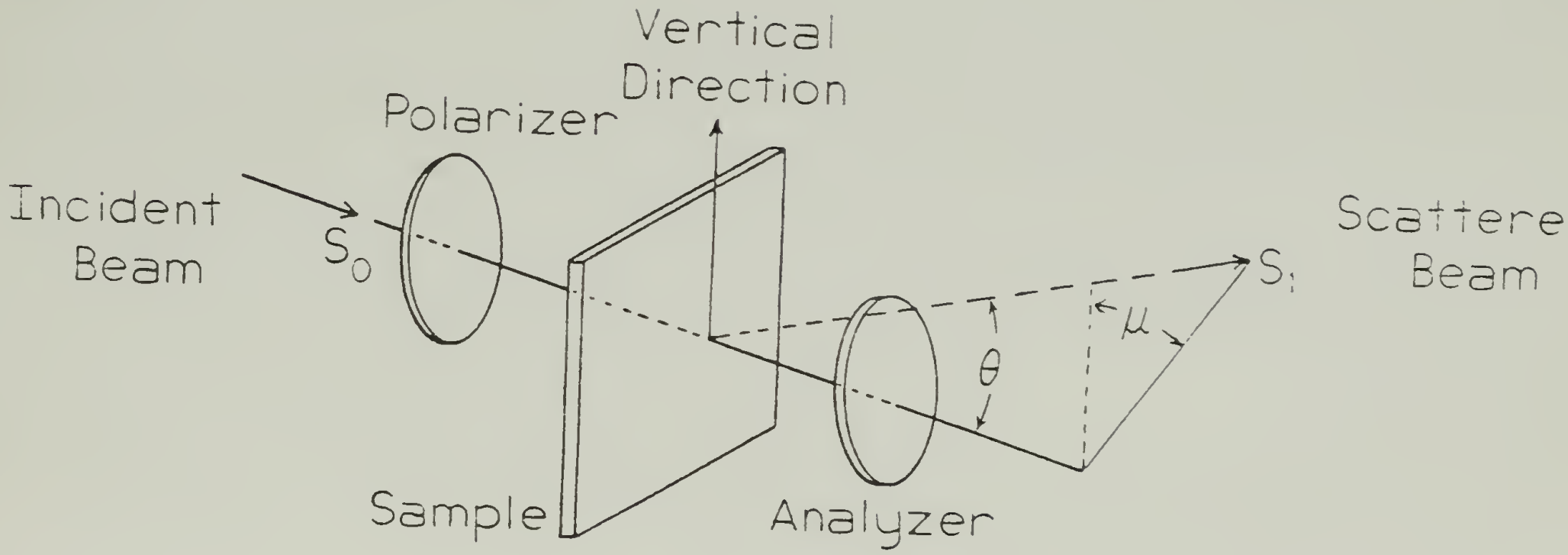

Figure 32. Schematic of light scattering experiment.

Figure 33. Conventional light scattering patterns for a 72.8 vol. % PVF_2 blend crystallized at 429 K, (a) small angle H_V, (b) small angle V_V, (c) wide angle H_V, (d) wide angle V_V.

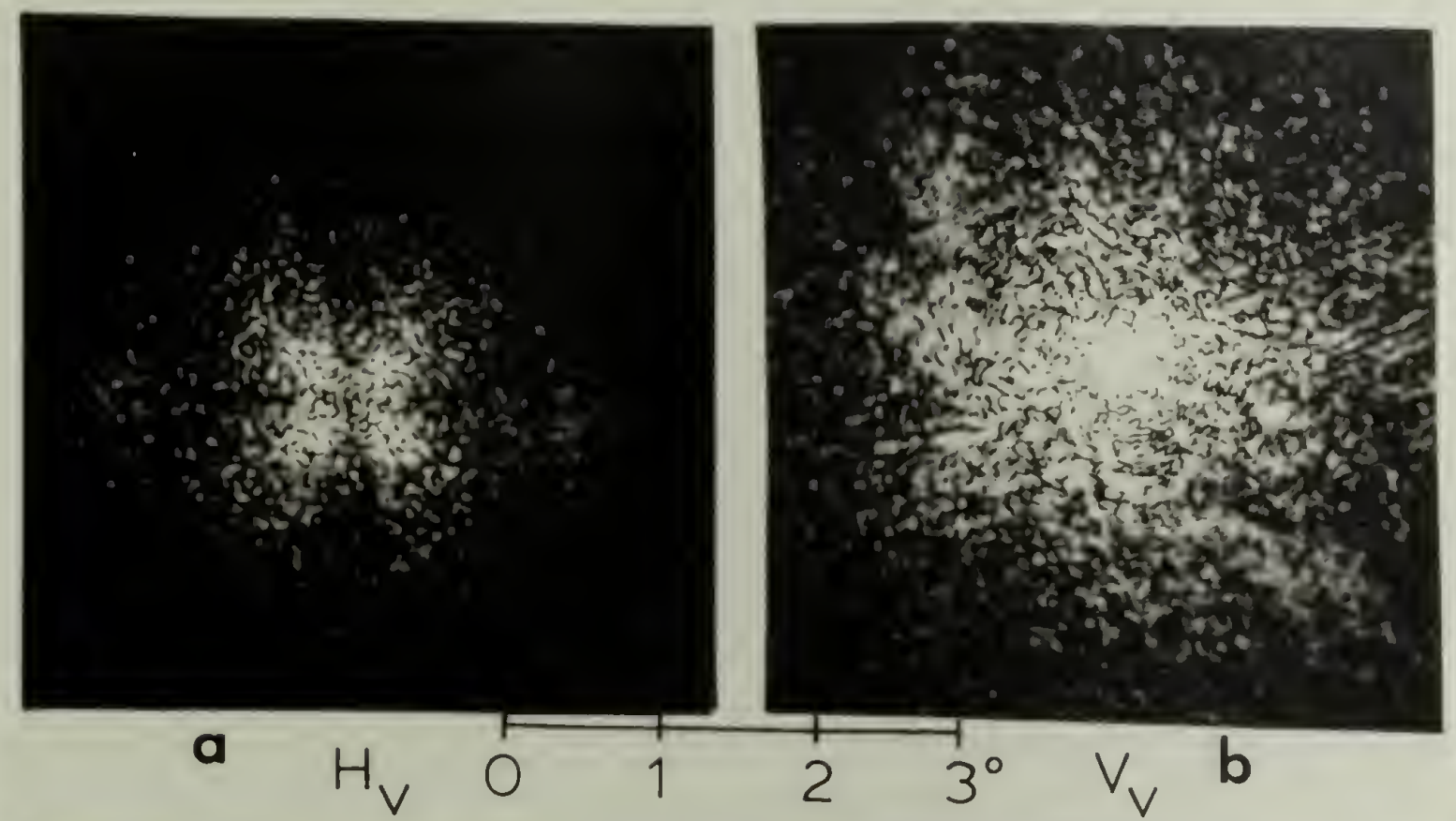

Fig. 33

clover pattern with the lobes at odd multiples of 45° in the azimuthal direction. This is typical of H_v light scattering patterns from spherulitic polymer films and has been thoroughly analyzed by Stein and coworkers (115-118). According to their analysis, the V_v pattern should have two lobes along the polarization direction. However, these are not seem in Figure 33b. The lack of these lobes in the small angle V_v pattern can be understood if one looks at the different polarizabilities in the spherulites. The polarizabilities of the spherulites in the radial, P_r, and tangential, P_t, directions, as well as the average polarizability of the surrounding medium, P_s, determine the small angle light scattering patterns. The V_v pattern is a function of $(P_r - P_t)$ and $(P_t - P_s)$, while the H_v pattern is only a function of the former quantity. In the V_v patterns, the former quantity contributes the two lobed anisotropic scattering while the latter adds intensity which is azimuthally independent. If the latter dominates, the V_v pattern produced could be similar to the one seen in Figure 33b. Samuels (119) has performed computer calculations of light scattering patterns and under conditions where $(P_t - P_s)$ is much greater than $(P_r - P_t)$ obtained similar V_v patterns.

The small angle patterns were similar for all of the samples. Sizes and intensities did vary, but the shapes remained constant. The variation of the maximum in

the θ direction for the H_v patterns can be related to the average spherulite radius (115-118), and was therefore dependent upon the composition and crystallization temperature of the sample.

The wide angle scattering patterns of Figure 33 have two features of interest. The first is the diffraction rings at a scattering angle of approximately 13° in this sample. These are due to the periodicity of the extinction bands in the spherulites and have been discussed previously. Secondly, the maxima in the azimuthal direction for the scattered intensity in the H_v wide angle patterns are along the directions of the polarizer and analyzer. This cross pattern is not common in spherulitic polymers and will be discussed below.

Looking at the wide angle patterns from different samples, other than the variation in the position of the diffraction rings, all the V_v patterns were similar. The wide angle H_v patterns, however, did change. The patterns were not the same over all parts of a given sample. With the beam hitting certain portions of the sample, the cross pattern pictured was seen, whereas by moving the sample slightly, the cross would disappear. For the 72.8% sample, the wide angle H_v pattern of Figure 33 was only observed for samples crystallized between 425 and 430 K. Lowering or raising the amount of PVF_2 would lower or raise this range slightly. In the pure PVF_2 samples the maxima at

μ = 0° and 90° were often distorted to approximately 20° and 70°, and were always much less distinct.

Ignoring the diffraction rings, wide angle patterns similar to those of Figure 33 have been observed from cotton cellulose (120), collagen (121,122), poly-γ-benzyl-L-glutamate (123) and hydroxypropylcellulose (124). In those studies, the patterns were attributed to rod-like structures in which the principal optic axis is inclined approximately 45° to the length direction of the rod. Therefore, the PVF_2/PMMA samples are scattering like spherulites in the small angle region and rods in the wide angle region.

This complex type of scattering involving both spherulite and rod-like patterns was also observed in poly(tetrafluoroethylene) (122,124,125), poly(chlorotrifluoroethylene), polypropylene-polyethylene block copolymers and poly(ethylene oxide)-polyisoprene block copolymers (124). An explanation was offered (126) for these patterns utilizing theories developed for disordered spherulites (127). The model suggested that the lamellae would rotate about the radial direction and that this rotation would be macroscopically random, but locally correlated. The parameters of importance were the polar angle of the optic axis with respect to the radius of the spherulite, χ, and the ratio of the radius, R, to the correlation distance, a, of the lamellar twist. Using computer simulations of scatter-

ing patterns, the best fits to both the small and wide angle scattering patterns were obtained for χ from 65° to 70°, and R/a = 100. These values for χ imply that the polymer chains are inclined 20° to 25° with respect to the radius. This is not unreasonable for the sample studied here considering the disorder of the blend spherulites. The value of R/a is somewhat high if one assumes the correlation distance to be the extinction band periodicity, but lower values would still give reasonable agreement (126). Therefore this model describes the data fairly well.

To obtain a better understanding of the morphology giving rise to these wide angle patterns, an experimental technique was devised which would enable one to view a particular region in an optical microscope and then observe a light scattering pattern from that area alone. As described in Chapter II, selected area light scattering patterns from areas about 50 μm in diameter could be obtained. This concept is the same as that used in μ, μ STEM diffraction, but it utilizes light instead of electrons as the incident radiation. In Figure 34, images and the corresponding light scattering patterns for both H_V and V_V polarization are shown for the same sample used in Figure 33. The diffraction patterns in Figure 34 were taken from a 300 μm region. They are similar to those shown in Figure 33 except somewhat more blurred. The diffraction rings in the H_V patterns are still present but are quite a bit weaker.

Figure 34. Images and light scattering patterns obtained in the microscope for a 72.8 vol. % PVF_2 sample crystallized at 429 K.

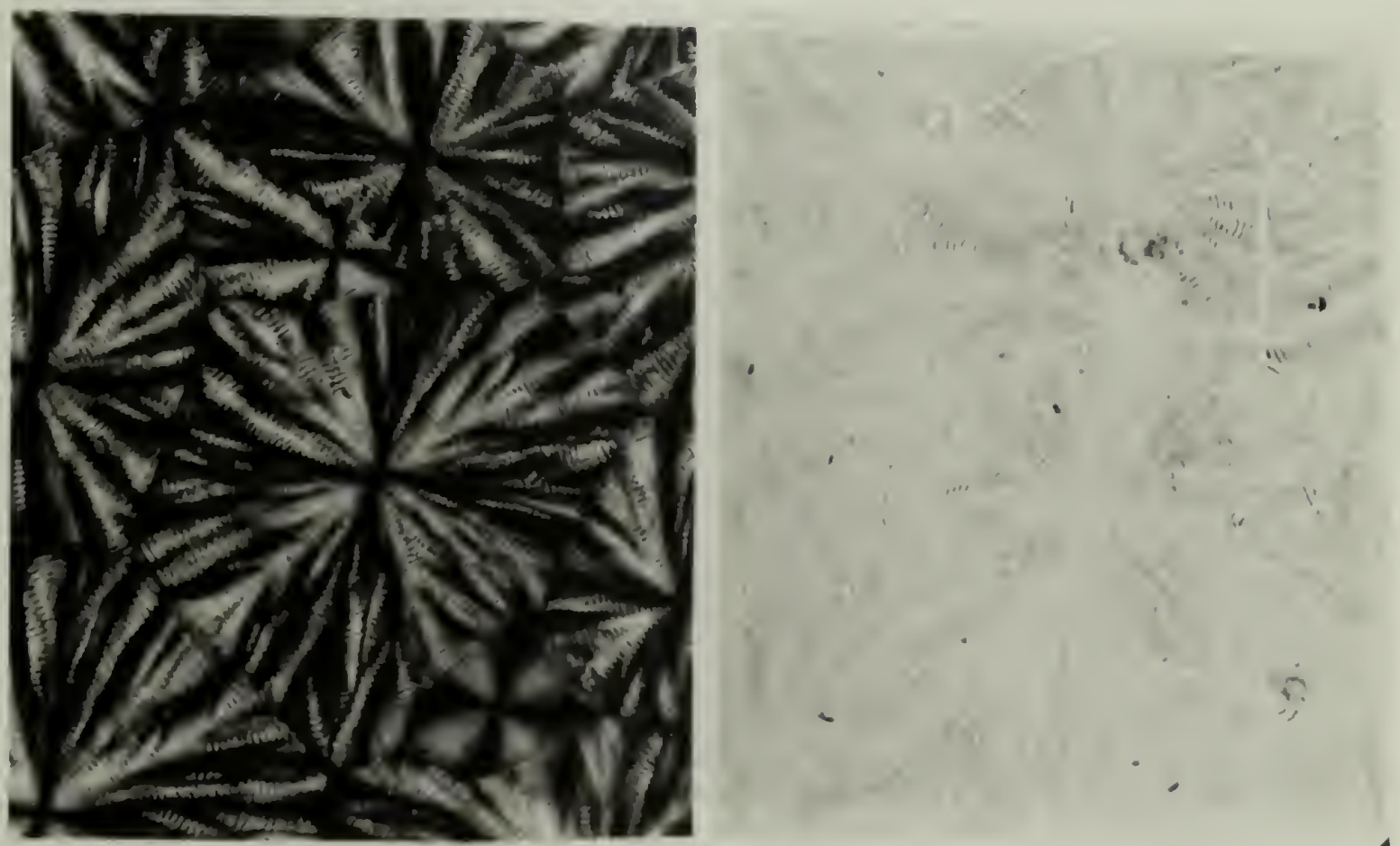

Fig. 34

Scattering patterns were then taken from selected areas in the sample. It was noted that neither the non-banded γ spherulites nor the small (less than 20 μm in diameter) banded spherulites produced the cross pattern in the H_V mode. This explains the limited temperature range for which this pattern was seen. If temperatures were too low, only very small spherulites would grow. If temperatures were too high, the γ spherulites would predominate. In either of these cases the H_V wide angle cross pattern would not be seen. This also explains why certain portions of the sample did not show a distinct H_V cross pattern.

By finding a large banded spherulite, scattering patterns from different areas within a given spherulite were obtained. Figure 35 depicts such a spherulite in the same sample used for Figures 33 and 34. Scattering patterns were taken from the areas contained by the black circles labeled a through d. Figure 36 shows the images of these areas taken with H_V polarization along with their respective H_V and V_V scattering patterns. The thin streaks in the V_V patterns were due to the lenses of the microscope and are not part of the polymer scattering pattern.

Stein and Rhodes (128) have performed computer simulations to determine the expected light scattering patterns from assemblies of oriented rods. Assuming the patterns of Figure 36 arose from rods oriented along the spherulite radius, comparisons can be made between these

Figure 35. Optical micrograph of a spherulite from a 72.8 vol. % PVF_2 blend crystallized at 429 K that was used for selected area light scattering. Patterns were obtained from the circled areas labelled a to d.

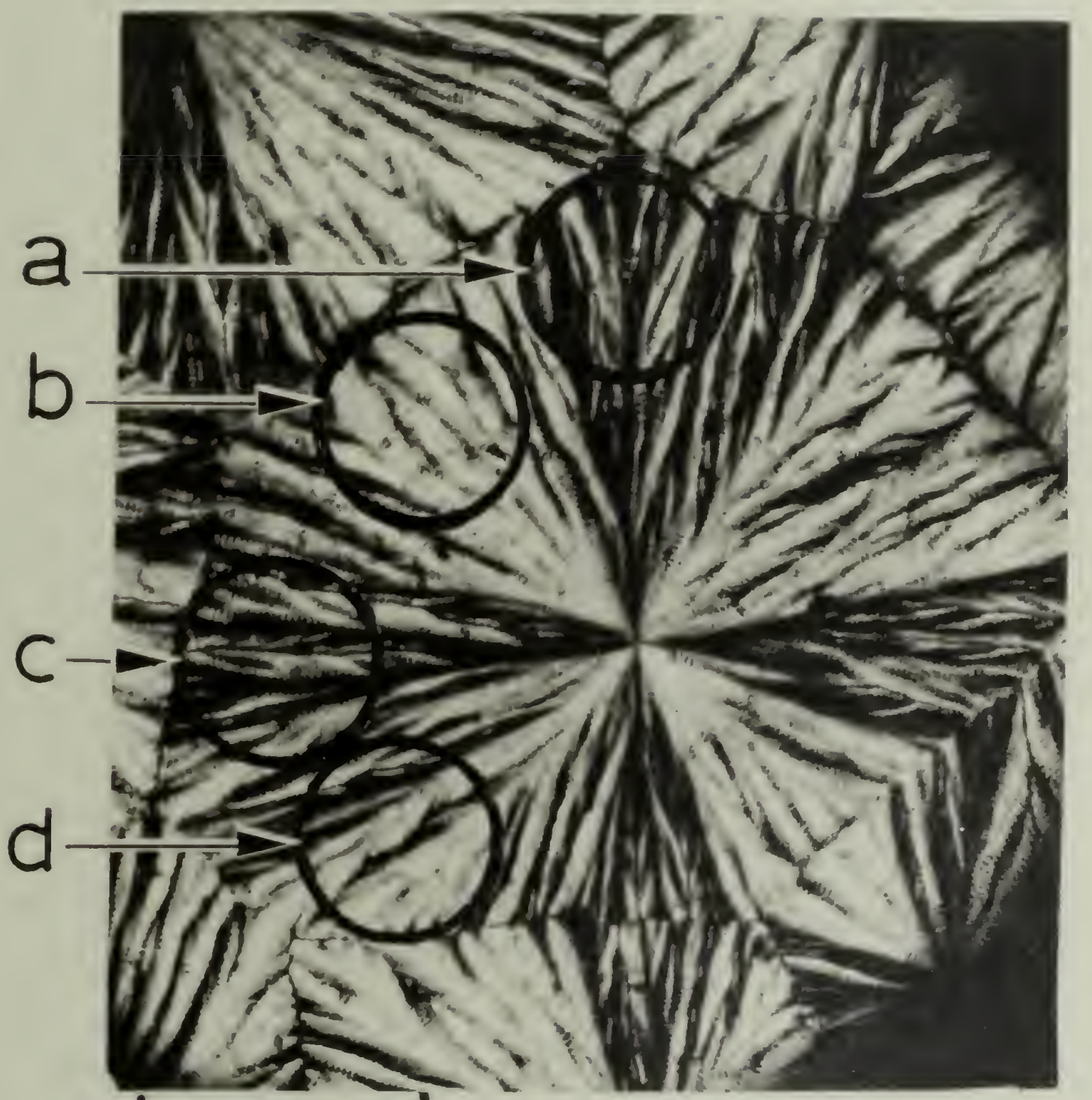

Fig. 35

Figure 36. H_V images along with H_V and V_V selected area light scattering patterns from the areas labelled a through d in the spherulite shown in Figure 35.

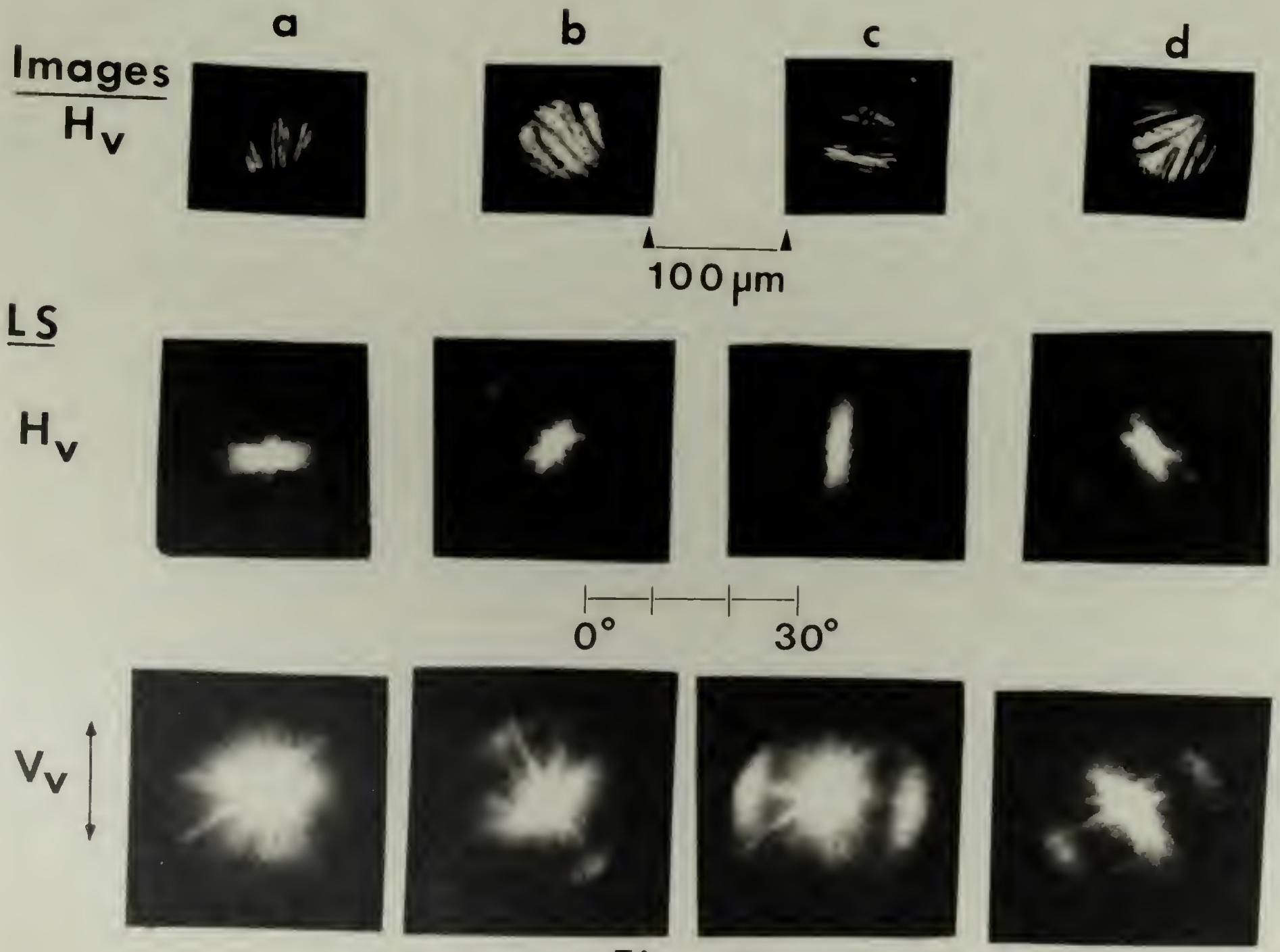

Fig. 36

patterns and the computer simulated ones. When the angle ω between the direction of maximum polarizability and the long axis of the rod was 45° and the rods had a highly oriented population; the simulated H_v and V_v patterns appeared similar to the experimental ones in the study. Therefore it is believed that rod-like structures within the spherulites which are oriented along the spherulite radius give rise to these patterns.

Further evidence from this comes from comparing the patterns of Figure 36 with those obtained from oriented polyethylene films (129,130). In these studies, the films crystallized from stressed polymer melts had light scattering patterns very similar to the ones observed in Figure 36. There were two differences in the patterns, however. Diffraction rings due to the extinction bands were absent in the polyethylene patterns. This was to be expected since the polyethylene was not spherulitic. Also, the polyethylene H_v patterns had a flattened x type appearance with azimuthal maxima at approximately 65°. The H_v patterns of Figure 36 taken from regions b and d also had this flattened x-like appearance but in general, the patterns in this work were more like streaks. Changing the orientation of the draw direction relative to the polarizers gave patterns in the polyethylene films which corresponded to the patterns observed here at different radial orientations of the spherulite. Utilizing various

techniques including computer simulation of the patterns (129) the morphology in the polyethylene was shown to be comprised of a network of optically anisotropic rod-like units preferentially oriented at an angle of ±22° to the draw direction. The computer simulations determined the length L of these rods to be approximately 40 λ', where λ' is the wavelength of the light in the medium. For the samples studied here, this would correspond to rods approximately 40 μm long.

Another method for estimating the size of rods which would give the wide angle H_v pattern of Figure 33c is offered by Murakami et al. (122). They show that the scattering angle θ', where there is the largest difference between the scattering along $\mu = 0°$ and $\mu = 45°$ can be related to L by

$$4.80 = 2\pi \frac{L}{\lambda'} \sin\left(\frac{\theta'}{2}\right) \qquad (3)$$

Using this equation gives values of L between 20 and 40 μm. Rods of this size can certainly exist within spherulites whose radii are over 100 μm.

Therefore, based on the above discussion, as well as suggestions of T. Hashimoto (131), it is believed that the wide angle patterns seen in these samples resulted from assemblies of rods within the spherulites. These rods appear to be 20-40 μm long and are most likely composed of a staggered array of twisting lamellae. Branching of the

lamellae results in orientation of the optic axes at large angles relative to the spherulite radius, thus giving the cross-like H_v patterns. A schematic representation of these rods is shown in Figure 37. Upon close inspection of Figure 35, these types of rods can be detected. The weakness of the wide angle H_v pattern in the pure PVF_2 compared to the blends is probably due to less branching of the lamellae in the homopolymer.

3. Conclusions. The extinction spacing, p, in the banded spherulites was observed to increase at higher crystallization temperatures, and as more PMMA was added to the blend. For each composition a lower limiting value of p seemed to be approached as T_c was increased. This limiting value decreased as more PMMA was added. Excluding the low T_c data, where this limiting value was approached, a plot of ln(p) vs. $1/\Delta T$ for the data from all the blends formed a single straight line. Thus p was a function of undercooling and not composition at high T_c, but the lower limiting value of p, at low T_c, was a function of composition and not undercooling. Viewing the ln(p) vs. $1/\Delta T$ plot as an activation energy plot gave E = 322 cal/mole from the slope, and an intercept of p_0 = .0438 μm. A possible explanation for the latter could be the extinction spacing a spherulite crystallized at T_m^o might have, while the former can be the

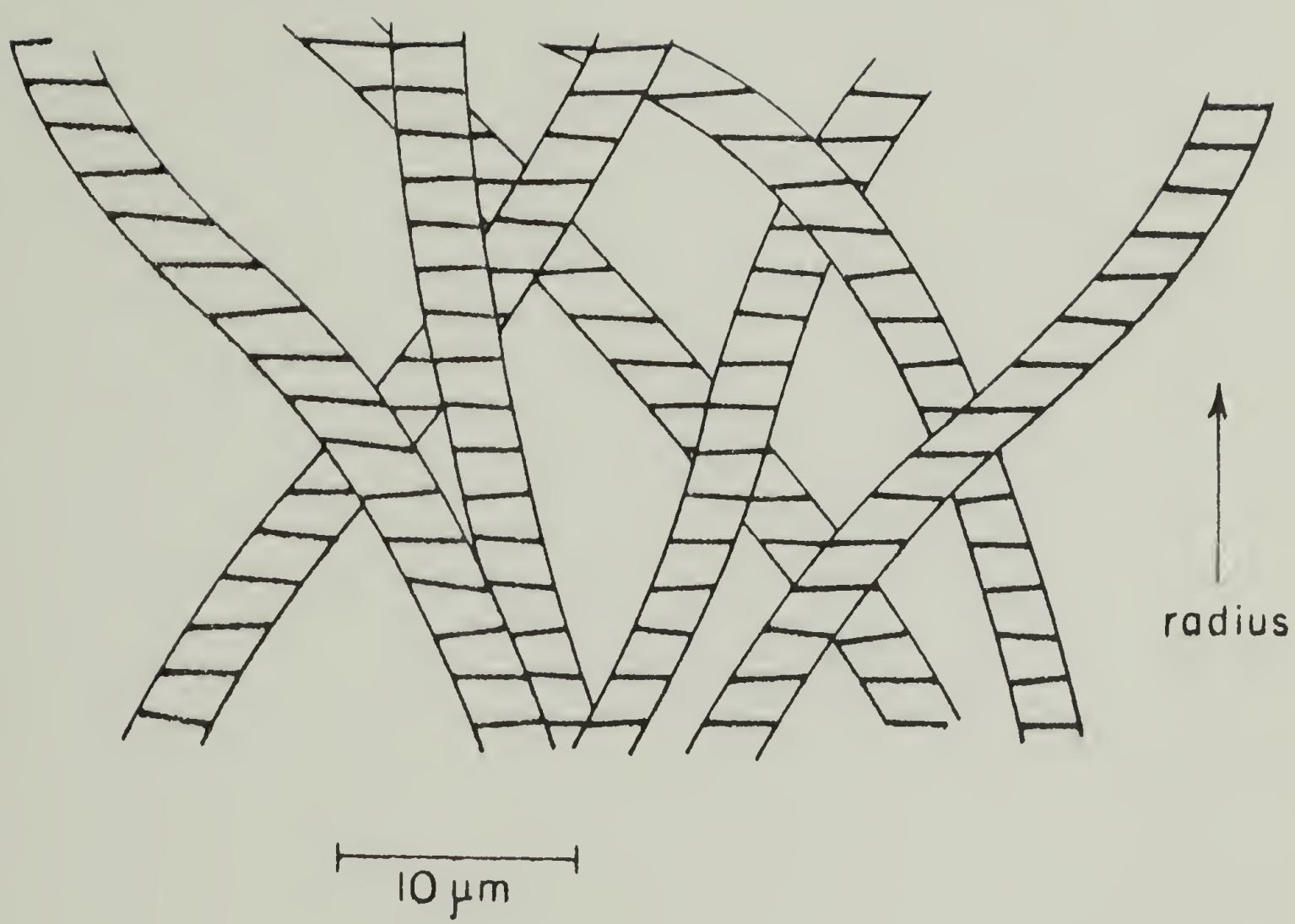

Figure 37. Schematic representation of rods formed from bundles of lamellae twisting and branching in a spherulite.

amount of energy relieved by reorienting the lamellae.

Diffraction patterns were taken from adjacent 670 nm regions along the radius of a banded spherulite using the μ, μ diffraction STEM technique. From these patterns it was apparent that the b unit cell axis was oriented radially, while the c and a axes twisted about the spherulite radius. It was not possible, however, to determine whether the twisting was alternating, oppositely directed half twists, or a continuous full twist. There was good agreement between the orientation of the unit cell and lamellar orientation observed from the STEM image.

Light scattering from films of these blends gave circular V_V patterns at both wide and small angles. This was most likely due to domination of the isotropic term in the V_V scattering equation. The H_V patterns displayed the typical four leaf clover appearance for spherulitic polymers in the small angle region, but a rod-like pattern with the maxima at $\mu = 0°$ and 90° in the wide angle region. Using the microscope, adapted to perform selected area light scattering, patterns from areas 50 μm in diameter taken from different regions within a given banded spherulite were obtained. These corresponded to rod patterns with the rods oriented along the spherulite radius. The rods are believed to be 20-40 μm long and composed of arrays of staggered lamellae. Formation of these rods results from branching and twisting of the lamellar bundles.

C H A P T E R I V

MELTING STUDIES

A. Background

The previous chapter contained a preliminary discussion of the complex melting behavior of PVF_2 crystals in blends with PMMA as well as in the homopolymer. The observed melting regions were related to the various crystal forms and morphologies present. In this chapter, a detailed study of the melting behavior in the blends as a function of crystallization temperature and composition will be discussed.

As mentioned in Chapter I, the melting point depression observed in blends of PVF_2 and PMMA has allowed various calculations of an interaction parameter between the two polymers (34,42,95). The interaction parameter was always less than or equal to zero and appeared to be constant over the entire composition range. Contrary to this, Wendorff (94), using SAXS, has found an interaction parameter which is negative, but varies as a function of composition. The present study will attempt to follow change in the melting points, T_m, of samples at high crystallization temperatures, T_c. According to Hoffman and Weeks (114), extrapolation of T_m vs. T_c plots should enable one to derive the equilibrium melting points. These equilibrium melting points can then be used to determine the interaction parameter for this system.

As shown in Chapter III, there are a variety of morphologies and melting points which are seen in the samples crystallized at high temperatures. In addition, Prest and Luca (25) have reported that a Hoffman-Weeks (114) plot of T_m vs. T_c for pure PVF_2 exhibits an increase in the slope for the α form crystals when these other crystal phases become present. In the present study, Hoffman-Weeks plots will be examined for this upturn, and a better understanding of the phenomena behind it will be attempted.

1. Hoffman-Weeks theory. An understanding of Hoffman-Weeks (114) theory of polymer crystallization is necessary before proceeding to the analysis of the plots suggested by this approach. Their ideas are based on the assumption that a folded chain lamellar crystal is formed with a thickness that is determined by the crystallization temperature. The melting point of this crystal is then shown to be a function of its thickness. If the crystal had no chain folds and was infinitely thick, it would melt at the equilibrium melting point, T_m^o. However, this type of crystal could only be grown at $T_c = T_m^o$ and would take infinitely long to do so. Therefore, the melting point observed for the folded chain crystal is always lower than T_m^o.

From surface nucleation theory (132) the initial thickness, ℓ^*, of a chain folded lamella, which is kinetically determined, is given by

$$\ell^* = \frac{2\sigma_e T_m^o}{\Delta H_f \Delta T} + \delta\ell \qquad (4)$$

where σ_e is the end surface interfacial free energy of the crystal, T_m^o the equilibrium melting point for a perfact crystal with an infinite thickness, ΔH_f the heat of fusion per unit volume of crystal, and ΔT the undercooling $T_m^o - T_c$. As will be shown, $\delta\ell$ represents the small thickening from ℓ^* necessary for crystal growth to continue. It has been approximated by $\frac{kT}{b_o\sigma}$ (103) with σ being the lateral surface free energy and b_o the thickness of a monomolecular layer in the 110 plane. There is very little variation of $\delta\ell$ with undercooling and it can be considered constant for our purposes.

Assuming that the heat of fusion is independent of temperature and the lateral dimensions of the crystal are much greater than its thickness, a straightforward thermodynamic argument (114) shows that the observed melting point, T_m, of a crystal with thickness ℓ is

$$T_m = T_m^o \left[1 - \frac{2\sigma_e}{\Delta H_f \ell}\right] \qquad (5)$$

If ℓ^* from equation 4 is now inserted for ℓ in equation 5, the result is

$$T_m = T_c - \Delta T \left(1 - \frac{1}{1+\delta\ell(\Delta H_f)(\Delta T)/2\sigma_e T_m^o}\right) \qquad (6)$$

Therefore, since $\delta\ell$ is small and positive, a crystal, for which no isothermal thickening from ℓ^* has taken place, has a melting point slightly above the temperature at which it

was grown. If $\delta\ell$ was zero, then $T_m = T_c$ and the crystal could never grow.

At low undercoolings the crystal can thicken from ℓ^* to a final thickness ℓ. This rate of thickening has been shown to be proportional to the logarithm of the age of the crystal (133,134). A simplifying assumption can be made that at long times, on the average, the thickness achieves a value which is η times larger than ℓ^* (35).

$$\ell = \eta\ell^* \qquad (7)$$

Assuming $\delta\ell$ is small compared to the term $2\sigma_e T_m^o/\Delta H_f \Delta T$ in equation 4, which is a good approximation at low undercoolings, the use of equation 4 and 7 in equation 5 gives the equation describing a Hoffman-Weeks plot.

$$T_m = T_m^o \left(1 - \frac{1}{\eta}\right) + \frac{T_c}{\eta} \qquad (8)$$

Plotting T_m vs. T_c should therefore result in a straight line with a slope of $1/\eta$. The intercept of such a plot with the $T_m = T_c$ line will occur at T_m^o.

B. Results and Discussion

DSC traces of samples isothermally crystallized from the melt are presented for different volume fractions of PVF_2, v_2, at two crystallization temperatures in Figure 38. All of the samples were run at 10K/min. unless otherwise noted. As discussed in the previous chapter, there are three types of crystals formed at these temperatures, each having a different

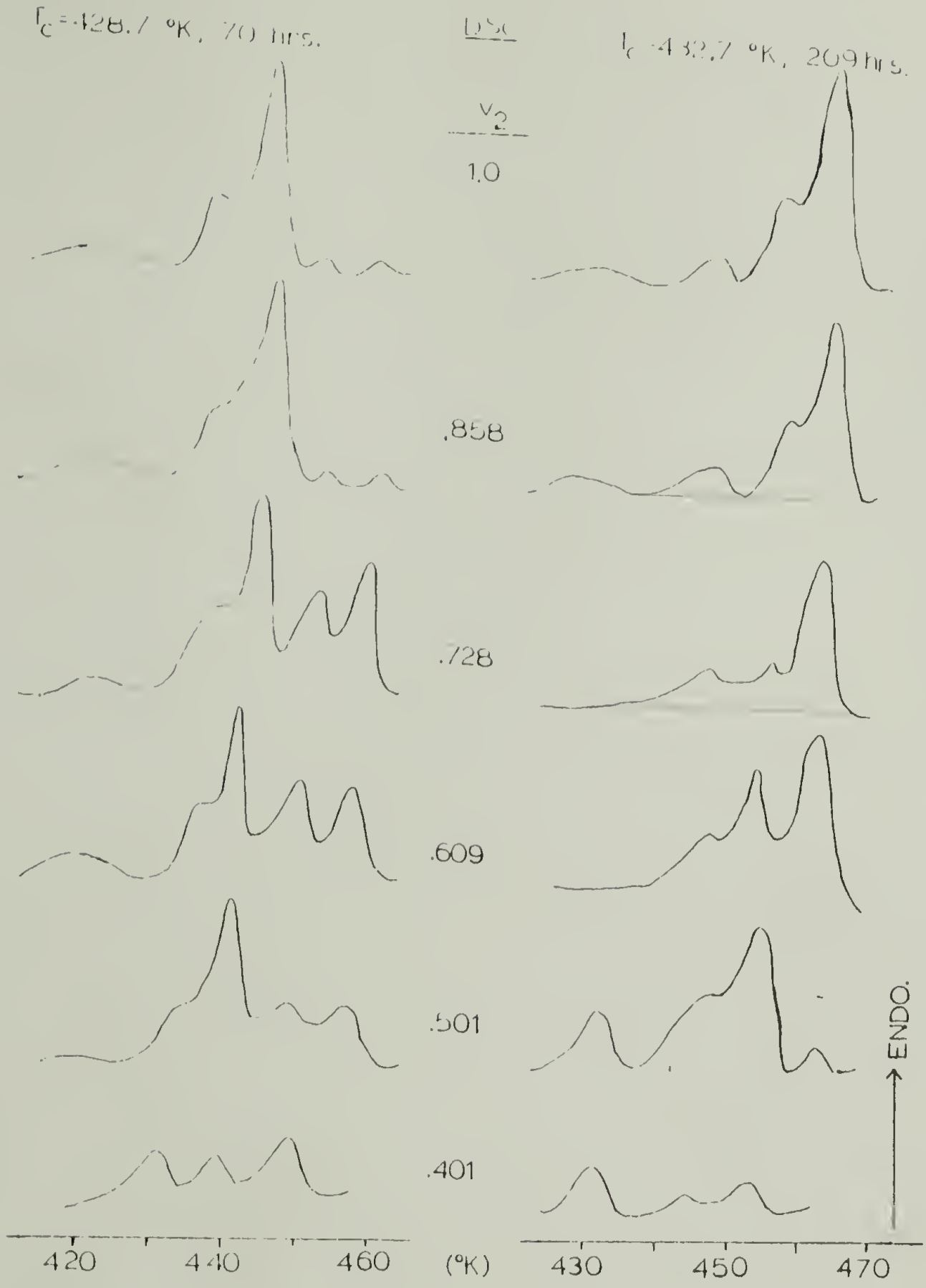

Figure 38. DSC melting traces of PVF_2/PMMA blends crystallized at two different temperatures. v_2 is the volume fraction of PVF_2.

melting point. These crystals are designated α, γ and γ' in order of increasing melting points. Though there are three types of crystals, there are only two crystal forms. The γ and γ' crystals have the same crystal unit cell, but the former is nucleated and grown from the melt, while the latter only develops from a crystal-crystal phase transition from the α crystals at the temperature of crystallization.

For crystallization times less than approximately 100 hours, or temperatures less than 425 K (this will vary with composition) the α melting peaks are predominant in the DSC traces. This can be seen in Figure 38 for samples crystallized at 428.7 K for 70 hours. The shoulder and broad endotherm at temperatures below the α peak are due to crystals formed during quenching, and recrystallization of these during melting. Changing heating rates from 1.25 to 80 K/minute altered the shape and position of these two low temperature endotherms but not the α peak nor the higher temperature γ and γ' peaks. Crystallization at slightly higher temperatures for longer times, as shown in Figure 38 by the samples grown at 432.7 K for 209 hours, enabled more crystals to transform from α to γ' and the latter peak now becomes much larger. In blends with 60.9 volume % or less PVF_2, the γ crystals often grow in preference to the α, therefore the penultimate peak will be very large.

The crystallinity for samples grown at 420 K for 72 hours is given in Figure 39 as a function of weight % PVF_2. These

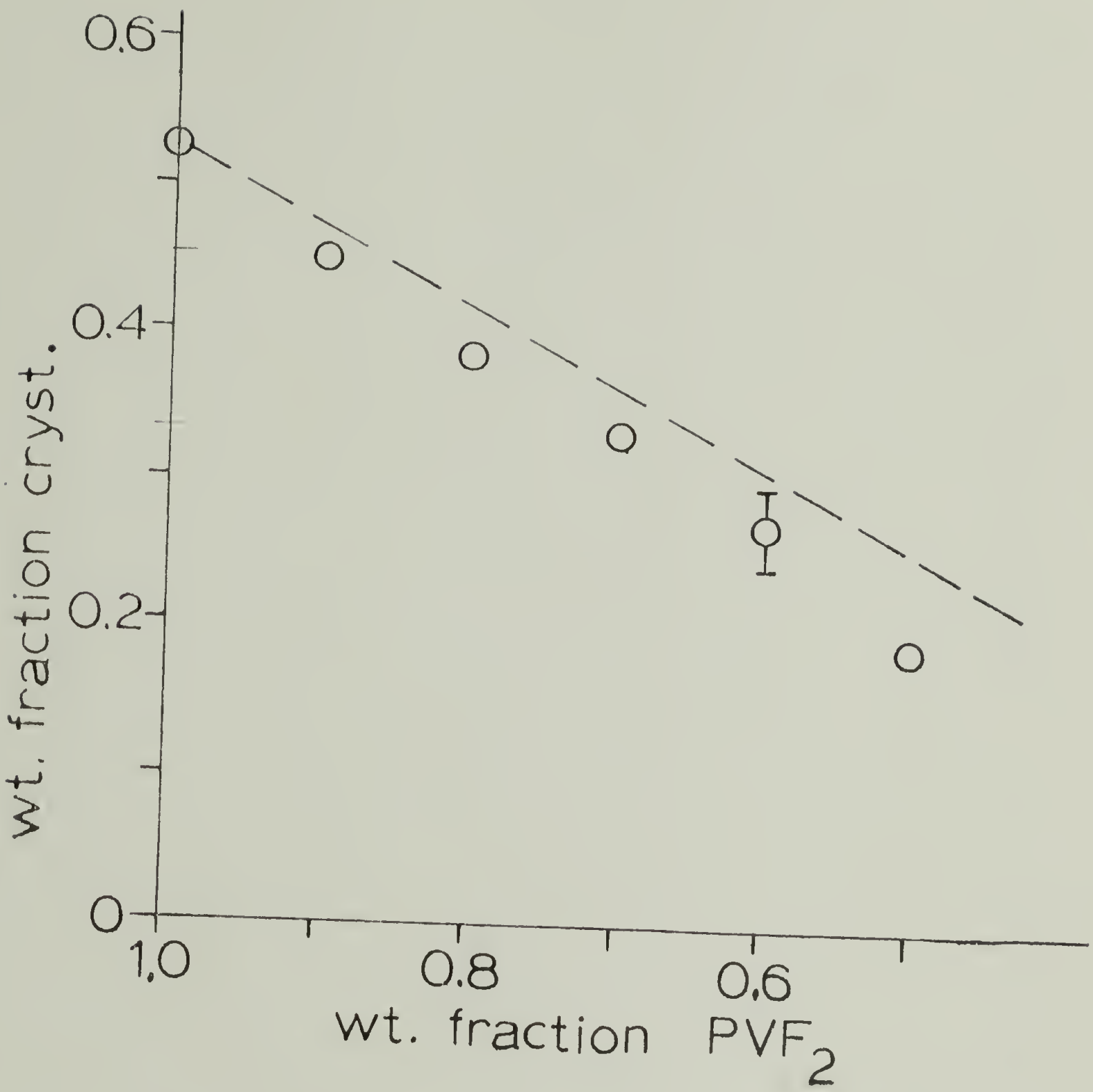

Figure 39. Crystallinity in PVF_2/PMMA blends vs. weight fraction of PVF_2. From DSC endotherms.

samples were used since they were entirely of the α polymorph for which a heat of fusion of 5965 j/mole has been calculated by Welch and Miller (31). Using the simple assumption that the heat of fusion is the same for the γ and γ' crystals, areas under the multiple melting endotherms observed at higher crystallization temperatures fall within the range of error for these points. The dashed line represents the crystallinity that would be expected if the PMMA had no effect on the PVF_2. As can be seen, the data for the blends fall below this line implying some interaction. Similar results were found by Nishi and Wang (34).

Figures 40-45 show Hoffman-Weeks plots of the six blend compositions studied. The observed T_m's were taken at the peaks of the DSC melting endotherms. Similar plots using the last trace of the melting endotherm as the observed T_m were identical except for an overall shift upwards of 2 K. The use of the peak temperatures was preferred because the accuracy of their determination is greater when multiple melting peaks are present, especially when there were only small amounts of some polymorphs. Determination of melting points by visual inspection, using the polarizing microscope and Mettler hot stage programmed at the same heating rate used in DSC studies, gave values in agreement with the DSC results. The temperature at which the loss of birefringence was most rapid was taken as the melting point. As in the DSC measurements, complete loss of birefringence was approximately two

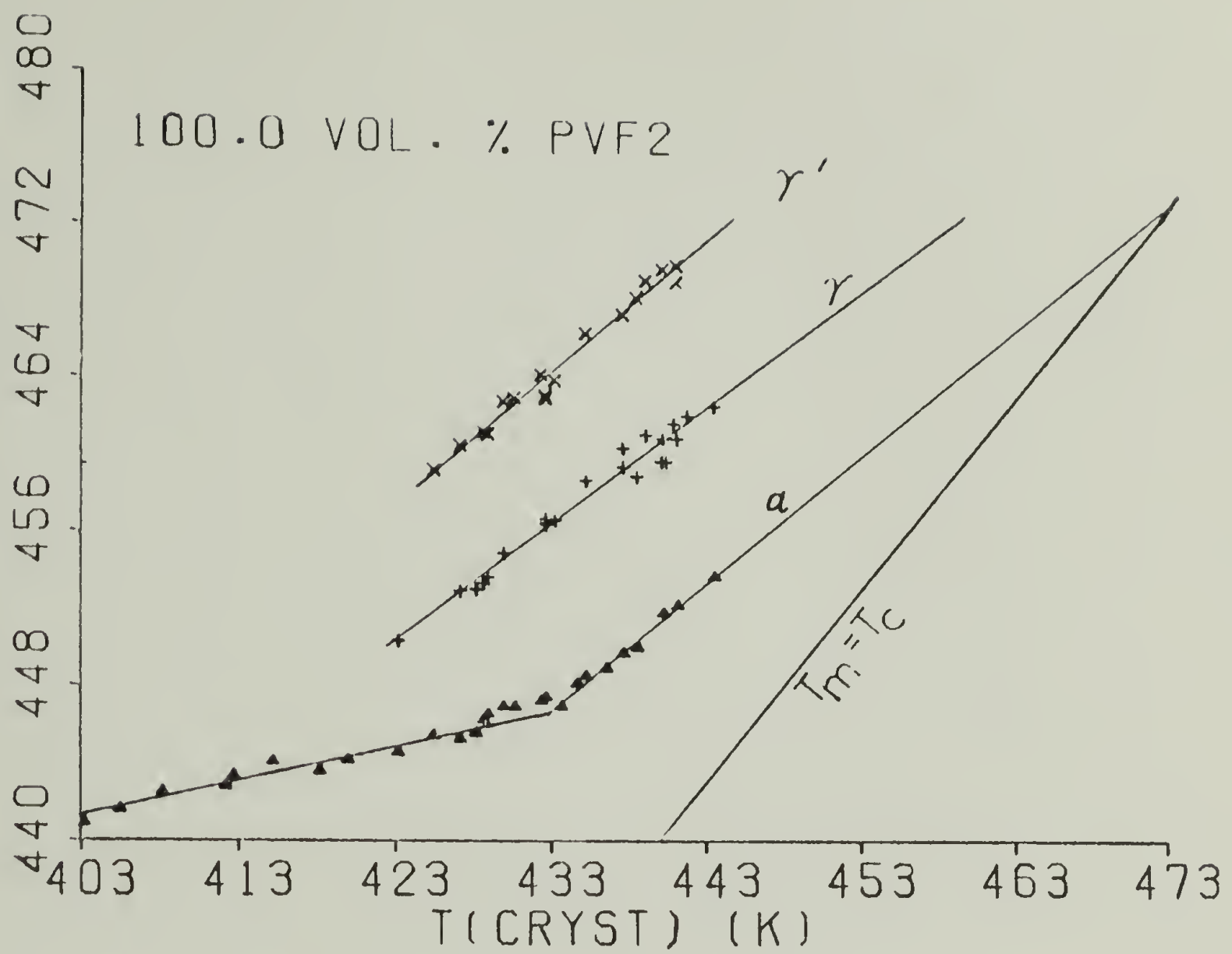

[>170]

Figure 40. Hoffman-Weeks plot of PVF_2.

Tm (lowest)
186. (γ')
177 (γ)
170 (α)

Tc (highest)
169 (γ')

170

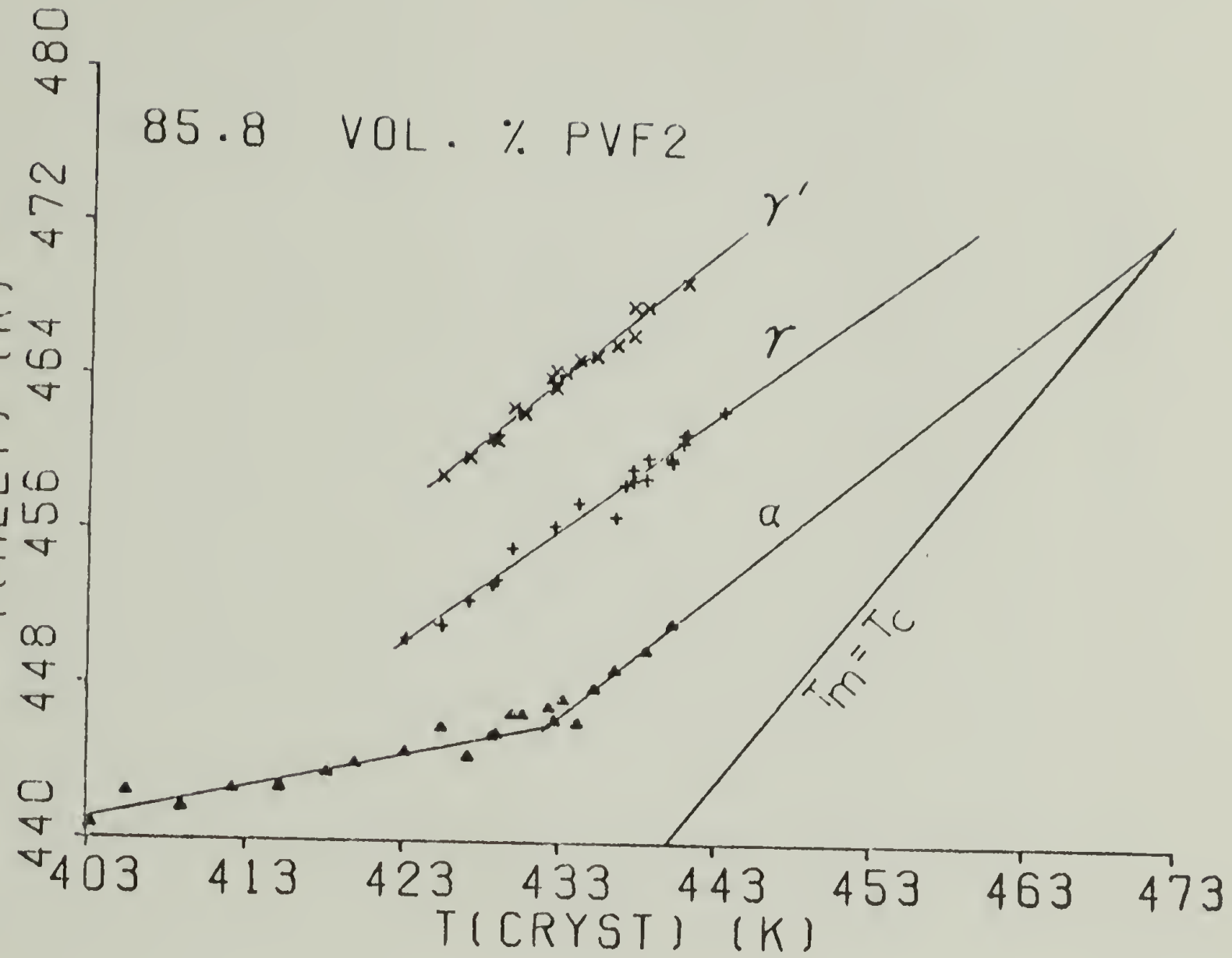

Figure 41. Hoffman-Weeks plot of an 85.8 volume % PVF_2 blend.

T_c (highest)	T_m (lowest)	T_m (γ')
170 °C	167	186

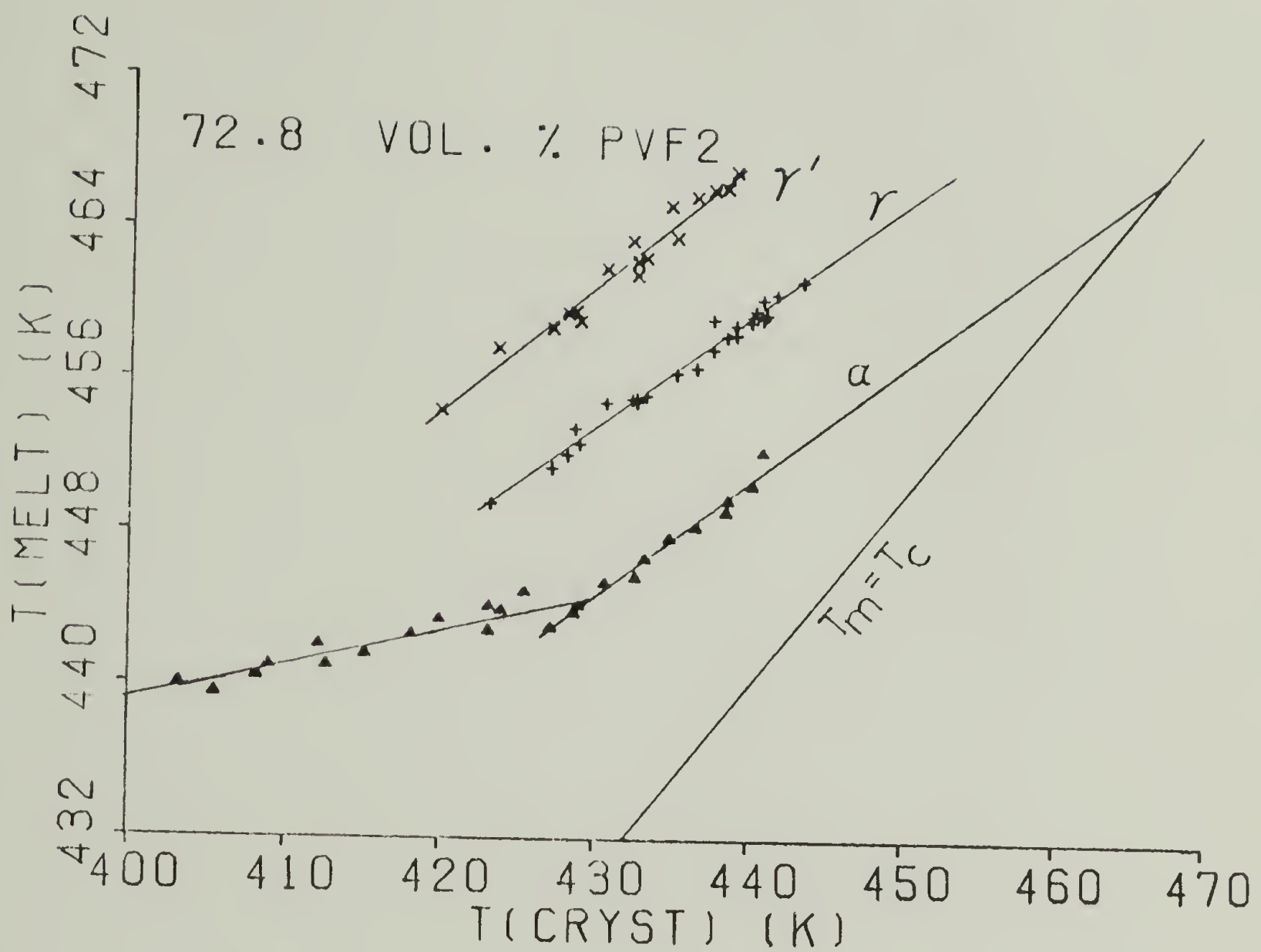

Figure 42. Hoffman-Weeks plot of a 72.8 volume % PVF_2 blend.

T_m (lowest T_c (highest)

182 (γ') 169

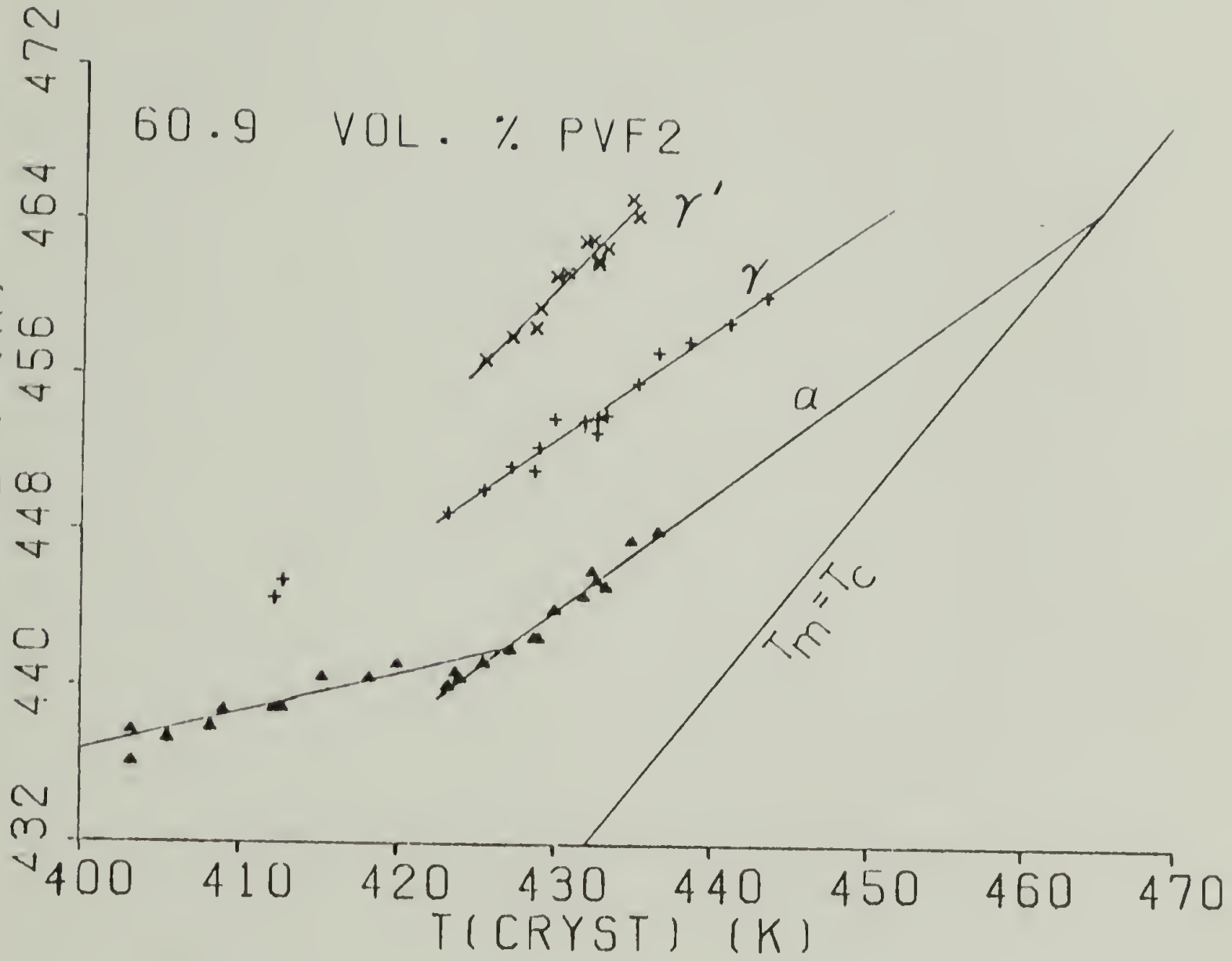

Figure 43. Hoffman-Weeks plot of a 60.9 volume % PVF_2 blend.

Tm

184

Tc/hy[illegible]

172

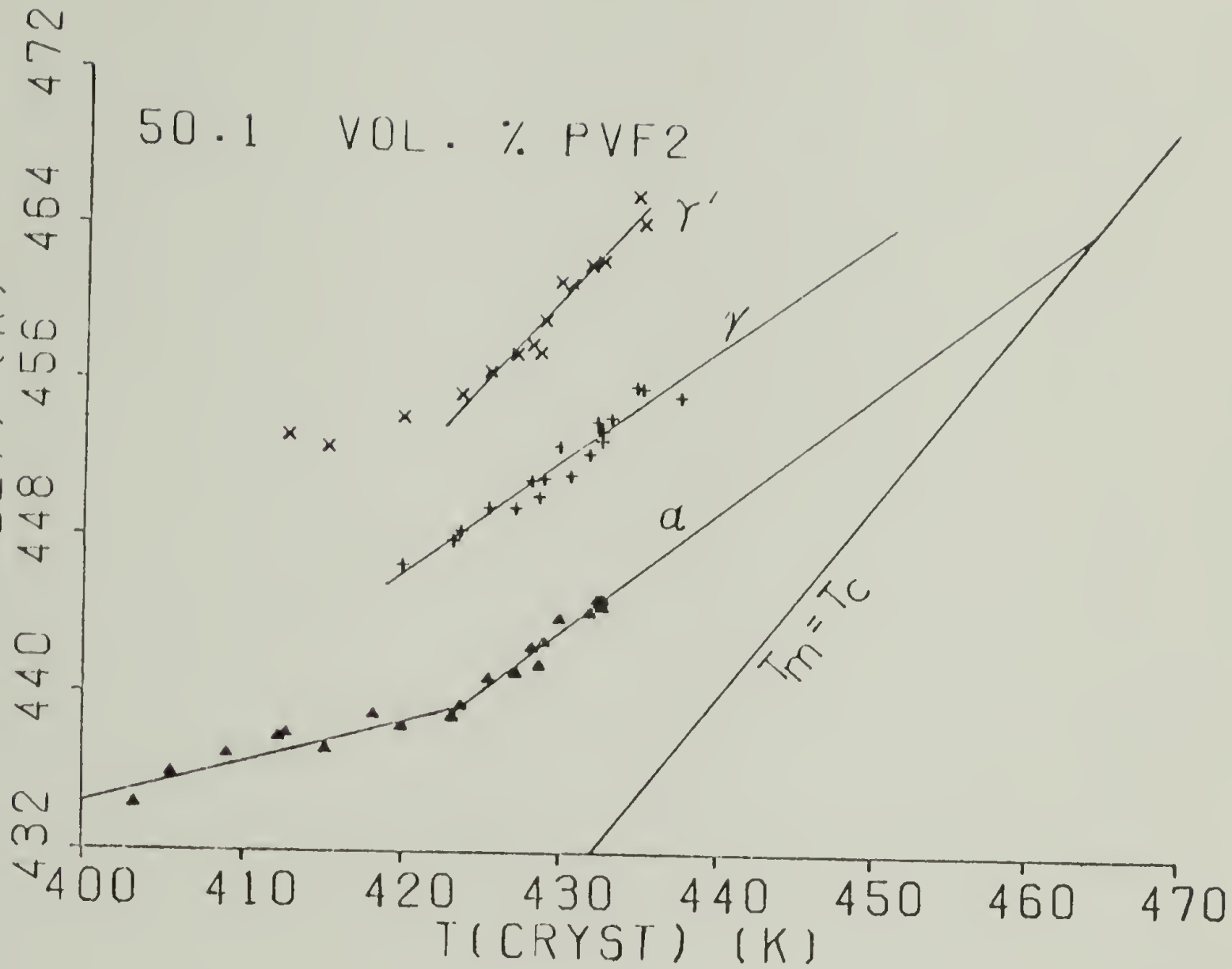

Figure 44. Hoffman-Weeks plot of a 50.1 volume % PVF_2 blend.

T_m	T_c
181	165

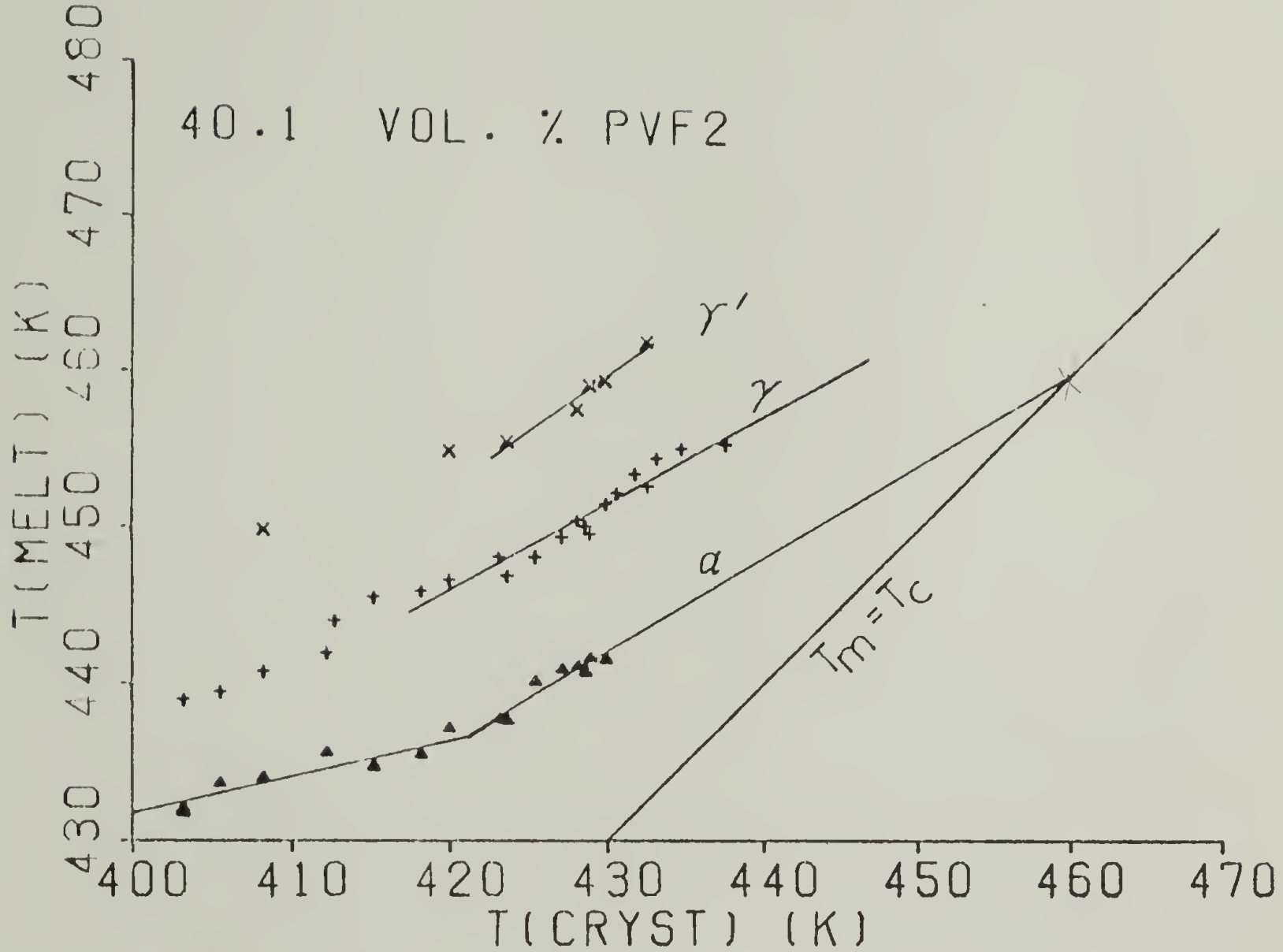

Figure 45. Hoffman-Weeks plot of a 40.1 volume % PVF_2 blend.

Tm Tc

177 165

degrees higher, but was harder to determine accurately since remaining orientation of the molecular chains, even after the crystals had melted, would be seen as a lingering birefringence. The microscopically determined melting points were especially useful at the highest crystallization temperatures when only very small amounts of α crystals were present.

As can be seen from Figure 40-45, the Hoffman-Weeks plots of all the blends have the same general features. At low crystallization temperatures, only the α form is present and the data fall on a straight line. At higher crystallization temperatures, the other crystal forms are grown and the melting points for the α form seem to rise above the line drawn from the low temperature data. As the blends became richer in PMMA, the main differences in these plots were: lowering of all observed T_m's, depression of the temperature at which the α form melting points start to deviate upwards from the line drawn through the low T_c data, and appearance of the higher melting crystal forms at lower temperatures.

In all of the blends, the data for the α crystals appears to form two linear segments. The transition from one segment to the other is most likely smooth, although this is hard to determine due to scatter in the experimental points. These two linear segments can each be extrapolated to the $T_m = T_c$ line, therefore implying two equilibrium melting points for the α crystals. This is obviously impossible. Past work on

melts of the blends (34,42,95) and the pure PVF_2 (24-26, 31-33) have always obtained T_m^o from data taken at low crystallization temperatures, before the change in slope would be seen. Only Prest and Luca (24,25) even noted that this upturn occurs at higher T_c's.

T_m^o's for the α crystals in the blends were first calculated by extrapolating the data from the lower crystallization temperatures. These are given in Table 2. It was then noted, however, that the melting points observed at the highest crystallization temperatures were higher than these T_m^o's. This violates the definition of the equilibrium melting point. To clear up the above anomolies one must consider what is causing the change in slope of the α form.

1. PVF_2 viewed as a copolymer. It is known from nuclear magnetic resonance studies of PVF_2 (24,33,135,136) that there is a small percentage of head-to-head linkages present in the polymer backbone, the amount of which varies with polymerization conditions. The PVF_2 can therefore be viewed as a copolymer made of head-to-tail and head-to-head repeat units. Since the fluorine and hydrogen atoms are of similar size, it is possible that some of the head-to-head linkages can be fitted into the regular head-to-tail crystal lattice.

Lando and Doll (13) actually examined this question and have shown that incorporation of the head-to-head PVF_2 units in the α crystals is highly unlikely since this would result

TABLE 2

T_m^o FOR THE γ CRYSTAL FORM AND FOR THE α CRYSTAL FORM EXTRAPOLATED FROM THE LOW T_c AND HIGH T_c DATA

Vol. % PVF_2	Wt. % PVF_2	T_m^o		
		α Form		
		Low T_c	High T_c	γ Form
100.0	100.0	449.5	474.1	492.6
85.8	90.0	449.0	472.4	490.3
72.8	80.0	447.9	467.6	487.2
60.9	70.0	445.8	465.3	483.1
50.1	60.0	442.8	464.5	482.4
40.1	50.0	440.8	460.3	479.0

must be typo - see Fig. 48

in significant strains on some of the fluorine atoms. At certain positions, two fluorine atoms would be placed 0.231 nm apart, while the sum of their van der Waals radii is 0.270 nm. However, the head-to-head units did fit very well in the β unit cell. Along this line, Takahashi et al. (19) have noted kink bands present in α crystallites which they believe are due to a few repeat units being in the all trans β conformation. It is possible therefore that the head-to-head units can be included in these regions. In any case, these units are acting as defects in the head-to-tail α crystal lattice.

Besides the existence of these kink bands, which may contain head-to-head units, there are a number of other observations in the literature which have been attributed to defect inclusion in the crystals. Kortleve et al. (137) found a concentration of 0.3 to 0.5 times the overall concentration of comonomer side groups in crystals from both ethylene-vinyl acetate and ethylene-acrylic acid copolymers. Various poly(oxymethylene) copolymers (138,139) as well as chlorinated polyethylene (139) have shown similar results. Defects due to alterations in stereoregularity can also be included in the crystals formed. D-lactide units have been seen in crystals of L-lactides grown from mixtures of the two (140). Therefore, the hypothesis of fitting head-to-head PVF_2 units to an α crystals, possibly in the form of β-type kink bands, seems reasonable.

Flory's original theory of copolymer crystallization (141), assumed that all non-crystallizable units, or defects, are excluded from the crystals. In view of the above, this appears to be an oversimplification. Sanchez and Eby (142, 143) have developed a theory for copolymer crystallization which takes into account the inclusion of comonomeric units in the crystal lattice. The melting point of the copolymer can then be related to the melting point of the homopolymer by considering both the enthalpic and entropic effects. For an infinitely large crystal containing a concentration, X_c, of comonomeric units, the relationship is (143),

$$\frac{1}{T_m^o} - \frac{1}{T_m} = -\frac{R}{\Delta H^o}\left\{\frac{\varepsilon X_c}{RT_m} + (1-X_c)\ln\left[\frac{1-X_c}{1-X}\right] + X_c \ln\left[\frac{X_c}{X}\right]\right\} \quad (9)$$

T_m and T_m^o are the equilibrium melting points of the copolymer and homopolymer respectively, ΔH^o is the heat of fusion for the homopolymer, X is the overall concentration of comonomer units, and ε is the excess free energy of the defect created by incorporating the co-unit in the crystalline lattice.

During equilibrium conditions, the value of X_c is given by (144)

$$X_c = X_{eq} = \frac{X\exp(-\varepsilon/RT)}{1-X+X\exp(-\varepsilon/RT)} \quad (10)$$

Theoretically, Helfand and Lauritzen (144) have shown that X_c becomes greater than X_{eq} as the crystals grow fast

relative to the equilibrium process. This should occur at large undercoolings. Verifaction of this was accomplished with the DL-lactides (140) and seemed to be true for some of the other copolymers as well (139).

In light of all this, it is proposed that the upturn in the slope of the Hoffman-Weeks plots of the α crystal form is predominantly due to a change in the concentration of head-to-head units in the crystals. At high crystallization temperatures, the crystals grow very slowly, giving the system a chance to approach equilibrium. Therefore, extrapolating this data to the $T_m = T_c$ line, represents T_m^o for crystals with $X_c = X_{eq}$. At larger undercoolings more head-to-head groups are trapped in the crystals and $X_c = X$. This will now be shown to be consistent with the theory of Sanchez and Eby (142,143).

Since equation 9 deals only with infinitely large crystals, the T_m's to be used in this equation will be the extrapolated T_m^o's from both the low and high crystallization temperature data of the α crystals. These are given in Table 2. The value of ΔH^o is related to the observed ΔH by (142)

$$\Delta H^o = \Delta H + \varepsilon X_c \qquad (11)$$

Therefore, when $X_c = X$, equation 9 becomes

$$\frac{1}{T_m^o} - \frac{1}{T_m(X)} = \frac{-\varepsilon X}{(\Delta H + \varepsilon X)\ T_m(X)} \qquad (12)$$

where $T_m(X)$ is the T_m^o extrapolated for the data where $X_c = X$. For $X_c = X_{eq}$, equation 9 is

$$\frac{1}{T_m^o} - \frac{1}{T_m(X_{eq})} = \frac{R}{(\Delta H+\varepsilon X_{eq})} \ln\left\{1-X+X\exp\left(\frac{-\varepsilon}{RT_m(X_{eq})}\right)\right\} \qquad (13)$$

with $T_m(X_{eq})$ being the T_m^o extrapolated for the data where $X_c = X_{eq}$.

Since T_m^o, for the pure homopolymer, is the same in both cases, equations 12 and 13 can be combined through this term giving a relationship between $T_m(X)$ and $T_m(X_{eq})$.

(14)

$$\frac{1}{T_m(X)} - \frac{1}{T_m(X_{eq})} = \frac{\varepsilon X}{(\Delta H+\varepsilon X)T_m(X)} + \frac{R \ln\left[1-X+X\exp\left(\frac{-\varepsilon}{RT_m(X_{eq})}\right)\right]}{\left[\Delta H + \frac{\varepsilon X\exp\left(\frac{-\varepsilon}{RT_m(X_{eq})}\right)}{1-X+X\exp\left(\frac{-\varepsilon}{RT_m(X_{eq})}\right)}\right]}$$

By inserting the values from Table 2 into equation 14 with the T_m^o's from the low T_c data as $T_m(X)$ and the T_m^o's from the high T_c data as $T_m(X_{eq})$ values of ε that make eq. 14 hold can be deduced. Within experimental error, the values were the same for all the blends. This is reasonable since one is looking at excess energy in the interior of the crystals due to defects. The amorphous phase composition should have negligible effect on this. It should be noted that the theory proposed would lead to curvature in the region in which X_c goes from X to X_{eq}. The two straight lines drawn for the

α form in Figures 40 through 45 were least square fits to data which appeared to be before or after the upturn. The actual region over which the upturn occurs is probably curved but this is not perceptible from the data. Beyond this temperature range, when $X_c = X_{eq}$, the data should again fall on a straight line. This appears to be the case at very high crystallization temperatures.

The values of ε as a function of X are plotted in Figure 46. Values of X from the literature (24,33,135,136) range from 0.05 to 0.11. This would correspond to ε in the range 10.3 to 6.3 kjoules/mole. Using poly(oxymethlene) copolymers, Droscher et al. (138) have determined ε from the decrease in enthalpy of melting as a function of composition. Their values varied from 7.5 to 57.6 kjoules/mole. It is expected that the values for PVF_2 should be low due to the similarities of the hydrogen and fluorine. It therefore seems that the deduced defect energies are in the proper range, and the hypothesis that the upturn in slope is predominantly due to changes in defect concentration of the crystal is consistent with these theories.

Further support for this argument is the fact that the Kurhea brand PVF_2 exhibits higher melting points than the Kynar brand. The former has been shown to have fewer head-to-head linkages (24,33) and therefore should have a smaller melting point depression from the pure-head-to-tail PVF_2. Prest (145) has looked at blends of Kynar and Kurhea PVF_2

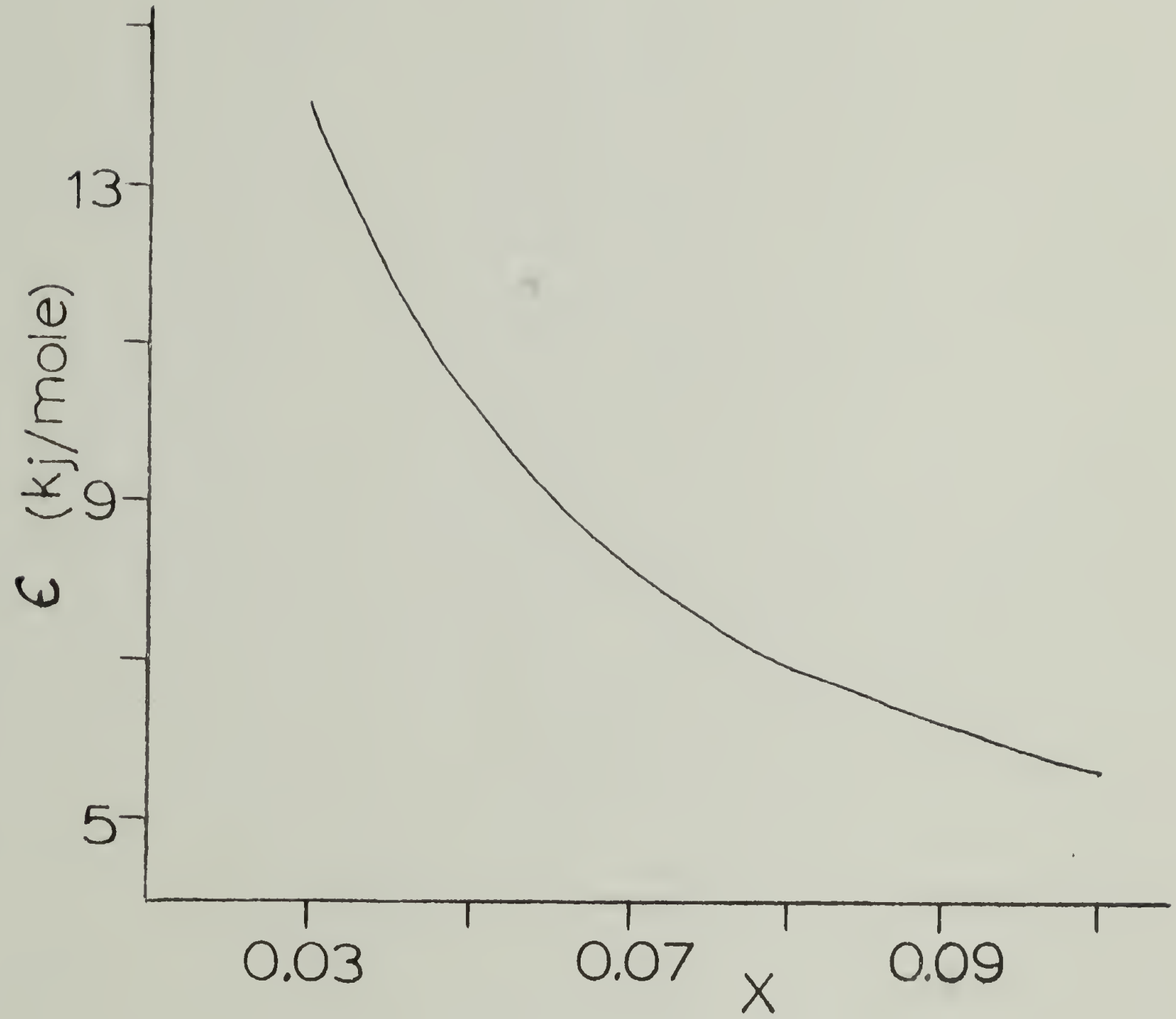

Figure 46. Defect energy, ε, vs. fraction of head-to-head units in PVF_2, X, using Eq. 14 and experimentally determined T_m^o's.

in which the observed and extrapolated melting points increase as the blend becomes richer in the Kurhea material. This is presented in Figure 47. The only data taken at high crystallization temperatures was for the pure Kurhea material. This shows the beginning of an upturn from the low temperature data as was seen in the Kynar PVF_2. It should be noted though that there are other differences in the two PVF_2's which could also affect this data.

This explanation is not the only one possible for the change in slope of the α form. Changes due to degradation, though these did not seem to be of major importance, can affect the data. Also, at these temperatures, as will be shown in Chapter VI, it is believed that a transition from regime II to regime I type growth as defined by Lauritzen (146) is occurring. Hoffman (147) has seen the Hoffman-Weeks plots of polyethylene become vertical when the growth changes from regime II to I. The plots of the PVF_2 certainly do not become vertical, but the onset of this transition could cause some of the slope change. If this were so, the values for ε would be slightly lower. In any case, they are still in the range of what would be expected, implying that a change in X_c is the major factor.

2. Slopes of the Hoffman-Weeks plots. As noted before, the slope of a Hoffman-Weeks plot is the ratio of the initial to final lamellar thickness, $\frac{1}{\eta}$. Therefore, using equation 4 to

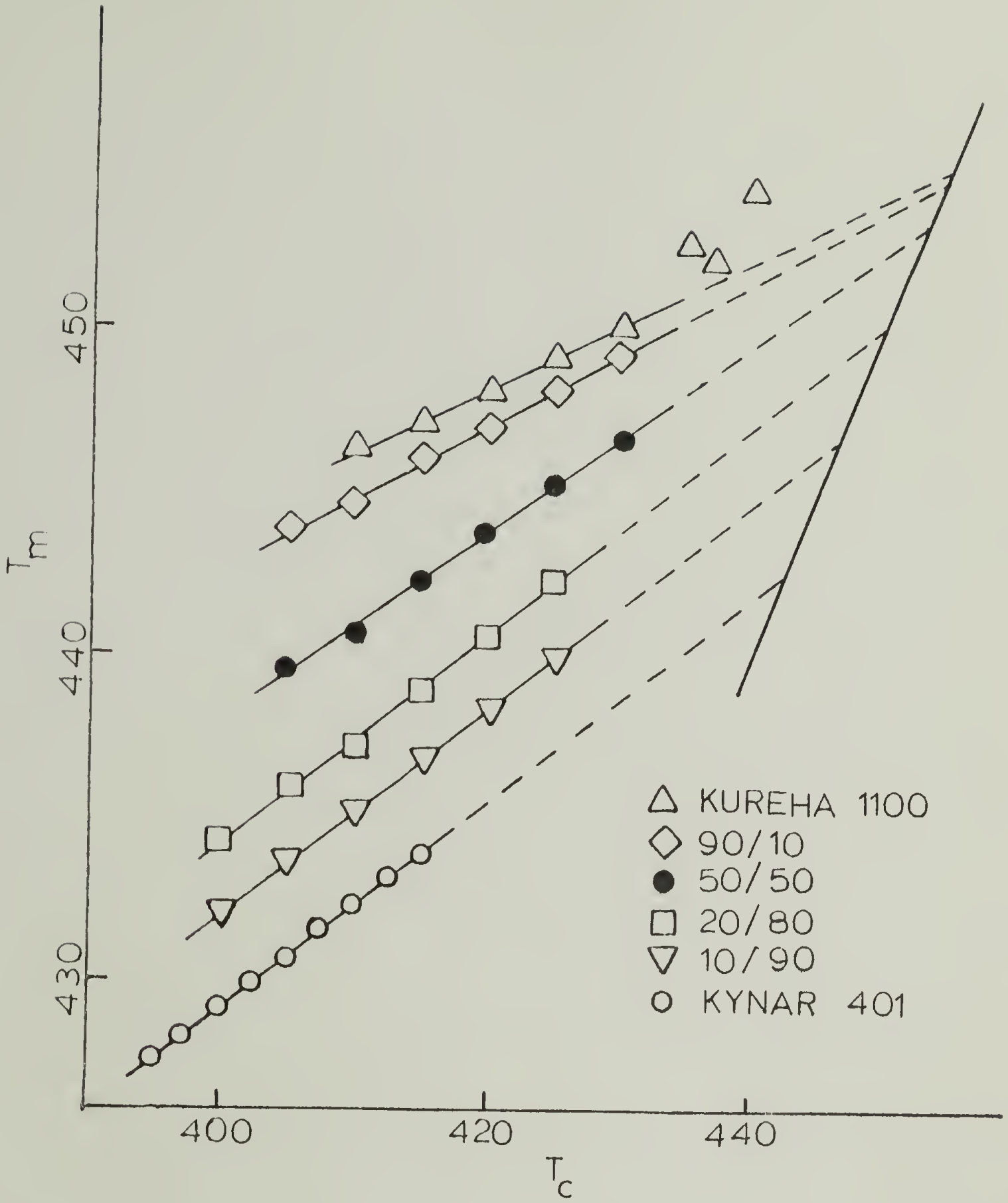

Figure 47. Hoffman-Weeks plots of mixtures of Kurehea 1100 and Kynar 401 PVF_2's. From Prest (145).

estimate the initial thickness ℓ^*, we can multiply this by the η values obtained from the slopes to arrive at a value for ℓ. From growth studies on these blends, Wang and Nishi (37) found that $\sigma = 9.76 \times 10^{-3}$ j/M^2 and σ_e varies from 4.05 to 5.08 $\times 10^{-2}$ j/M^2 using $\Delta H_f = 1.986 \times 10^8$ j/M^3, and b_o = 0.445 nm. Using these values with the T_m^o's found from the low T_c data and the approximation for $\delta\ell$ given previously, ℓ^* calculated for the α polymorph ranged from 5.8 nm at 400 K to 14 nm at the change in slope of the Hoffman-Weeks plots. Using the T_m^o's from the high T_c data on the samples crystallized in that region, ℓ^* ranged from 6.8 to 9.2 nm. These values varied approximately 15% over the composition range of the blends. Table 3 gives the η's calculated from the slopes of the Hoffman-Weeks plots. Using the η's from the low T_c data, the final lamellar thicknesses must range from about 30 nm at 400 K to about 65 nm at the change in slope. Employing the η's from the high T_c data, the final thicknesses vary from about 11 nm to 16 nm. These latter values are in much better agreement with lamellar thicknesses obtained from electron microscopy (30). Lamellar thicknesses were also determined by SAXS and will be discussed in the following chapter. The SAXS values, for samples crystallized at 418 K, ranged from 4.2 to 8.8 nm depending upon the sample and method of analysis employed. These are obviously significantly below the thicknesses prodicted from the slopes of the Hoffman-Weeks plots in the low crystallization temperature

TABLE 3

η = 1/SLOPE OF HOFFMAN-WEEKS PLOTS

Vol. % PVF_2	α Form		γ Form
	Low T_c	High T_c	
100.0	5.65	1.50	1.65
85.8	5.75	1.52	1.68
72.8	5.43	1.64	1.70
60.9	5.05	1.66	1.76
50.1	4.83	1.63	1.73
40.1	4.59	1.67	1.79

range. They are only slightly below the values predicted using the slopes of the high T_c data, and this small difference could be explained by the lower crystallization temperatures of the SAXS samples. Therefore, the slopes from the high T_c data for the α crystal form appear to be more reasonable than those from the low T_c data. The slopes for the γ crystals fall in the same range as the α crystals from the high temperature crystallizations.

Slopes as well as extrapolated T_m^o's for the γ' data are meaningless since these crystals never nucleate from the melt and therefore, Hoffman-Weeks theory cannot be applied to them. Being the same crystal structure as the γ crystals necessitates that the γ' crystals would have the same T_m^o's if they had been determined. The fact that they do melt at higher temperatures than the α crystals they arose from implies that the structure is more thermodynamically stable, not that the lamellae are thicker. For the latter to be true, complex rearrangement must take place during the α to γ' transition. This would cause changes in the morphology as well, which are not seen (Chapter III). The γ' crystals must be larger than the γ crystals though, since they both have the same structure, but the former melt at a higher temperature.

3. Melting point depression. The melting point depression observed in the blends is a result of kinetic and thermodynamic

factors. As in any polymer, the kinetic effects arise because crystals are formed at temperatures below the equilibrium melting point. The perfect extended chain crystals can only grow at T_m^o, but would take infinitely long to do so. At lower temperatures thinner lamellae develop, which therefore, melt below T_m^o. To understand the thermodynamic factors, we can view the blend as a solution, with the PMMA acting as a good solvent for the PVF_2. Welch (31), using low molecular weight solvents, found a melting point depression in PVF_2 of about 40 K with dimethylphthalate and 75 K with dimethylacetamide in solutions containing 40 vol.% PVF_2, the same region covered with the blends in the present work. Classical polymer thermodynamics predict that this solution effect should be negligible in high molecular weight blends due to the unfavorable entropy of mixing, and no depression of the T_m^o's should occur. If this was true, the slopes of the Hoffman-Weeks plots should increase as more PMMA is added so that the extrapolated T_m^o's would coincide. This is exactly opposite to the trend that is seen in Table 3 for the α form in the high T_c region and the γ form. The slopes of the α form from the low T_c region increase as more PMMA is added, but not enough to make the T_m^o's coincide. It is therefore believed that there are very favorable enthalpic interactions between the two polymers which cause the depression of the T_m^o's and enable them to form a compatible blend.

Coleman et al. (82) have seen alterations in the carbonyl

absorbance band in Fourier transform infrared spectra from these blends. They were not able to account for these changes by co-adding the spectra of the individual homopolymers. This could imply that the enthalpic factors are from hydrogen bond-type interactions between the carbonyl of the PMMA and the electropositive hydrogens of the PVF_2. In order to measure the amount of enthalpic interaction, the kinetic factors first must be removed. This is done by using only the equilibrium melting points for each composition, determined from the Hoffman-Weeks plots.

Applying the Flory-Huggins approximation (141), Scott (86) derived the following equation for polymer-polymer blends.

$$\mu_{2u} - \mu_{2u}^{o} = \frac{RT\ V_{2u}}{V_{1u}} \left[\frac{\ln v_2}{m_2} + \left(\frac{1}{m_2} - \frac{1}{m_1} \right) v_1 + \chi_{12} v_1^2 \right] \quad (15)$$

The subscripts 1 and 2 represent the noncrystallizable and crystallizable polymers, respectively. The chemical potential per mole of repeat units for the crystallizable polymer is μ_{2u}^{o} in the pure melt and μ_{2u} in the blend. The specific volumes are V, and the volumes fractions v. χ_{12} is the polymer-polymer interaction parameter and m is essentially the degree of polymerization.

The free energy of fusion per mole of repeat units of a homopolymer, ΔF_u^{o}, and a blend, ΔF_u, is by definition:

$$\Delta F_u^{o} = \mu_u^{o} - \mu_u^{c} \quad (16)$$

$$\Delta F_u = \mu_u - \mu_u^c = (\mu_u - \mu_u^o) + (\mu_u^o - \mu_u^c) \qquad (17)$$

where μ_u^c is the chemical potential per mole of repeat units in the crystalline state. Combining equations 15-17 gives

$$\Delta F_{2u} = \Delta F_{2u}^o + \frac{RT\ V_{2u}}{V_{1u}}\ \chi_{12}\ v_1^2 \qquad (18)$$

where now ΔF_{2u} is shown to be equal to ΔF_{2u}^o for the pure polymer plus a term due to the interaction between the two components in the blend.

Sanchez and DiMarzio (148) have shown that the free energy changes upon crystallization can be related to the equilibrium melting points for polymer solutions by:

$$\Delta F_{2u}^o = \frac{\Delta H_{2u}\ (T_m^o - T)}{T_m^o} \qquad (19)$$

$$\Delta F_{2u} = [\Delta H_{2u} + \bar{\Delta} h_{2u}] \left(\frac{T_d^o - T}{T_d^o} \right) \qquad (20)$$

where $\bar{\Delta} h_{2u}$ is the average partial molar heat of solution per mole of monomer units and T_d^o, the equilibrium dissolution temperature. In this case, T_d^o is T_m^o for the blend.

By definition of $\bar{\Delta} h_{2u}$ it can be shown that:

$$\bar{\Delta} h_{2u} = \left. \frac{\partial \Delta H_m}{\partial n_{2u}} \right|_{T,P,n_{1u}} = RT\ \frac{V_{2u}}{V_{1u}}\ \chi_{12}\ v_1^2 \qquad (21)$$

where ΔH_m is the heat of mixing per mole of repeat units and n is the number of moles of repeat units.

By using equations 19-21 in equation 18 the relationship between the interaction parameter and the equilibrium melting point depression is obtained.

$$\left(\frac{T_m^o - T_d^o}{T_m^o}\right) = \frac{RT}{\Delta H_{2u}} \frac{V_{2u}}{V_{1u}} \chi_{12} v_1^2 \qquad (22)$$

Neglecting the entropic contributions (86), χ_{12} can be given as

$$\chi_{12} = \frac{BV_{1u}}{RT} \qquad (23)$$

with B being the interaction energy density of the two polymers. Inserting this into equation 22 and rearranging gives:

$$\left(1 - \frac{T_d^o}{T_m^o}\right) = \frac{-B\ V_{2u}}{\Delta H_{2u}} v_1^2 \qquad (24)$$

A plot of the left side of equation 24 vs. v_1^2 would therefore have a slope proportional to B. Note that this equation, as opposed to similar ones previously developed (34,95), uses only equilibrium melting points. Since it was derived from thermodynamic arguments it is important that any kinetic factors which would affect the magnitude of the melting point depression be removed. Using the T_m^o's given in Table 2 for the low T_c data of the α polymorph in such a manner gave the plot shown in Figure 48. With V_{1u} = 84.9 cm^3/mole, V_{2u} =

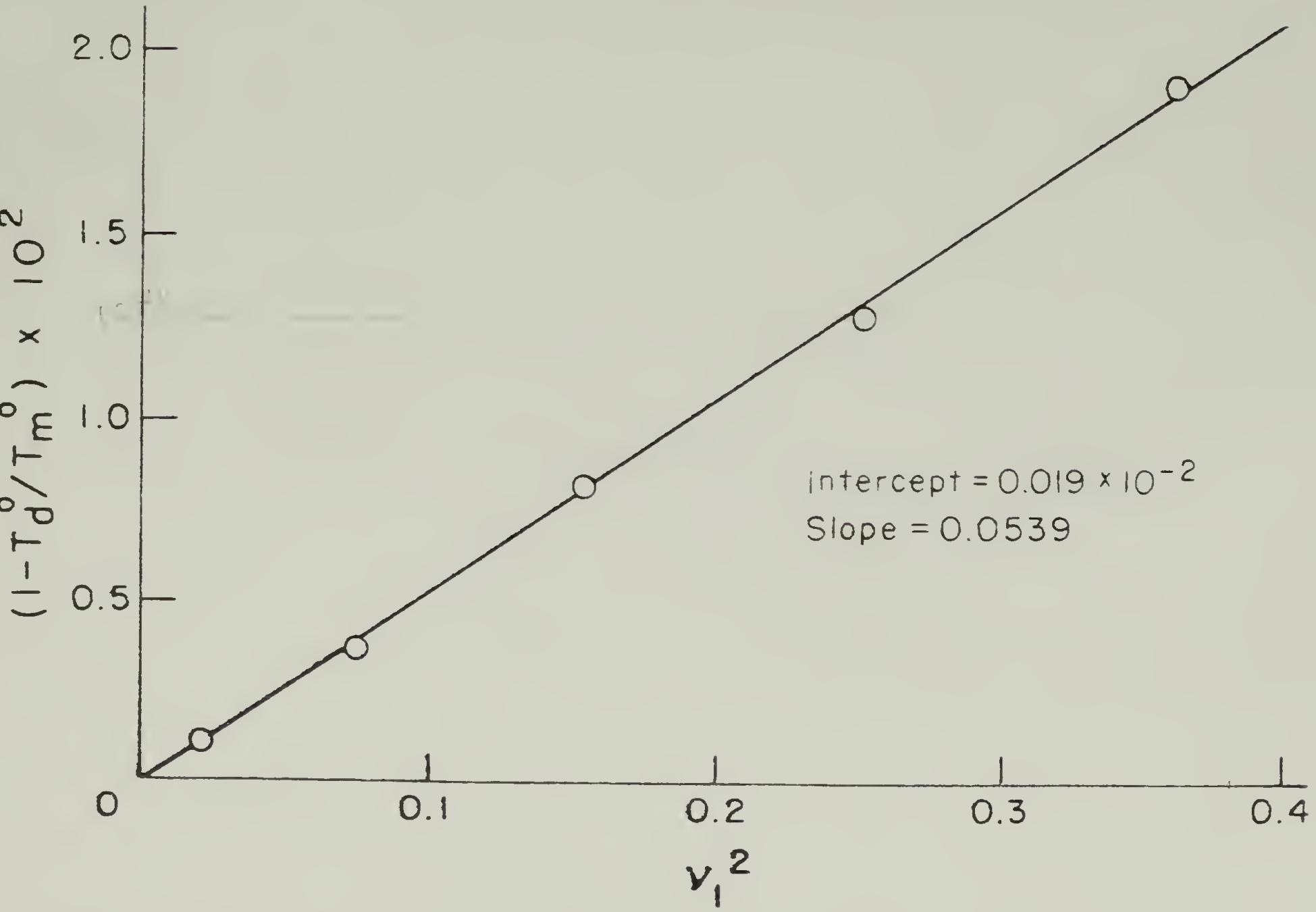

Figure 48. Plot of Eq. 21 for PVF_2/PMMA blends using T_m^o's from low T_c data of α form.

36.4 cm^3/mole (149) and densities of ρ_1 = 1.20 g/cm^3 and ρ_2 = 1.80 g/cm^3, the value found for B was -8.83×10^6 $j/(m^3$ of PMMA).

The large negative B verifies that this system is compatible in the melt. The absolute value of B is larger than that found by Nishi and Wang (34) and Paul et al. (95) for the same crystallization region, since they did not use equilibrium melting points. Note that the intercept is very close to zero, verifying the assumption used with equation 23 that entropic effects contribute little to χ_{12}.

The high crystallization temperature region is more representative of the equilibrium interactions occurring between PMMA and PVF_2, as opposed to the low T_c data. Therefore, analysis of the results from the former region should yield a better estimate of the interaction between the polymers. The values for the equilibrium melting points for the high T_c α crystals and for the γ form given in Table 2 are plotted against the volume fraction of PVF_2 in Figure 49. Since the depression of the melting points is similar for both forms, analysis of each according to equation 24 gave results falling on the same curve. This is shown in Figure 50. Note now the data do not form a straight line. Assuming entropy effects to still be negligible, the curve is drawn through the origin. Paul et al. (95) have shown that for polymers of this size, entropy effects could only lower the melting points a maximum of 0.2 K in the range of compositions

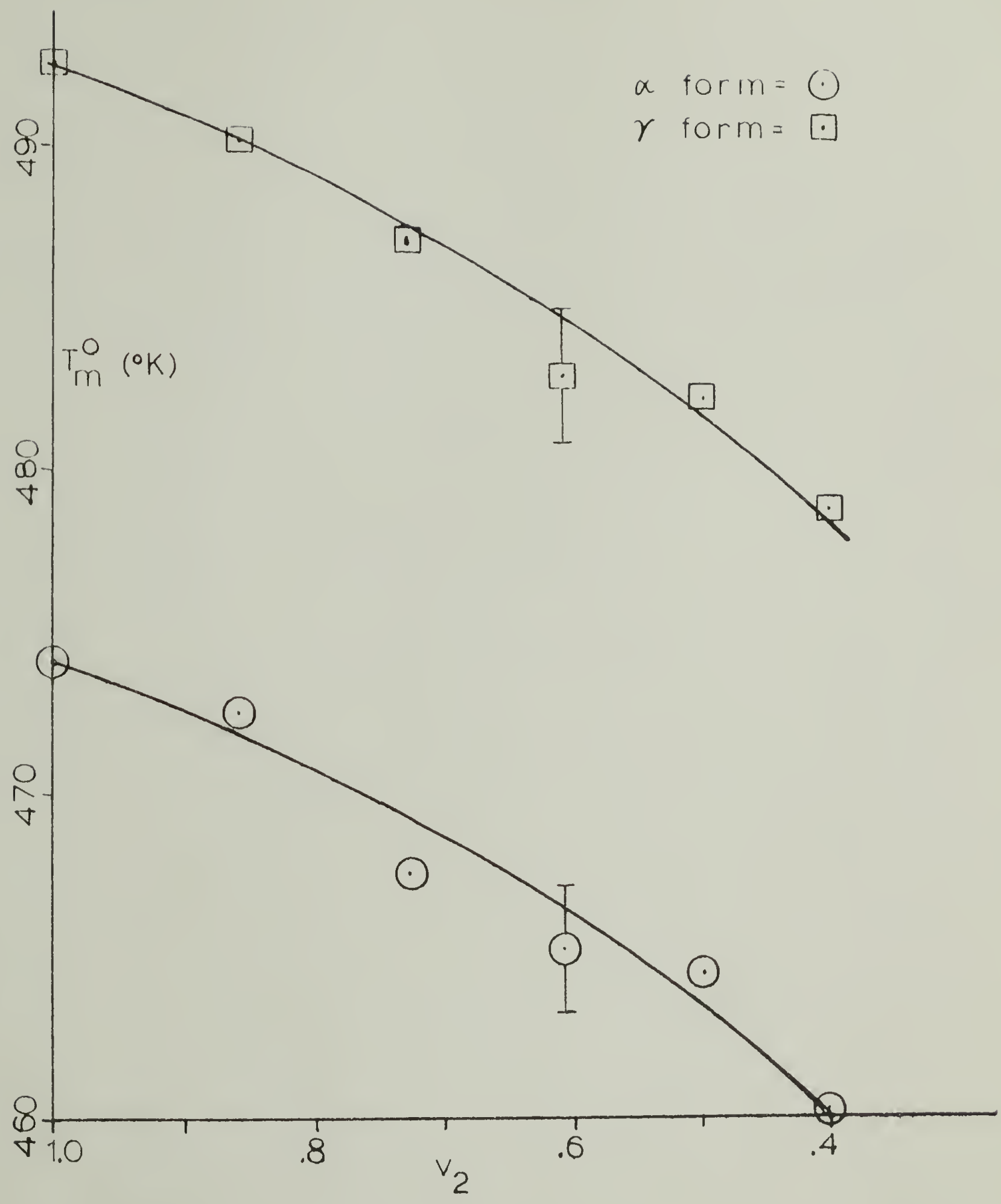

Figure 49. T_m^o's extrapolated for γ form and high T_c region of α form from Hoffman-Weeks plots of PVF_2/PMMA blends.

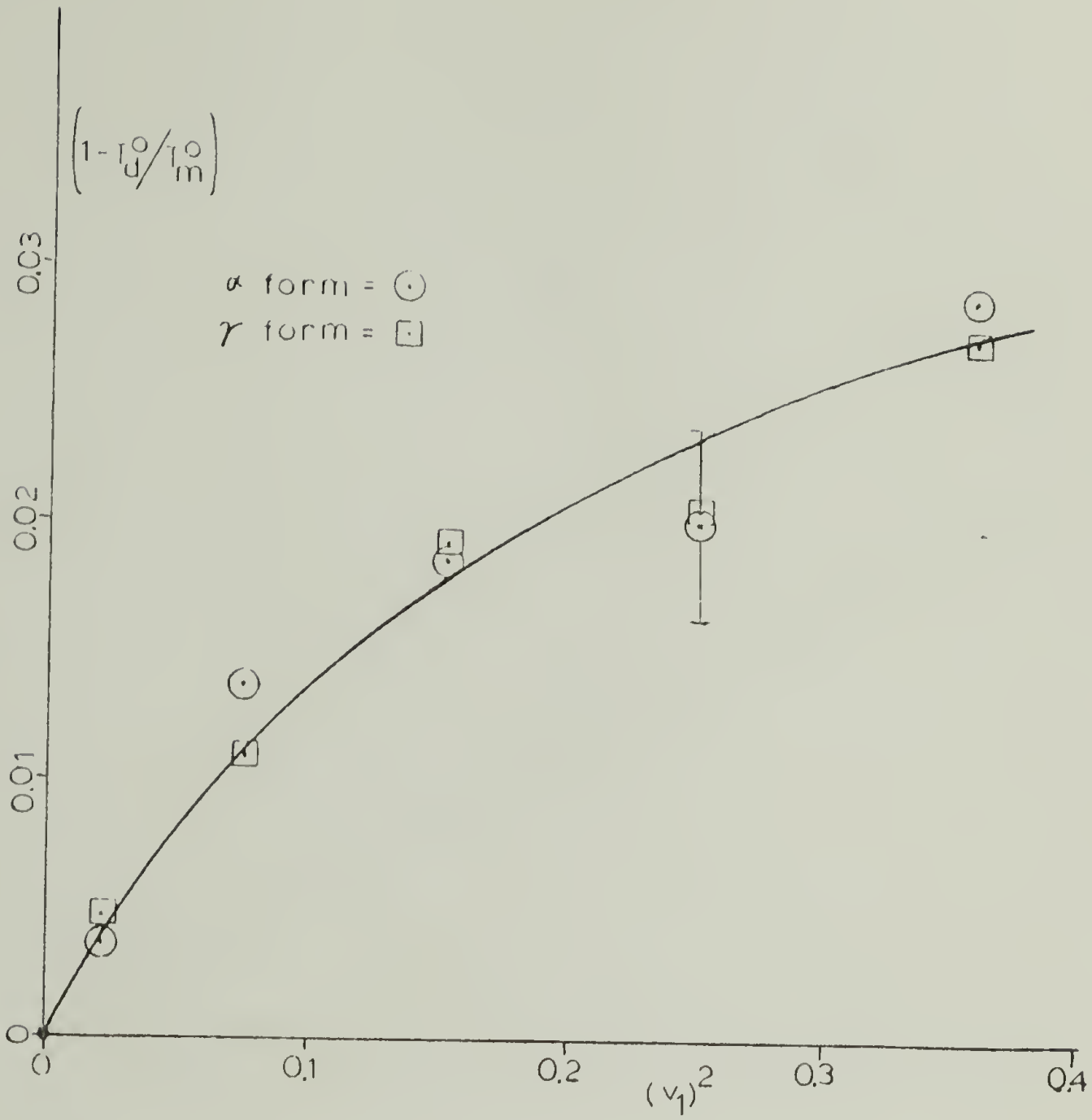

Figure 50. Plot of eq. 21 for PVF_2/PMMA blends using T_m^o's of λ form and high T_c data of α form.

explored. This corresponds to a maximum intercept of 4 x 10^{-4} in Figure 50 which is equivalent to zero within experimental error. Since this plot is not a straight line, it implies that B is a function of composition. In all cases it is still negative, but its absolute value decreases as more PMMA is added. A plot of -B vs. volume fraction of PVF_2 is shown in Figure 51.

Recently, Wendorff (94) has also analyzed blends of PMMA and PVF_2 to determine interaction parameters. His results from both SAXS and melting point depression gave concentration dependent interaction parameters which were in excellent agreement with the values found here. The T_m^o's Wendorff obtained were approximately 8-9 K higher than those determined in the present study. These discrepancies can be due to the fact that Wendorff used a different PVF_2, most likely having a different amount of head-to-head linkages. Since T_m^o was shown to be a function of X_{eq} and thus X, variation of X will alter the T_m^o determined. However, since his interaction parameters were close to those established here, it appears as though B is not a function of X.

There are other systems which have also appeared to have concentration dependent interaction parameters. Using vapor sorption measurements, χ_{12} was found to vary with composition in blends of polystyrene/poly(vinyl methyl ether) (90). The interaction parameters for many polymer-solvent mixtures is known to be a function of the amount of solvent

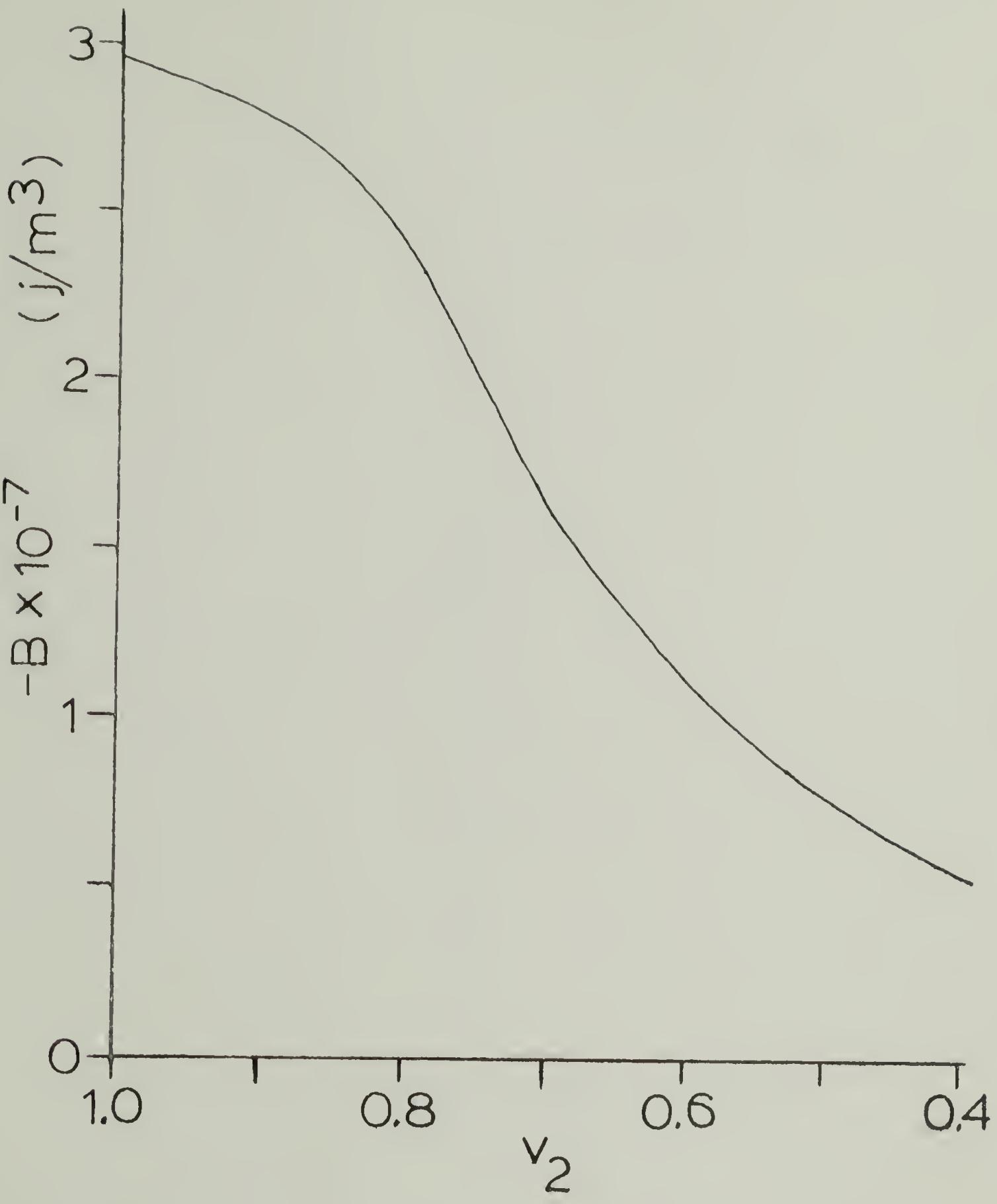

Figure 51. Interaction energy density B of PVF_2/PMMA blends as a function of volume fraction of PVF_2. Values of B are from the slope of the curve in Figure 50.

present (150). Therefore, a composition dependent interaction parameter is not unreasonable. Flory (151) has actually attempted to account for this fact in the development of his equation of state thermodynamics.

C. Conclusions

The melting behavior of PVF_2/PMMA blends is very complex. Decreases in the crystallinity of the blends beyond what is due to dilution suggest interactions between the two components. Construction of Hoffman-Weeks plots for different blend compositions were similar, but had aspects which did not agree with the theory behind these plots. At low crystallization temperatures, only α form crystals grow. At high crystallization temperatures, two new higher melting species are obtained. The highest melting species, γ', is a result of a solid-solid transition from the α form and thus cannot be analyzed using Hoffman-Weeks theory. The other is from a γ crystal form which starts to grow concurrently with the α phase at these temperatures. The data for the α phase undergoes a change in slope at the same temperatures at which the γ' phase becomes apparent. This change in slope enables the extrapolation of two T_m^o's to explain this. The PVF_2 can be viewed as a copolymer with the head-to-head linkages as the co-units. At high crystallization temperatures the amount of these linkages incorporated in the crystal approaches the equilibrium value. Rapid growth at low

crystallization temperatures results in entrapment of these units in the crystal, in an amount equal to the overall concentration of head-to-head units in the polymer. The difference in the head-to-head unit concentration in the α crystal causes the change in slope of the Hoffman-Weeks plots. Using this analysis, defect energies of 10.3 to 6.3 kjoules/mole are calculated for values of X ranging from 0.05 to 0.11. From the two different slopes, estimates of lamellar thicknesses are made. The high T_c data gives values in close agreement with what is observed by other techniques while the low T_c data seemed to be too large.

The melting point depression in the blends is due to both kinetic and thermodynamic factors. Using the Hoffman-Weeks plots to determine T_m^o's enables the kinetic effects to be removed. Applying a thermodynamically based theory to the depression of the T_m^o's in the blends allows calculation of the interaction energy density, B. A value for B of -8.83×10^6 j/m^3 is found using the α form data at low crystallization temperatures. Using the data at higher crystallization temperatures, which is more representative of equilibrium conditions, B is found to be a function of composition from both the α and γ crystal melting points.

C H A P T E R V

SAXS

A. Background

If impinged upon by x-rays of incident intensity I_o the electrons in a material will emit coherent scattered intensity I(h) given by (152)

$$I(h) = \frac{i_e I_o}{p^2} F^2(h) \qquad (25)$$

where i_e is the Thompson scattering factor equal to 7.96 x 10^{-26} cm^2, p is the distance from the scattering material to the observer and F(h) is a structure factor related to the internal morphology of the material. The scattering vector h can be shown to be

$$h = 2\pi \cdot s = \frac{4\pi}{\lambda} \sin \theta \qquad (26)$$

where the angle between the incident intensity of wavelength λ and the observer is 2θ. The scattered intensity may also be expressed in a normalized format given by the Rayleigh factor

$$R(h) = \frac{I(h)p^2}{I_o V_o} \qquad (27)$$

where V_o is the volume of the scattering system.

The scattering profile itself can be divided into four

regions of scattering angles, each containing information on different scales of size. The very small angle scattering, known as the Guinier region provides information on the average radius of gyration, $\bar{R}_g$, of isolated particles in a dilute solution (153-155). The range of applicability for this analysis is generally accepted as $\bar{R}_g h<1$. The intermediate angle, central portion of the scattering curve is the particle interference region. Analysis of this region is usually accomplished by employing morphological models to describe the scattering. Discussion of the models used to treat lamellar semi-crystalline polymers will be presented below. The Porod law region is the tail of the small angle scattering curve. This region gives information on the surface to volume ratio of the particles and sizes of interfacial boundaries between areas differing in electron densities (155-158). At angles larger than the Porod law region, the scattering is due only to small scale concentration and thermal density fluctuation within a phase. This type of scattering is superimposed upon the entire curve, but its relatively small intensity makes it difficult to observe in the other regions. This region is actually the onset of the wide angle scattering.

Two approaches can be taken to analyze experimental scattering curves. For systems of unknown particle shapes a statistical approach is used wherein the scattering is considered to arise from fluctuations in electron density

throughout the medium. On the other hand, for systems of more well-defined geometry, the structure factors can be calculated from predetermined models.

In the statistical approach, the local electron density ρ_j is given by

$$\rho_j = \bar{\rho} + \Delta\eta_j \tag{28}$$

where $\bar{\rho}$ is the average electron density of the medium and $\Delta\eta_j$ is the deviation of the jth volume element from this average. A three dimensional correlation function can then be described as (152,154,155,157)

$$\gamma'(\underset{\sim}{r}) = \frac{\langle \Delta\eta_j \ \Delta\eta_k \rangle_{\underset{\sim}{r}}}{\overline{\eta^2}} \tag{29}$$

where $\langle \ \rangle_{\underset{\sim}{r}}$ represents the average over all volume elements j and k separated by the vector $\underset{\sim}{r}$, and $\overline{\eta^2}$ is the mean square fluctuation at $\underset{\sim}{r} = 0$. The correlation function will be 1 when $\underset{\sim}{r} = 0$ and approaches 0 as $\underset{\sim}{r}$ goes to ∞.

Guinier (155) has shown that the scattered intensity for an isotropic system can be represented using the correlation function by

$$I(s) = \frac{i_e I_o}{p^2} \overline{\eta^2} \ V_o \int_0^\infty \gamma'(r) \exp(2\pi isr) dr \tag{30}$$

where r is now a scalar and $s = \frac{2}{\lambda} \sin\theta$. A Fourier transform of equation 30 enables one to solve for $\gamma'(r)$ in terms of I(s).

$$\gamma'(r) = \frac{p^2}{i_e I_o} \frac{1}{V_o \overline{\eta^2}} \int_0^\infty I(s) \exp(2\pi i s r) ds \qquad (31)$$

which is shown to be equivalent to

$$\gamma'(r) = \frac{\int_0^\infty I(s) \cos(2\pi r s) ds}{\int_0^\infty I(s)\, ds} \qquad (32)$$

To apply the model approach, one can choose from a variety of models found in the literature. Four of the more widely known ones used to describe lamellar semicrystalline polymers are: (1) the Tsvankin-Buchanan model (158); (2) the Vonk model for a theoretical correlation function (159); (3) the Hosemann paracrystalline lattice (160); and (4) Ruland's interface distribution function approach (161). Other recent works dealing with these four models (73,162-165) are also suggested for a more in-depth understanding.

1. SAXS models.

a. Tsvankin-Buchanan model. This model describes a distorted one dimensional infinite lattice of alternating amorphous and crystalline phases separated by a linear transition zone. The thickness distributions of the crystalline and amorphous regions are assumed to be rectangular and Gaussian respectively. A series of calibration curves are thus calculated. One can then measure the position and the peak width at half height of the scattering maximum and uniquely determine the crystallinity and model parameters. Although this is an appealing model which is easily applied,

previous studies (73,166) have not found good agreement with the experimentally determined scattering profiles. Therefore, this approach was not utilized in this work.

b. Vonk model for a theoretical correlation function. Debye et al.'s (167) model describing scattering from a system of random voids was adapted by Vonk and Korleve (159) to an infinite stack of alternating crystalline lamellae and amorphous regions. A theoretical correlation function is calculated from this model by examining the correlations in the electron density fluctuations of two points separated by a distance r perpendicular to the lamellar surfaces. Since the experimentally determined scattering intensity is from a three dimensional system, it must be corrected to compare to this theoretical one dimensional model. This is known as the Lorentz correction and amounts to multiplying $I(s)$ by s^2 (163,168,169). The experimental one dimensional correlation function is therefore

$$\gamma(r) = \frac{\int_0^\infty s^2 I(s) \cos(2\pi sr) ds}{\int_0^\infty s^2 I(s)\, ds} \qquad (33)$$

In the model, the crystals of thickness r_c have a thickness distribution function $P_c(r_c)$ with a mean thickness C. The amorphous layers are distributed according to $P_a(r_a)$ with a mean value A. The volume fraction crystallinity is therefore

$$\phi_c = \frac{C}{A + C} \qquad (34)$$

If a rod of length r is placed in such a system of alternating crystalline and amorphous regions, the probability that both ends will be in a crystal phase is given by p_{cc}. The probability that a given rod has both ends in the same crystalline lamellae is q_c, whereas the probability that one end of the rod is in another lamella separated by one amorphous region is q_{cac}. This can be extended to the probability that the ends are in different lamellae separated by two amorphous and one crystalline region, q_{cacac}, and on ad infinitum. Thus, p_{cc} is the sum of all these probabilities.

$$p_{cc} = q_c + q_{cac} + q_{cacac} + \ldots \tag{35}$$

Vonk has shown that

$$q_c = \frac{1}{\phi_c(C+A)} \int_r^\infty (r_c - r) P_c(r_c) dr_c \tag{36}$$

By convoluting the individual distributions one obtains

$$q_{cac} = \phi_c(C+A)\ Q(r_1)\ P_a(r_a)\ Q(r_2) \tag{37}$$

where

$$Q(r_1) = Q(r_2) = \frac{1}{\phi_c(C+A)} \int_{r_1}^\infty P_c(r_c)\ dr_c \tag{38}$$

The subscripts refer to the layer number in the stack. Values of the additional probabilities, e.g., q_{cacac}, can also be computed in this manner.

The correlation function can then be calculated by

$$\gamma(r) = (p_{cc} - \phi_c)/(1 - \phi_c) =$$

$$\frac{\phi_c}{1-\phi_c}\left[\frac{1}{\phi_c^2}\int_0^\infty (r_c - r)P_c(r_c)dr_c + P_{cac} + \cdots - 1\right] \quad (39)$$

Therefore, $\gamma(r)$ can be calculated given ϕ_c and the distribution functions of the crystal and amorphous phases. In performing this calculation, renormalization of the distribution functions must be done to avoid negative thicknesses. Satisfactory results have been obtained from this model with several polymer systems (73,112,159,170).

c. Hosemann paracrystalline lattice. The Hosemann model (160) is a refinement of the Tsvankin-Buchanan model in which the infinite lattice is replaced by a finite stack of N parallel lamellae. This causes broadening of the scattering curve and zero order scattering from the entire stack. The amorphous and crystalline layers are arranged according to paracrystalline statistics with a finite transition zone between them. Theoretical scattering intensities are calculated from

$$I(s) = \frac{1}{2\pi s^2}\,\mathrm{Re}\left\{\left(N\frac{(1-f_a)(1-f_c)}{(1-f_af_c)}\right) + f_c\left(\frac{1-f_a}{1-f_af_c}\right)^2\left(1-(f_af_c)^N\right)\right\} \cdot Z(s) \quad (40)$$

The amorphous and crystalline structure factors, f_a and f_c, are defined by the Fourier transforms of the thickness

distributions, $H_i(r)$.

These thickness distributions are assumed to be Guassian and given by

$$H_i(r) = \left(\frac{1}{\sqrt{2\pi}\ \overline{\Delta r_i}}\right) \exp\left[\frac{-(r-\bar{r}_i)^2}{2(\overline{\Delta r_i})^2}\right] \tag{41}$$

with $\bar{r}$ being the average thickness. The parameters are simplified somewhat by using (171)

$$g_i = (\overline{\Delta r_i})^2/\overline{r_i}^2 \tag{42}$$

A transition zone of thickness E is incorporated by the term Z(s), where

$$Z(s) = \frac{1}{2\pi i s^2 E}\left[1-\exp(-2\pi i s E)\right]^2 \tag{43}$$

The parameters needed are therefore the standard deviations and average thicknesses of both the crystalline and amorphous layers, as well as E and N. Previous studies (73, 164,166,171) have obtained values of N less than or equal to 2.0. Interpretations of these low values suggest that N represents the equivalent number of perfectly parallel lamellae (164) or that N can be looked at as a measure of angular disorder in the lamellar stack (171).

d. Ruland interface distribution approach. This method (161) utilizes the derivative of the electron density profile to calculate the interface distribution. From this, the crystal and amorphous distributions can be obtained. This

approach emphasizes lower order distance distribution and therefore demands very accurate data in the tail of the scattering curve. In both this approach and the correlation function method, analysis is done on the Fourier transform of the scattering curve which can introduce additional errors.

e. More general models. Aside from the models specifically designed for lamellar crystalline polymers, more general approaches to scattering can also be applied. Two which can be of use in the present work are Bragg's law (113) and the diameter distribution approach of Vonk (172).

If the centers of adjacent lamellae are assumed to form a macrolattice, a Bragg spacing d can be derived from the angle of the scattering maxima, through the use of Bragg's law (113) given in equation 1. The position of the intensity maximum must be taken from the Lorentz corrected desmeared data (73,162,163,168) since the only concern here is the distance between lamellae in the same stack, and these stacks are randomly oriented in the sample. The periodicity obtained is known as the long period.

The application of Bragg's law implies that there is an infinite lattice with no disorder. Since neither of these assumptions actually hold, the values of the long period obtained will not be exact. Even so, reasonable agreement has been found between long periods obtained via Bragg's law, and those derived from various models (73,112,163).

The diameter distribution function approach assumes that

the scattering arises from an isotropic system of particles of equal shapes but different sizes R. The total integrated x-ray intensity is then expressed as an integral over the particle size distribution function D(R), multiplied by a common single particle function of hR. To apply this to a lamellar system, the objects are assumed to be plate like giving

$$\int_0^\infty I(h)dh = \int_0^\infty D(R)\ m^2(R)\ \frac{\sin^2(hR)}{(hR)^2}\ dR \qquad (44)$$

where m(R) is the excess number of electrons in a plate-like particle of thickness 2R, over and above the number of electrons in the same volume of the surrounding medium. Solutions of equation 44 are then obtained at discrete values of D(R) via the method of least squares thus yielding the distribution of lamellar thicknesses.

In light of the above discussion, and results of previous studies (73,112,164,166,171), theoretical comparison to the experimental data will be performed utilizing the Vonk correlation function and Hosemann paracrystalline models. The diameter distribution function of the lamellar thicknesses as well as the long period from Bragg's law will also be calculated.

2. Porod's law and the invariant. From investigations of a wide variety of systems, with varying morphologies, Porod (156) found that regardless of the shape of the scattering

entity and assuming the electron density profile was rectangular, the limiting intensity is given by

$$\lim_{s\to\infty} \quad I(s) = \frac{K}{s^4} \tag{45}$$

where the constant K is related to the specific inner surface of the system S/V, and the volume fractions of the phases ϕ_i, by

$$K = \left(\frac{S}{V}\right) \frac{Q}{8\pi^3 \phi_1 \phi_2} \tag{46}$$

Q is the Porod invariant

$$Q = 4\pi \int_0^\infty I(s) s^2 ds \tag{47}$$

To obtain Q (experimentally), the integral of equation 47 is divided into two parts, above and below the point at which Porod's law can be assumed to hold, s_p,

$$Q = 4\pi \int_0^{s_p} s^2 I(s) ds + 4\pi \int_{s_p}^\infty s^2 I(s) ds \tag{48}$$

The second term can be evaluated numerically giving K/s_p with K determined from a plot of Is^4 vs. s^2 utilizing data in the tail region of the scattering curve. The first term is obtained directly from I(s).

The Porod invariant can be related to $\overline{\eta^2}$ by

$$\overline{\eta^2} = \frac{Q\ p^2}{i_e N_a^2\ t} \tag{49}$$

where N_a is Avagadro's number. The mean square fluctuation of the electron density is an important quantity since it is proportional to the volume fractions of the phases ϕ_i in the scattering material, and their electron density differences (155,167). For an ideal two phase system with sharp phase boundaries,

$$\overline{\eta^2} = \phi_1 \phi_2 (\rho_1 - \rho_2)^2 \qquad (50)$$

This can be extended to an ideal n phase system to give

$$\overline{\eta^2} = \frac{1}{2} \sum_i^n \sum_j^n \phi_i \phi_j (\rho_i - \rho_j)^2 \qquad (51)$$

If the electron density profile is not rectangular and there is a finite transition zone, corrections to Porod's law must be made (160,173-176). This is accomplished by convoluting the ideal (rectangular) electron density profile with a function describing the interface profile

$$\rho(x)_{real} = \rho(x)_{ideal} * h'(x) = \int_{-\infty}^{\infty} \rho(y) h'(x-y) dy \qquad (52)$$

where * represents the convolution product. The resultant modification to the intensity is

$$I(s)_{obs} = I(s)_{ideal} \cdot H^2(s) \qquad (53)$$

with H(s) being the Fourier transform of h'(x). Two basic functions for h'(x) have been applied. Ruland (175) and Vonk (179) assumed a linear transition of thickness E such

that

$$h'(x) = \begin{cases} 1/E & 0 \leq x \leq t \\ 0 & t \leq x \end{cases} \tag{54}$$

$$H(s) = \frac{\sin^2 \pi Es}{(\pi Es)^2} \approx 1 - 2\pi^2 E^2 s^2/3 + \ldots . \tag{55}$$

while Hashimoto (176) used a Gaussian transition zone,

$$h'(x) = 2\pi\sigma^2 \exp(-x^2/2\sigma^2) \tag{56}$$

$$H(s) = \exp(-4\pi^2 \sigma^2 s^2) \tag{57}$$

There are a number of ways these interface functions can be applied, which involve various approximations made on the form of $H^2(s)$. An extensive review of these as well as a semi-empirical model approach to this problem is discussed in detail by Koberstein et al. (173). In all cases, however, a negative deviation from Porod's law is seen.

An alternative method to calculate a linear transition zone through the use of the correlation function has been proposed by Vonk (174). In this method, a quantity R is calculated from

$$R = 4\pi^2 \frac{\int s^4 I(s) ds}{\int s^2 I(s) ds} \tag{58}$$

and used in conjunction with the slope of the three dimensional correlation function evaluated at r = E giving

$$E = -\frac{4}{R}\left(\frac{d\gamma'(r)}{d\,r}\right)_{r = E} \tag{59}$$

The three dimensional correlation function can be related to the one dimensional correlation function for a lamellar model by (174)

$$\left(\frac{d\gamma(r)}{dr}\right)_{r=E} = 2\left(\frac{d\gamma'(r)}{dr}\right)_{r=E} \qquad (60)$$

If a finite transition zone of thickness E exists, $\overline{\eta^2}$ is reduced (174) and equation 50 becomes

$$\overline{\eta^2} = (\phi_1\phi_2 - \frac{E\ S}{6\ V})\ (\rho_1 - \rho_2)^2 \qquad (61)$$

For a one dimensional lamellar model of average periodicity L perpendicular to the lamellae this equation can be expressed as (174).

$$\overline{\eta^2} = (\phi_1\phi_2 - \frac{E}{3L})\ (\rho_1 - \rho_2)^2 \qquad (62)$$

Another factor to be considered is thermal density fluctuations occurring within a phase which gives rise to background scattering and positive deviations from Porod's law. These must be removed before any of the above equations can be applied. Weigand and Ruland (177) have shown that this background intensity can be developed as a power series of s. Empirical approximations to this series have been proposed (174,178), but they necessitate measurements into the wide angle region. If wide angle data are not available,

Ruland (175) has shown that a reasonable approximation is to assume this background intensity to be a constant, Fl, independent of s. Therefore, utilizing equations 45 and 53, the intensity in the tail region of the curve can be expressed by

$$I(s)\ s^4 = K\ H^2(s) + Fl\ s^4 \qquad (63)$$

Assuming that at large values of s, $H^2(s)$ goes to zero, a plot of Is^4 vs. s^4 should therefore have a slope Fl and intercept zero (175,179). Though a constant slope has been found, intercepts are usually greater than zero. One attempt to explain the positive intercepts has involved dividing the function $H^2(s)$ into two functions for sharp and diffuse boundaries (179). The positive intercepts can also be due to the fact that $H^2(s)$ is still of significant magnitude in the region of s being used (173). However, the final value obtained for the interface width has been shown to vary less than 10% with different background subtraction techniques (174,180).

3. Absolute intensity. Interpretation of the SAXS invariant requires that the measured intensity be placed on an absolute scale. This can be accomplished by either measuring the incident beam intensity I_o, or using a secondary standard (181). In the present work, a Lupolen standard (designated 17/4) supplied by Professor O. Kratky (182) was used. The sample attenuated intensity, $I_s A_s$, of the Lupolen (17/4)

standard is measured at $2\theta = 0.59$ degrees. The incident intensity is then calculated by

$$I_o = \frac{(I_s A_s) p}{K A} \tag{64}$$

where A is the illuminated area of the sample, A_s is the Lupolen attenuation factor and the calibration constant, K, was 68.7 for this work.

The Rayleigh factor for sample intensities, I(s), is therefore

$$R(s) = \frac{I(s) p K}{(I_s A_s) t} \tag{65}$$

with t being the sample thickness.

Pilz (183) has shown that the temperature dependence of the standard intensity is

$$I_s = \frac{I_{s,meas.}}{[1 + 0.0077(T-21.°C)]} \tag{66}$$

where T is the temperature of measurement; 31.0°C in this work.

4. Smearing effects. The above theoretical analysis was derived assuming pinhole collimation of the x-ray beam. In practice, however, slit collimation is often used. The advantages of the latter are that it allows for much larger intensities and decreased parasitic scattering. On the other hand, the profile is smeared if slit collimation is used, and either the experimental intensities must be desmeared,

or the theory smeared, to account for this.

Guinier and Fournet (155) have shown for an incident beam of negligible width, the slit can be assumed to be an array of pinholes, and the smeared intensity, $\tilde{I}(s)$, is given by

$$\tilde{I}(s) = 2 \int_0^\infty W_\ell(u) I(\sqrt{s^2 + u^2}) du \qquad (67)$$

where $W_\ell(u)$ is the weighting function describing the slit. Different cameras therefore have different weighting functions. This is normalized so that

$$\int_0^\infty W_\ell(u) du = 1 \qquad (68)$$

If the slit can be assumed to be of infinite height, and negligible breadth, many of the equations for smeared intensity can be simplified. Porod's law in this case is (173)

$$\lim_{s \to \infty} \tilde{I}(s) = \frac{K'}{s^3} \qquad (69)$$

where $K' = K\pi/2$, and equation 63 then becomes

$$\tilde{I}(s)\, s^3 = K' H^2(s) + Fl\, s^3 \qquad (70)$$

The smeared invariant $\tilde{Q}$ is related to Q by

$$\tilde{Q} = 4\pi \int_0^\infty s\tilde{I}(s) ds = 8\pi \int_0^\infty s^2 I(s) ds = 2Q \qquad (71)$$

B. Results and Discussion

A computer program kindly supplied by C. G. Vonk (184) with slight adaptations was used to perform many of the calculations described above.

The samples used in this study were all crystallized from the melt at 418 K for 24 hours. These samples will be referred to by their volume percent PVF_2, e.g., sample 72.8 contains 72.8 volume percent PVF_2. Looking at thin sections from these samples with a polarizing microscope verified that the 60.9 to 100 samples were volume filled with spherulites. The 50.1 and 40.1 samples had approximately 95% of their volumes filled by spherulites. Wide angle x-ray analysis verified that only α form PVF_2 crystals existed.

The infinite slit height assumption is often applied to data from a Kratky camera. For the angular range scanned in the present study, up to $2\theta = 3.3°$, this assumption is valid according to the criteria defined by Kratky (185). The slit smeared equations were therefore used for much of the analysis. In certain cases though, desmearing of the data was desired. This was performed utilizing the experimentally measured slit profile which is presented in Figure 52.

Measurement of both sample scattering intensities as well as the parasitic scattering obtained with no sample were made by dividing the detector wire into 1024 channels. Calibration of the detector wire at each of these channels

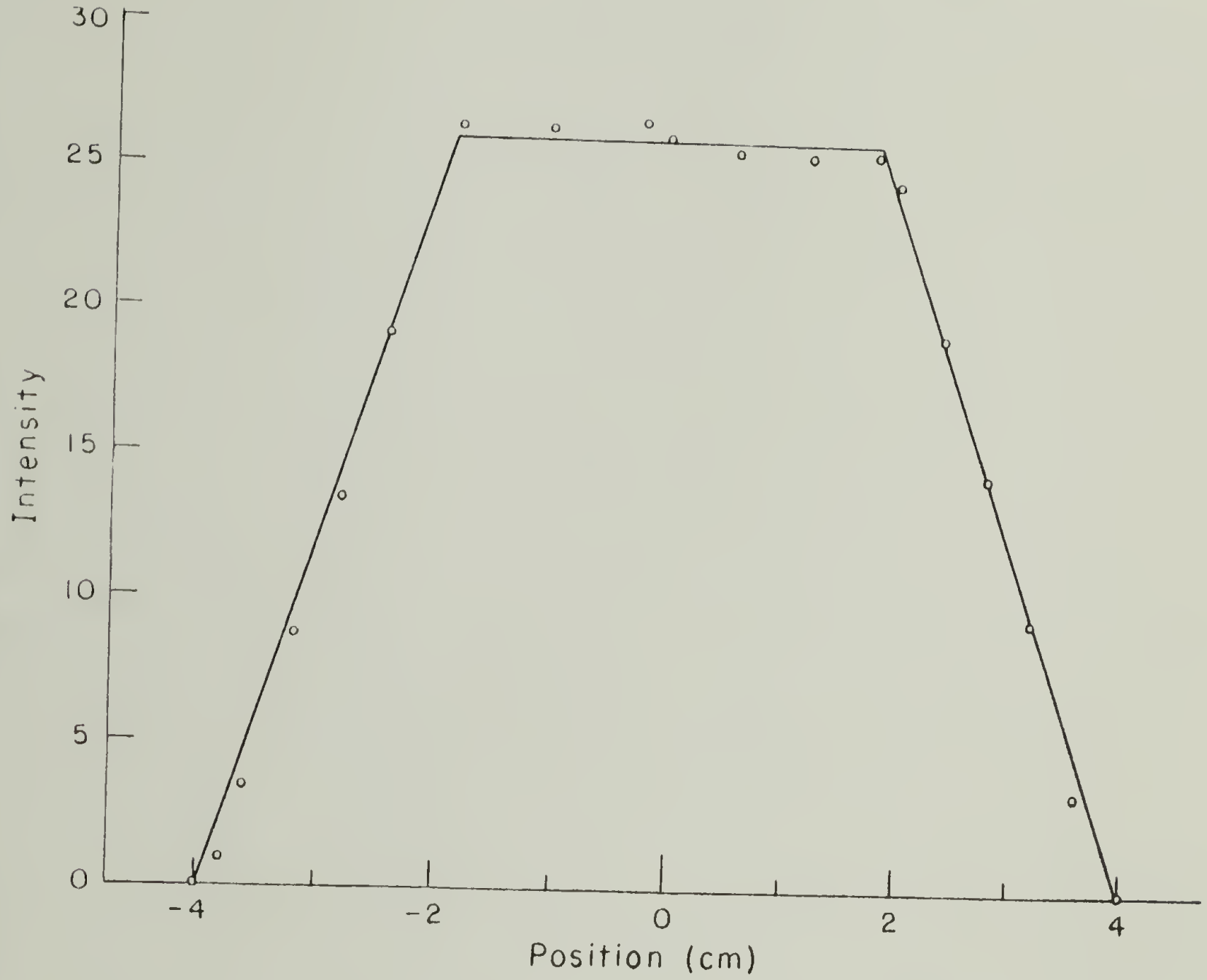

Figure 52. Slit intensity profile for the Kratky camera taken with sample to detector distance set at 53.0 cm.

was accomplished using an iron 55 source which gave a constant incident intensity at all angles. Both the sample data and the parasitic scattering were corrected by this calibration to eliminate effects due to deviations in the wire.

The sample and parasitic data were each independently smoothed using an 8-point interval. The parasitic scattering was then scaled to the sample scattering, using the sample attenuation factors, and subtracted from it. The results were then smoothed again with the same interval.

To measure the attenuation factors, the Lupolen standard was placed in the sample position and a solid scintillation detector was positioned at $2\theta = 0.59°$. Intensities were then measured with and without a sample placed in front of the detector. The ratio of the intensity with the sample to that without is the attenuation factor. These are presented along with sample thickness in Table 4.

The parasitic scattering was extremely small in all the curves. Its largest relative contribution was in the weakest scatterer, the 100 sample. Figure 53 shows a comparison of the smeared scattered intensity to the parasitic scattering for this sample. The corrections for both the parasitic scattering and the detector wire sensitivity did not alter any of the sample curves appreciably.

The pure PVF_2 is seen to have a small peak which shifts to a shoulder in the 85.8 sample. This shoulder becomes less

TABLE 4

SAXS SAMPLE THICKNESSES AND ATTENUATION FACTORS

Sample	Thickness (cm)	Attenuation Factor
100.0	.0724	.263
85.8	.0737	.298
72.8	.0800	.310
60.9	.0721	.352
50.1	.0749	.385
40.1	.0749	.397

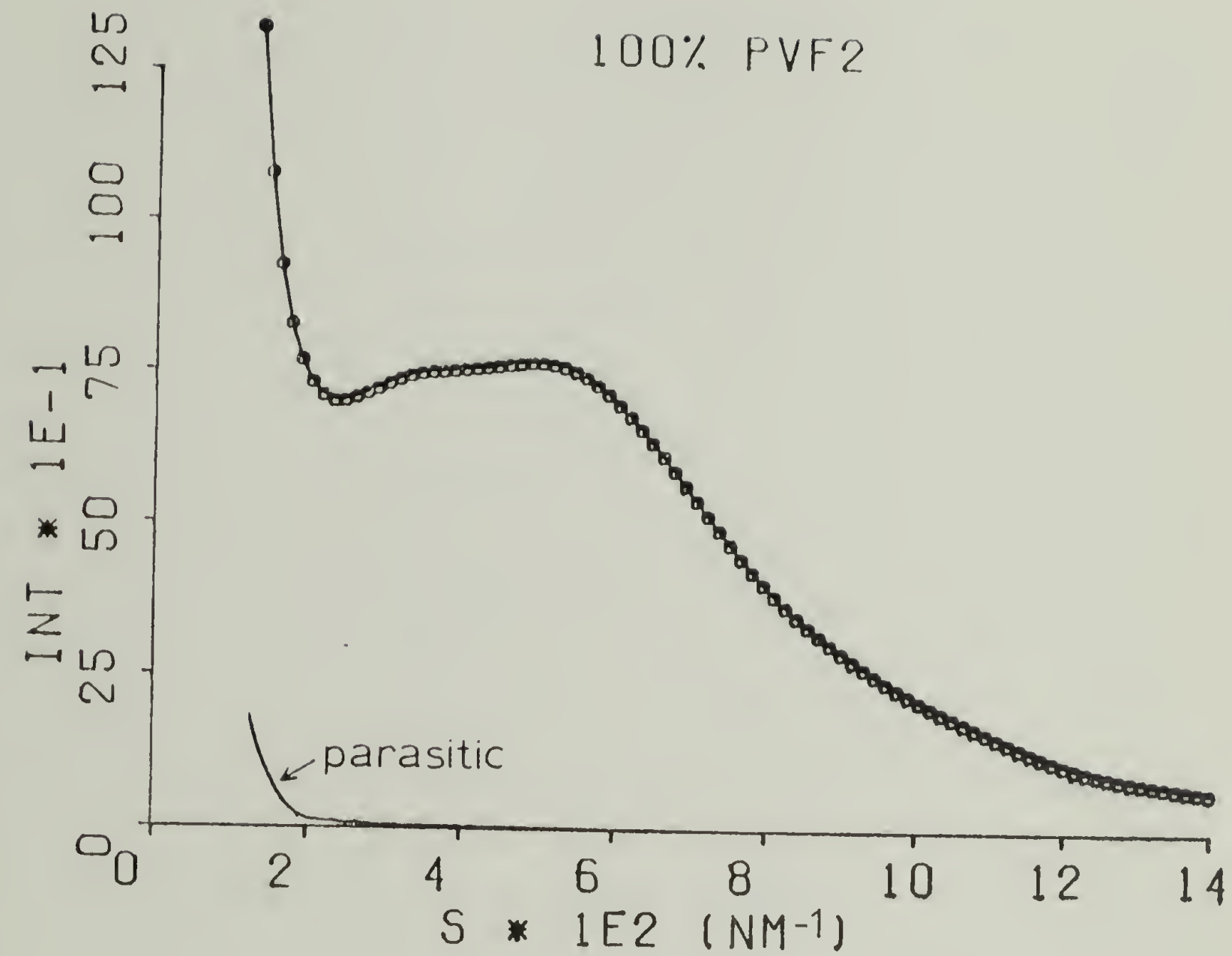

Figure 53. Smeared intensity for pure PVF_2 (connected circles) compared to parasitic scattering (lower curve).

and less pronounced as more PMMA is added to the system. Comparison of the 100, 85.8 and 50.1 samples is shown in Figure 54. Besides the change in the peak shape, there is obviously a tremendous increase in the total scattering with decreasing PVF_2. This will be discussed in detail later.

To perform quantitative analyses on the scattering arising from lamellar interferences, scattering due to fluctuations in the amorphous phase must first be removed. Since data were not collected at wide angles, the assumption of a flat liquid scattering background was made. Through the use of equation 70, plots of $\tilde{I}s^3$ vs. s^3 were made for each sample. A sample plot for the 72.8 sample is shown in Figure 55 and a comparison of these plots for the 100, 85.8 and 50.1 samples is given in Figure 56. As can be seen from these plots, reasonable fits to a straight line can be made in the high s region. The scatter of the data is large in this region because the measured intensities were very small and this type of plot amplifies any experimental errors.

According to equation 70, the slope is equal to Fl and the intercept should be zero. A plot of Fl vs. v_2, where v_2 is the volume fraction of PVF_2 is given in Figure 57. In this figure, Fl is the actual background calculated for each sample from plots of $\tilde{I}s^3$ vs. s^3, and Fl_n is the background normalized for the volume fraction of amorphous material present.

$$Fl_n = \frac{Fl}{(1-\phi_c)} \qquad (72)$$

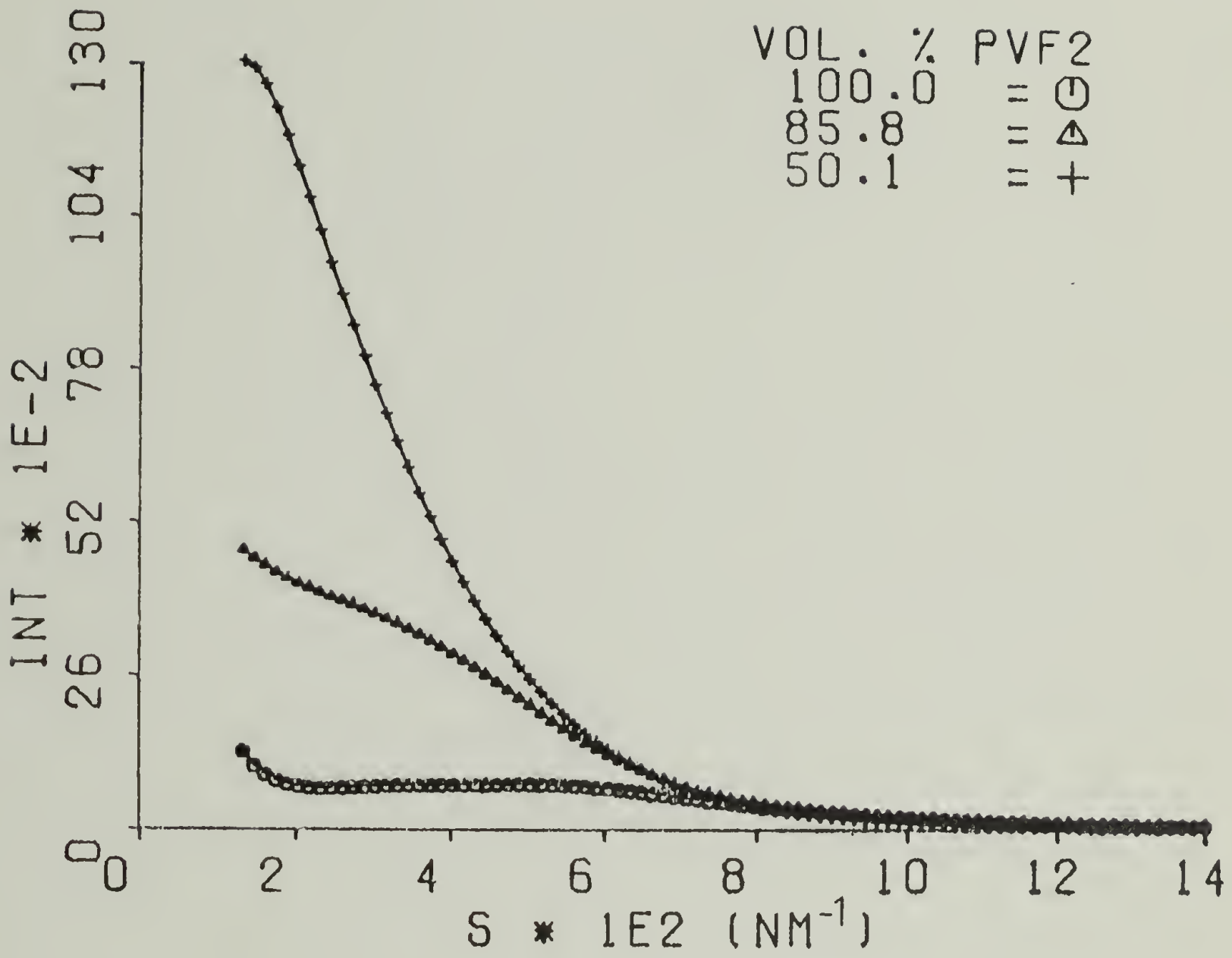

Figure 54. Smeared intensities for samples 100, 85.8, and 50.1.

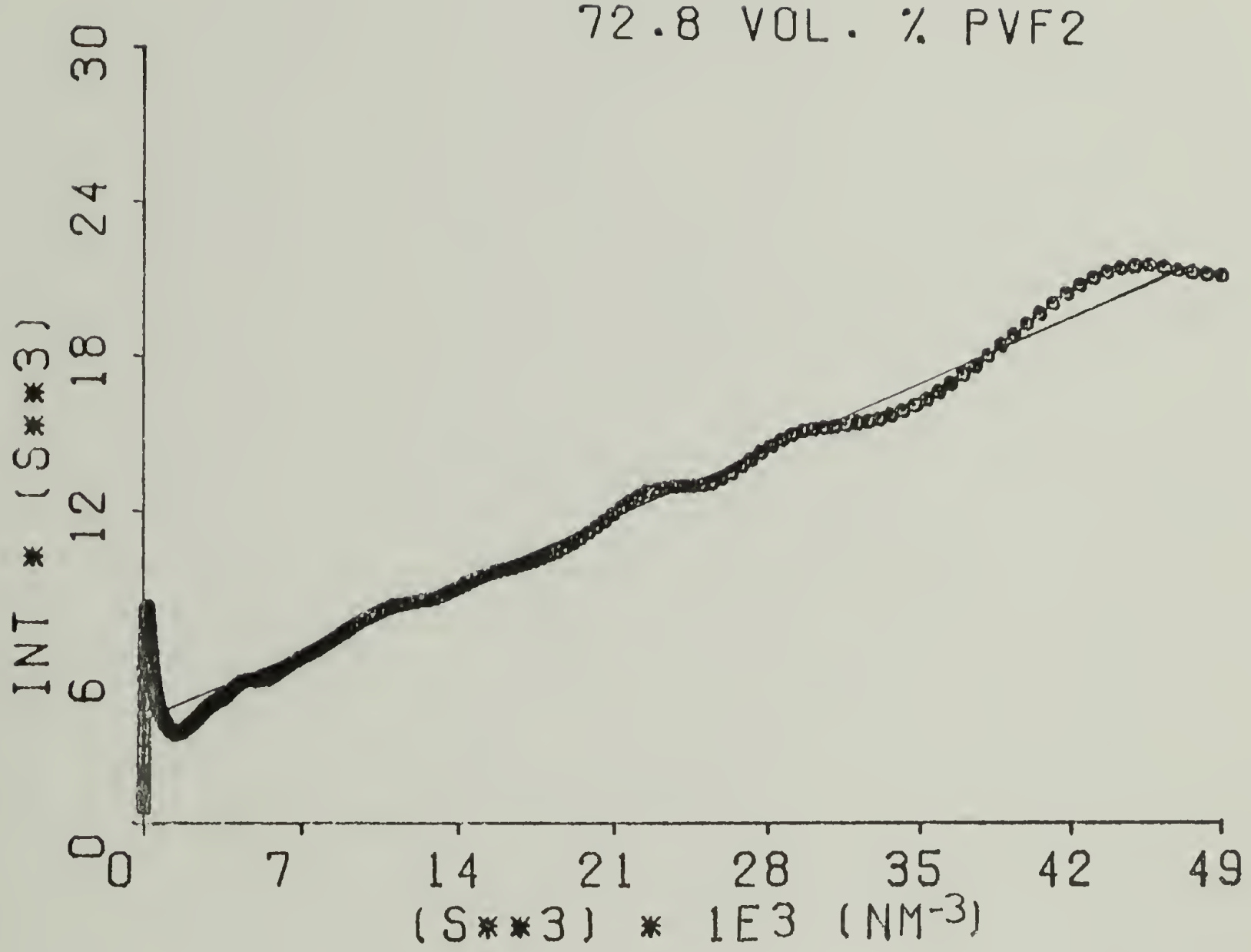

Figure 55. Smeared intensity x s^3 vs. s^3 for sample 72.8.

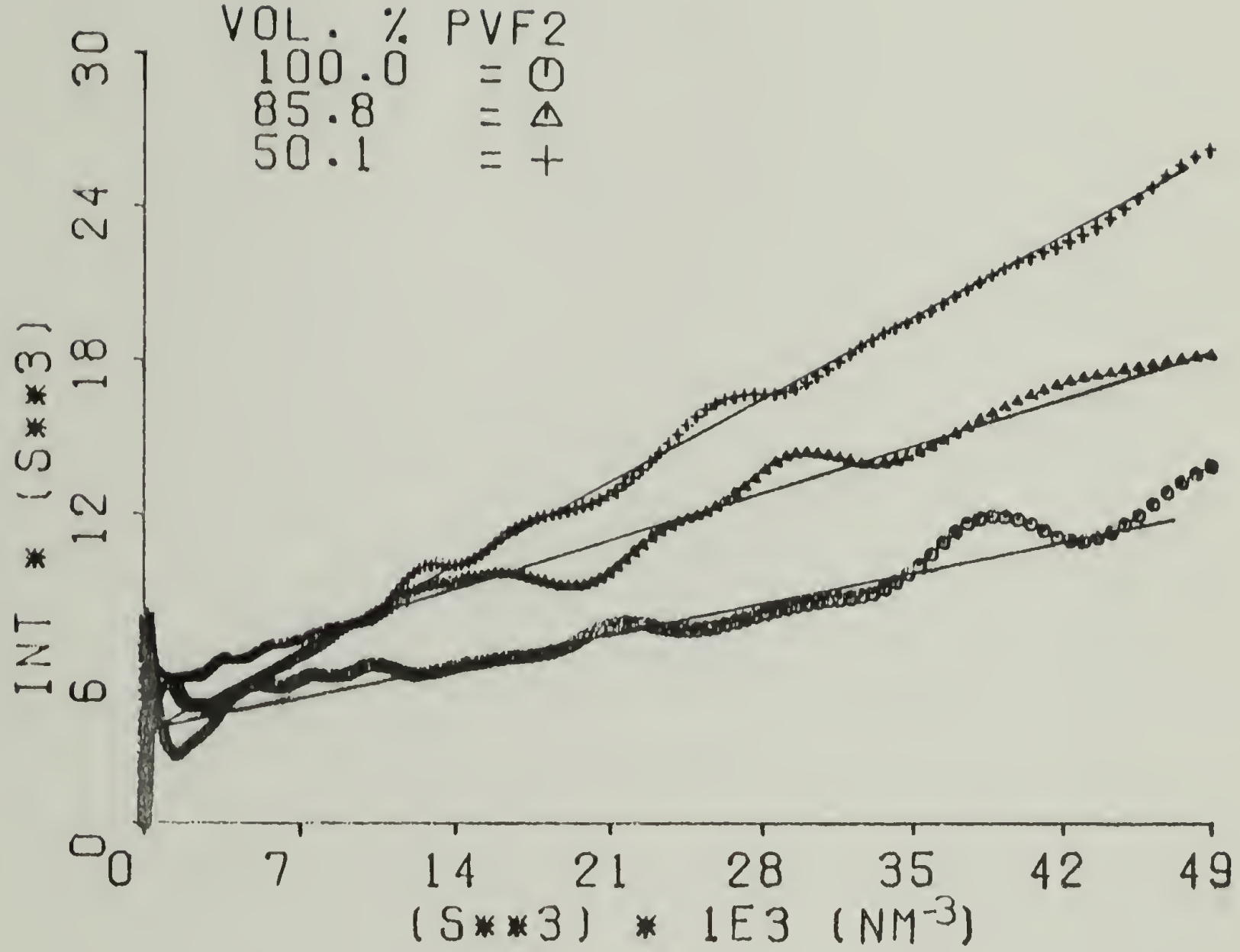

Figure 56. Comparison of smeared intensity x s^3 vs. s^3 for samples 100, 85.8, and 50.1.

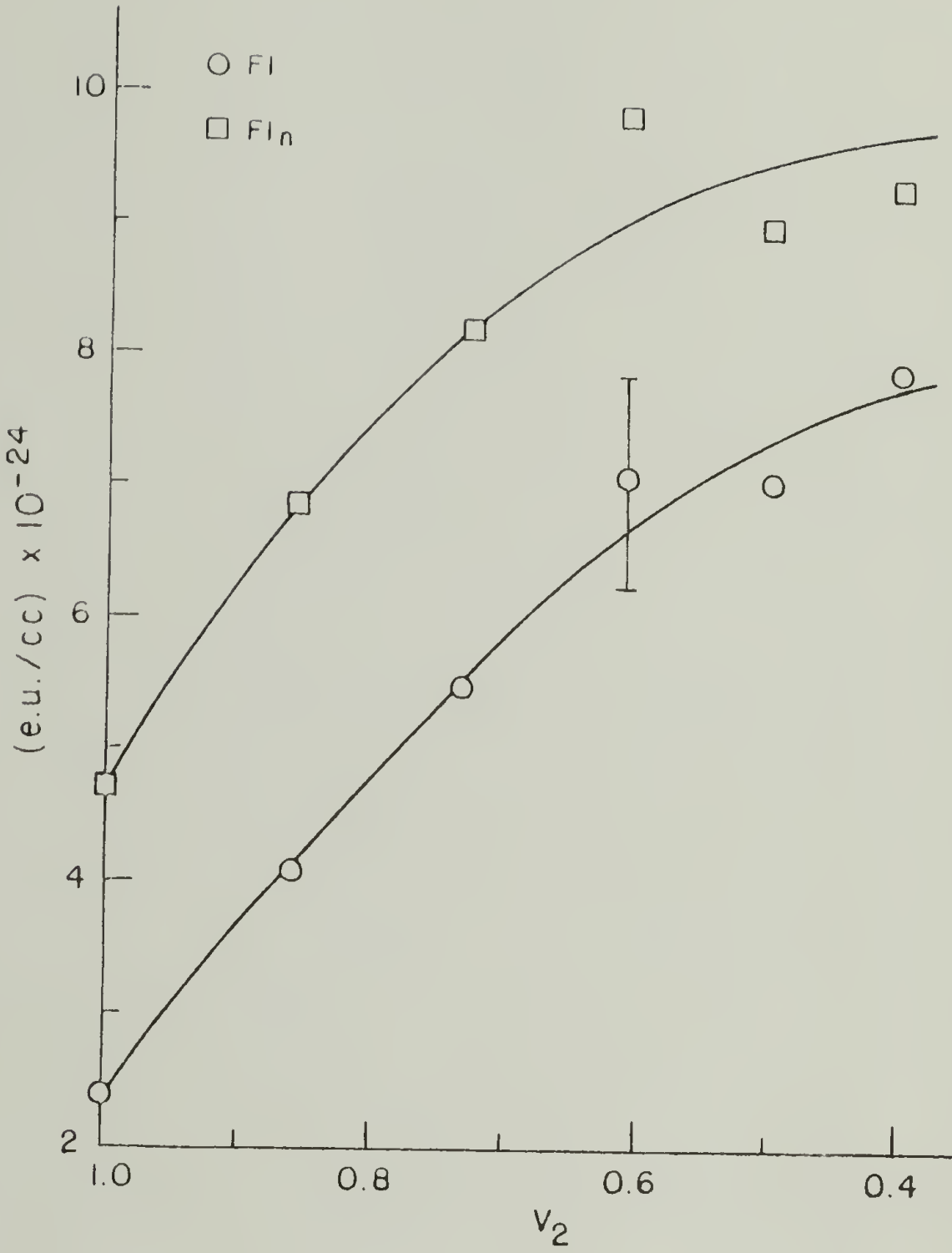

Figure 57. Constant fluctuation background as a function of v_2. Fl is measured from the samples, Fl_n is normalized to the volume fraction of amorphous material.

ϕ_c is the volume fraction crystallinity obtained from DSC measurements. The values of ϕ_c are listed in Table 5. The measured Fl values were subtracted from the scattering curves to remove liquid scattering, but Fl_n values are useful in comparing samples.

The treatment of the background as a constant is actually a simplification since it is really a function of s. It has been shown that the background can be given as a power series in even powers of s (177) and empirical methods have been developed which are actually approximations to this series (161,174). Thus, the liquid scattering is actually composed of a constant term, independent of s, plus another term (or terms) which are functions of s. For a binary mixture, Wendorff (94) has shown that the constant term can be attributed to density fluctuations at constant concentration, while the s-dependence is related to concentration fluctuations at constant particle number density. The application of this approach assumes that the scattering intensities are at a high enough angular region so that interference effects from structures present are negligible, i.e., it is beyond the Porod law region. It also assumes that there are no wide angle scattering effects.

For various polymer melts and glasses (186,187), there was no s-dependence of the intensity seen in this region. Therefore, the fluctuation background is constant and arises only from density fluctuations. In Wendorff's work on PVF_2

/PMMA blends (94), a large s-dependence of the intensity in this region was observed. This was divided into s-independent and s-dependent terms. The former corresponded to the values of the pure components using simple mixing rules and was attributed to the density fluctuations at constant concentration. The latter term arose from the concentration fluctuations at constant particle number density and was strongly dependent upon composition. From the absolute value of the latter term, a concentration dependent interaction parameter between the components was derived.

In light of this, the values of Fl obtained in the present study appear to actually be composed of the concentration and density fluctuation terms. The increase of Fl_n for the blends can most likely be related to the interaction between the two components in the amorphous state. If the two species were phase separated in the amorphous regions, only particle number density fluctuations from each individual phase would be seen. As Wendorff (94) has shown, this would only give rise to a background comparable to those for the homopolymers. Therefore, this data, in agreement with Wendorff, verifies the intimate mixing in the amorphous phase. However, the aim of the present study is to evaluate the crystalline morphology via the interference effects between crystalline and amorphous regions manifested at smaller scattering angles. Therefore, subtraction of these fluctuation intensities arising solely from within the amorphous phase

is necessary.

In all samples, the intercept of the $\tilde{I}s^3$ vs. s^3 plot was a positive value, and not zero as expected. As mentioned previously, this positive intercept was also seen by previous workers (179), who handled this problem by dividing the smoothing function, $H^2(s)$, into two parts corresponding to sharp and diffuse boundaries. The alternative explanation of H^2 not reaching zero in the interval observed (173) seems more realistic and is therefore preferred.

Subtraction of the constant backgrounds from the scattering curves lowered the invariants by less than 5% in all cases. Other studies (174,180) have shown that the final value of interface width calculated varies only 10% about the average depending upon the method of background subtraction. Therefore, even though Fl was subtracted from the curves before further calculations were performed, it had small effects on the final results.

Following the model of Ruland (175) and Vonk (174), a linear transition zone of thickness E was assumed to exist between the crystalline and amorphous layers. Using equations 55 and 69 therefore gives for the tail region

$$\tilde{I} = \frac{K'}{s^3}\left(1 - \frac{2\pi^2 E^2 s^2}{3}\right) \qquad (73)$$

A plot of $\tilde{I}s$ vs. $1/s^2$ should then be a straight line with a negative intercept proportional to E. Sample plots of this type are given in Figures 58, 59, and 60 for samples 100,

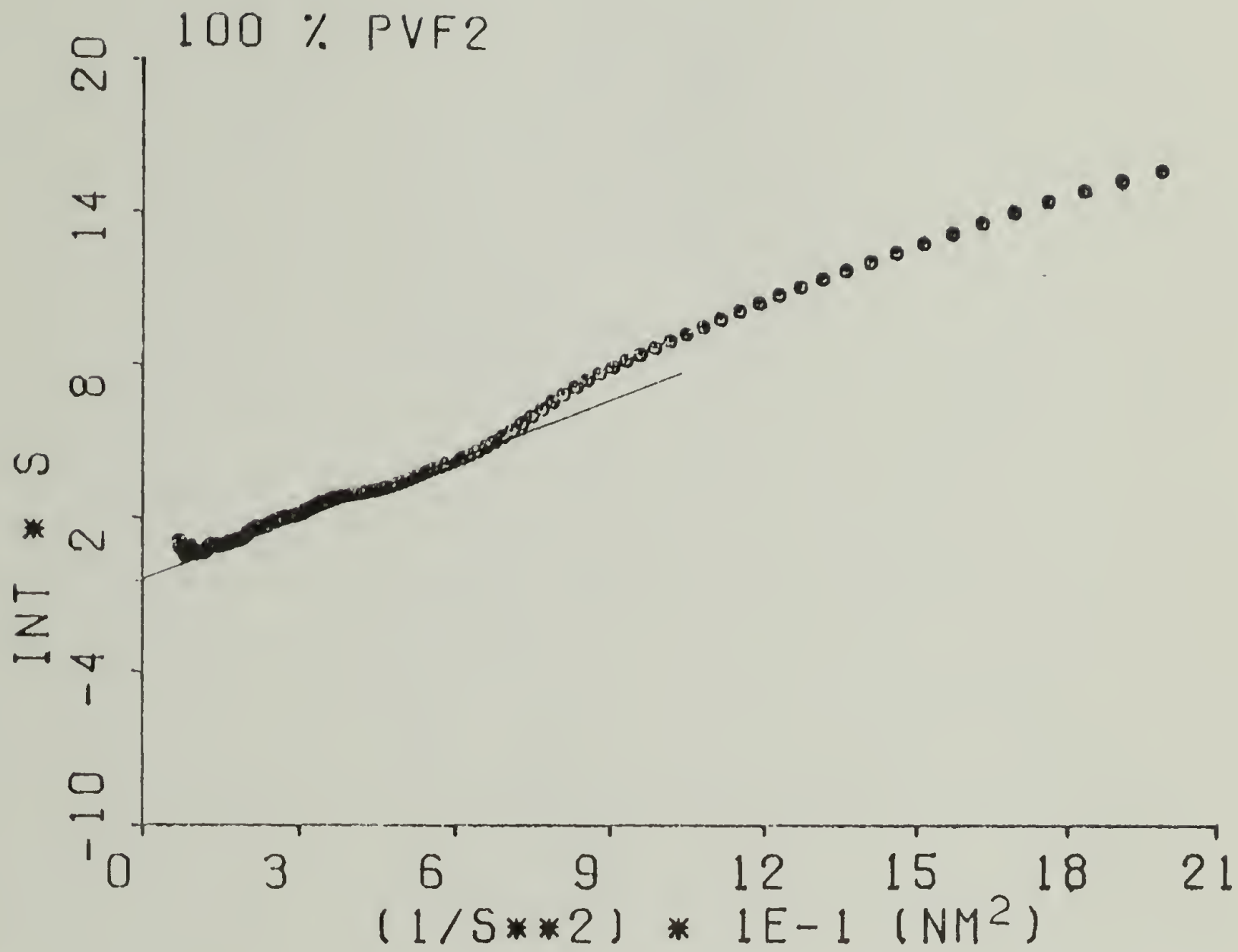

Figure 58. Smeared intensity x s vs. $1/s^2$ to determine E_R for sample 100.

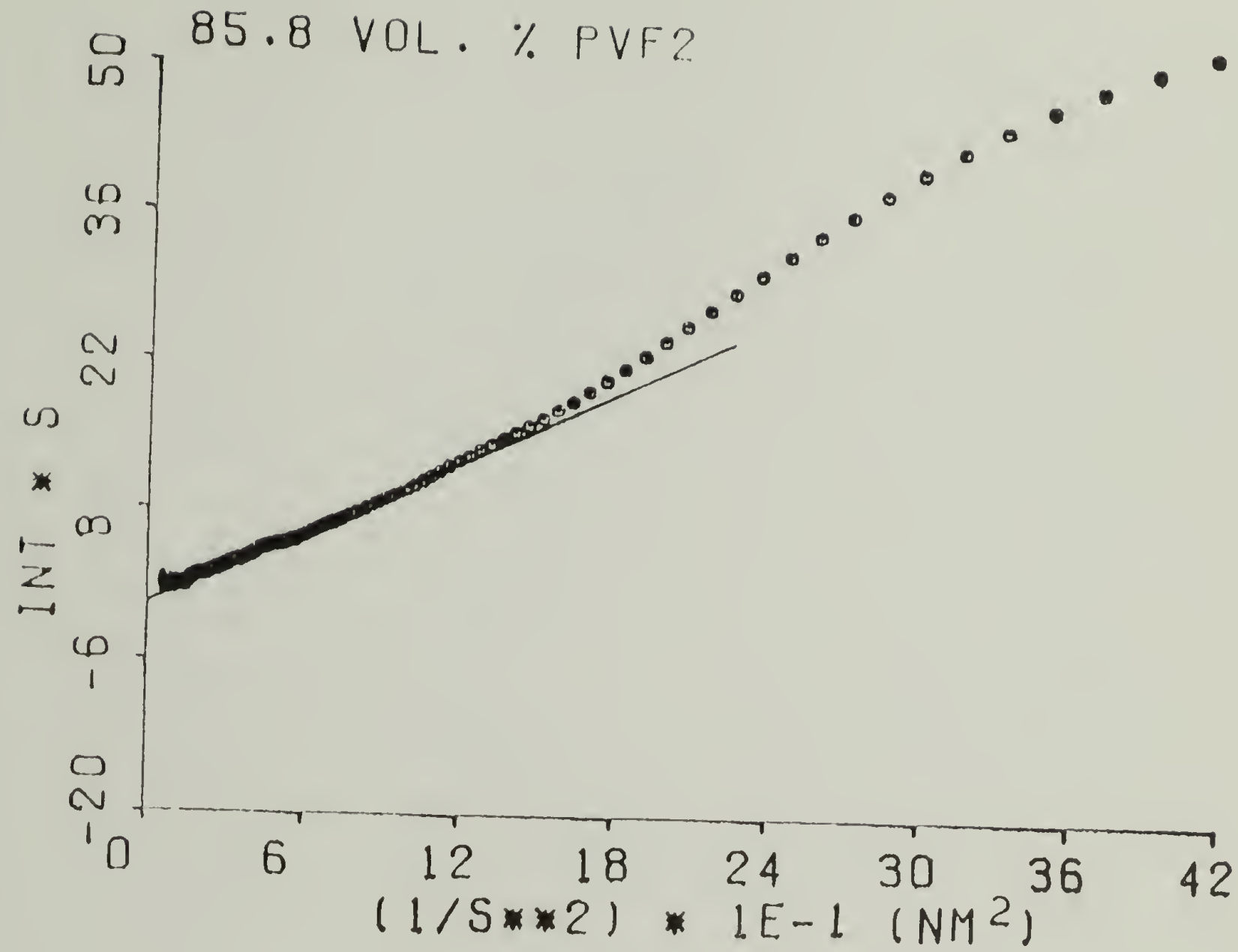

Figure 59. Smeared intensity x s vs $1/s^2$ to determine E_R for sample 85.8.

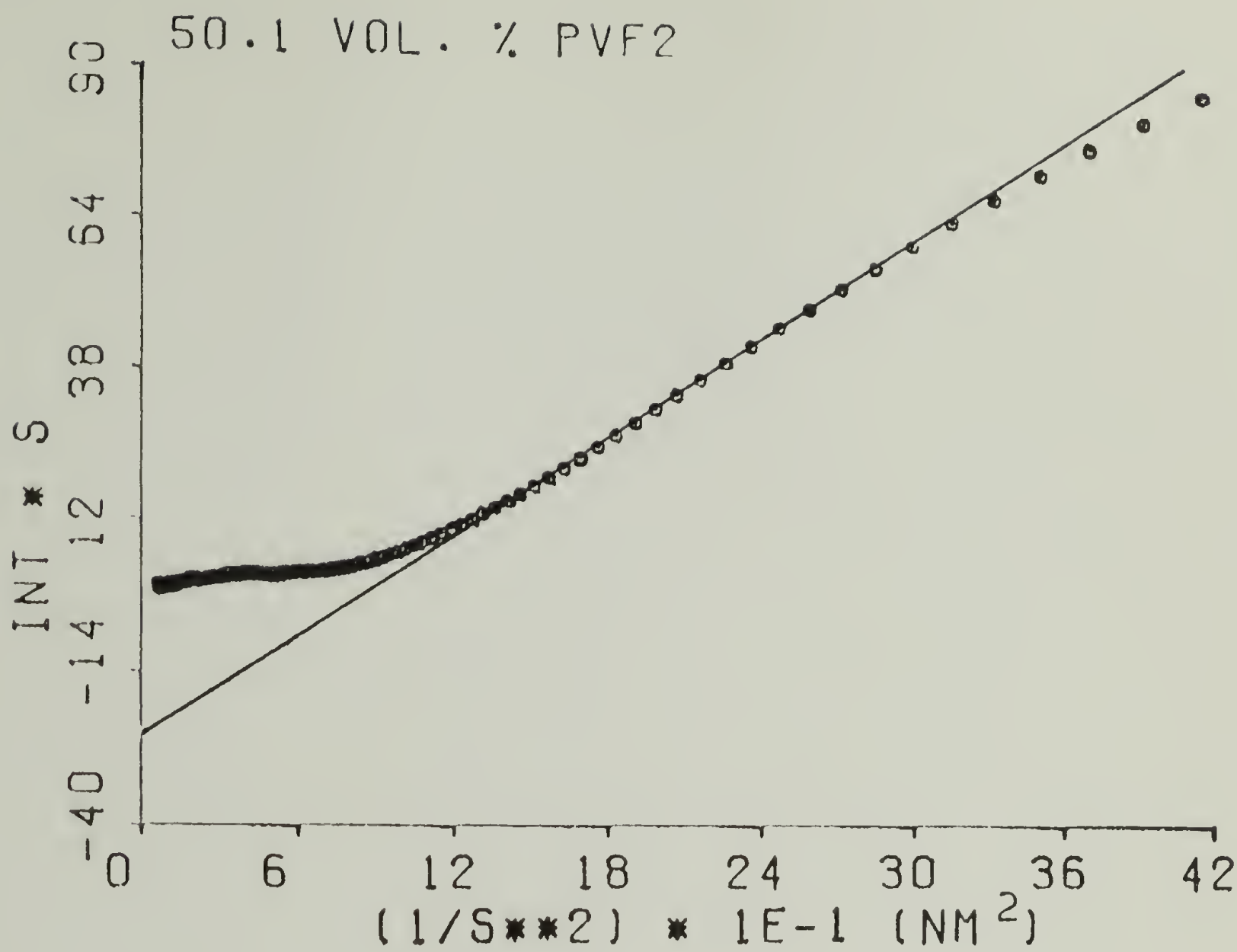

Figure 60. Smeared intensity x s vs $1/s^2$ to determine E_R for sample 50.1.

85.8 and 50.1 respectively. As can be seen from these representative figures, the samples had straight line portions with negative intercepts. Deviations from this straight line portion at low values of s are due to the particle interference scattering. At the high s end, the data cannot follow the straight line because $\tilde{I}$ can never be negative.

Ruland (161) states that Porod's law should not be applied until s is larger than the position at which a second peak maximum should occur. Using the first peak in the Lorentz corrected desmeared intensity curves (to be discussed later), the position where a second maximum should occur was calculated and no s values below this were used in the fit. On the other hand, Koberstein et al. (173) have shown that the transition zone calculated is within 5% of the actual transition zone if Es<.1. In the present study, it was necessary to utilize Es values as high as .12 to .30. Thus, even though the results of this calculation might have errors greater than 5%, the relative values obtained are still useful for comparison amongst one another.

The small range of data points which could be fit to a straight line in the $\tilde{I}s$ vs. $1/s^2$ plots may also be a result of the use of a constant liquid scattering subtraction. As discussed previously, the backgrounds subtracted most likely had some s-dependence. This would affect the Porod law region more than any of the other analyses to be performed.

The transition zone thicknesses were also calculated

from the one dimensional correlation functions as described by Vonk (174) using equations 58-60. These values will be designated E_V to distinguish them from the values calculated using Ruland's (175) method of the $\ln s$ vs. $1/s^2$ plots. The latter thickness will be referred to as E_R.

Both sets of thicknesses are plotted as a function of v_2 in Figure 61, and, as can be seen, there is good agreement between E_V and E_R. An increase is seen to occur for blends with v_2 less than 85.8. It is believed that in these systems, the larger transition zone is predominantly due to the decrease in the perfection of the lamellar surfaces. Irregularities in the lamellae which are much larger than the wavelength of the exciting radiation would appear in the interference scattering at lower angles. If, however, imperfections or corragations were on the order of the radiation (or not very much larger), they would not be seen as individual structures and would create a region where the average electron density is between that of the amorphous and crystalline region. This would cause a rise in the transition zone measured.

A comparison of the Lorentz corrected desmeared curves for samples 100, 85.8 and 50.1 are presented in Figure 62. Desmearing was performed according to Vonk (188) using the measured slit intensity profile of Figure 52. The Lorentz correction, as mentioned earlier, amounts to multiplying the intensities by s^2 (163,168,169). As can be seen from this figure, the peak position shifts towards smaller s and the

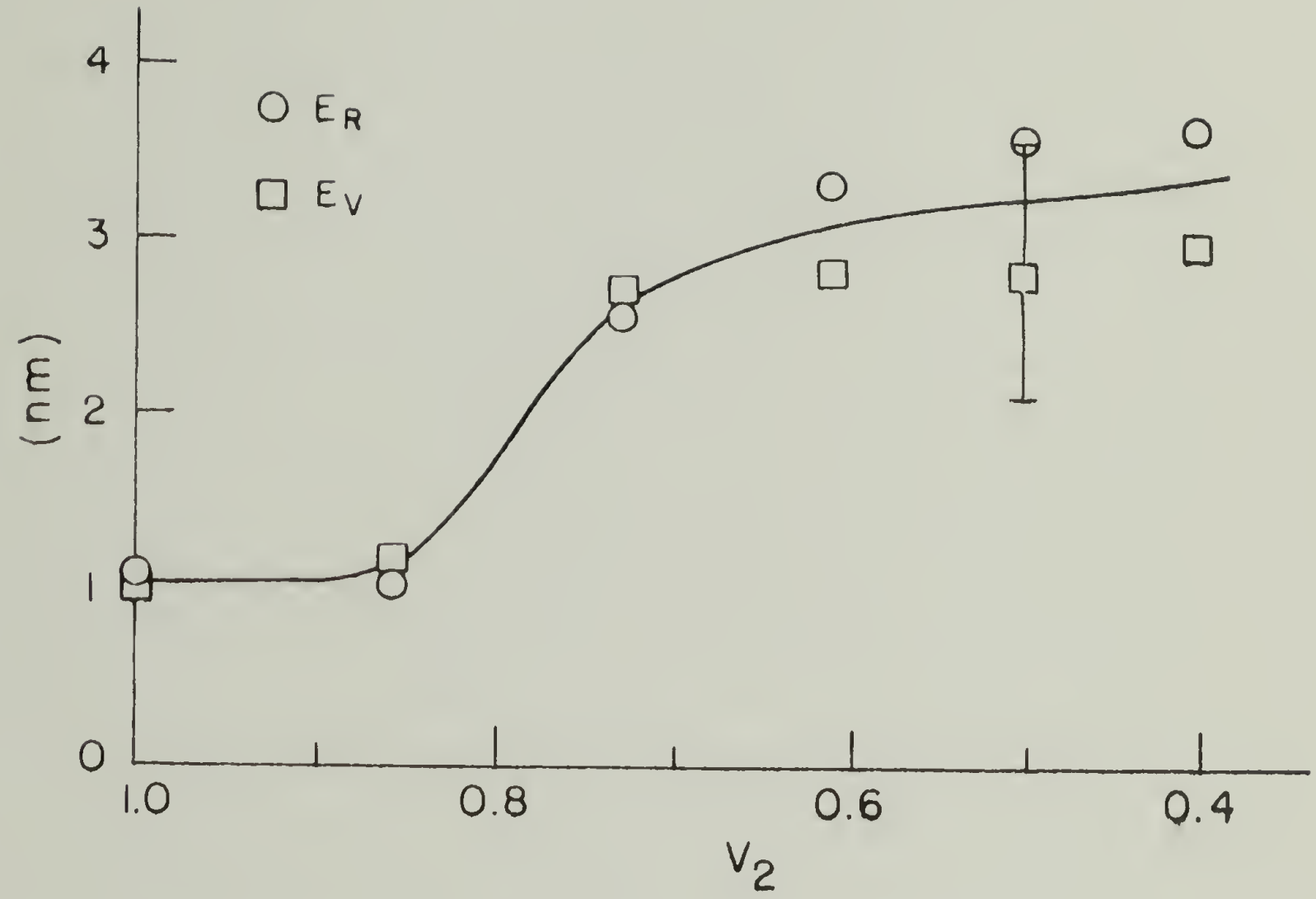

Figure 61. E_v and E_R as a function of volume fraction PVF_2, v_2.

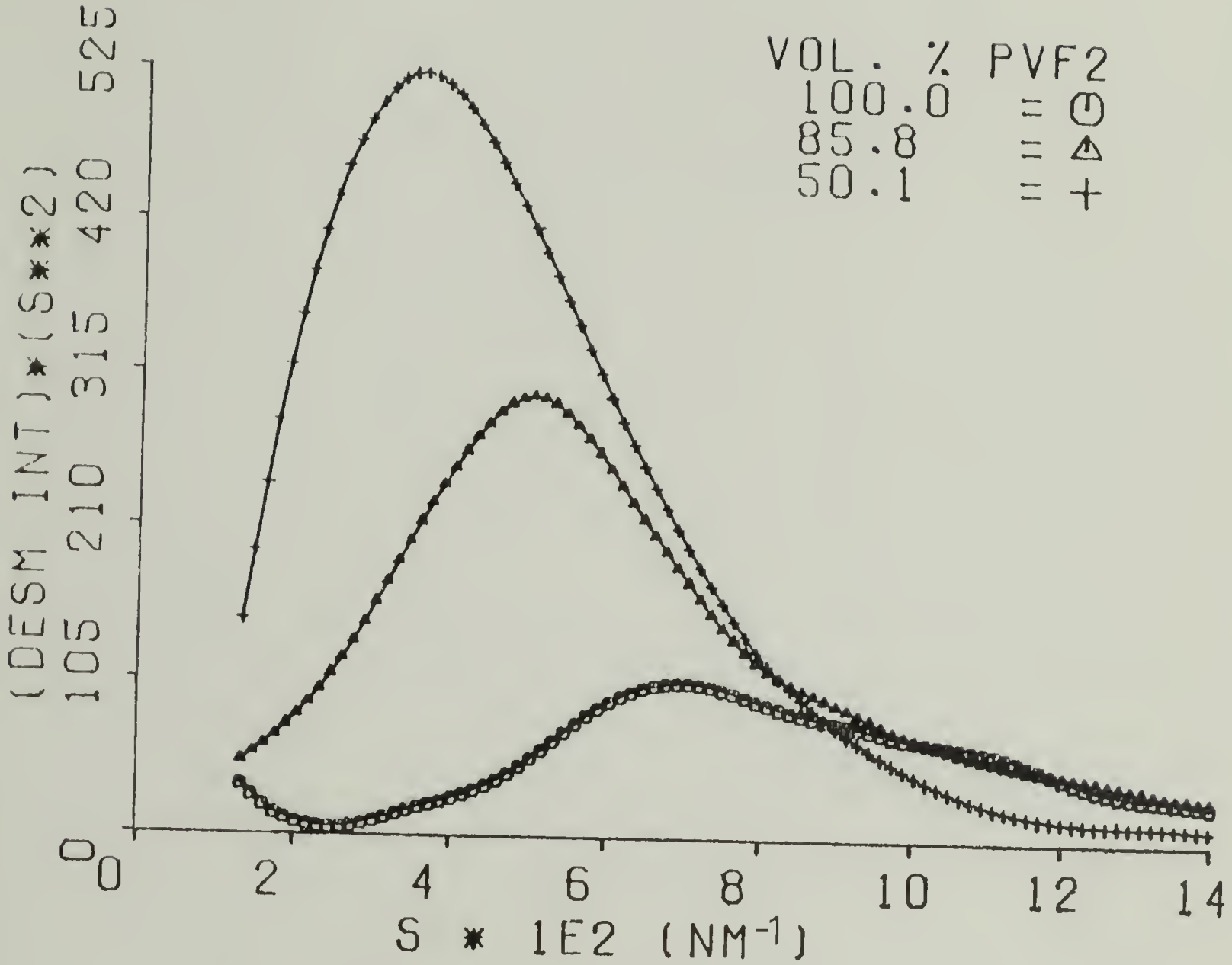

Figure 62. Comparison of Lorentz corrected desmeared curves for samples 100, 85.8, and 50.1.

total scattering increases as more PMMA is added. Using Bragg's law, the long periods calculated from the peak position are shown in Figure 63. The diameter distribution functions were also calculated and two representative distributions for the 100 and 50.1 samples are shown in Figure 64. The average lamellar thicknesses calculated from such distributions are included in Figure 63.

A large increase in the long period along with a slightly larger lamellar thickness is seen as more PMMA is added. Therefore, the small increase in lamellar size is accompanied by a large increase in the interlamellar amorphous regions, for the more dilute blends.

Another method of determining the sizes of the crystalline and amorphous regions is through the application of the Hosemann model (160). Model curves were generated for each sample and fit to the Lorentz corrected desmeared data. Comparison of the theoretical and experimental scattering curves are shown for all samples in Figure 65-70. The circles connected by the smooth lines are the experimental points, while the triangles represent the best fit from the model.

The shoulder seen at approximately .11 nm^{-1} in the experimental data for sample 100 is not thought to be real. Intensities for this sample were very weak and therefore much more sensitive to small statistical fluctuations. Fluctuations of this type are amplified by desmearing and can result in the shoulder observed.

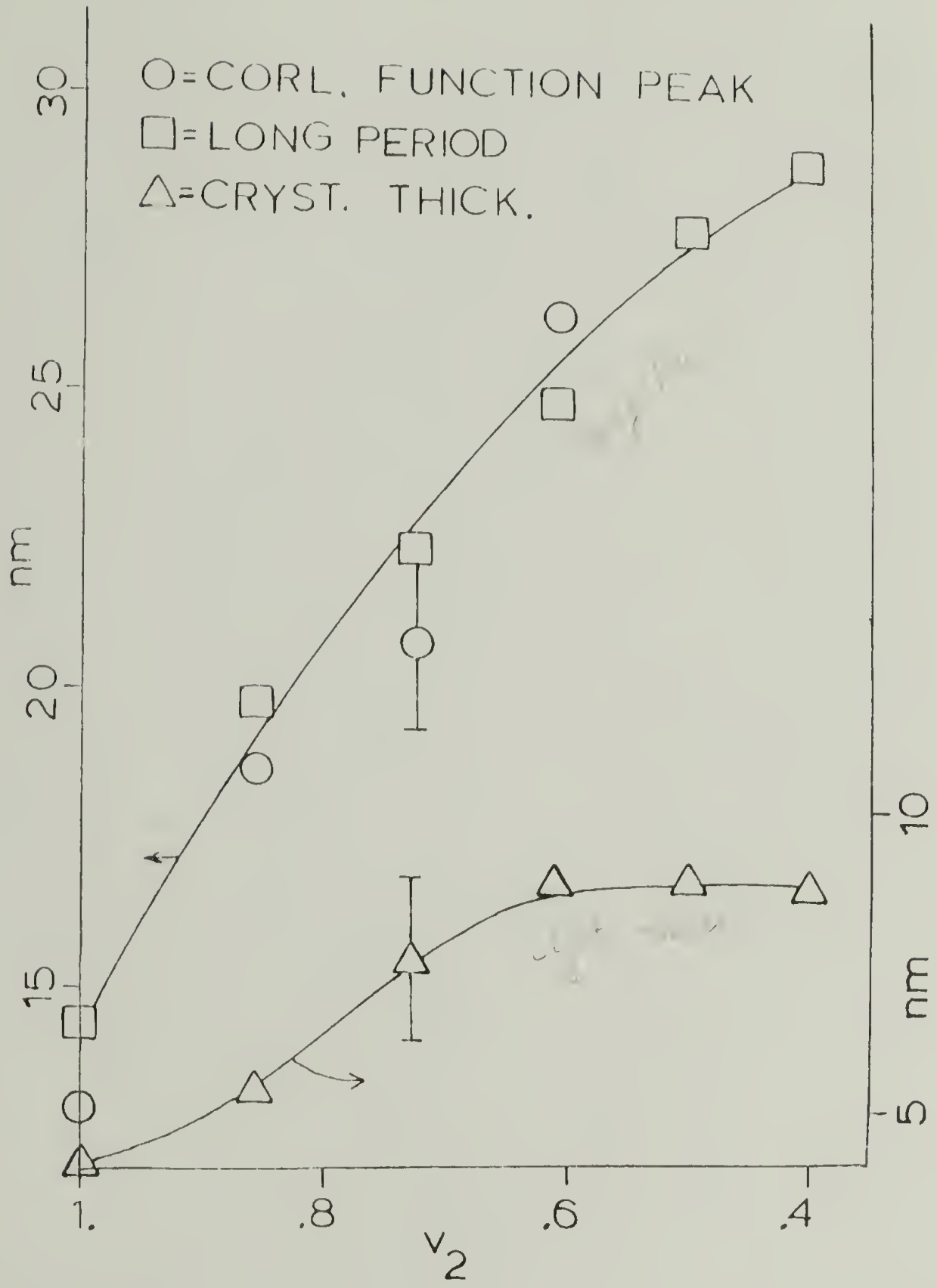

Figure 63. Long period, correlation function peak, and average crystal thickness as a function of volume fraction PVF_2, v_2.

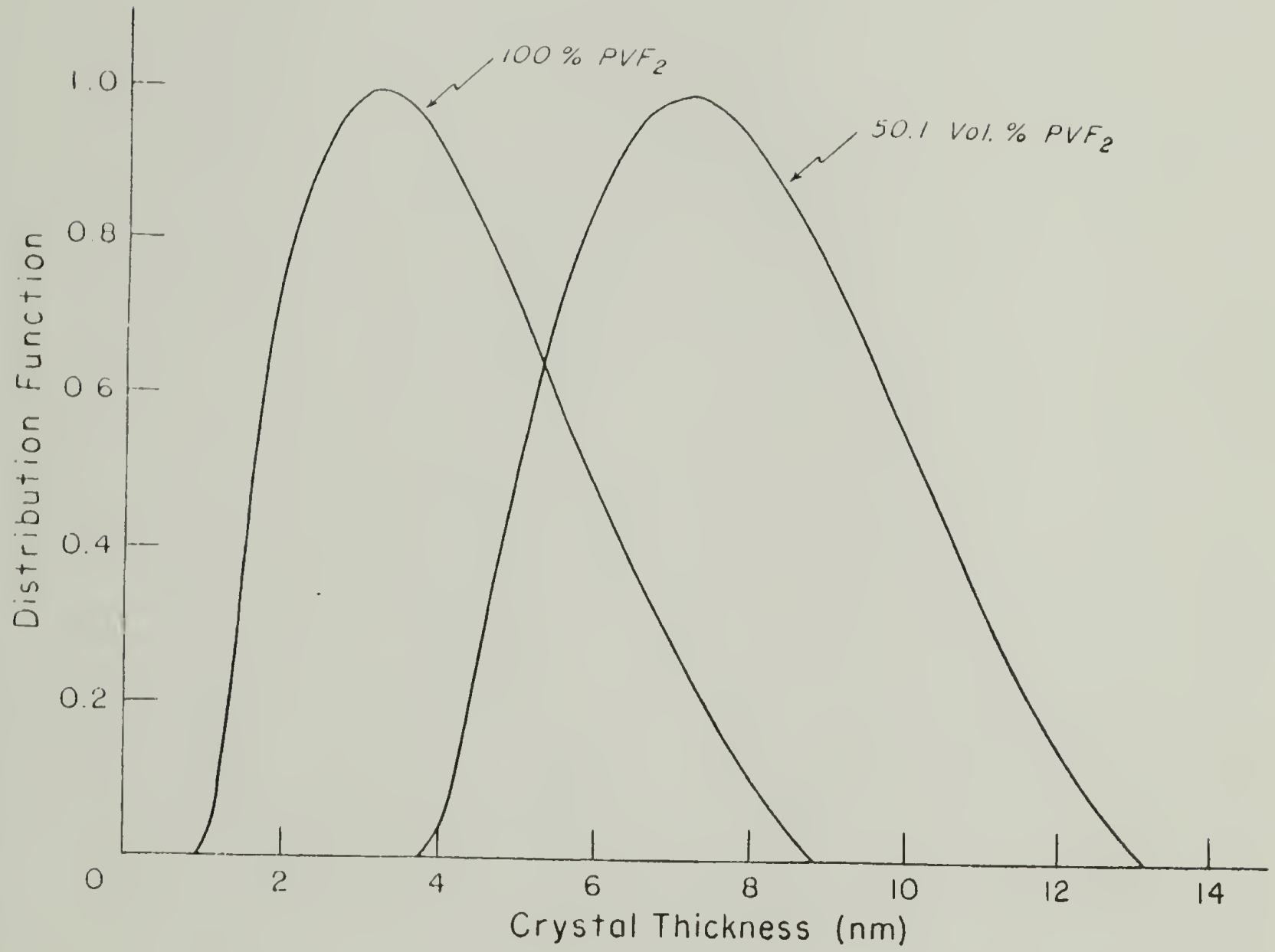

Figure 64. Distribution functions of lamellar thicknesses calculated from Eq. 44 for samples 100 and 50.1.

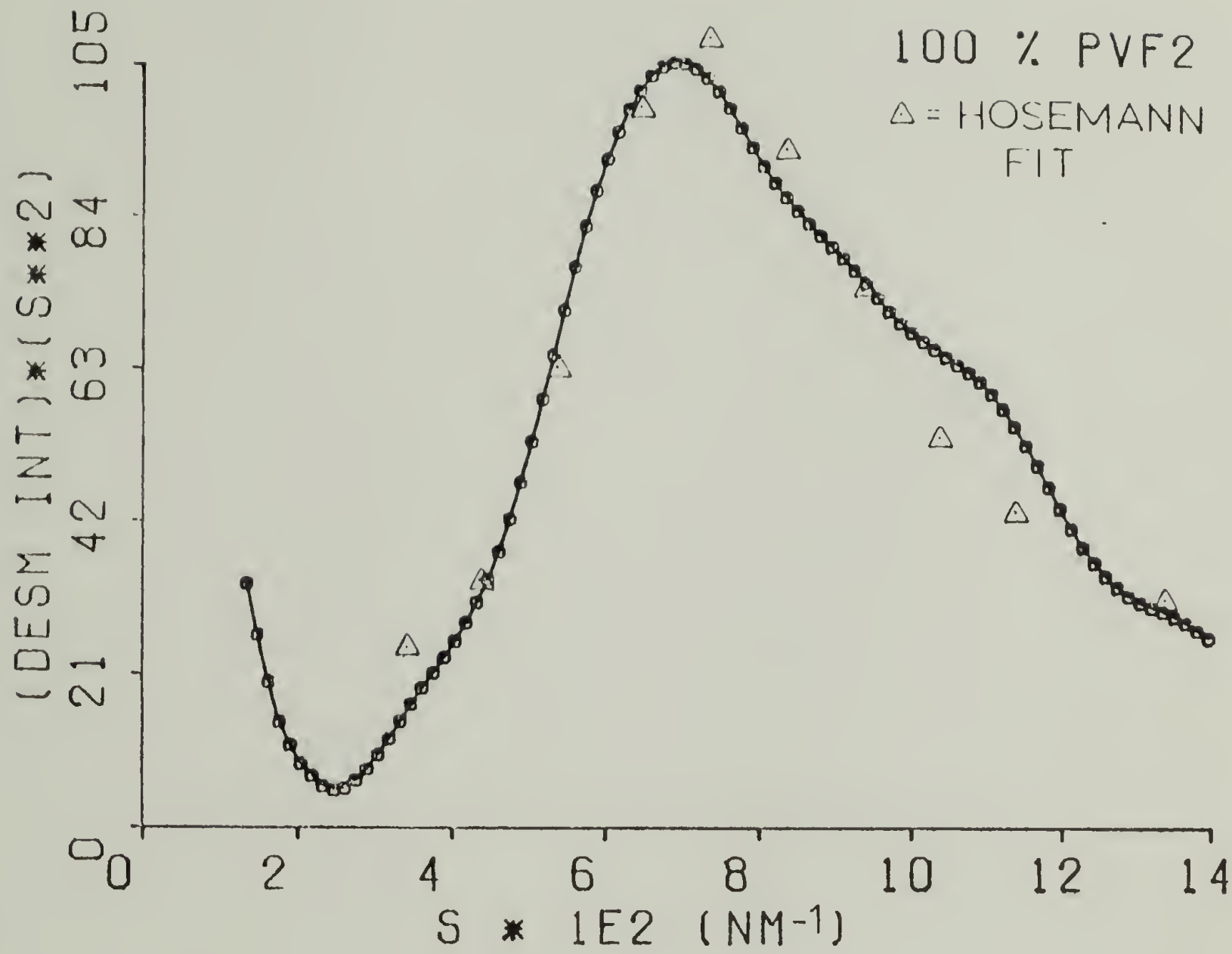

Figure 65. Lorentz corrected desmeared intensity for sample 100. The circles connected by the line represent experimental data. The triangles are the Hosemann model fit.

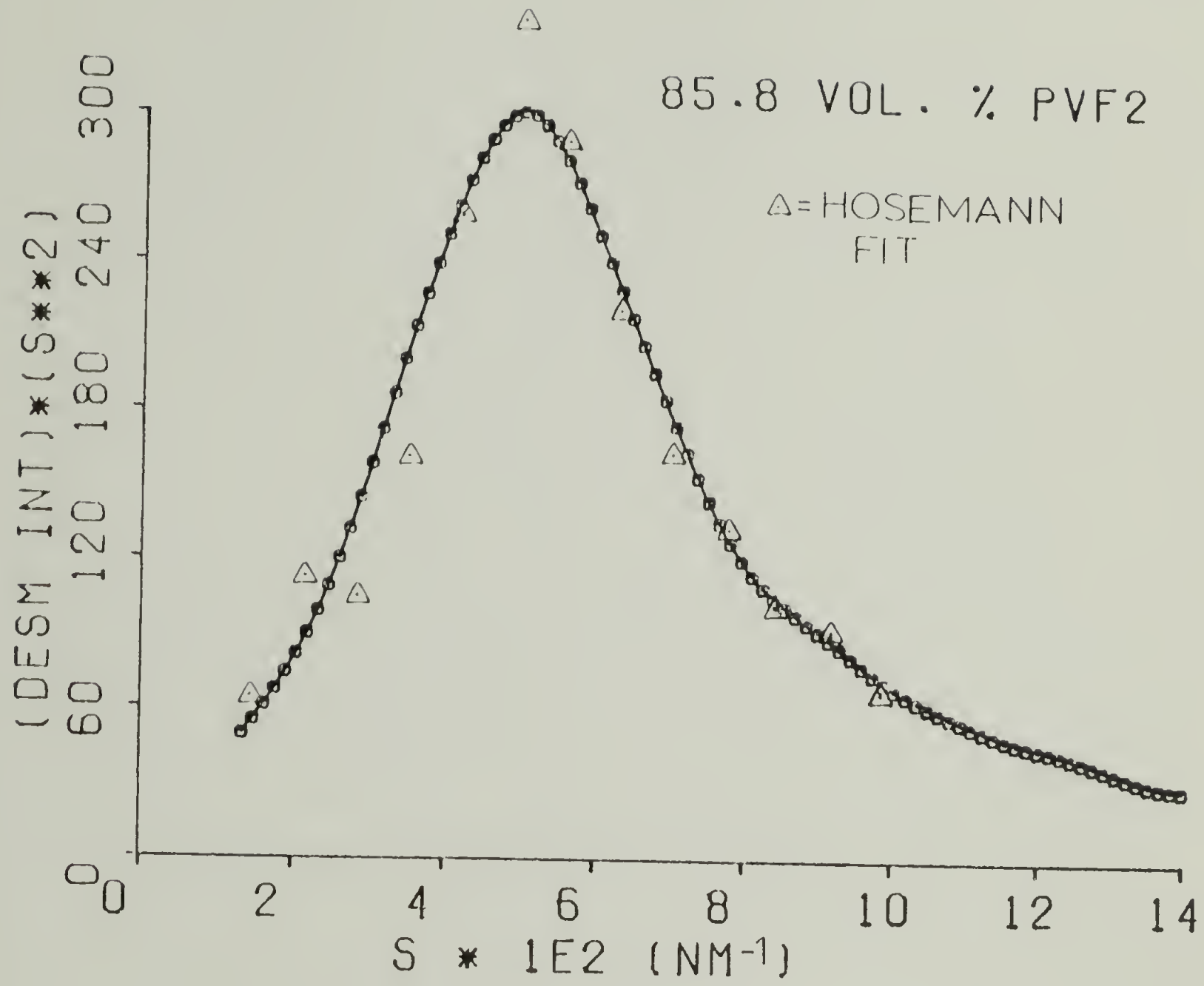

Figure 66. Lorentz corrected desmeared intensity for sample 85.8. The circles connected by the line represent experimental data. The triangles are the Hosemann model fit.

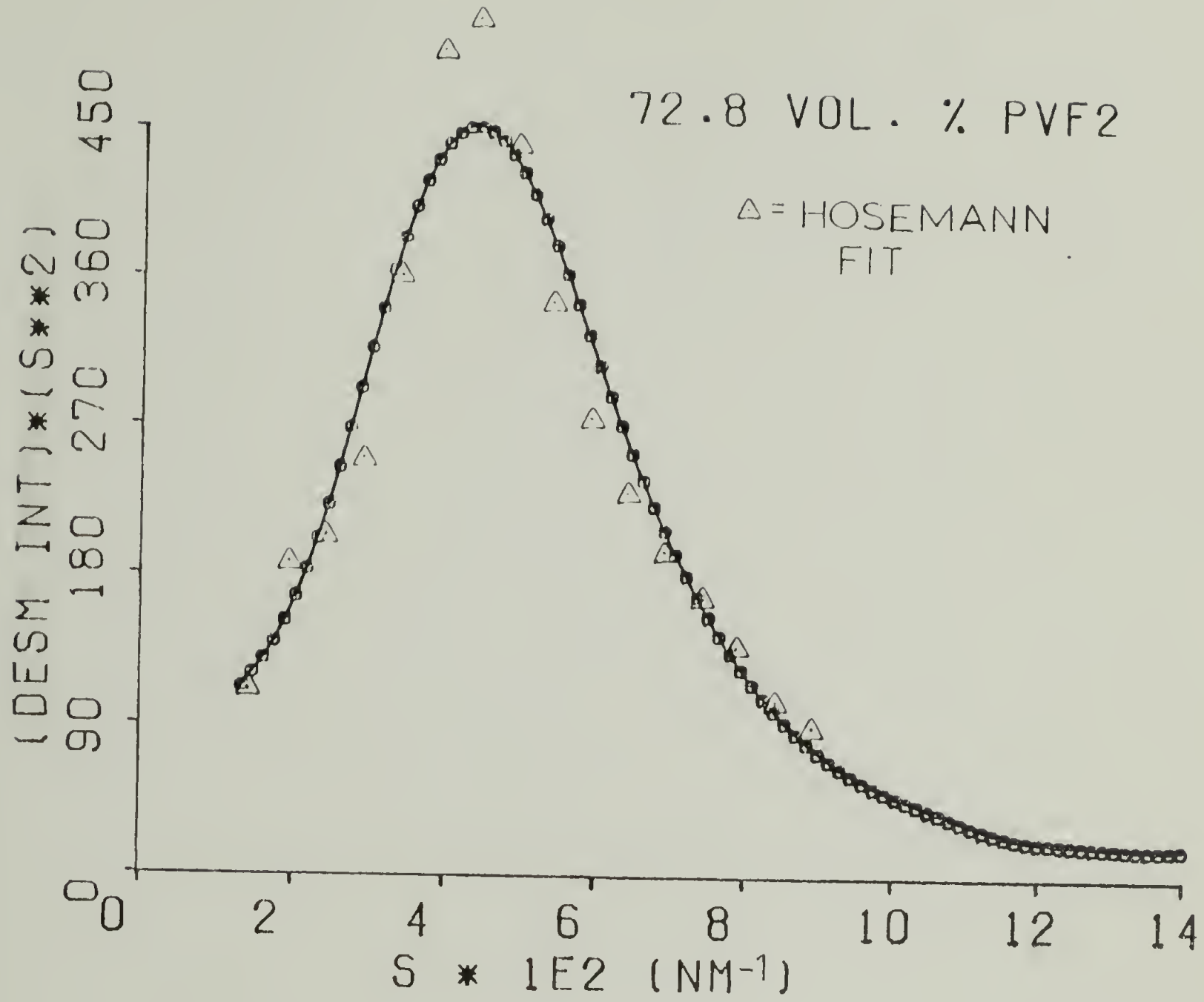

Figure 67. Lorentz corrected desmeared intensity for sample 72.8. The circles connected by the line represent experimental data. The triangles are the Hosemann model fit.

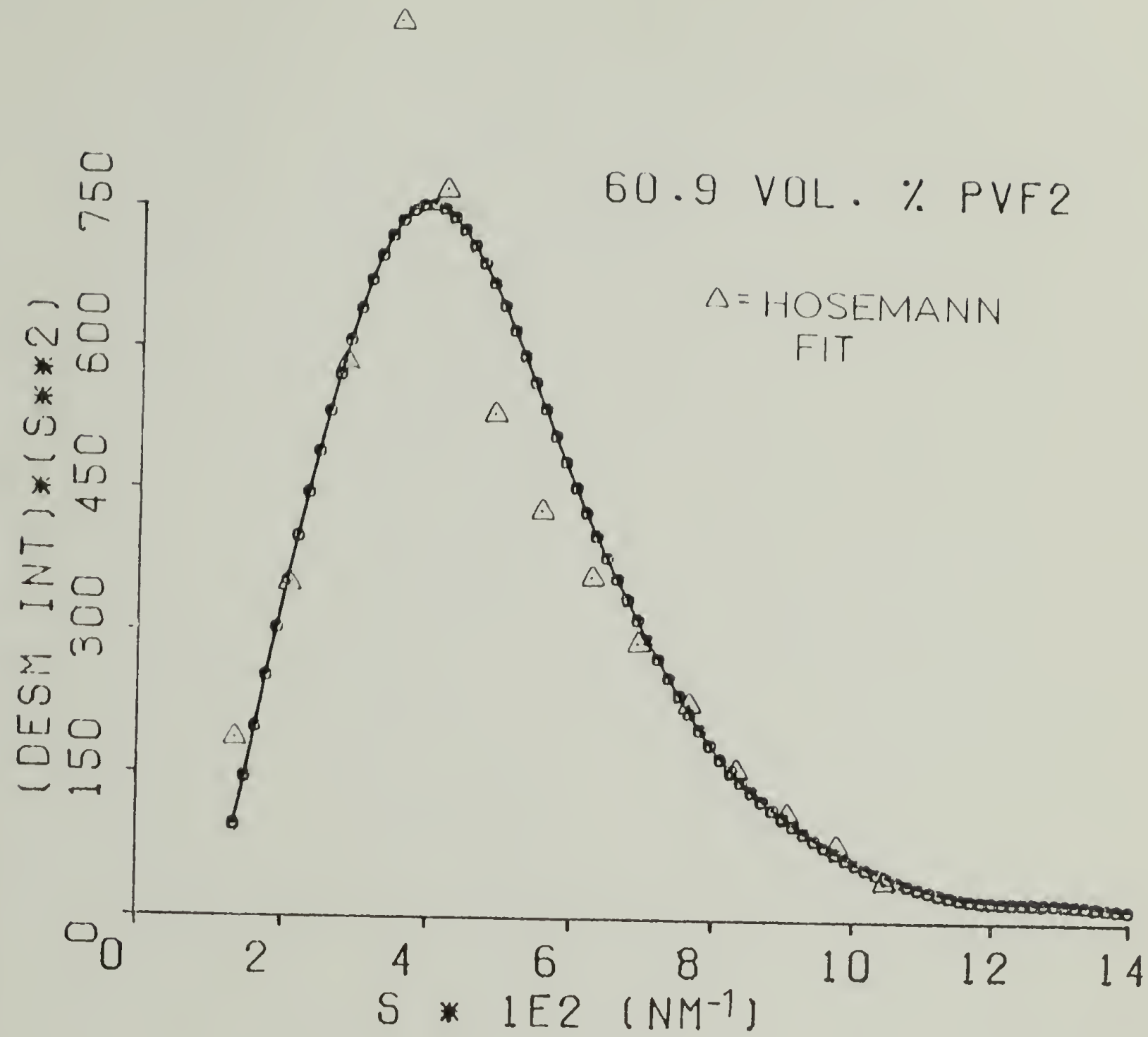

Figure 68. Lorentz corrected desmeared intensity for sample 60.9. The circles connected by the line represent experimental data. The triangles are the Hosemann model fit.

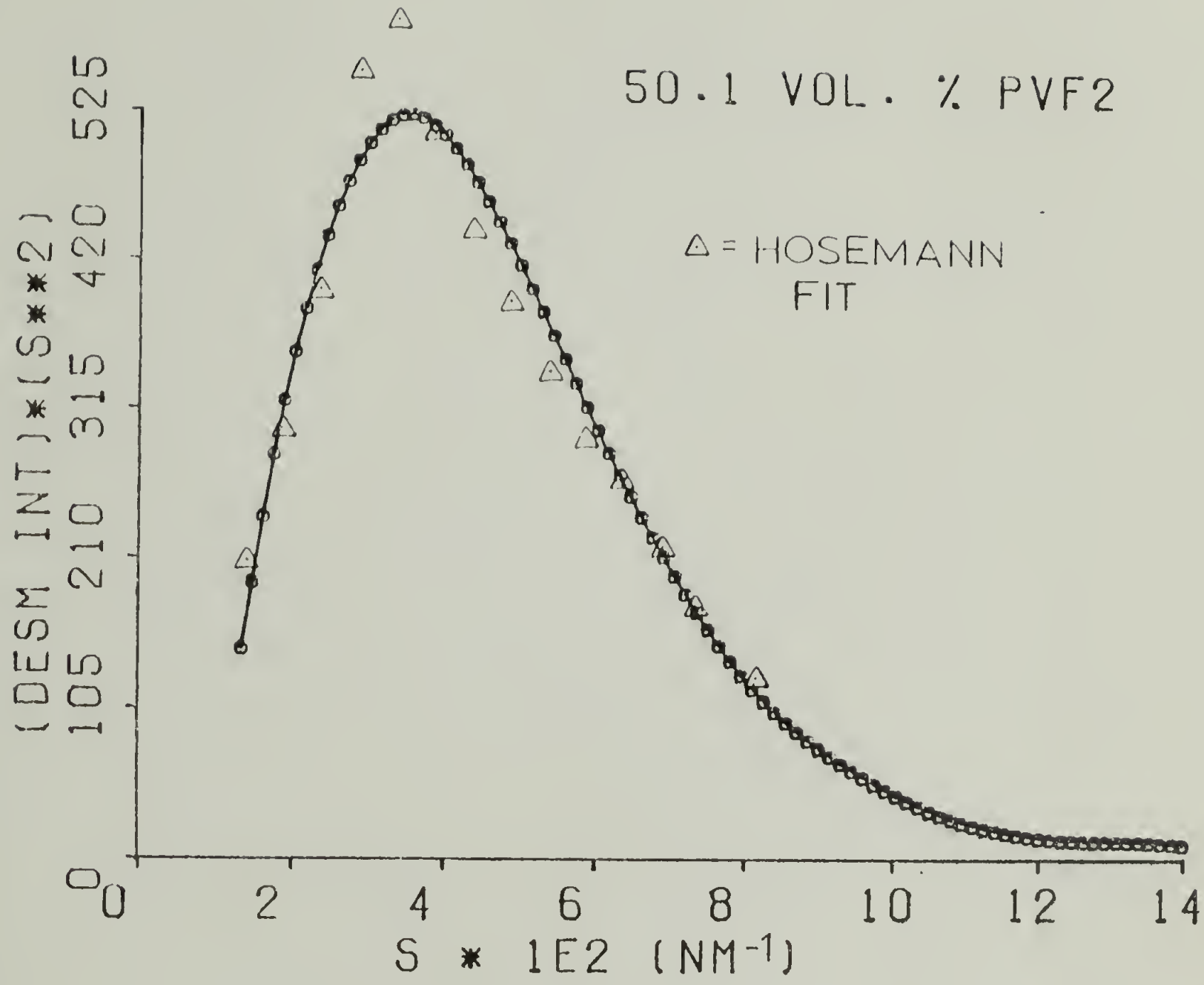

Figure 69. Lorentz corrected desmeared intensity for sample 50.1. The circles connected by the line represent experimental data. The triangles are the Hosemann model fit.

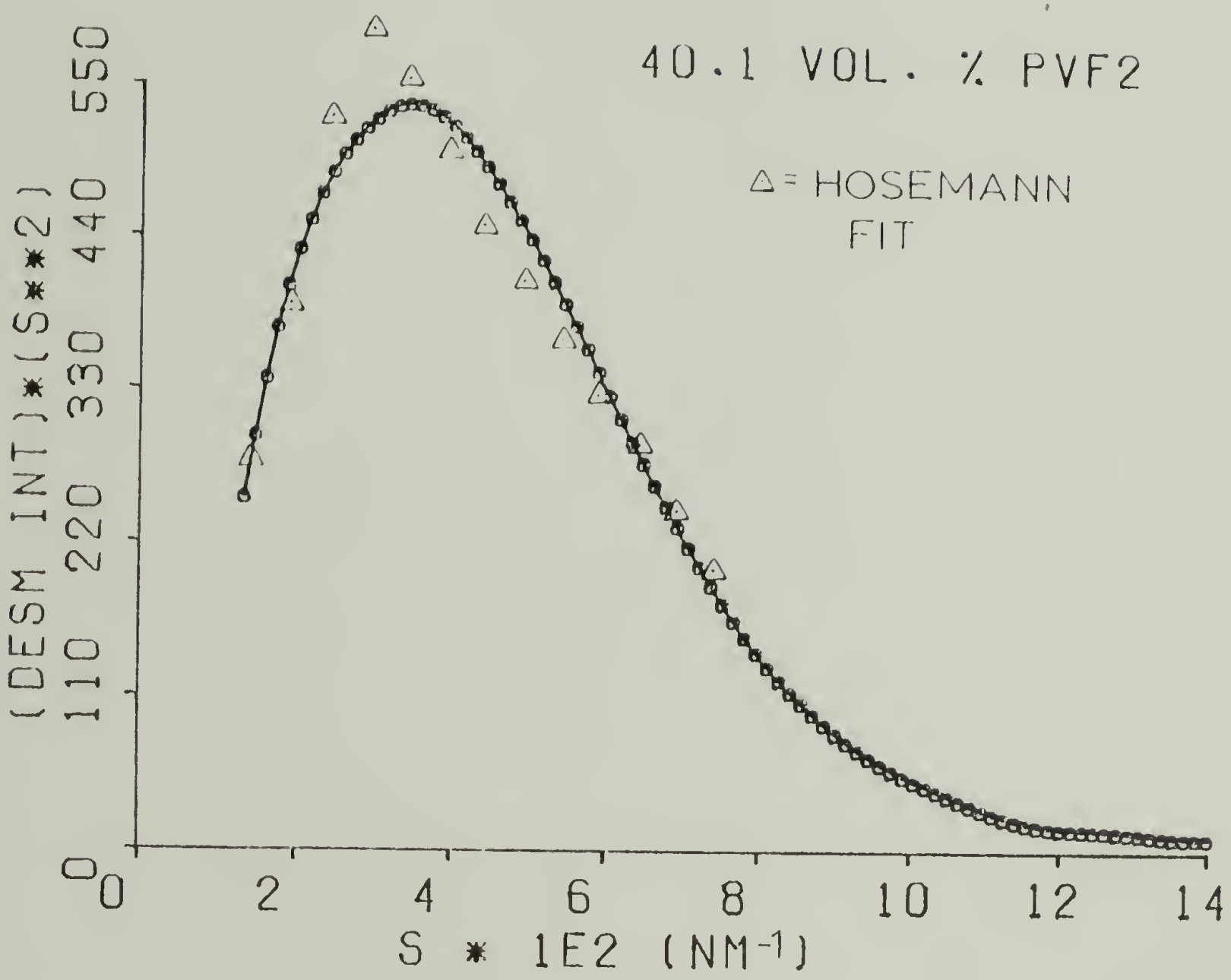

Figure 70. Lorentz corrected desmeared intensity for sample 40.1. The circles connected by the line represent experimental data. The triangles are the Hosemann model fit.

Approximately 10^5 theoretical curves were generated for each sample. The best model curves were chosen by normalizing the theoretical curve $I(s)_T$, to the experimental curve $I(s)_E$, on a total integral basis and minimizing the deviation Δ, where

$$\Delta = \int_{s_{min}}^{s_{max}} \frac{\left| I(s)_T - I(s)_E \right|}{I(s)_E} \qquad (74)$$

Δ was between 7 and 11% for all samples except 60.9 for which it was 14.5%. The fitting parameters for the theoretical curves having the smallest Δ's curves are presented in Table 5.

Discussion of the volume fraction crystallinities derived from this model as compared to those from the Vonk model and from DSC experiments will be presented at a later point. Values for the average crystal and amorphous thicknesses, C and A respectively, determined from the Hosemann model are plotted against the volume fraction of PVF_2 in Figure 71. As was seen with the Bragg's law and diameter distribution calculations, there is a slight increase in crystal size coupled with a drastic enlargement of the amorphous region as more PMMA is added. There is good agreement between these two sets of data (Figures 63 and 71).

The slight increase in the crystal size of the more dilute samples is most likely due to the lower relative undercooling of these systems. All samples were crystallized at a constant temperature, but as shown in the previous

TABLE 5

FITTING PARAMETERS FOR VONK CORRELATION FUNCTION AND HOSEMANN PARACRYSTALLINE MODELS

VONK

Vol. % PVF_2	ϕ_c (DSC)	ϕ_c (Vonk)	β_c	β_a
100.0	.50	.45	.11	.36
85.8	.40	.45	.11	.40
72.8	.33	.44	.05	.42
60.9	.28	.40	.03	.50
50.1	.22	.37	.03	.55
40.1	.15	.32	.02	.55

HOSEMANN

Vol. % PVF_2	ϕ_c	C(nm)	A(nm)	g_c	g_a	N	E(nm)
100.0	.34	4.2	8.2	.08	.38	2.2	1.0
85.8	.35	6.5	12.0	.05	.44	3.9	1.0
72.8	.34	7.2	14.0	.09	.44	3.3	3.1
60.9	.28	7.3	18.3	.09	.38	2.9	3.4
50.1	.27	7.2	19.3	.05	.49	2.7	3.6
40.1	.23	6.6	22.0	.05	.54	2.6	3.9

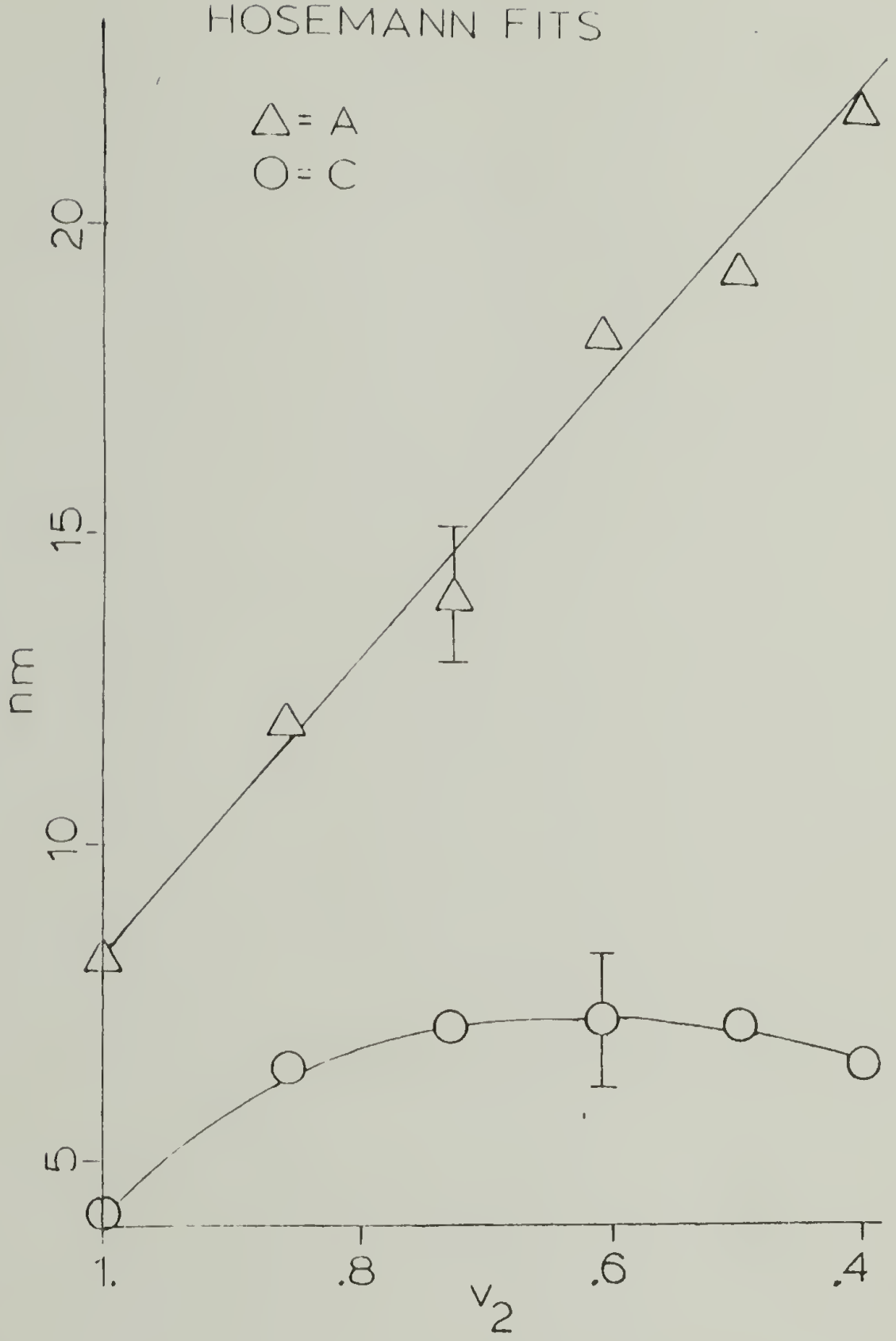

Figure 71. Average crystal, C, and amorphous, A, phase sizes obtained from the Hosemann model.

chapter, the equilibrium melting points of the blends are depressed as more PMMA is added. Therefore, the more dilute blends are actually crystallized closer to their melting points, which results in thicker lamellae being formed.

The much greater variation of the interlamellar amorphous phase size with composition is believed to be caused by the inclusion of the PMMA between the crystalline lamellae. These amorphous regions should therefore be homogeneous mixtures of the two components. If the PMMA was excluded from these interlamellar regions, the long period should stay relatively constant with composition, and increases in C should be balanced by decreases in A. Similar increases in the long period were also observed as more amorphous poly(vinyl chloride), PVC, was added to blends of PVC and poly(ε-caprolactone), PCL (73), while for blends of isotactic and atactic polystyrene, PS (166,189), the long period was not a function of composition.

A theoretical calculation can be made to predict what the long period of these blends would be if all of the amorphous component added were to be included between the lamellae of the semi-crystalline component. To accomplish this, simple additivity of the volumes is assumed. Letting the long periods of the homopolymer and blend be L_o and L respectively, and using a one-dimensional model of alternating crystalline and amorphous phases, the volume fraction of the semi-crystalline component in the blend, v_2, can be given by,

$$v_2 = \frac{L_o}{L} \qquad (75)$$

From this equation, values of L as a function of v_2 can be calulated and compared to experimental results. This has been done for the samples studied using the average of the long periods from Bragg's law and the Hosemann model for pure PVF_2 as L_o, and is shown in Table 6.

From this exercise, it is seen that the calculated L's are less than the experimental ones for the PVF_2 rich systems, the values are approximately the same in the 50.1% blend, and the calculated value is greater than the experimental value for the 40.1% PVF_2 sample. If some of the PMMA was not included between the lamellae, as was assumed in the calculation, the experimental value should be less than the calculated one. Apparently in the 40.1% blend a small amount of the PMMA is not interlamellar. For the other systems, the fact that the calculated values are less than or equal to the experimental ones implies that all of the PMMA is between the crystalline lamellae. If this was not the case, the calculated long periods would be even less and in poorer agreement with the measured values. Ideally, the long periods calculated in this manner should never be less than the experimental ones. The fact that in some samples they are is most likely a result of errors in the application of Bragg's law and the Hosemann model, as well as the simplicity of the method used to calculate long periods.

TABLE 6

COMPARISON OF LONG PERIODS FROM BRAGG'S LAW AND THE HOSEMANN MODEL TO THE VALUES CALCULATED ASSUMING ALL OF THE PMMA TO BE INTERLAMELLAR

Vol. % PVF_2	Long Period (nm)		
	Bragg	Hosemann	Calculated
100.0	14.4	12.4	13.4
85.8	19.8	18.5	15.6
72.8	22.4	21.2	18.4
60.9	24.8	25.6	22.0
50.1	27.8	26.5	26.7
40.1	28.9	28.6	33.4

The breadth of the amorphous thickness distribution is much larger than that for the lamellar crystals. The former increases in width as more PMMA is added while the latter remains relatively constant or shows a slight decrease. The change in the amorphous thickness distribution is most likely representative of a less uniform lamellar stack.

Another measure of the order of the system is the parameter N, which is assumed to be a measure of the average number of lamellae in a stack. N is larger than what was determined in studies of other systems (73,164,166,171), but is still somewhat smaller than what one might expect. As mentioned earlier, N can be viewed as the equivalent number of perfectly parallel lamellae (164). The relatively low value of N for the pure PVF_2 is not fully understood but the steady decrease of N in going from 85.8 to 40.1 volume % PVF_2 most likely is related to more angular disorder of the lamellar stack as a result of lower crystallinities and large, broadly distributed amorphous layers between the lamellae.

The Hosemann model also takes into account a linear transition zone E. The values from the model are in excellent agreement with those found from the experimental data using the methods described previously.

In order to calculate correlation functions and invariants, extrapolation of the experimental data to $s = 0$ must be made. To accomplish this, the data for the straight line portion of the $\tilde{I}s$ vs. $1/s^2$ curve, as described above, were

fitted by the Vonk computer program (184). The intensities in this region and beyond were then replaced by the fitted values, given by

$$\tilde{I}(s) = \frac{c_1}{s} + \frac{c_2}{s^3} \qquad (76)$$

with the first term representing the intensity change caused by a finite transition zone and the second term being Porod's law for the infinite slit case. To avoid negative values of $\tilde{I}(s)$, at very large values of s (determined by the computer program) the intensities were replaced by c_3/s^5. This arises from higher order terms in the series expansion of the sine functions which were used in equation 55 (174).

The experimentally determined one-dimensional correlation functions are shown for the six different samples by the solid lines in Figures 72-77. The circles in these figures represent the best fits to the data using the Vonk correlation function model with Guassian thickness distributions for both the amorphous and crystalline phases.

The peak in the correlation function is related to the periodicity of the system and should correspond to the long period measured from the Lorentz corrected desmeared data. These peak positions, determined from the experimental data, have been included in Figure 63. Good agreement with the long periods is seen in the 100-60.9 samples. Correlation functions for the 50.1 and 40.1 samples were so spread out that no peak was observed.

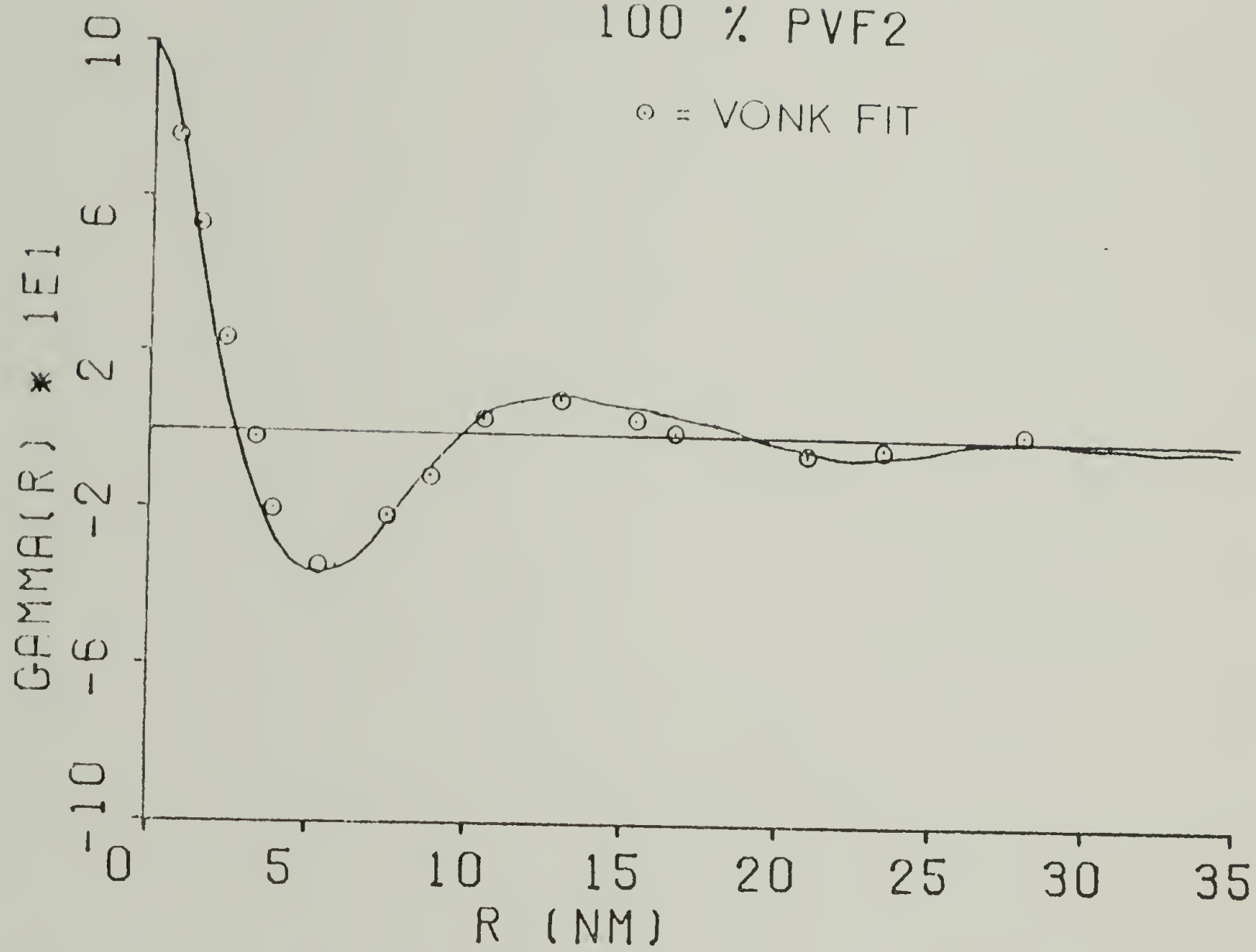

Figure 72. One dimensional correlation function for sample 100. The straight line is experimental data. The circles represent the Vonk model fit.

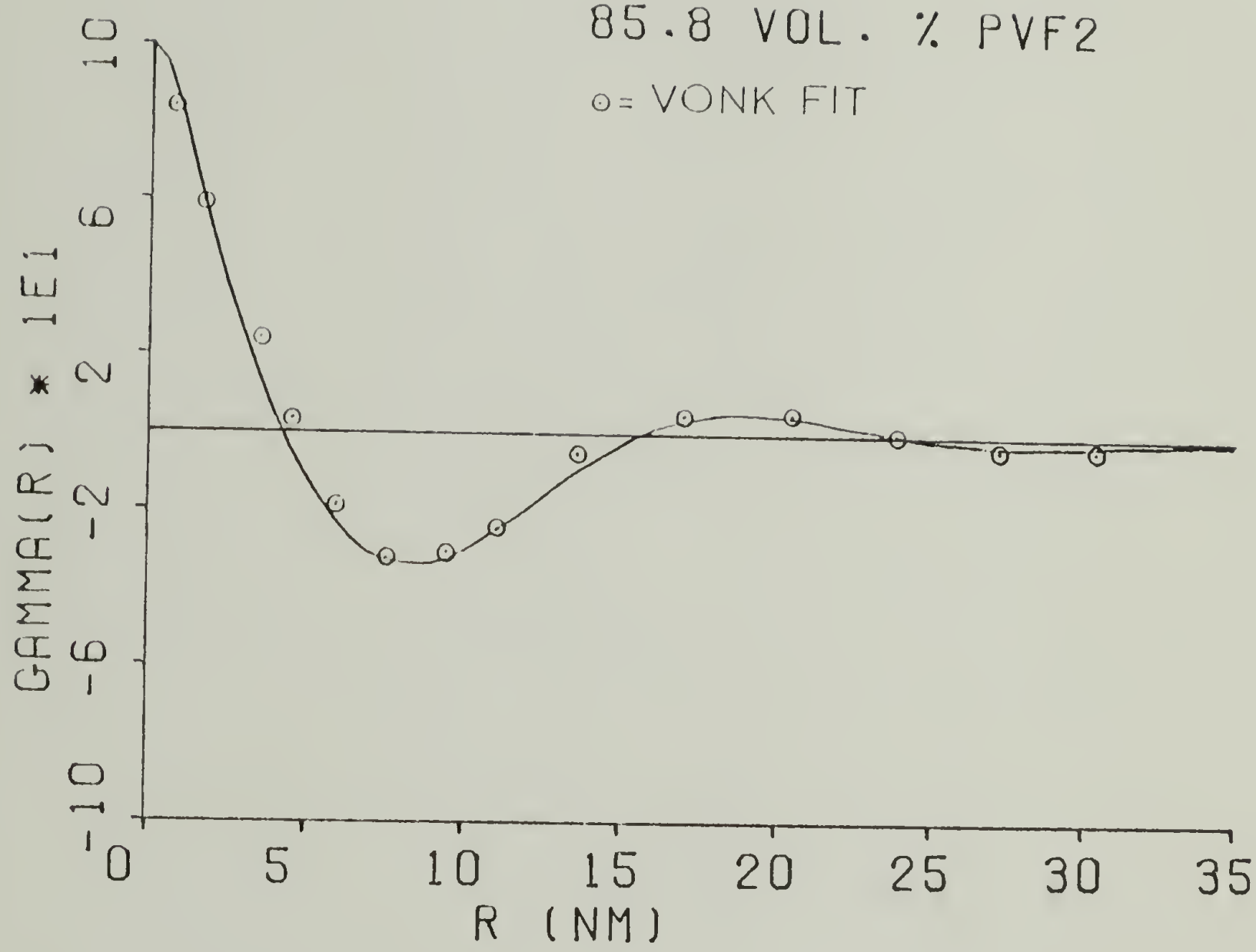

Figure 73. One dimensional correlation function for sample 85.8. The straight line is experimental data. The circles represent the Vonk model fit.

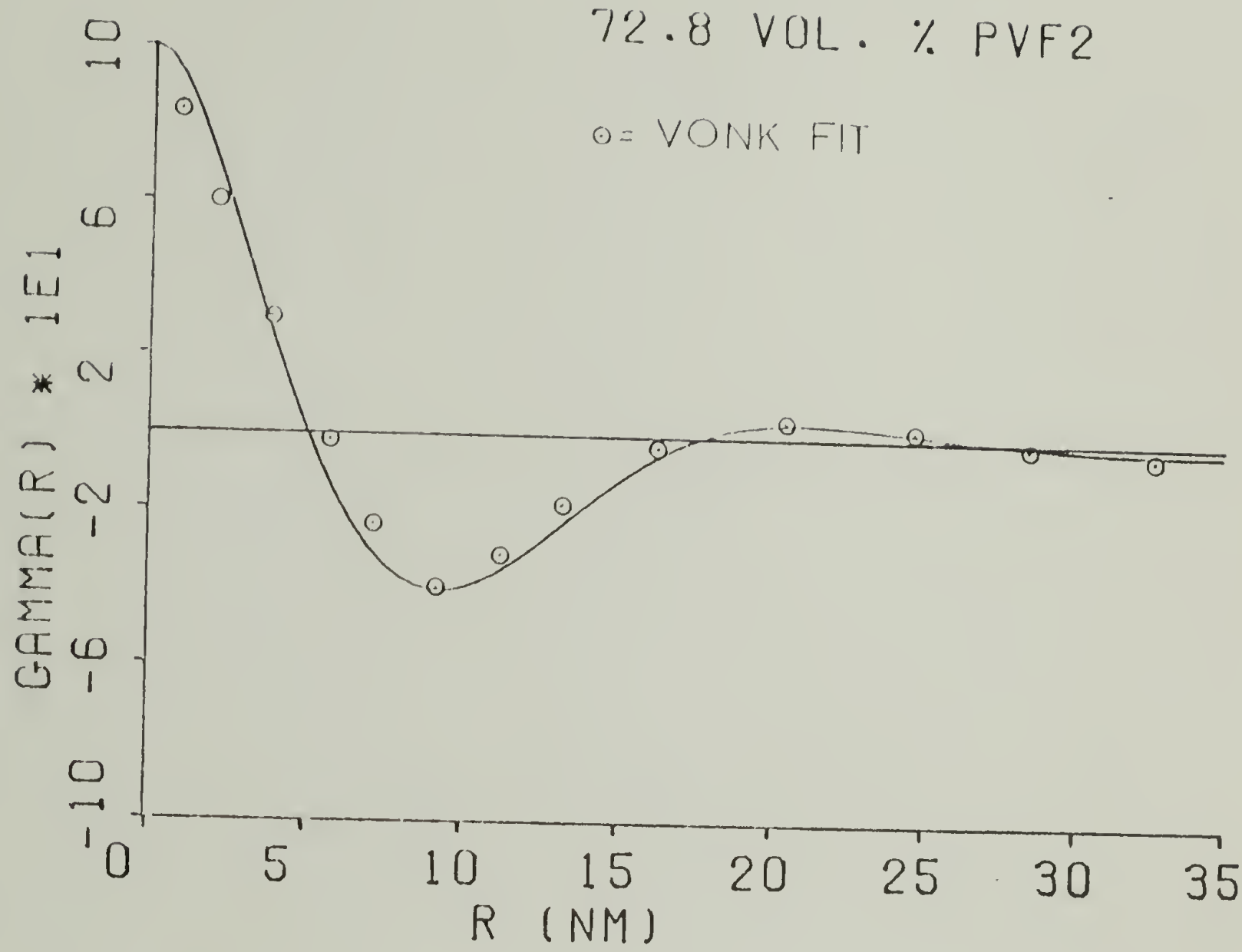

Figure 74. One dimensional correlation function for sample 72.8. The straight line is experimental data. The circles represent the Vonk model fit.

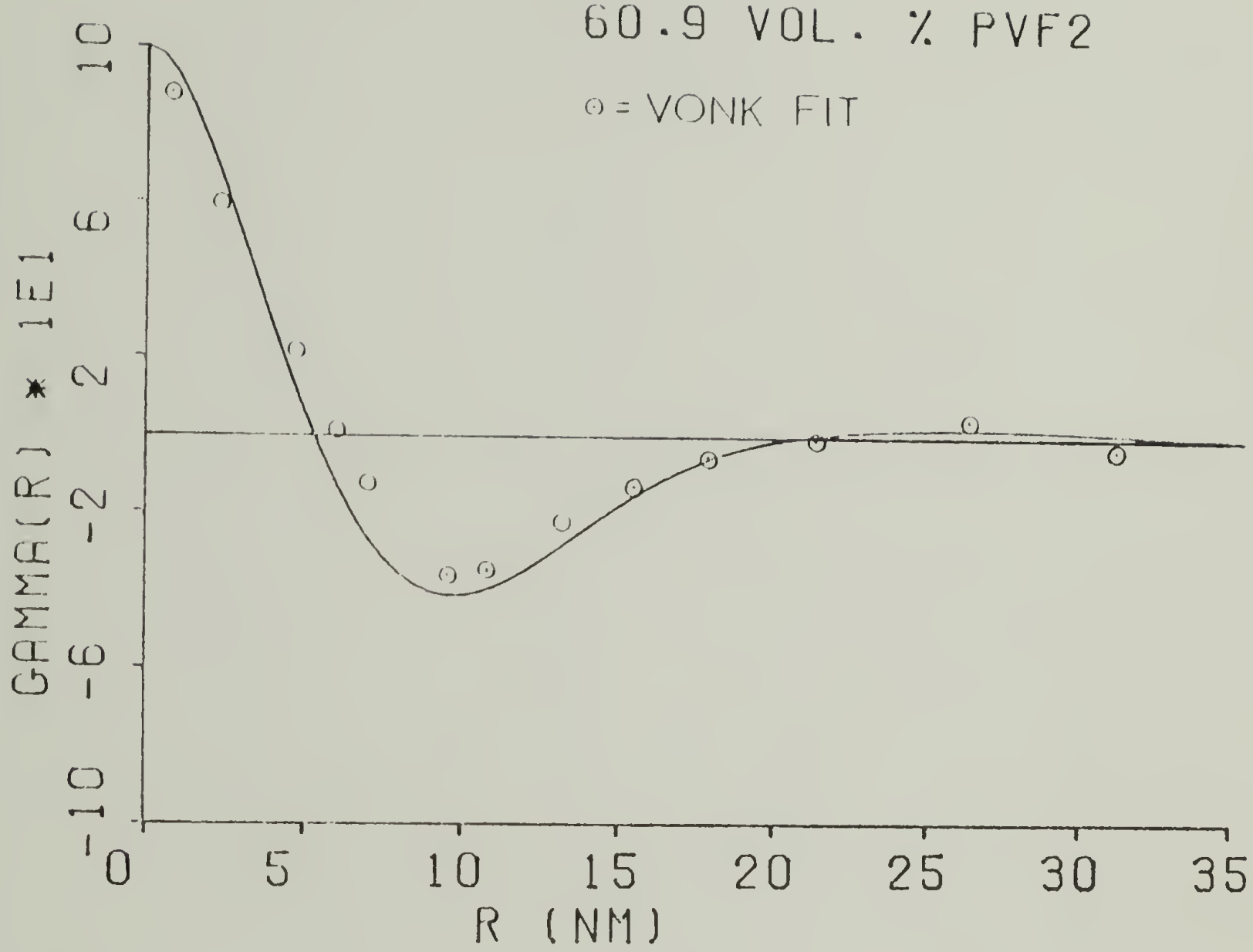

Figure 75. One dimensional correlation function for sample 60.9. The straight line is experimental data. The circles represent the Vonk model fit.

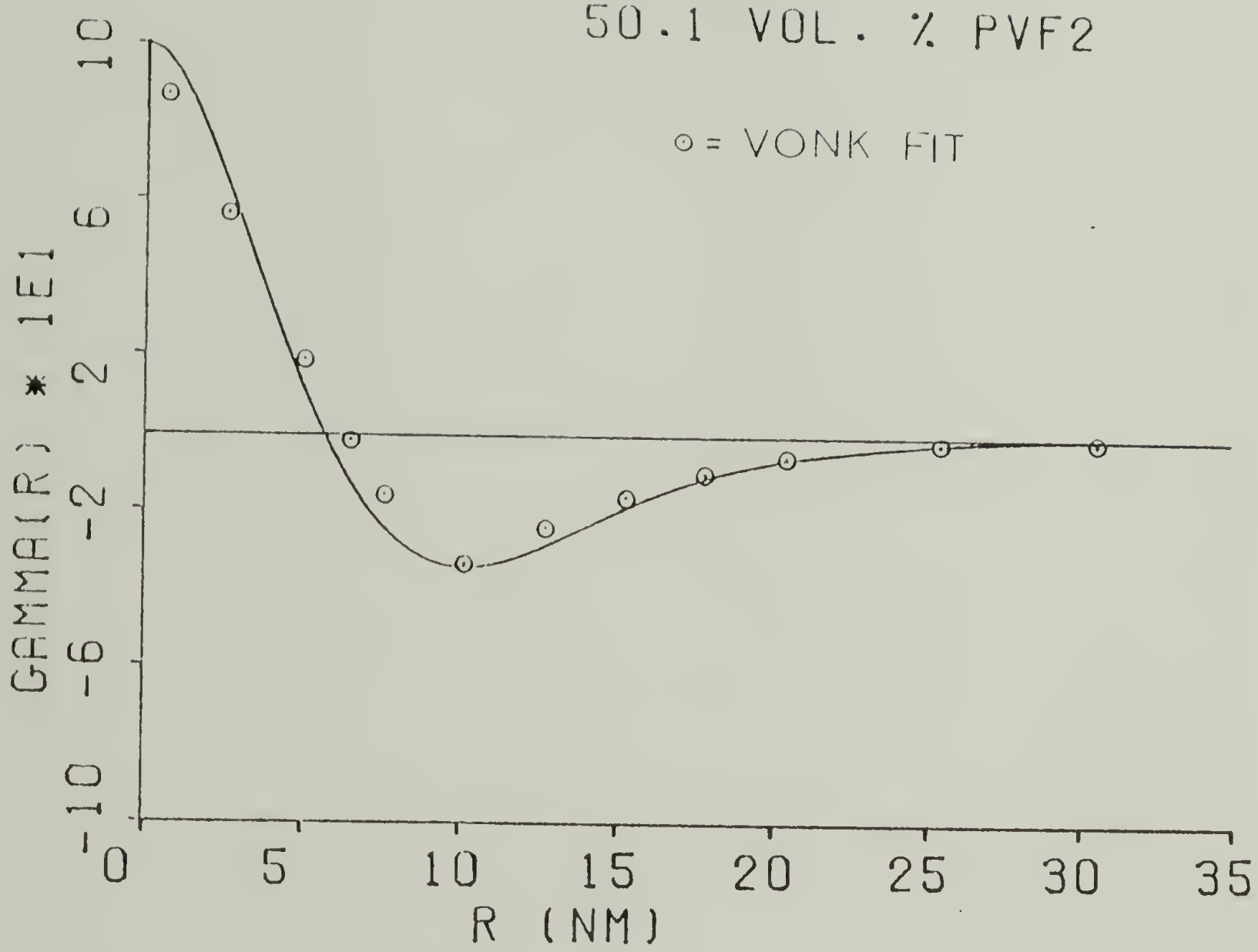

Figure 76. One dimensional correlation function for sample 50.1. The straight line is experimental data. The circles represent the Vonk model fit.

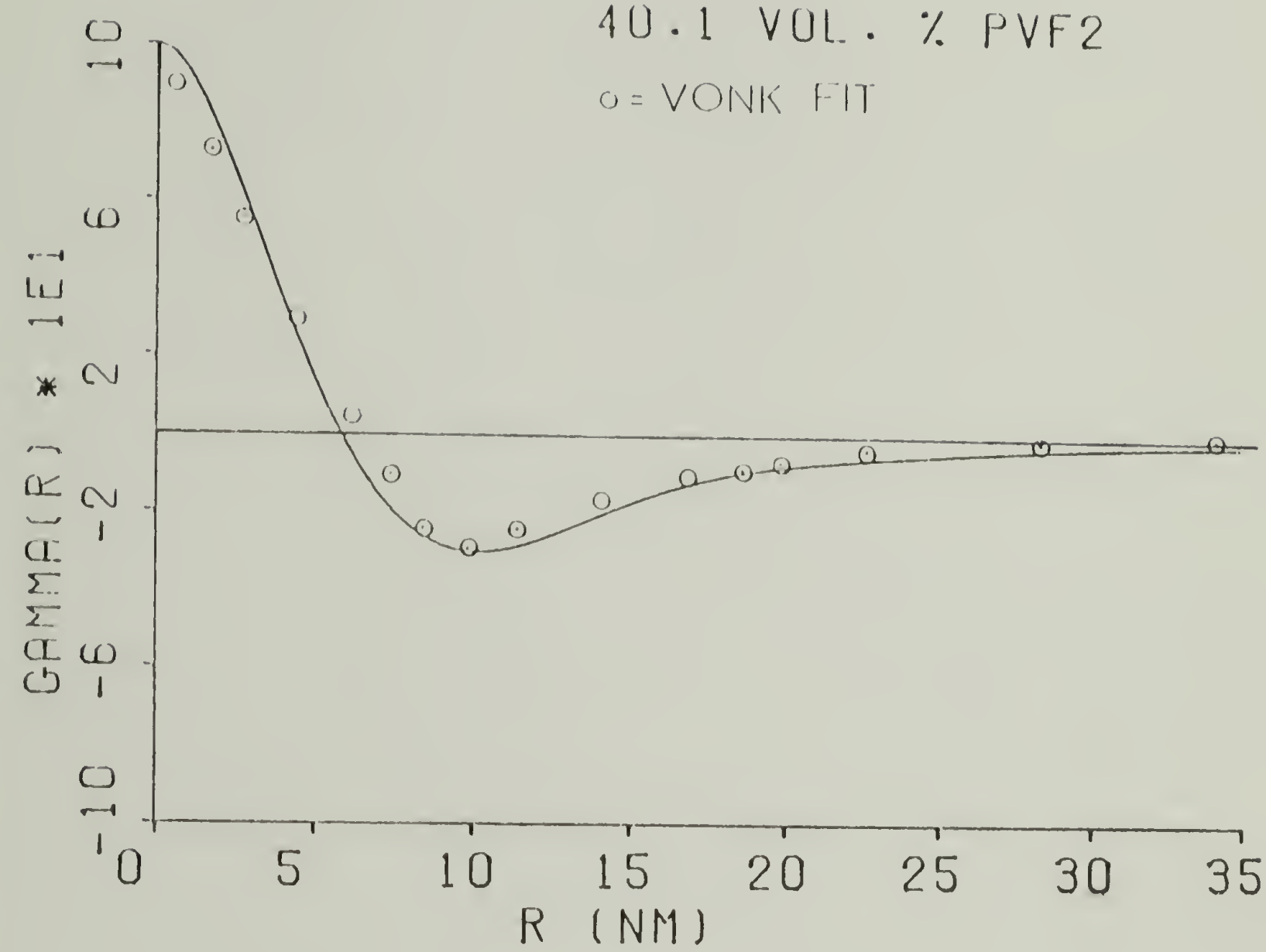

Figure 77. One dimensional correlation function for sample 40.1. The straight line is experimental data. The circles represent the Vonk model fit.

Slightly more shallow minimums in the correlation functions are observed as additional PMMA is added to the blends. Three factors can contribute to this: (1) decrease of the crystallinity below .5; (2) broad phase distributions; and (3) stacking disorder of the lamellae, such as angular branching or stacks of limited size (166).

As has been shown by DSC and Hosemann model fits, as well as with the Vonk model parameters given in Table 5, the crystallinities decrease in the more dilute blends. The stacking order, measured by N of the Hosemann model, is also lower in these systems. The breadth of the crystal and amorphous distributions from the Vonk model are given by β_c and β_a respectively. These parameters, which are in reasonable agreement with those obtained from the Hosemann model, show that the width of the thickness distribution decreases for the crystal but increases for the amorphous phase as more PMMA is added. Adjustment of these parameters implied that the amorphous phase distribution had the largest effect on spreading out the correlation function, but the depth of the minimum was altered more by the crystal distribution. Since the width of the crystal distributions decreased as the minimum in the correlation function moved towards zero, opposite to what one would expect, this factor was believed to play a minor role in determining the depth of the minimum. Changes in crystallinity and stacking disorder were therefore the main reasons for the alterations observed in the minimum

of the correlation function.

One drawback to using the Vonk model is that it assumes an ideal electron density profile with no transition zone. As was shown earlier, however, an appreciable transition zone does exist in these samples. This will effect the fit most at small values of r as well as the absolute values of the crystallinities. Even though, reasonable fits were obtained yielding parameters which are in fairly good agreement with those obtained from the Hosemann model.

Another qualification must also be made regarding both the Vonk and Hosemann models. Given the large number of parameters, many fits to the data are possible, but these other fits gave either crystallinities which were unreasonable or distributions of crystal sizes which would have necessitated many very small crystallites. Therefore, though the parameters chosen represent only a local best fit, it is believed that they are fairly accurate and useful in analysis of the data.

Volume fractions of crystallinity calculated from the two models presented above are shown in comparison to those measured on the DSC in Figure 78. There is fairly good agreement between the results. Since the Vonk model does not take into account phase boundaries, the crystallinities from the Hosemann model are believed to be more representative of the SAXS data. As can be seen, both SAXS values appear to be somewhat lower than the DSC results near the concentrated

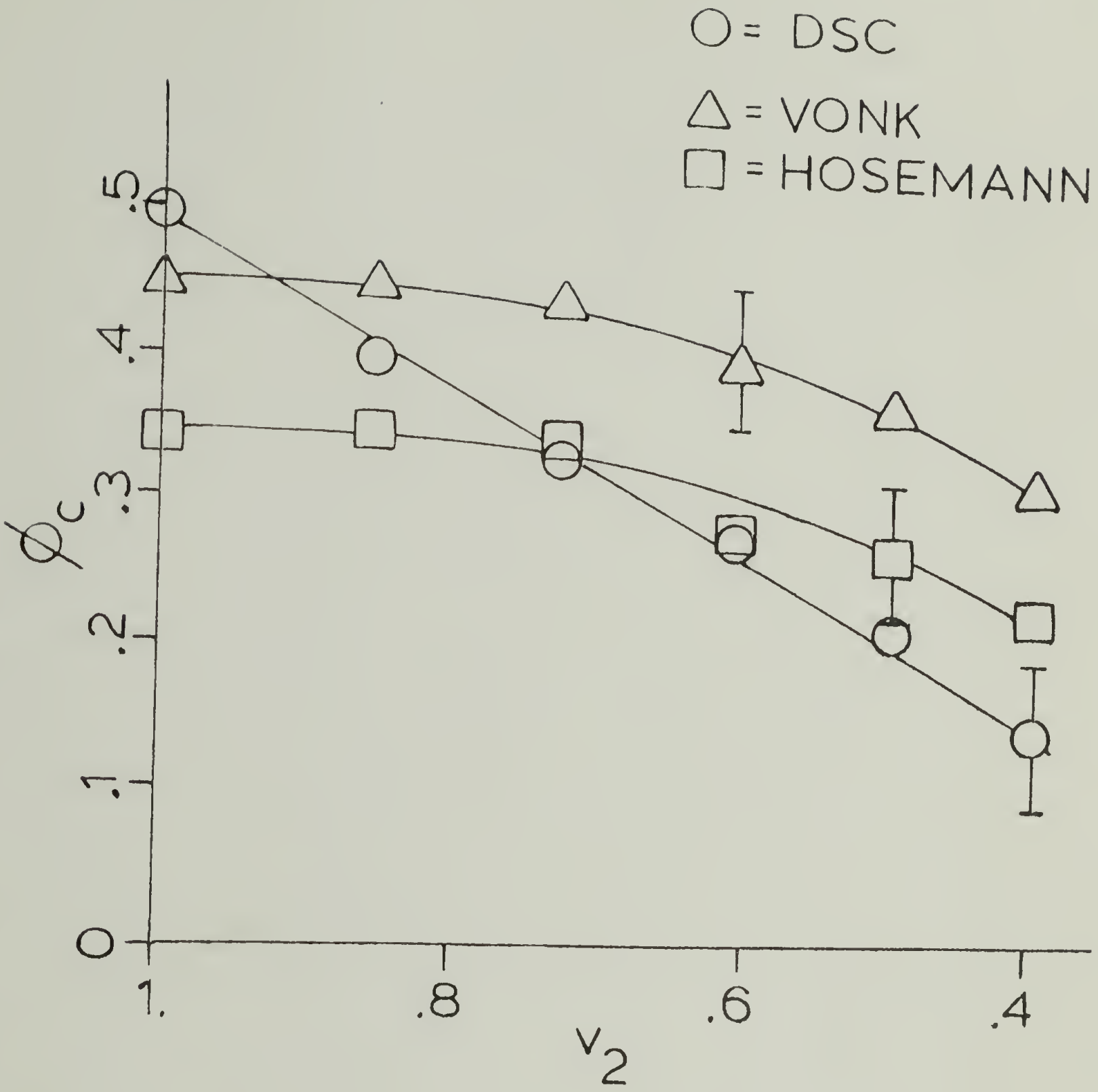

Figure 78. Volume fraction crystallinity ϕ_c, as a function of volume fraction PVF_2, v_2, from DSC experiments, the Vonk model and the Hosemann model.

PVF_2 range and higher than the DSC results in the more dilute blends. Two opposing factors are considered to cause this phenomena.

The PVF_2 crystals are thought to contain a certain amount of defects, resulting from inclusion of the head-to-head units, as discussed in Chapter IV. This will cause the SAXS crystallinities to seem somewhat depressed due to a lowering of the crystal electron density. In a DSC experiment though, these defective crystals have a higher enthalpy than a pure crystal and will give a larger melting endotherm, which is then interpreted as a higher crystallinity than what is actually present.

On the other hand, only the scattering arising from regions containing alternating crystal and amorphous phases has been analyzed to give the SAXS crystallinities. Large areas of pure amorphous polymer which certainly exist in the blends (see Chapter III), are not taken into account. These regions are considered in a DSC experiment since the crystallinities are based on the total sample weight. This factor thus causes the SAXS crystallinities to appear higher than those from the DSC.

In samples of high crystallinity, the first factor seems to predominate, while the second factor becomes controlling in systems of low crystallinity which contain large areas of pure amorphous polymer.

As discussed above, the increased long periods of the

blends containing more PMMA is due to the inclusion of this component between the crystalline lamellae. Further evidence showing that the PMMA is located in the interlamellar regions can be seen by changes in the mean squares of the electron density fluctuations $\overline{\eta^2}$, which are obtained from the invariants. In a lamellar semi-crystalline polymer, $\overline{\eta^2}$ is proportional to the volume fractions of the phases, and the square of the difference between the electron densities of the crystalline lamellae and the interlamellar amorphous regions. A plot of $\overline{\eta^2}$ vs. v_2 is presented in Figure 79. The increase of $\overline{\eta^2}$ with increasing content of PMMA can be understood by looking at the relative electron densities of the components presented in Table 7. The electron density of amorphous PMMA is much lower than that for amorphous PVF_2. Therefore, if PMMA is included between the crystalline lamellae, the difference in the electron densities between the crystal and amorphous regions will rise, causing $\overline{\eta^2}$ to increase. On the other hand, if the PMMA were excluded from the interlamellar regions, $\overline{\eta^2}$ would remain constant in all samples. The large rise observed for $\overline{\eta^2}$ therefore proves that PMMA exists between the lamellae.

It is possible to calculate a theoretical $\overline{\eta^2}$ for the model of crystalline PVF_2 separated by an amorphous blend of PVF_2 and PMMA. Assuming that the amorphous regions of the sample are homogeneous after crystallization of the PVF_2, the average volume fraction of PVF_2 in the remaining

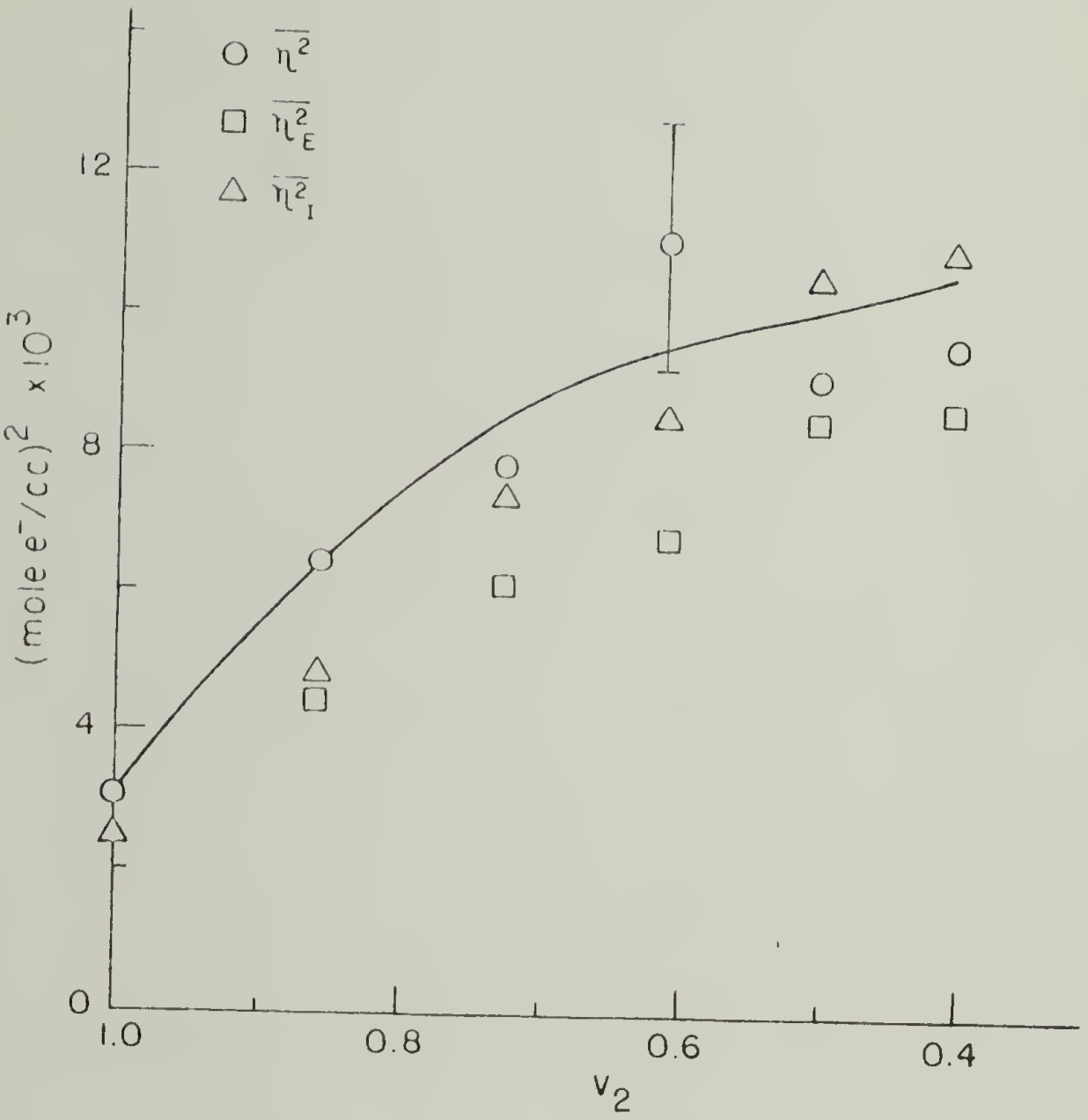

Figure 79. Comparison of experimental (o) and two calculated values for the mean square electron density fluctuation.

where ρ_m is the mass density and $\underline{v}$ is the barycentric velocity and t is time (212). In this case however a volume average frame of reference is more useful. The volume average velocity v is defined as

$$v = \sum_i \rho_{mi} \underline{v}_i \bar{V}_i \tag{92}$$

where ρ_{mi} and $\underline{v}_i$ are the mass density and the barycentric velocity of component i, and $\bar{V}_i$ is the partial specific volume of this component.

Fick's law (212) in the volume average frame of reference relates the mass flux (with respect to the volume average velocity) j_i to the gradient of mass density:

$$j_i = \rho_{mi} (\underline{v}_i - v) = -\mathcal{D} \nabla \rho_{mi} \tag{93}$$

where $\mathcal{D}$ is the diffusion coefficient. Assuming constant $\bar{V}_i$, the equation of continuity thus simplifies in this frame of reference to (209,212)

$$\nabla \cdot v = 0 \tag{94a}$$

In spherical coordinates, equation 94a can be written as

$$\frac{1}{r^2} \frac{\partial}{\partial r} (r^2 v_r) = 0 \tag{94b}$$

TABLE 7

ELECTRON DENSITIES OF PVF_2 AND PMMA

	Density (g/cc)	$\frac{\text{mole } e^-}{g}$	$\rho(\frac{\text{mole } e^-}{cc})$
PMMA	1.20	.5394	.647
Amorphous PVF_2	1.67*	.4997	.834
Crystalline PVF_2	1.88*	.4997	.939

*From ref. 40.

amorphous phase $v_{2,a}$ is given by

$$v_{2,a} = \frac{v_2 - \phi_c}{1 - \phi_c} \tag{77}$$

The value of the electron density of the amorphous phase ρ_a, can then be assumed to be given by a weighted average of the electron densities of the components in this phase.

$$\rho_a = \rho_{2,a} v_{2,a} + \rho_1 (1-v_{2,a}) \tag{78}$$

where $\rho_{2,a}$ and ρ_1 are the electron densities of amorphous PVF_2 and PMMA respectively. The results of these calculations are presented in Table 8.

For the ideal two phase case, $\overline{\eta^2}_I$ is given using equation 50.

$$\overline{\eta^2}_I = \phi_c(1-\phi_c) (\rho_c-\rho_a)^2 \tag{79}$$

with ρ_c being the electron density of crystalline PVF_2. When finite transition zones are present, this will be reduced according to equation 62 to $\overline{\eta^2}_E$.

$$\overline{\eta^2}_E = \left[\phi_c(1-\phi_c) - \left(\frac{E}{3L}\right)\right] (\rho_c-\rho_a)^2 \tag{80}$$

In both of these calculations, ϕ_c was taken from the Hosemann fits since this was thought to be the most representative of the SAXS data. The values of E used were averages of E_v and E_R.

TABLE 8

PARAMETERS USED IN CALCULATION OF THEORETICAL MEAN SQUARE ELECTRON DENSITY FLUCTUATIONS

Sample	ϕ_c (Hosemann)	$v_{2,a}$	(mole e^-/cc) ρ_a	$\overline{\eta^2}_I$	$\overline{\eta^2}_E$	$\overline{\eta^2}$
100.0	.34	1.00	.834	.00247	.00221	.00307
85.8	.35	.782	.794	.00484	.00444	.00646
72.8	.34	.588	.757	.00743	.00612	.00785
60.9	.28	.457	.733	.00860	.00687	.0115
50.1	.27	.316	.707	.0107	.00859	.00919
40.1	.23	.222	.689	.0111	.00872	.00971

The estimates of $\overline{\eta^2}_I$ and $\overline{\eta^2}_E$ are also plotted in Figure 79. Fairly good agreement between the experimental and theoretical results lends additional support to the hypothesis that the PMMA is included between individual lamellae. Slight differences in these values most likely result from errors in the estimation of E, different interlamellar amorphous concentrations than the average values assumed, as well as errors in measuring the area under the scattering curve to infinite s.

Preliminary work on pure PVF_2 and 72.8 vol.% PVF_2 blend samples crystallized at 433 K for 48 hours also showed a large increase in the scattered intensity for the blend relative to the homopolymer. Though no quantitative analysis has been performed on these samples, the relative intensities of the experimentally observed scattering for these two samples was similar to the relative intensities observed in the experimentally measured data for the same two blend compositions crystallized at 418 K. This implies that the plot of $\overline{\eta^2}$ vs. v_2 for the samples crystallized at the higher crystallization temperatures would be similar to that given in Figure 79 for the 418 K samples. From this it would be concluded that most of the PMMA is still between the lamellae at T_c = 433 K.

Contrary to this, other data suggests that at least a portion of the PMMA is not interlamellar at these higher crystallization temperatures. Previous work presented in

Chapter III concluded that at these temperatures at least some of the PMMA is in amorphous regions between bundles or fibrils of lamellae, often called the interfibrillar regions. Part of the PMMA is also excluded from the spherulite itself, as can be seen by nonlinear spherulitic growth at high temperatures (Chapter VI). This intimates that the amount of PMMA in the interfibrillar and interspherulitic regions is relatively small, and that the invariant calculation is not very sensitive to small changes in interlamellar amorphous composition. However, the data from the SAXS experiments at higher crystallization temperatures is far from complete. A thorough analysis of all samples along the lines of what was done for the 418 K samples should be performed before any quantitative comparisons to other experiments can be made.

A serious problem in the high temperature samples is that multiple morphologies and crystal forms exist. These could very likely include a large fraction of crystals grown after quenching the samples if the crystallization times at high temperatures were not long enough. Therefore, these factors must also be taken into account when performing SAXS experiments on samples crystallized at high temperatures.

It is useful to look at the changes in $\overline{\eta^2}$ for the PVF_2/PMMA system compared to those observed in other compatible semi-crystalline blends. The normalized experimental values of $\overline{\eta^2}/\overline{\eta^2}_o$, where $\overline{\eta^2}_o$ is the value for the pure

semi-crystalline polymer, are shown as a function of the volume fraction of the semi-crystalline polymer v_2 for the PVF_2/PMMA system, the PCL/PVC (73) and the isotactic/atactic PS (166,189) systems in Figure 80. As shown above, $\overline{\eta^2}$ is a function of both the volume fraction crystallinity and the difference in the electron densities of the crystalline and amorphous phases. In the first two systems, the electron density difference is the controlling factor. The rise of $\overline{\eta^2}$ for the PVF_2/PMMA system has been shown to be caused by the inclusion of PMMA, having a lower electron density than PVF_2, between the crystalline lamellae. On the other hand, the electron density of the PVC is higher than the crystalline PCL. This results in less of an electron density difference between the phases if the PVC is between the lamellae, and thus lowers $\overline{\eta^2}$. Therefore, though the trends seen for $\overline{\eta^2}$ as a function of composition are opposite for these two systems, the conclusion for both is that the noncrystalline component resides between the individual lamellae of the semi-crystalline polymer. This agrees with changes in the long periods for these two systems.

In the isotactic/atactic PS system, both polymers have the same electron densities, thus the location of the components will not alter $\overline{\eta^2}$. Variations of crystallinity will change $\overline{\eta^2}$ in this blend and cause the fluctuations observed. However, from the consistency of the long period, the atactic

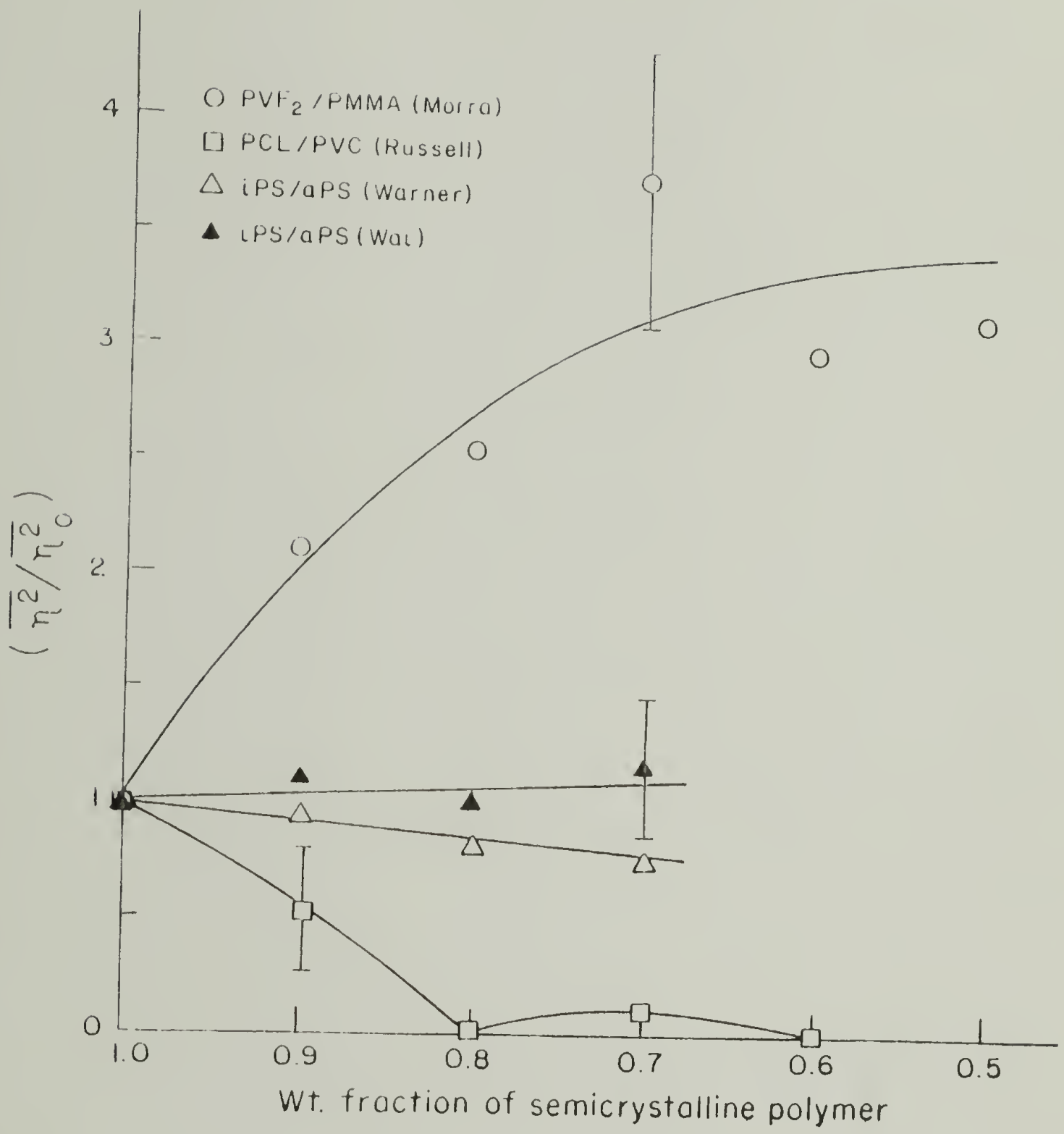

Figure 80. Experimental values for the mean square electron densities as a function of composition for the blends: PVF_2/PMMA, PVC/PCL (73), and iPS/aPS (166,189).

PS seems to be excluded from the regions between the lamellae.

Keith and Padden (190) view the noncrystallizable polymer in a blend as an impurity added to the crystallizable polymer. The location of this "impurity" is then related to the parameter $\delta = \frac{D}{G}$, where D is the diffusion coefficient of the noncrystallizable impurity in the melt, and G is the crystal growth rate. If δ is large, the impurity has time to diffuse away from the growing crystals and it should be excluded from the interlamellar regions, whereas a small δ would imply that the impurity is entrapped between the lamellae. This suggests the δ's in the PVF_2/PMMA and PVC/PCL systems were smaller than δ for the PS blend. The interaction parameters for the first two systems (73, Chapter IV) suggest large favorable interactions between the polymers, whereas in the PS system, since the only difference between the components is tacticity, any interactions present would probably be relatively small. Therefore, there may be a correlation between δ and the interactions in a blend.

Another factor which should alter δ is the molecular weights of the polymers. Increasing the molecular weights of the polymer should decrease D and therefore δ, but even at molecular weights of 10^6, the atactic polystyrene still seems to be excluded from the interlamellar region (189). Thus, for these systems, it appears that favorable interactions between the components are more important to the δ

parameter than the molecular weight.

A possible explanation for these findings may be that favorable interactions act to prevent the impurities from being segregated. This would result in a lower D, thereby decreasing δ. Obviously it is very difficult to draw accurate conclusions from such a small sample, therefore this argument is offered not as a proven theory, but just as a suggestion to stimulate future work.

C. Conclusions

In conclusion, the SAXS studies have been a good tool for understanding the interactions between the two components in a semi-crystalline blend. Enhanced liquid scattering from the blends confirms compatibility in the amorphous regions. Larger transition zone thicknesses were observed as more PMMA was added. Small increases in lamellar thicknesses were coupled with large increase in the long periods as the blends become more dilute in PVF_2. Theoretical fits to the data using Hosemann's paracrystalline model and Vonk's correlation function approach were useful in describing the internal morphology. Larger measured invariants coupled with the increasing long period in the blends verified that the PMMA is included between the crystalline PVF_2 lamellae. Comparison to similar work on other systems gives rise to a possible explanation for this behavior.

C H A P T E R VI

SPHERULITE GROWTH KINETICS

A. Background

There are two studies in the literature which have analyzed the spherulite growth kinetics of PVF_2. Wang and Nishi (37) have studied the growth rates of spherulites in PVF_2/PMMA blends in temperature ranges at which only α form crystals are grown. Lovinger (23) has observed growth rates in pure PVF_2 at higher temperatures finding that the γ spherulites had a smaller temperature dependence than the α spherulites.

To quantitatively analyze the growth rate data, Wang and Nishi (37) utilized the Lauritzen-Hoffman (191) modified Turnbull-Fisher equation (192) for homopolymers in which they assumed the front factor, G_o, was function of the initial volume fraction of PVF_2, v_2.

$$G = G_o \exp\left[-U^*/R(T-T_\infty)\right] \exp\left[-\Delta\phi^*/kT\right] \qquad (81)$$

where G = radial growth rate

G_o = constant

U* = activation energy for transport of crystallizable segments through the melt to the site of crystallization

R = universal gas constant

T = temperature

T_∞ = hypothetical temperature where all molecular associated viscous flow ceases.

$T_\infty = T_g - C$, C = constant

$\Delta\phi^*$ = free energy required to form a critical nucleus

k = Boltzman's constant.

Hoffman et al. (132,191) have shown that the free energy necessary to form a two dimensional surface nucleus having a thickness, b_o, of one molecular layer can be expressed as

$$\Delta\phi^* = \frac{cb_o\sigma\sigma_e}{(\Delta F_u/A)} \qquad (82)$$

where σ and σ_e are the apparent lateral and end surface energies, ΔF_u in free energy of fusion per mole of repeat units, A is Avagadro's number and c is a constant being either 4 or 2 depending on whether the kinetics are either regime I or II, respectively. Regime I kinetics describes the situation where formation of the surface nucleus is followed by rapid completion of the substrate, whereas if a large number of nuclie are being formed and spread slowly the crystallization is said to follow regime II kinetics (132).

Therefore, from equation 82, and following the suggestions of Lauritzen and Hoffman (191), the second exponential in equation 81 can be written as

$$\exp\left[\frac{-\Delta\phi^*}{kT}\right] = \exp\left[\frac{-K_g}{T\Delta Tf}\right] \qquad (83)$$

where K_g is a nucleation parameter, independent of crystallization, given by

$$K_g = \frac{cb_o\sigma\sigma_e T_m^o}{R(\Delta H_u + \bar{\Delta} h_u)}$$

f is a correction factor for the change in ΔH_u as a function of temperature, and T_m^o is the equilibrium melting point of the blend.

The first exponential in equation 81 is related to diffusion in the melt and is expressed as a modified segmental jump rate term (191). This can also be expressed in terms of the empirical relation of Williams, Landel, and Ferry (WLF) (193) where U* and C would be the WLF universal constants C_1 and C_2 respectively.

Substitution of equation 83 into equation 81 suggests that a plot of $\ln(G) + U^*/R(T-T_\infty)$ vs. $1/T\Delta Tf$ should be linear with an intercept $\ln(G_o)$ and slope $(-K_g)$. The values thus attained for K_g allow the determination of $\sigma\sigma_e$ if the regime of crystallization is known. The Z test of Lauritzen (146) can be used to decide whether regime I or II conditions are followed. Z is defined by

$$Z \tilde{=} 10^3 (W/2a_o) \exp[-X/T\Delta T] \qquad (85)$$

where W is the effective lamellar width and a_o is the width of the molecular chain in the crystal. If X is taken as K_g

and the value of Z is less than or equal to 0.01, crystallization occurs by regime I kinetics. However, if $X = 2K_g$ and Z is greater than or equal to 1, regime II kinetics is obeyed.

Wang and Nishi (37), using the above analysis, found that all the crystallization observed conformed to regime II. They determined that $\sigma\sigma_e$ was fairly constant from pure PVF_2 to a 55 weight % blend, but seemed to decrease slightly for a 50 weight % blend. They also concluded that G_o was a function of the composition.

For polymer diluent mixtures, Mandelkern (194,195) has noted that an additional term related to the volume fraction of polymer material should be added to the right side of equation 82 for the free energy of nucleus formation. This term represents the probability of selecting the required number of crystalline sequences from the mixture. Boon and Azcue (196) have derived the analog of equation 81 for a two dimensional nucleus, using this additional free energy term. They have also multiplied G_o by v_2, the volume fraction of crystallizable polymer, which according to Mandelkern (195) is necessary since nucleation is proportional to the concentration of crystallizable units. Their growth rate equation is given as

$$G = v_2 G_o \exp\left\{-\frac{C_1}{R(C_2+T-T_g)}\right\} x \exp\left\{-\frac{4b_o\sigma\sigma_e T_m^o}{kT\Delta H_u \Delta T} + \frac{2\sigma T_m \ln v_2}{b_o \Delta H \Delta T}\right\} \quad (86)$$

where they have used a WLF diffusion term. However, when applying this equation to PS/benzophenone mixtures, the theory was not very accurate in predicting the experimental data.

Ong and Price (197) have also used equation 86 to analyze spherulitic growth in PVC/PCL blends. Using the empirical relation $\sigma = 0.1 b_o \Delta H_u$ (198,199), they rearranged equation 86 to

$$Y = \ln(G_o) - m\left(\frac{T_m^o}{T(T_m^o - T)}\right) \tag{87}$$

where

$$Y = \ln(G) + \frac{C_1}{R(C_2 + T - T_g)} - \ln v_2 \left(\frac{1.2T_m^o - T}{T_m^o - T}\right) \tag{88}$$

and

$$m = \frac{4 b_o \sigma_e \sigma}{k \Delta H_u} \tag{89}$$

By varying C_2, they found that the data for all samples at all temperatures fell on a straight line when plotted as Y vs. $T_m^o/T(T_m^o - T)$. From this plot, they calculated values of G_o and σ_e for the PVC/PCL blend.

There seems to be some question as to whether or not the correction for v_2 should be included in the growth rate equation. This type of correction was first suggested by Flory (200), who included a parameter D in this term. Many of the uncertain quantities in the growth model, such as lattice coordination numbers, number of segments per

structural unit in the lattice, the amount of order in the amorphous chains at the crystal surface, and corrections for the end of a crystal were included in D. It was shown that D should lie between zero and one. Thus, the relative importance of the v_2 term depends on the value of D. Another consideration is the value of v_2 to be used. The bulk concentration value is often used (196,197), but this is most likely incorrect. Ideally, one would want to use the concentration of the material at the growth front. Depending upon G, this can be different from the overall composition. Therefore, since the proper values of certain parameters in the v_2 term are difficult to determine, and this term can be close to zero, the importance of the correction for v_2 is uncertain.

In this study, growth rates of spherulites in PVF_2/PMMA blends will be measured in the temperature range at which both α and γ spherulites are grown. Quantitative analysis will be attempted utilizing the models presented above. Also, a new model describing nonlinear growth rates observed in the blends at high temperatures will be developed.

B. Results and Discussion

Growth rates were all measured from optical micrographs recorded at various times during the crystallization. Temperatures of crystallization ranged from 424 to 434 K. Most samples had two populations of spherulites in this

range, the non-banded γ form and the banded α form spherulites. As discussed in Chapter III, the γ spherulites would often develop axialite-like protrusions. There were also platelet-like crystal structures which had very low birefringence resulting from their chain orientation being almost perpendicular to the film surface. Only the spherulitic morphologies were used for analyzing growth rates.

From the studies in Chapter III, it is also known that some of the α spherulites underwent a phase change to γ' spherulites. This was almost always initiated by contact with a γ spherulite. If this transition occurred, it did not affect the growth rates of the spherulites unless the transition front caught up with the growth front and a mixed spherulite resulted. Therefore, the growth rates observed for banded spherulites which did not convert to mixed spherulites, were the growth rates of the α phase crystals.

In both the α and γ spherulites grown at the higher temperatures, nonlinearities in the growth rates were observed. Plots of the spherulite radius vs. crystallization time at 434 K are shown for the banded α and the non-banded γ spherulites in Figures 81 and 82 respectively. In the blends, the growth rates decreased with time at this temperature. The dashed lines in the figure represent a straight line fit to the linear segments of the curves at early time. By lowering the crystallization temperature, the growth rates became more linear, but nonlinearities could still be

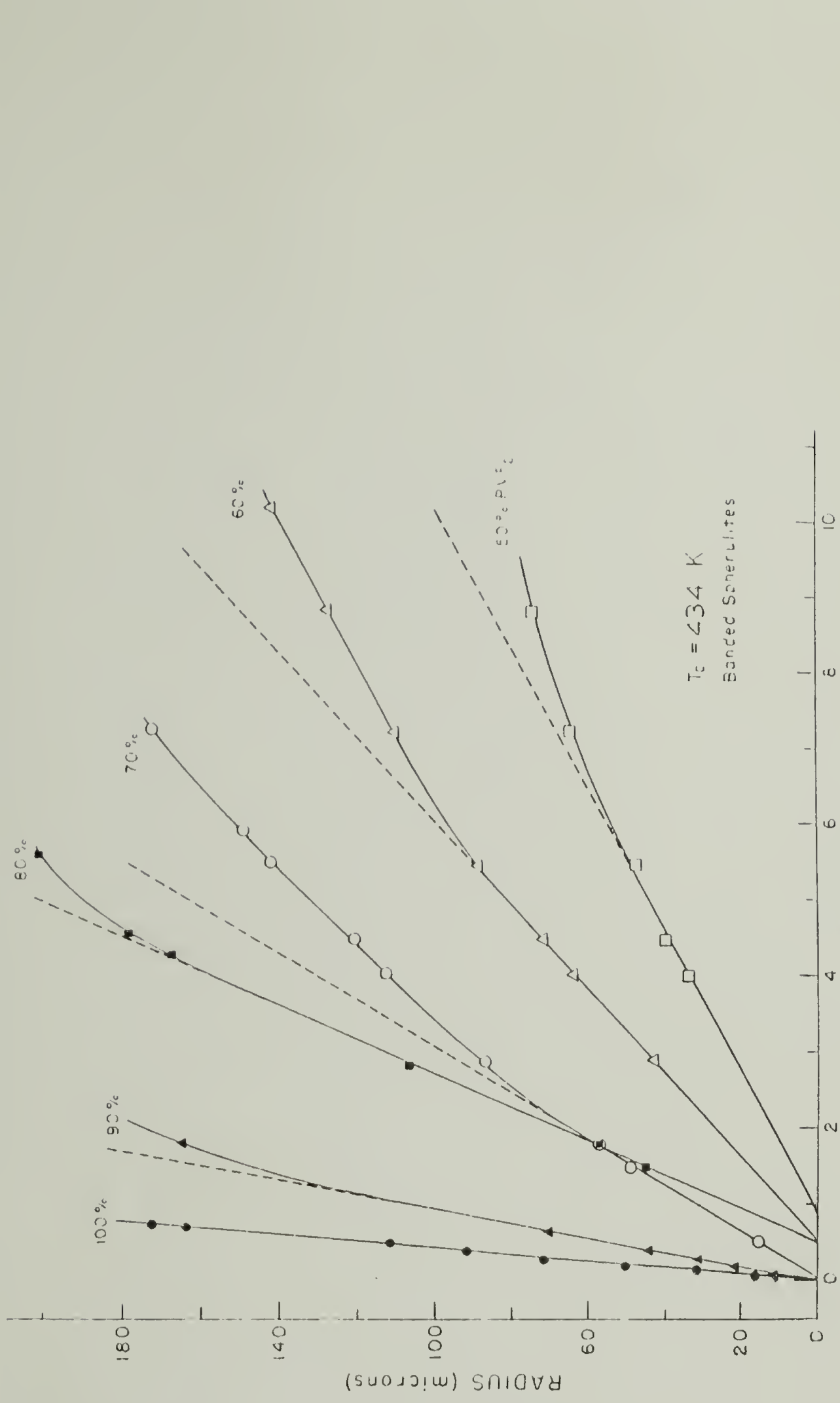

Figure 81. Radii of the banded α form spherulites vs. crystallization time for different weight % PVF_2 blends. Dashed lines are the initial slopes of the curves.

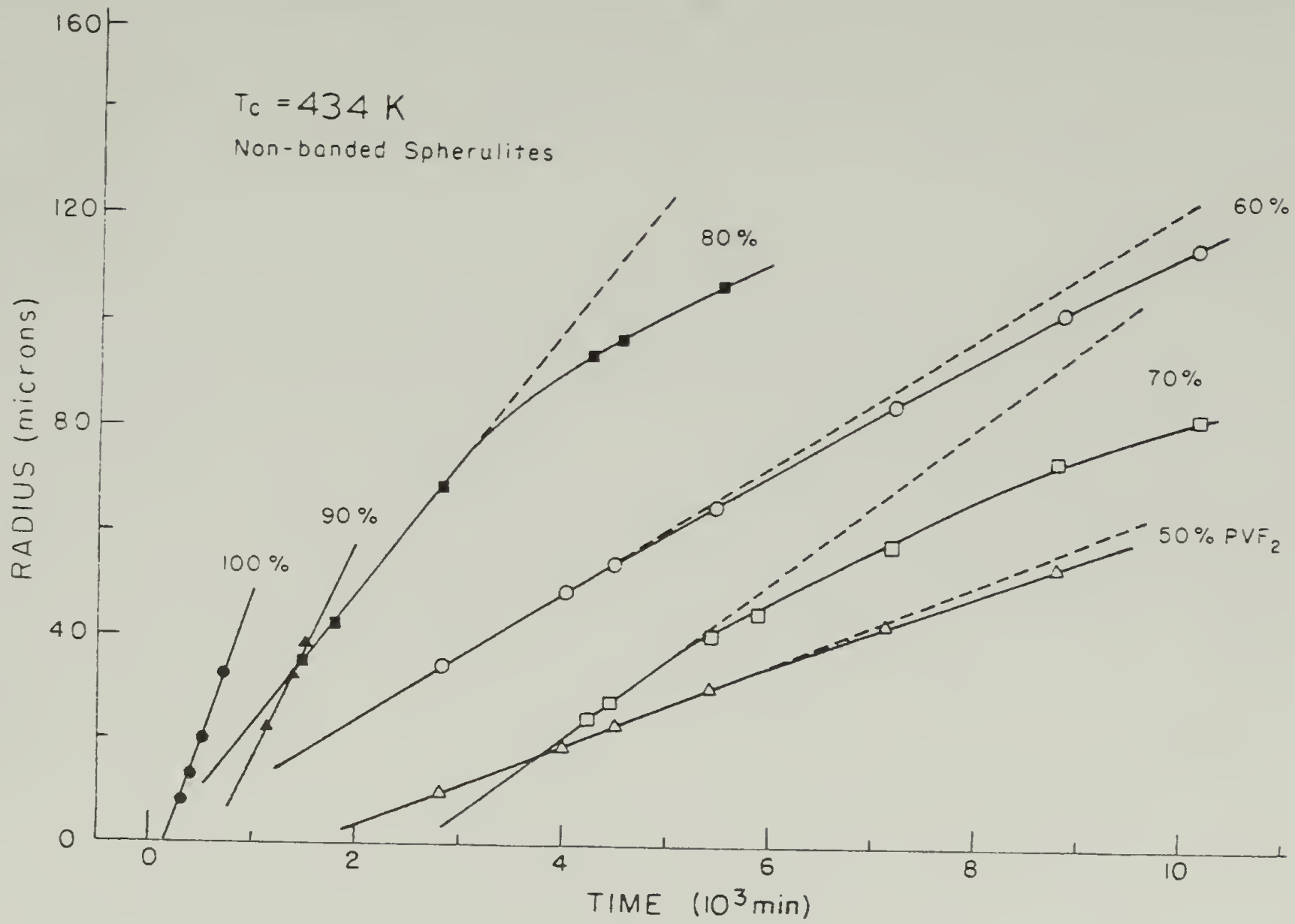

Figure 82. Radii of the banded γ form spherulites vs crystallization time for different weight % PVF_2 blends. Dashed lines are the initial slopes of the curves.

seen at long times in the more dilute blends. Discussion of this behavior and a proposed model for the growth will be presented in the next section.

To apply the equations describing spherulitic growth developed in the background section, the initial slopes of the radius vs. time plots were used.

1. Analysis of initial growth rates. A typical plot of the initial growth rates for both types of spherulites as a function of composition is given in Figure 83 for a crystallization temperature of 429 K. The depression of G with decreasing amounts of PVF_2 is much more drastic for the banded spherulites. It appears that if the data were extended to lower PVF_2 concentrations, the non-banded spherulites might grow faster than the banded ones. This change in relative growth rates is exactly what happened in pure PVF_2 when the crystallization temperatures were raised (23). The effect of T_c on G in the various blends is shown in Figure 84 for the banded spherulites and Figure 85 for the non-banded ones. The results of Lovinger (23) for pure PVF_2 of slightly higher molecular weight are shown by the dashed lines in these figures.

A better way to view this data is to plot G vs. a reduced temperature T_r defined as

$$T_r = \frac{T-T_g}{T_m^o-T_g} \qquad (90)$$

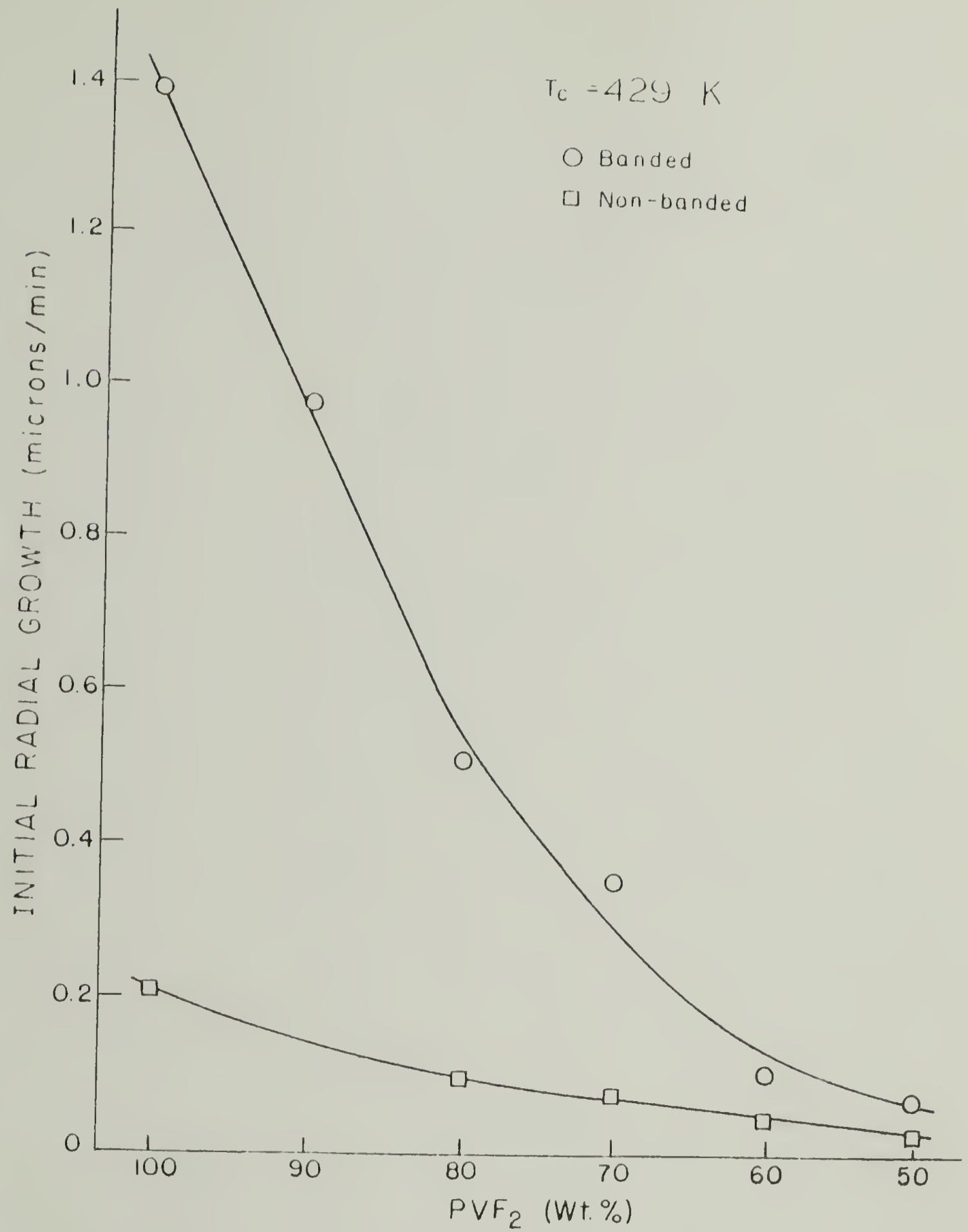

Figure 83. Initial radial growth rates at 429K of banded and non-banded sperulites as a function of composition.

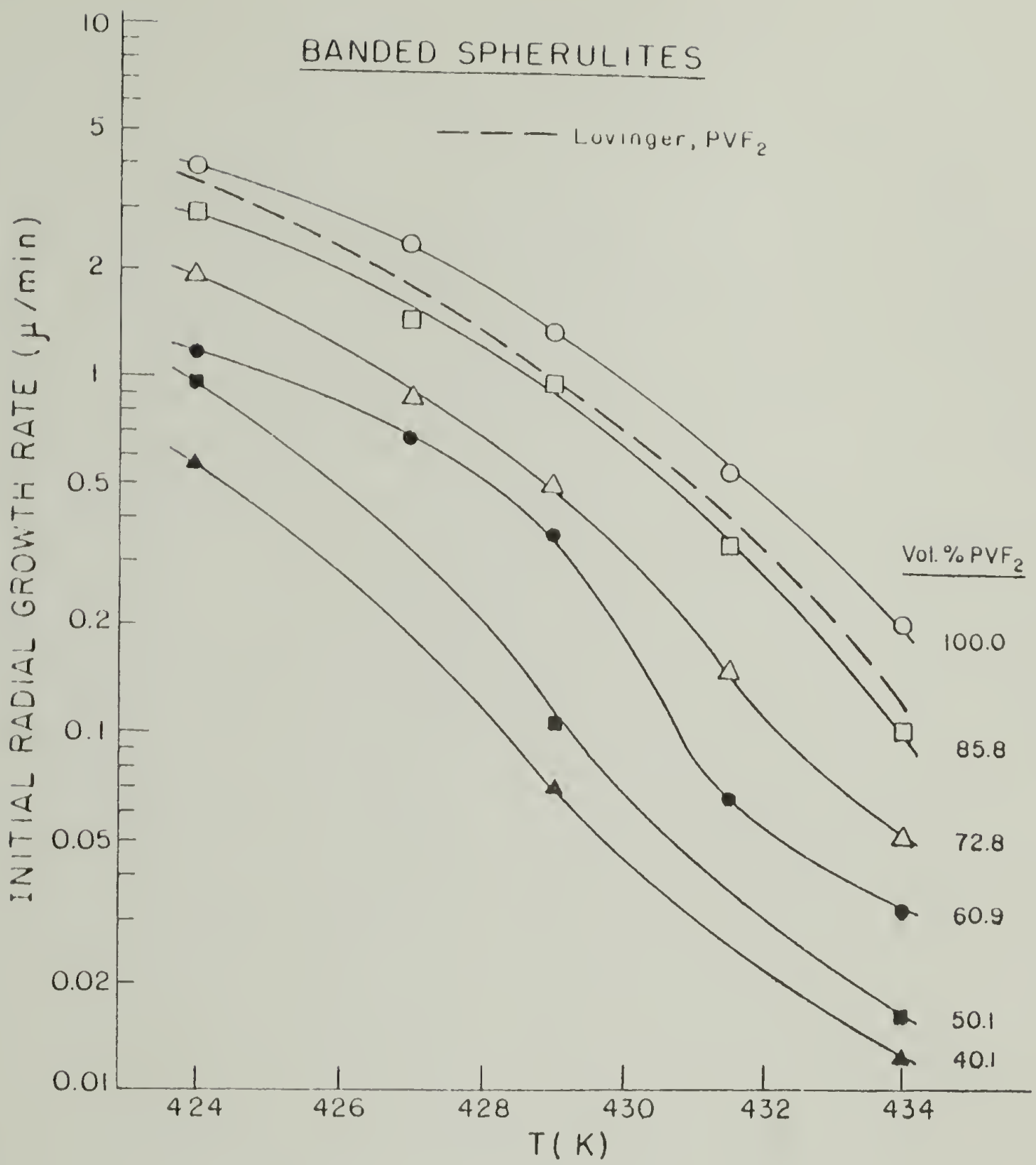

Figure 84. Initial radial growth rates of banded α spherulites as a function of crystallization temperature for various blend compositions. The dashed line is data for PVF_2 from Lovinger (23).

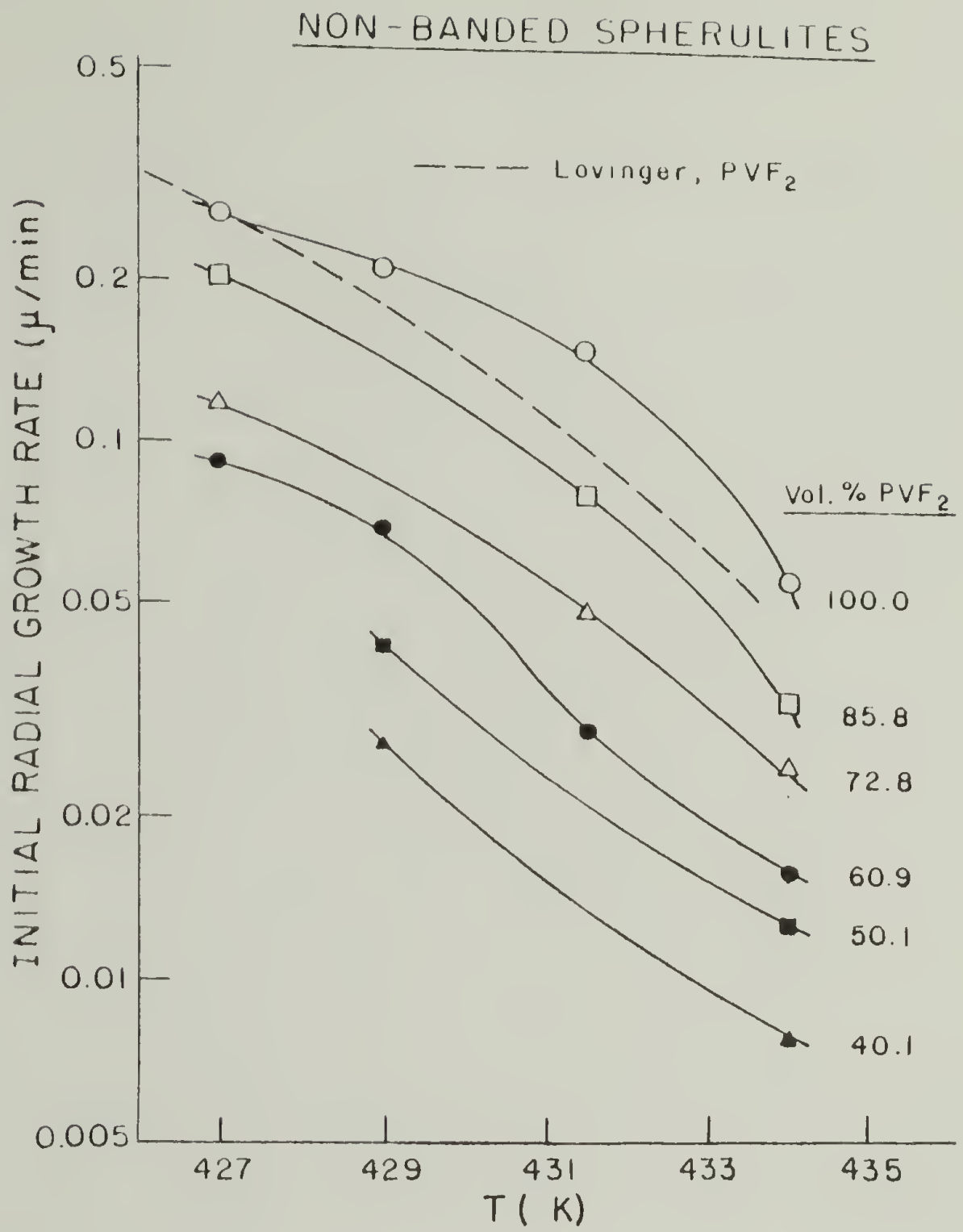

Figure 85. Initial radial growth rates of non-banded γ spherulites as a function of crystallization temperature for various blend composition. The dashed line is data for PVF_2 from Lovinger (23).

where the appropriate T_m^o and T_g for each composition are used. The melting points as a function of composition are given in Table 2. A compilation of T_g data as a function of composition, taken from several studies (34,37,39,56) is presented in Figure 86. If alterations in T_g and T_m^o with concentration are the main reasons for the observed depression of G in the blends, plots of G vs. T_r should superimpose. These types of plots are shown in Figures 87 and 88 for the banded and non-banded spherulites respectively. Since the data for the different blends obviously do not fall on the same curve, other effects beside changes in T_m^o and T_g must be important. These effects are most likely related to the strong interactions between the two polymers. As was shown in Chapter IV, these interactions are a function of composition. Thus, their influence on the growth kinetics will vary for each mixture.

Following Ong and Price (197), the data was plotted, according to equation 86, as Y vs. $T_m^o/T(T_m^o-T)$. This was done for both the α and γ spherulites. Unlike their results for the PVC/PCL system, straight line plots were not obtained when all the data for a given crystal form were plotted in this manner. By varying C_2, and even C_1, as much as 750% straight line plots were still not observed for either crystal form. Often, the data for a given blend composition did not even form a straight line in this type of plot.

These results can be due to a number of factors.

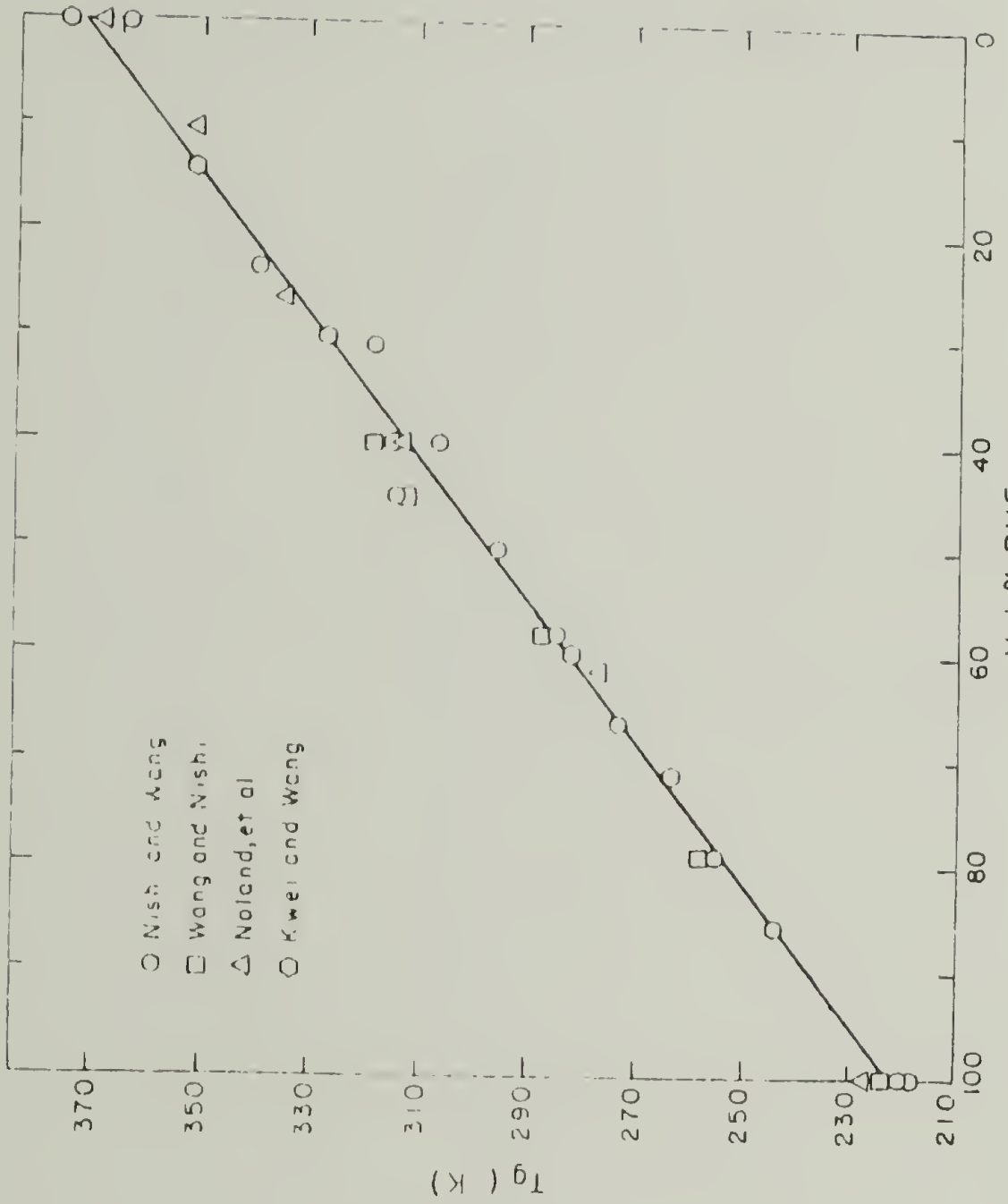

Figure 86. Compilation of T_g data as a function of composition in PVF_2/PMMA blends. Taken from references 34, 37, 39 and 56.

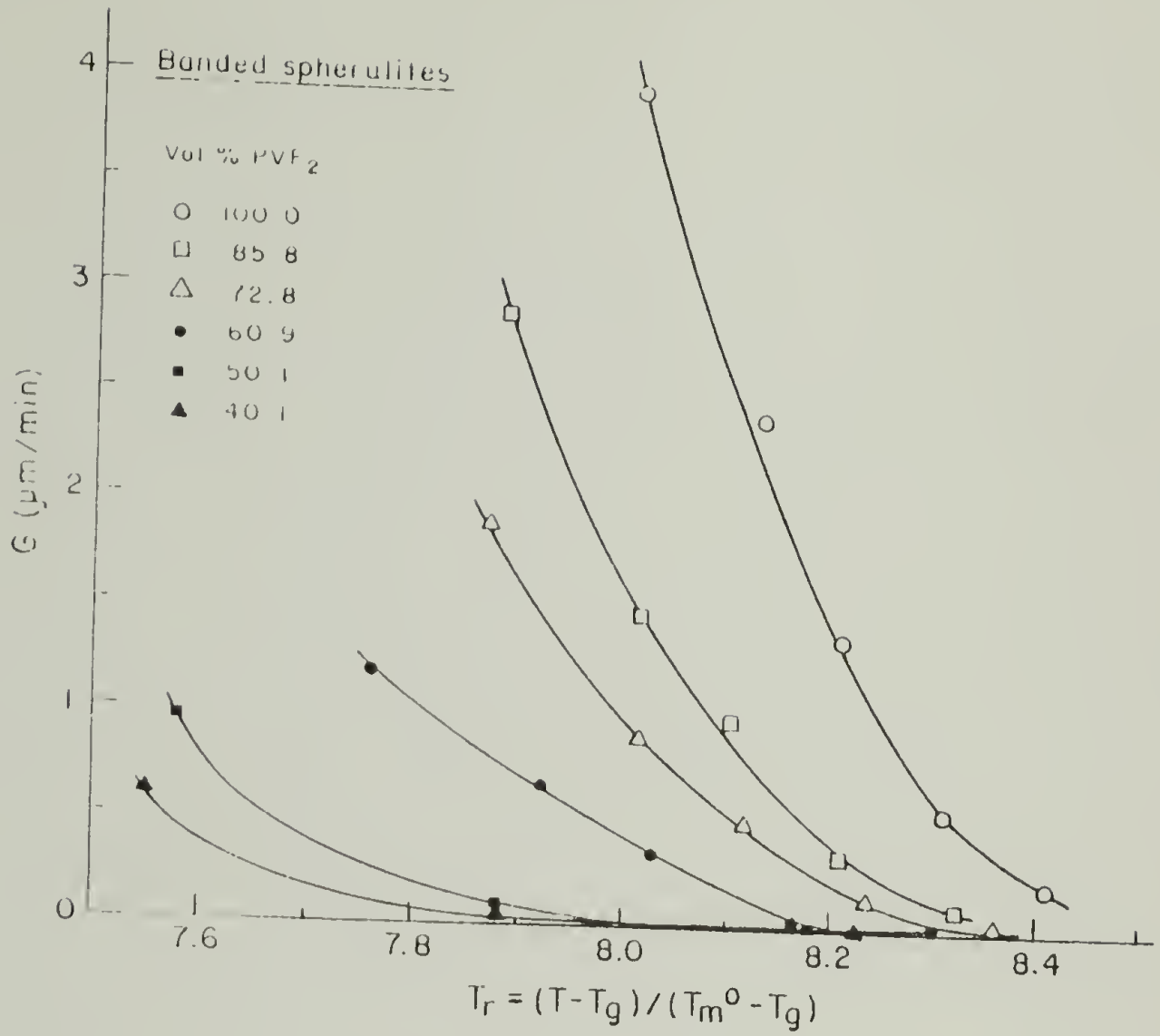

Figure 87. Initial radial growth rates of banded α spherulites in various blend compositions plotted against a reduced temperature.

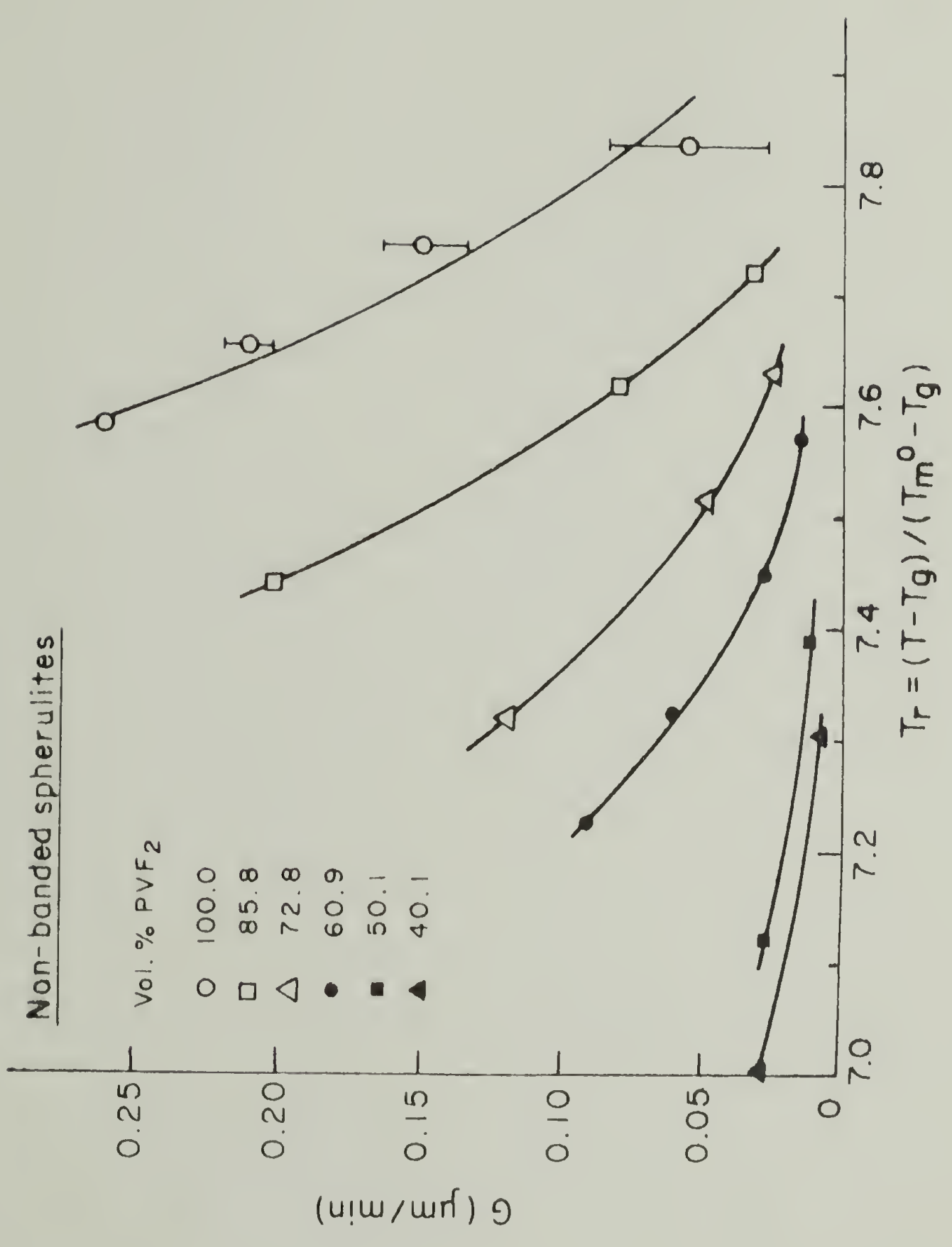

Figure 88. Initial radial growth rates of non-banded γ spherulites in various blend compositions plotted against a reduced temperature.

Equation 86 includes the correction for v_2. As discussed earlier, the proper incorporation of this is not fully understood. It has also been shown that the interaction parameter varies with composition (Chapter IV) so $\sigma\sigma_e$ might also. Actually since there are strong interactions between the polymers, these could have additional effects on the growth beyond those accounted for in equation 86. Lastly, equation 86 does not recognize the different growth regimes.

Another problem which must be considered in analysis of the growth at these temperatures is the proper T_m^o to use. As discussed in Chapter IV, two T_m^o's for the α form can be extrapolated from Hoffman-Weeks plots. These different T_m^o's are believed to be due to changes in the amount of head-to-head PVF_2 units incorporated in the crystals. Therefore, depending upon the temperature of growth, the proper T_m^o may be different. It happends that the temperatures used in this study fall right around the range where the change in the slope of the Hoffman-Weeks plots was observed. Use of the different T_m^o's did not cause the data analyzed by equation 86 to fall on one line, but at any rate this consideration should be noted.

Analysis of the initial growth rates was also performed utilizing equation 81. Following Wang and Nishi (37) plots of $\ln(G) + U^*/R(T-T_\infty)$ vs. $1/T(\Delta T)$ were made to determine K_g. (The factor f is negligible at these undercoolings.) Hoffman et al. (132) found that equation 81 fit growth rate

data from a number of polymers with U* and C approximately equal to 1500 cal/mole and 30 K respectively. Wang and Nishi (37) showed that these values fit the growth rate data in their work on PVF_2/PMMA. Therefore, these same numbers were utilized in this study. In any case, it was found that large variations of these parameters only changed the values of K_g slightly. Plots were prepared using both the high and low T_m^o's from the α crystals, and on the γ crystals as well. A typical plot for the α spherulites using the T_m^o from the high T_c data is shown in Figure 89.

According to the theory, straight lines were drawn through the data points, though in some cases the data seemed to have some curvature. Possible explanations for any curvature are: the fact that the appropriate T_m^o's might be changing in this region, the growth kinetics might be changing from one regime to the other, and errors in the data, especially in the dilute blends. To determine the regime of growth, Lauritzen's (146) criteria were applied to the slopes of these plots. Using the T_m^o's obtained from the low T_c α crystals, W had to be less than 0.04 to 0.33 nm for regime I kinetics and greater than 6 to 350 nm for regime II kinetics to be followed. The range of values for a given regime of kinetics to apply is the result of the different slopes and crystallization temperatures. Remembering that W is the width and not the thickness of the lamellae, the values obtained with regime II kinetics are within reason, but those

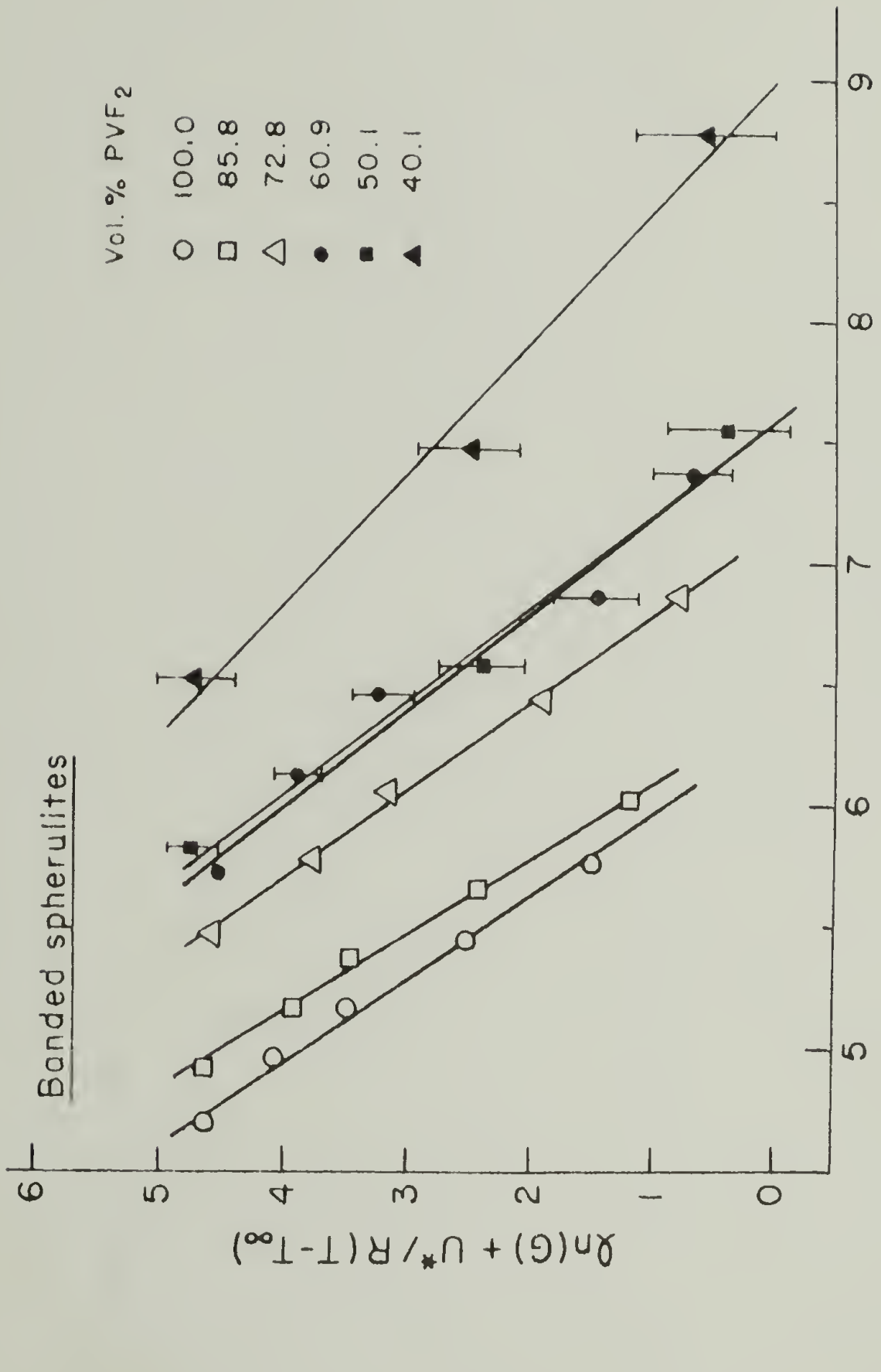

Figure 89. Plots of $\ln(G) + U^*/R(T-T_\infty)$ vs. $1/T(\Delta T)$ for the α spherulites in various blend compositions using the T_m^o's from the high T_c samples.

for regime I are not. The product $\sigma\sigma_e$ can then be determined from the slope for each blend using equation 84 with b_o = 0.445 nm (37), ΔH_u = 1425 cal/mole (31), and $\overline{\Delta h}_u$ calculated from equation 21. These are presented in Table 9. Deviations from linearity in the 50.1 and 40.1 volume % blends are a factor contributing to the large decrease in $\sigma\sigma_e$, though some of the depression is believed to be real. In comparison, the values found by Wang and Nishi (37) for samples crystallized in a lower temperature range were between 463.7 and 495.5 $(erg/cm^2)^2$ for pure PVF_2 to a 45.3 volume % blend, but dropped to 395.7 in a 40.4 volume % blend.

Lauritzen's (146) criteria were very ambiguous when applied to plots such as Figure 89 for the α spherulites using the high T_m^o's and for the γ spherulites. In the former case, the criteria required W to be less than 1.2 to 45 nm for regime I kinetics to hold, and greater than 4.8×10^3 to 6.0×10^6 nm for regime II kinetics to apply. The values determined for the γ spherulites were: W less than 0.5 to 46 nm for regime I and greater than 7.5×10^2 to 6.2×10^6 nm for regime II. Except at the extremes of the ranges, all of these requirements suggest unreasonable values for W. The data from the lower temperatures give numbers which point more towards regime II kinetics, while those from the higher temperatures lean towards regime I. Therefore, the

TABLE 9

$\sigma\sigma_e$ VALUES CALCULATED FROM INITIAL GROWTH RATES

Vol. % PVF_2	α Form Using *Low T_m^o	α Form Using +High T_m^o	+γ Form
100	316	1220	1730
85.8	334	1250	1880
72.8	329	1110	1520
60.9	274	1050	1550
50.1	182	1070	1380
40.1	118	790	1280

*Assuming regime II kinetics

+Using the average from regime I and regime II kinetics

crystallization appears to be changing from regime II to regime I kinetics as T_c is raised.

This phenomenon has also been noted in polyethylene spherulites when crystallized at low undercoolings (132). The morphology of the polyethylene spherulites underwent a change from spherulitic to axialite-like structures when the kinetics went from regime II to I. This could account for the axialite-like and platelet-like structures, discussed in Chapter III, which are observed in the PVF_2/PMMA samples at low undercoolings.

Because the kinetics appear to be undergoing a change in this temperature region, and the data for plots such as those in Figure 89 occasionally show curvature, calculations of $\sigma\sigma_e$ are very tenuous. In the case of the α spherulites using the high T_m^o's, and the γ spherulites, the calculations can be done assuming either regime I or II kinetics. Since there are not enough data points from each composition to determine where a break in the curve might occur, an average value of $c = 3$ was used in equation 84. The results for $\sigma\sigma_e$ thus calculated are included in Table 9.

The numbers obtained for the α spherulites are much higher when the high T_m^o's are used, even if one accounts for the different c's applied. In the γ spherulites, still larger values are derived. In all cases,

the magnitude of $\sigma\sigma_e$ seems to decrease as more PMMA is added. As mentioned previously, this could be related to the favorable interactions between the polymers. The range of values obtained for the α spherulites using the high T_m^o's and the γ spherulites are much larger than those obtained by Wang and Nishi (37), but similar to values obtained in polyethylene and other polymer systems (132). Differences between these results for the α form and those of Wang and Nishi's are mostly due to the use of higher T_m^o's in this study.

2. Nonlinear growth rates. The nonlinear spherulitic growth rates depicted in Figures 81 and 82 have also been observed in other systems. Barnes et al. (201) noted that the growth rates of two approaching spherulites were decreasing in polyethylene oxide. They attributed this to a local rise in temperature brought about by the latent heat of fusion generated at the two growth fronts. Coupled with the large negative temperature coefficient of growth, this would cause G to decline. Keith and Padden (190) observed nonlinear growth rates in blends of isotactic and atactic PS, but believed that the dilution effect of the atactic PS was a much more important factor than the temperature effect. Since typical thermal diffusivity constants (202) are orders of magnitude lower than mass diffusivity constants (65,202) for

polymeric materials, Keith and Padden's hypothesis certainly seems correct for blends.

The nonlinear growth rates alter the circular shapes of the two dimensional spherulites. Figure 90 shows optical micrographs of the same region in a 60.9 volume % PVF_2 blend at two different times during crystallization at 434 K. The spherulite from which the two arrows labelled f and i radiate from in Figure 90a is the same spherulite the arrow points towards in Figure 90b. At 1486 minutes, this spherulite is circular (except for the impingement on the left), but by 7126 minutes it has become oblong. The two spherulites below this one also became distorted at 7126 minutes.

The arrows labelled f and i in Figure 90a designate two perpendicular radial directions in the spherulite they emanate from. The former is the growth direction of the free surface of this spherulite, i.e., the surface growing towards a region of amorphous melt in which the immediate vicinity is free of any other spherulites. The i arrow points in the growth direction of the inhibited surface of the spherulites, i.e., a surface growing towards, but not impinged upon by, other spherulites. A plot of the spherulite's radii in these two directions vs. time is given in Figure 91. Both surfaces grow nonlinearly, but the growth rate of the

Figure 90. Optical micrographs of the same region in a 60.9 vol. % PVF_2 blend at two different times during crystallization at 434 K. a) 1486 minutes. The arrows f and i refer to the free and inhibited growth directions respectively. b) 7128 min. The arrow points to the same spherulite from which the arrows radiate in a).

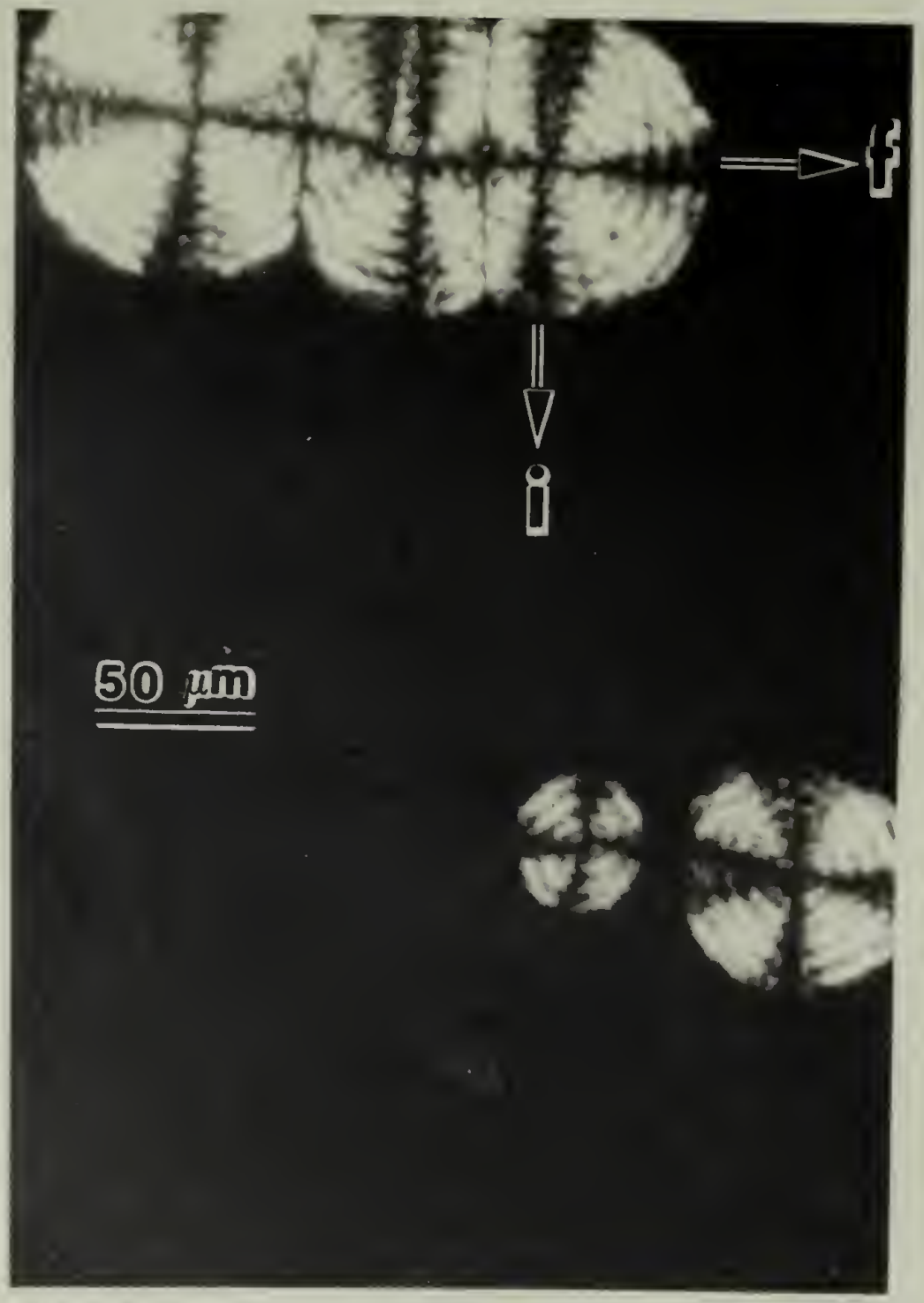

1486 min. a

b 7126 min.

Fig. 90

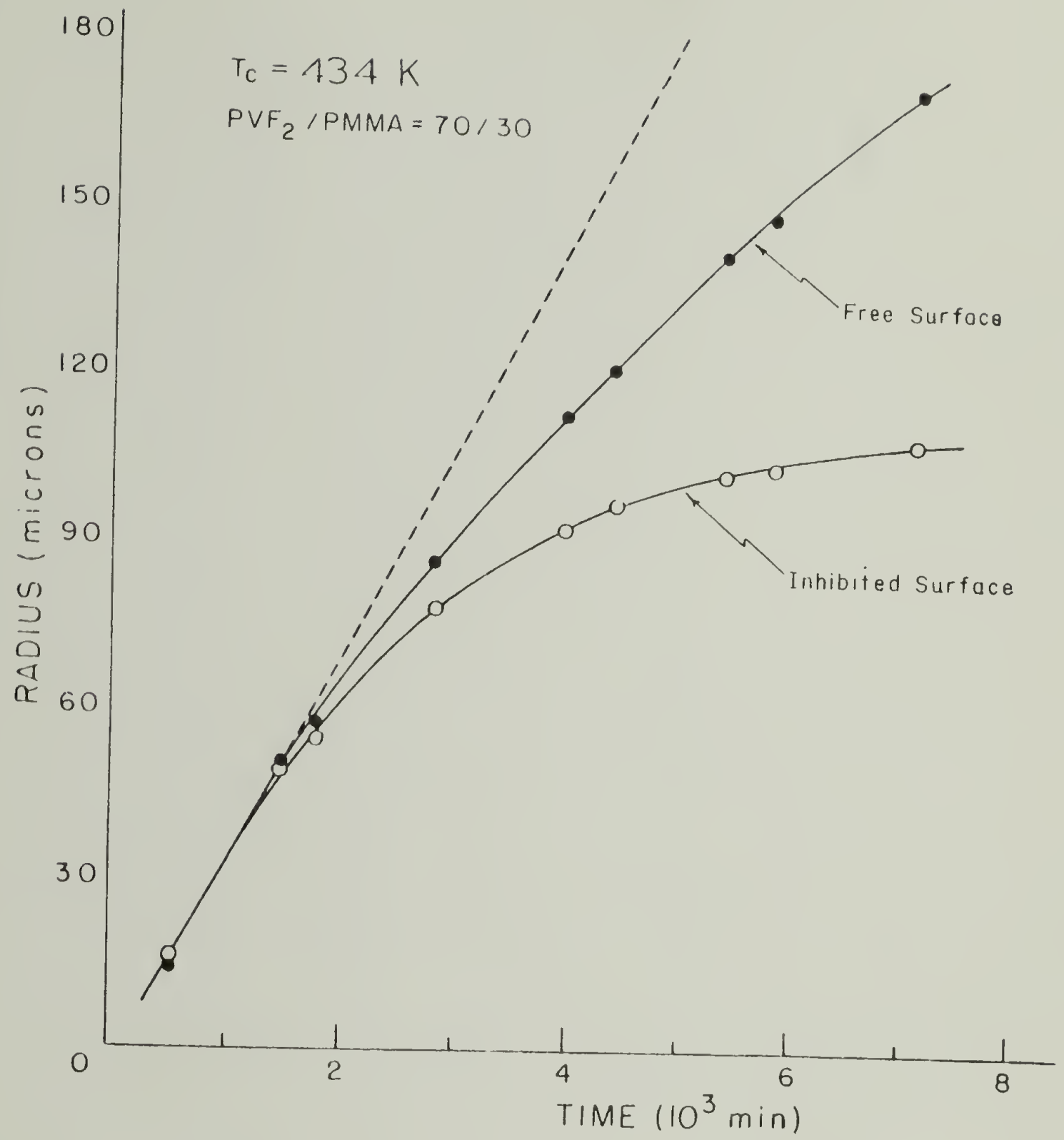

Figure 91. Plot of the radii vs. time for the spherulite in Figure 90a with two arrows emanating from it. The free and inhibited surfaces refer to the directions given by the f and i arrows (in figure 90a) respectively.

inhibited surface decreases at a much faster rate.

As mentioned above, mass diffusion is certainly more of a limiting factor than thermal diffusion in polymer blends. Thus, the growth rate of the free surface must be slowed by partial exclusion of the PMMA from the growing spherulite. This causes a concentration profile to be set up at the spherulite's surface. Proof of this profile can be seen in Figure 8 in which the tiny spherulites grown after quenching are not seen in the areas immediately surrounding the large spherulites, due to lower concentrations of PVF_2 in these regions.

The amorphous region adjacent to the inhibited surface is affected much more by this phenomenon. The amount of PMMA in this region is higher because the two spherulites growing towards each other are both rejecting some PMMA into the amorphous melt. Also, diffusion of additional PVF_2 into this area is physically limited by the positions of the spherulites. Therefore, the inhibited surface grows much slower than the free surface causing the oblong shape.

Keith and Padden (190) found that the nonlinear growth in the PS blends could be described by $R \times t^{1/2} = \text{constant}$, where R is the radius and t is time. The data in this study did not follow this relation. The analysis of Keith and Padden is actually a

simplification to this very complicated situation in which there is a moving boundary (the spherulite surface), coupled with a constantly changing boundary condition (the concentration of this surface). The growth rate is being controlled by the surface concentration of PVF_2, which is a function of the rate of diffusion of rejected PMMA away from the spherulite surface. To fully understand the nonlinear growth, one must determine how the concentration at the moving surface varies with time.

This diffusion controlled growth of a sphere is also of importance in several other physical phenomena. These include cavitation in liquids (203), aging of a precipitate in a saturated solution (204) and growth and dissolution of bubbles in solution (205-211). The analysis of this problem has taken a variety of forms which are discussed in detail in the references cited. Many of these investigations also take into account heat transfer, which should have similar solutions to the mass transfer problem. Unfortunately, these studies usually assume steady state, which gives constant boundary conditions. This is not believed to be a valid assumption in the present case.

This study will attempt to develop a model for spherically symmetric phase growth in which diffusion

effects are taken into account. The constantly changing boundary position, concentration and concentration gradient will be examined over time. From this model, one should be able to predict the growth rates of the spherulites in the blends. This model will also be adaptable to some of the other physical systems mentioned above.

The problem will be solved for an isolated sphere in an infinite liquid. This solution should represent the free surface of a spherulite. An extension of this model can then be used to solve the more complicated problem involving two or more spherulites growing towards each other. For the sake of generality, this model is solved in spherical coordinates. To actually compare the results to the data on spherulite growth, the problem has to be reformulated in cylindrical coordinates since the structures observed are actually two dimensional. The solution techniques will nonetheless be the same.

a. Model for diffusion controlled growth of a sphere. The equation of continuity is

$$\frac{\partial \rho_m}{\partial t} + \nabla \cdot (\rho_m \cdot \underline{v}) = 0 \qquad (91)$$

where ρ_m is the mass density, $\underline{v}$ is the barycentric velocity and t is time (212). In this case however a volume average frame of reference is more useful. The volume average velocity v is defined as

$$v = \sum_i \rho_{mi} \underline{v}_i \bar{V}_i \tag{92}$$

where ρ_{mi} and $\underline{v}_i$ are the mass density and the barycentric velocity of component i, and $\bar{V}_i$ is the partial specific volume of this component.

Fick's law (212) in the volume average frame of reference relates the mass flux (with respect to the volume average velocity) j_i to the gradient of mass density:

$$j_i = \rho_{mi} (\underline{v}_i - v) = -\mathcal{D} \nabla \rho_{mi} \tag{93}$$

where $\mathcal{D}$ is the diffusion coefficient. Assuming constant $\bar{V}_i$, the equation of continuity thus simplifies in this frame of reference to (209,212)

$$\nabla \cdot v = 0 \tag{94a}$$

In spherical coordinates, equation 94a can be written as

$$\frac{1}{r^2} \frac{\partial}{\partial r} (r^2 v_r) = 0 \tag{94b}$$

with v_r being the volume average velocity in the radial direction r. Upon integration, one finds

$$r^2 v_r = B_1 \tag{95a}$$

where B_1 is a constant of integration which can vary with time but is independent of r. Therefore, at the surface of the growing sphere of radius R

$$r v_r = R^2 \dot{R} \tag{95b}$$

where $\dot{R} = G$ and the liquid near the surface moves with a velocity v_r.

Assuming a two component system of a and b with no chemical reaction and a constant diffusion coefficient $\mathcal{D}$, a

mass balance on component b gives

$$\frac{\partial c_b}{\partial t} + v_r \frac{\partial c_b}{\partial r} = \mathcal{D} \left(\frac{\partial^2 c_b}{\partial r^2} + \frac{2}{r} \frac{\partial c_b}{\partial r} \right) \tag{96}$$

with c_b being the concentration of b. By substituting for v_r from equation (95), one obtains

$$\frac{\partial c_b}{\partial t} + \frac{R^2(t)}{r^2} \dot{R}(t) \frac{\partial c_b}{\partial r} = \mathcal{D} \left(\frac{\partial^2 c_b}{\partial r^2} + \frac{2}{r} \frac{\partial c_b}{\partial r} \right) \tag{97}$$

Assuming that the sphere starts with a radius R_o and that there is a uniform concentration in the liquid phase initially, the initial conditions are

$$R\ (o) = R_o \tag{98}$$

$$c_b(r,o) = c_{bo} \tag{99}$$

As r approaches infinity, the concentration is assumed to be unperturbed by the growing sphere. Therefore, one boundary condition is

$$c(\infty,t) = c_{bo} \tag{100}$$

By assuming the concentration inside the growing sphere, c_{bi}, is constant, two relations between the radial flux of b at the sphere surface, N_{bR}, and the concentration of b at the sphere surface, $c_b(R)$, can be established.

$$N_{bR} = \dot{R}\ (c_b(R) - c_{bi}) \tag{101}$$

$$N_{bR} = c_b(R)v_r - \mathcal{D}\left.\frac{\partial c_b}{\partial r}\right|_{r=R} \tag{102}$$

Combination of equations 101 and 102 and using equation 95 for v_r gives the boundary condition at the sphere surface.

$$\text{at } r = R(t) \qquad \dot{R}c_{bi} = \mathcal{D}\left.\frac{\partial c_b}{\partial r}\right|_R \tag{103}$$

The last item necessary is an equation describing the motion of the sphere surface. This equation should relate $\dot{R}$ to c_b. Ideally, one can use one of the equations for G presented in the first section, in which all of the variables are assumed to be functions of c_b. In this model, $\dot{R}$ will be given by a generalized function of c_b.

$$\dot{R} = f(c_b) \tag{104}$$

where the function $f(c_b)$ can be introduced at some later point.

The problem as it is presently posed can be simplified somewhat by converting it into a dimensionless format in which the spacial frame of reference moves with R. This can be accomplished with the following change of variables (213):

$$\xi = \frac{R(t)}{r} \tag{105}$$

$$y = \frac{c_b - c_{bo}}{c_{bi} - c_{bo}} \tag{106}$$

$$\tau = \int_0^t \frac{D}{R^2(t)}\, dt \tag{107}$$

$$\phi = \frac{R(t)}{R_o} \tag{108}$$

Equations 97 and 103 are then restated as:

$$\frac{\partial y}{\partial \tau} = \xi^4 \frac{\partial^2 y}{\partial \xi^2} + (\xi^4 - \xi) \frac{R\dot{R}}{D} \frac{\partial y}{\partial \xi} \tag{109}$$

and

$$\text{at } \xi = 1, \quad \left.\frac{\partial y}{\partial \xi}\right|_{\xi=1} = -K_2 \frac{R\dot{R}}{D} \tag{110}$$

where $K_2 = c_{bi}/(c_{bi} - c_{bo})$

After using equation 110 to replace $\frac{R\dot{R}}{D}$ in equation 109, equation 110 can then be expressed in terms of the new variables by realizing that

$$\dot{R} = R_o\dot{\phi} = R_o \frac{d\phi}{d\tau} \frac{\mathcal{D}}{(R_o\phi)^2} \tag{111}$$

The problem therefore becomes solving

$$\frac{\partial y}{\partial \tau} = \xi^4 \frac{\partial^2 y}{\partial \xi^2} - \frac{1}{K_2} (\xi^4 - \xi) \left(\left.\frac{\partial y}{\partial \xi}\right|_{\xi=1} \right) \frac{\partial y}{\partial \xi} \tag{112}$$

$$\frac{\partial \phi}{\partial \tau} = \frac{R_o\phi^2}{\mathcal{D}} f'(y_b) \tag{113}$$

subject to the boundary conditions

$$\xi \to 0, \; y \to 0 \tag{114}$$

$$\left.\frac{\partial y}{\partial \xi}\right|_{\xi=1} = \frac{-K_2}{\phi} \frac{d\phi}{d\tau} \tag{115}$$

and the initial conditions

$$\text{at } \tau = 0, \; \phi = 1, \text{ and } y = 0 \tag{116}$$

where $f'(y_b)$ in equation 113 is just $f(c_b)$ transformed to the new variables through the use of equations 105-108.

Equations 112 to 116 can be solved using numerical techniques. With the help of R. L. Laurence, F. Baginski, and L. Berthiaume (213), a procedure for solving these equations using orthogonal collocation with Lagrange interpolating polynomials (214) was developed and a preliminary computer program designed. The actual solution procedure is presented in the appendix.

Due to the complexity of the problem and the computer program, comparison between experimental growth rates and those predicted by the model have not been made as yet. Nonetheless, this model is a first step in understanding the complicated problem of diffusion-controlled spherulitic growth.

C. Conclusions

The initial growth rates, G, of both the banded α

form spherulites as well as the non-banded γ form spherulites decreased as crystallization temperatures were raised from 424 to 434 K, and as more PMMA was added to the blends. For a given sample, the non-banded spherulites always grew slower than the banded ones though the rates became closer as T_c was raised and v_2 decreased. The change in growth rates could not be fully accounted for by compositional changes in T_m^o and T_g.

Quantitative analysis of G using two variations of the Turnbull-Fisher (192) equation were only partially successful. Unlike the PCL/PVC system, the data for the PVF_2/PMMA blends would not fall on a straight line when the form of the equation explicitly accounting for v_2 was used. The more general form of the Turnbull-Fisher equation gave values of σo_e for the α form which were slightly lower than those found by Wang and Nishi (37) when the lower T_m^o's were used but higher when the upper T_m^o's were used. A problem exists in determining the right T_m^o to use for the α spherulites since the change in slope of the Hoffman-Weeks plots occurs within the temperature range studied. The γ form spherulites had higher $\sigma\sigma_e$ values than the α form, though both showed a decrease as the blends became richer in PMMA.

At long times, the growth rates in the blends became nonlinear. The decrease in G with time was more apparent at higher T_c's. These nonlinearities are caused by partial exclusion of PMMA from the spherulites. A general model for

diffusion controlled spherulitic growth has been developed. Though still in its preliminary stages, with additional refinements, it can be used to model the nonlinear spherulitic growth rates as well as other physical systems where there is diffusion controlled growth of a sphere.

C H A P T E R V I I

CONCLUDING REMARKS

The crystalline morphology of PVF_2 grown from the pure melt or from compatible blends with PMMA becomes very complex at low undercoolings. Crystal forms, melting points and large scale structures vary with both temperature and composition. In addition to this, the amount of head-to-head PVF_2 linkages also appears to be an important parameter to consider. By measuring the depression of the equilibrium melting points in the blend, the interaction parameter was shown to be a function of the composition as well.

There are three possible locations for the PMMA in the semicrystalline blend. It can be interlamellar, interfibrillar or excluded from the spherulites and axialite-like structures. Evidence for the existence of PMMA in all three of these regions has been presented. At crystallization temperatures of 418 K, SAXS studies have shown almost all of the PMMA to be in the interlamellar regions. Microscopy studies at temperatures approximately 10 K higher suggest that some of the PMMA is in the interfibrillar regions. Non-linear growth rates of the spherulites, which become readily apparent at slightly higher temperatures still, are due to the partial exclusion of the PMMA

from the growing spherulites. However, preliminary SAXS studies at these higher temperatures imply that most of the PMMA still resides in the interlamellar regions. Therefore, it appears that the location of the PMMA is a function of crystallization temperature, though the largest amount seems to remain between the individual lamellae.

Comparing this to the PVC/PCL and isotactic PS/atactic PS systems suggests that the location of the non-crystalline polymer in a semi-crystalline blend is also a function of the compatability. In addition to this, the molecular weight of the polymer will affect its mobility and therefore its location as well. Thus by varying temperature compatibility and molecular weight in a variety of semi-crystalline blends, one should be able to control the location of the non-crystalline component.

A. Suggestions for Future Work

At high temperatures, the PVF_2 in both the homopolymer and the blends undergoes an α to γ' phase transition. This process is not well understood. A detailed study of the kinetics of this transformation as a function of both composition and temperature might lend some insight into the mechanics of this transition.

There are other morphological features which should be studied in greater depth. Spherulites with a front of increased birefringence which follows the growth front were

noted in some of the blends (Figure 13). This phenomenon occurs only over a limited composition and temperature range and at present cannot be explained. The appearance of the 0.358 nm reflection in some of the α and γ' diffraction patterns cannot be indexed to any of the crystal structures currently proposed for PVF_2. This could imply that the proposed structures need reworking or that there exists yet another form of PVF_2. Many questions also remain regarding the phenomenon of lamellar twisting, which gives rise to the banded spherulites. Additional studies on blends of PVF_2 with other polymers as well as different systems forming banded spherulites can be performed. The results of these, coupled with the results presented in Chapter III may render a better understanding of this behavior.

Equilibrium melting points have been obtained by extrapolation of T_m vs. T_c plots. Another method of determining T_m^o is through a plot of T_m vs. (lamellar thickness)$^{-1}$ as suggested by equation 5. The lamellar thicknesses can be measured from shadowed, fracture surface replicas in the electron microscope. A series of samples crystallized at different temperatures should be examined. Measurement of lamellar thicknesses from the different types of spherulites will give T_m^o's for the α and γ forms which can be compared to those obtained from T_m vs. T_c plots. It would also be of interest to determine if breaks in the α

data occur, but since one would not be able to tell if the α spherulites had already undergone the transition to γ', a break in the α data can be either due to this transition or to the break seen in the T_m vs. T_c plots.

Hypotheses have been proposed for the discrepancies between crystallinities measured from DSC and those derived from SAXS data. The validity of these hypotheses can be evaluated by comparing crystallinities measured from other techniques, such as WAXS and infra-red spectroscopy. The latter utilizes the areas under the crystalline and amorphous absorbance bands. This can be particularly useful in samples containing multiple crystal forms since the different phases absorb at different frequencies.

The full analysis of SAXS from samples crystallized at high temperatures should be performed. Comparison of the results with other experiments on samples crystallized at high temperatures as well as the SAXS results on the samples crystallized at 418 K should help in understanding the relative effect temperature has on the location of the PMMA. It is possible that at high enough temperatures, the majority of the PMMA will be excluded from the interlamellar regions. It would also be of interest to apply Ruland's interface distribution approach (161) in the analysis of both sets of SAXS data and compare the results to those from the Hosemann (160) and Vonk (159) models.

Two recently developed techniques which can also be

used to determine the location of the PMMA in these blends are fluorescence polarization and electron energy loss spectroscopy (EELS). The former technique involves tagging the PMMA molecule with a group that will fluoresce when excited, such as anthracene. Blends containing these tagged PMMA molecules can then be viewed under the microscope and measurement of the relative intensities of fluorescence can be made as a function of position. The relative intensities will be proportional to relative concentrations of PMMA. Comparison of the concentration within lamellar bundles, from the interfibrillar regions and outside the spherulite can be made.

The EELS technique, performed on a STEM, measures the energy loss of an electron beam passed through the sample. This method is much more sensitive to lighter elements than energy dispersive x-ray spectroscopy, often used in electron microscopy, and can therefore be used to measure relative concentrations of fluorine and possibly oxygen. As with the fluorescence polarization experiments, these can be performed as a function of position within and outside of the spherulites. However, there are two major obstacles to overcome before obtaining acceptable data from EELS. The samples must be extremely thin to get good signal to noise ratios, and care must be taken to avoid radiation damage which may alter concentrations.

As was noted, the location of the noncrystallizable

component in semi-crystalline blends appears to be affected by temperature and compatability, and should also be related to molecular weight. A systematic study of different blend systems in which these parameters are varied should be performed. This would enable the development of a unified theory concerning the location of the components in a semi-crystalline blend as a function of these parameters.

A generalized model has been developed for diffusion controlled growth of a sphere. This model is a sound foundation, but needs refinements before it can be used. Once this is done, comparison of the predictions from the model to the actual data on nonlinear spherulitic growth as well as to data involving some of the other applications mentioned should be made. This would give a better understanding of these very complicated processes.

The present work has taken an in-depth look at the structure and morphology of the PVF_2/PMMA blends. Eventually, information regarding this structure and morphology should be related to the properties of these blends. The wide variety of properties which could be evaluated should certainly include the interesting electrical phenomena noted in pure PVF_2. A good understanding of these structure-property correlations is necessary to develop further applications of these materials.

REFERENCES

1. Pennwalt Corp., product literature on Kynar PVF_2 (1977).

2. M. Tamura, K. Ogasawara and T. Yoshimi, Ferroelectrics, 10, 125 (1976).

3. G.R. Crane and A.A. Comparini, Soc. Plast. Eng. Tech. Pap. 23, 380 (1977).

4. A.L. Robinson, Science 200, 1371 (1978).

5. H. Kawai, Japan, J. Appl. Phys. 8, 975 (1969).

6. J.G. Bergman, Jr., J.H. McFee, and G.R. Crane, Appl. Phys. Lett. 18, 203 (1971).

7. N. Murayama, J. Polym. Sci.: Polym. Phys. Ed. 13, 929 (1975).

8. S. Edelman, Nat. Bur. Std. (U.S.), Interagency Report, NBSIR 75-760, 210 (1975).

9. Ye. L. Gal'perin, Yu. V. Strogalin and M.P. Mlenik, Vysokomol. Soyed. 7, 933 (1965).

10. J.B. Lando, H.G. Olf and A. Peterlin, J. Polym. Sci. A-1, 4, 941 (1966).

11. W.W. Doll and J.B. Lando, J. Macromol. Sci.-Phys. B2(2), 219 (1968).

12. K. Sakaoku and A. Peterlin, J. Macromol. Sci.-Phys. B1(2), 401 (1967).

13. J.B. Lando and W.W. Doll, J. Macromol. Sci.-Phys. B2(2), 205 (1968).

14. W.W. Doll and J.B. Lando, J. Macromol. Sci.-Phys. B4(2), 309 (1970).

15. R. Hasegawa, Y. Takahashi, Y. Chatani and H. Tadokoro, Polym. J. 3(5), 600 (1972).

16. R. Hasegawa, M. Kobayashi and H. Tadokoro, Polym. J. 3(5), 591 (1972).

17. G.M. Bartenev, A.A. Remizova, I.V. Kuleshov, M.A. Martynov and T.N. Sarminskaya, Vysokolm. Soyed. 9, 2063 (1975).

18. R.L. Miller and J. Raisoni, J. Polym. Sci.-Polym. Phys. Ed. 14, 2325 (1976).

19. Y. Takahashi, M. Kohyama, H. Tadokoro, Macromol. 9(5), 870 (1976).

20. S.K. Tripathy, R. Potenzone, Jr., A.J. Hopfinger, N.C. Banik and P.L. Taylor, Macromol. 12(4), 656 (1979).

21. S. Weinhold, M.H. Litt and J.B. Lando, J. Polym. Sci.-Polym. Letters Ed. 17, 585 (1979).

22. A.J. Lovinger and H.D. Keith, Macromol. 12, 919 (1979).

23. A.J. Lovinger, J. Polym. Sci., Polym. Phys. Ed. 18, 793 (1980).

24. W.M. Prest, Jr., and D.J. Luca, J. Appl. Phys. 46, 4136 (1975).

25. W.M. Prest, Jr., and D.J. Luca, J. Appl. Phys. 49, 5042 (1978).

26. G. Gianotti, A. Capizzi and V. Zamboni, Chem. e Indust. 55, 501 (1973).

27. M. Bachmann, W.L. Gordon, S. Weinhold and J.B. Lando, to be published.

28. G.T. Davis, J.E. McKinney, M.G. Broadhurst, and S.C. Roth, J. Appl. Phys. 49, 4998 (1978).

29. G.R. Davies and H. Singh, Polymer 20, 772 (1979).

30. D. Naegele, D.Y. Yoon, and M.G. Broadhurst, Macromol. 11, 1297 (1978).

31. G.J. Welch and R.L. Miller, J. Polym. Sci., Polym. Phys. Ed. 14, 1683 (1976).

32. K. Nakagawa and Y. Ishida, J. Polym. Sci., Polym. Phys. Ed. 11, 2153 (1973).

33. S. Osaki and Y. Ishida, J. Polym. Sci., Polym. Phys. Ed. 13, 1071 (1975).

34. T. Nishi and T.T. Wang, Macromol. 8, 909 (1975).

35. J.D. Hoffman and J.J. Weeks, J. Res. Nat. Bur. Stand. U.S.A. 66, 13 (1962).

36. C. Mancarella and E. Martuscelli, Polymer 18, 1240 (1977).

37. T.T. Wang and T. Nishi, Macromol. 10, 421 (1977).

38. A. Sharples, Introduction to Polymer Crystallization, Arnold, London (1966).

39. J.S. Noland, N.N.-C. Hsu, R. Saxon and J.M. Schmitt, Adv. Chem. Ser. 99, 15 (1971).

40. D.R. Paul and J.O. Altamirano, Polym. Preprints, Am. Chem. Soc., Div. Polym. Chem. 15, 409 (1974).

41. D.J. Hourston and I.D. Hughes, Polymer 18, 1175 (1977).

42. E. Roerdink and G. Challa, Polymer 19, 173 (1978).

43. G.D. Patterson, T. Nishi and T.T. Wang, Macromol. 9, 603 (1976).

44. D.C. Douglass and V.J. McBrierty, Macromol. 11, 766 (1978).

45. R.L. Imken, D.R. Paul and J.W. Barlow, Poly. Eng. Sci. 16(9), 593 (1976).

46. T.K. Kwei, G.D. Patterson, and T.T. Wang, Macromol. 9, 780 (1976).

47. D.C. Wahrmund, R.E. Bernstein, J.W. Barlow and D.R. Paul, Poly. Eng. Sci. 18(9), 677 (1978).

48. R.E. Bernstein, D.R. Paul and J.W. Barlow, Poly. Eng. Sci. 18(9), 683 (1978).

49. R.E. Bernstein, D.C. Wahrmund, J.W. Barlow and D.R. Paul, Poly. Eng. Sci. 18(16), 1220 (1978).

50. T.K. Kwei, H.L. Frisch, W. Radigan and S. Vogel, Macromol. 10(1), 157 (1977).

51. S. Krause, J. Macromol. Sci., Rev. Macromol. Chem. C7, 251 (1972).

52. J. Manson and L. Sperling, Polymer Blends and Composites, Plenum Press, N.Y., N.Y. (1976).

53. N.A.J. Platzer, Ed., Multicomponent Polymer Systems (Adv. Chem. Series No. 99), Am. Chem. Soc., Washington, D.C. (1971).

54. N.A.J. Platzer, Ed., Copolymers, Polyblends and Composites (Adv. Chem. Series No. 142), Am. Chem. Soc., Washington, D.C. (1975).

55. P.F. Bruins, Ed., Polyblends and Composites (J. Appl. Polym. Sci., Appl. Polym. Symp. No. 15), Interscience, N.Y., N.Y. (1970).

56. D.R. Paul and S. Newman, Eds., Polymer Blends (Volumes I and II), Academic Press Inc., N.Y., N.Y. (1978).

57. O. Olabisi, L.M. Robeson and M.T. Shaw, Polymer-Polymer Miscibility, Academic Press, N.Y. (1979).

58. S.L. Rosen, Polym. Eng. Sci. 7, 115 (1967).

59. T.G. Fox, Bull. Am. Chem. Soc. 2, 123 (1956).

60. E.J. Perry, J. Appl. Polym. Sci. 8, 2605 (1964).

61. L.J. Hughes and G.L. Brown, J. Appl. Polym. Sci. 5, 580 (1961).

62. E. Fischer, J. Macromol. Sci. Chem. A2, 1285 (1968).

63. G.L. Wilkes and R.S. Stein, J. Polym. Sci. A2, 7, 1525 (1969).

64. S.D. Hong, M. Shen, T.P. Russell, and R.S. Stein, in Polymer Alloys, ed. D. Klempner and K.C. Frisch, Plenum Press, N.Y., N.Y. (1978).

65. P. Gilmore, Ph.D. Dissertation, Polymer Science and Engineering, University of Massachusetts, Amherst, MA (1978).

66. J.J. Hickman and R.M. Ikeda, J. Polym. Sci., Phys. Ed. 11, 1713 (1973).

67. B.H. Zimm, J. Chem. Phys. 16, 1093, 1099 (1948).

68. O. Kratky, G. Porod, and L. Kahovec, Z. Electrochem. 55, 53 (1951).

69. O. Kratky, Z. Physikalische Chem. 9, 237 (1955).

70. O. Kratky, Prog. Biophys. 13, 105 (1963).

71. W. Krigbaum and R. Godwin, J. Chem. Phys. 43, 4523 (1965).

72. H. Hayashi, F. Hamada and A. Nakajima, Macromol. 7, 959 (1974); 9, 543 (1976), Polymer 18, 638 (1977).

73. T. Russell, Ph.D. Dissertation, Polymer Science and Engineering, University of Massachusetts, Amherst, MA (1979).

74. J. Cotton, D. Decker, H. Benoit, B. Farnoux, J. Higgins, G. Jannenk, R. Ober, C. Picot and J. Des Cloizeaux, Macromol. 7, 863 (1974); Annals des Physique 1, 112 (1976).

75. J. Shelten, D. Ballard, G. Wignall, G. Longman, and W. Schmatz, Polymer 17, 751 (1976).

76. D. Ballard, J. Schelten, and G. Longman, Polym. Preprints 18(2), 167 (1977).

77. R. Kirste, W. Kruse and K. Ibel, Polymer 15, 120 (1975).

78. J. Shelten and R.W. Hendricks, J. Appl. Cryst. 11, 297 (1978).

79. J.S. Higgins and R.S. Stein, J. Appl. Cryst. 11, 346 (1978).

80. R.G. Kirst and B.R. Lehnen, Makromol. Chemie 177, 1137 (1976).

81. W.A. Kruse, R.G. Kirst, J. Haas, B.J. Schmitt and D.J. Stein, Mackromol. Chemie 177, 1145 (1976).

82. M.M. Coleman, J. Zarian, D.F. Varnell, and P.C. Painter, J. Polym. Sci.: Polym. Let. Ed. 15, 745 (1977).

83. M.M. Coleman and P.C. Painter, J. Macromol. Sci.-Rev. Macromol. Chem. C16(2), 197 (1978).

84. P.J. Flory, Principles of Polymer Chemistry, Cornell University Press, Ithaca, N.Y. (1953).

85. P.J. Flory, J. Chem. Phys. 9, 660 (1941); 10, 51 (1942).

86. R.L. Scott, J. Chem. Phys. 17, 279 (1949).

87. C.H.M. Jaques and H.B. Hopfenberg, Polym. Eng. Sci. 14, 441, 449 (1974).

88. A.A. Tager, Poly. Sci. U.S.S.R. 14, 3129 (1972).

89. A.A. Tager, T.I. Scholokhovich and J.S. Bessonov, European Polym. J. 11, 321 (1974).

90. T.K. Kwei, T. Nishi and R.F. Roberts, Macromol. 7, 667 (1974).

91. O. Olabisi, Macromol. 8, 316 (1975).

92. J.E. Guillet, J. Macromol. Sci., Chem. 4, 1669 (1970).

93. J.E. Guillet, in Progress in Gas Chromatography, J.H. Purnell, Ed., Wiley-Interscience, N.Y., N.Y. (1973).

94. J.H. Wendorff, J. Polym. Sci., Polym. Letters Ed. 18, 439 (1980).

95. D.R. Paul, J.W. Barlow, R.E. Bernstein and D.C. Wahrmund, Polym. Eng. Sci. 18, 1225 (1978).

96. H. Lee, R.E. Salomon and M.M. Labes, Macromol. 11, 171 (1978).

97. T.T. Wang and T. Nishi, Macromol. 10, 421 (1977).

98. A.J. Lovinger and T.T. Wang, Polymer 20, 725 (1979).

99. J.B. Lando, private communication.

100. A. Keller, J. Polym. Sci. 17, 291 (1955); 39, 151 (1959).

101. F.P. Price, J. Polym. Sci. 38, 71 (1959); 39, 139 (1959).

102. H.D. Keith and F.J. Padden, Jr., J. Polym. Sci. 39, 101, 123 (1959); 51, S4 (1961).

103. J.D. Hoffman and J.I. Lauritzen, Jr., J. Res. Nat. Bur. Stds. 65A, 297 (1961).

104. A. Keller and S. Sawada, Makromol. Chem. 74, 190 (1964).

105. J.R. Burns, J. Polym. Sci. A-2, 7, 593 (1969).

106. J.E. Breedon, J.F. Jackson, M.J. Marcinkowski and M.E. Taylor, Jr., J. Nat. Sci. 8, 143, 1071 (1973).

107. G. Kanig, Kolloid Z. 251, 782 (1973).

108. A. Low, P. Allan, D. Vesely and M. Bevis, Inst. Phys. Conf. Ser. No. 36, 395 (1977).

109. D.C. Bassett and A.M. Hodge, Polymer 19, 469 (1978).

110. Naono, J. Sci. Hiroshima Univ. A23, 653 (1960).

111. P.H. Lindenmeyer and V.F. Holland, J. Appl. Phys. 35, 55 (1964).

112. F.B. Khambatta, F. Warner, T. Russell and R.S. Stein, J. Polym. Sci., Polym. Phys. Ed. 14, 1391 (1976).

113. W.L. Bragg, Proc. Cambridge Phil. Soc. 17, 43 (1913).

114. J.D. Hoffman and J.J. Weeks, J. Res. Nat. Bur. Std., U.S.A. 66, 13 (1962).

115. R.S. Stein and M.B. Rhodes, J. Appl. Phys. 31, 1873 (1960).

116. S. Clough, J.J. van Aartsen, and R.S. Stein, J. Appl. Phys. 36, 3072 (1965).

117. R.E. Prud'homme and R.S. Stein, J. Polym. Sci., Polym. Phys. Ed. 11, 1357, 1633 (1973).

118. D.Y. Yoon and R.S. Stein, ibid., 12, 735, 763 (1974).

119. R.J. Samuels, J. Polym. Sci. A2, 9, 2165 (1971).

120. J. Borch and R.H. Marchessault, J. Polym. Sci. C, 28, 153 (1969).

121. J.C.W. Chien and E.P. Chang, Macromol. 5, 610 (1972).

122. Y. Murakami, N. Hayashi, T. Hashimoto and H. Kawai, Polym. J. 4, 452, 560 (1973).

123. G.L. Wilkes, Mol. Cryst. Liq. Cryst. 18, 165 (1972).

124. T. Hashimoto, Y. Murakami, N. Hayashi, and H. Kawai, Polym. J. 6, 132 (1974).

125. T. Hashimoto, K. Yamaguchi, H. Kawai, Polym. J. 9, 405 (1977).

126. T. Hashimoto, Y. Murakami, Y. Okamori, and H. Kawai, Polym. J. 6, 554 (1974).

127. R.S. Stein and W. Chu, J. Polym. Sci. A-2, 8, 1137 (1970).

128. M.B. Rhodes and R.S. Stein, J. Polym. Sci. A-2, 7, 1539 (1969).

129. T. Hashimoto, K. Nagatoshi, A. Todo, and H. Kawai, Polymer 7, 1075 (1976).

130. M. Matsuo, F. Ozaki, H. Kurita, S. Sugawara, and T. Ogita, submitted to Macromol.

131. T. Hashimoto, private communication.

132. J.D. Hoffman, G.T. Davies and J.I. Lauritzen, Jr., in Treatise on Solid State Chemistry, Vol. 3, N.B. Hannay, Ed., Chapt. 7, Plenum Press (1976).

133. J.J. Weeks, J. Res. Nat. Bureau Std., U.S.A. 67A, 441 (1963).

134. A. Peterlin, J. Polym. Sci. B1, 279 (1963).

135. S. Yano, J. Polym. Sci. A-2, 8, 1057 (1970).

136. G. Welch, Polymer 15, 429 (1974).

137. G. Kortleve, C.A.F. Tuijnman, and C.G. Vonk, J. Polym. Sci. A-2, 10, 123 (1972).

138. M. Dröscher, K. Herturg, H. Reimann and G. Wegner, Makromol. Chem. 177, 1695 (1976).

139. V. Kalepky, E.W. Fischer, P. Herchenröder, J. Schelten, G. Lieser, and G. Wegner, J. Polym. Sci.: Polym. Phys. Ed. 17, 2117 (1979).

140. E.W. Fischer, J.H. Sterzel, G. Wegner, Kolloid-Z.u.Z. Polymere 251, 980 (1973).

141. P.J. Flory, Principles of Polymer Chemistry, Cornell University Press, Ithaca, N.Y. (1953).

142. I.C. Sanchez and R.K. Eby, J. Res. Nat. Bur. Std. 77A, 353 (1973).

143. I.C. Sanchez and R.K. Eby, Macromol. 8, 638 (1975).

144. E. Helfand and J.I. Lauritzen, Jr., Macromol. 6, 631 (1973).

145. W.M. Prest, private communication.

146. J.I. Lauritzen, Jr., J. Appl. Phys. 44, 4353 (1973).

147. J.D. Hoffman, private communication.

148. I.C. Sanchez and E.A. DiMarzio, Macromol. 4, 677 (1971).

149. R.M. Joshi, Encyclopedia of Polymer Science and Technology, Vol. 13, Interscience Press, New York (1970).

150. See for example: R. Konigsveld, L.A. Kleintjens and H.M. Schoffeleers, Pure Appl. Chem. 39, (1-B), 1 (1974); and E.F. Casassa, J. Polym. Sci.: Symp. #54, 53 (1976).

151. P.J. Flory, Discuss. Faraday Soc. 49, 7 (1970).

152. R.S. Stein and R.L. Rowell, Eds., Electromagnetic Scattering, Gordon and Breach Pub. Co., N.Y., N.Y. (1978).

153. A. Guinier, Ann. Phys. (Paris) 12, 161 (1939).

154. P. Debye, J. Phys. Chem. 51, 18 (1947).

155. A. Guinier and G. Fournet, Small-Angle Scattering of X-rays, John Wiley and Sons, N.Y., N.Y. (1955).

156. G. Porod, Kolloid. Z. 124, 83 (1951); 125, 51 (1952); 125, 108 (1952).

157. P. Debye and A.M. Bueche, J. Appl. Phys. 20, 518 (1949).

158. D. Buchanan, J. Polym. Sci. A-2, 9, 645 (1971).

159. K. Vonk and G. Korleve, Kolloid Z. Z. Polym. 220, 19 (1967); 224, 225 (1968).

160. R. Hosemann and S.N. Bagchi, Direct Analysis of Diffraction by Matter, N. Holland Pub. Co., Amsterdam (1951).

161. W. Ruland, Colloid and Polym. Sci. 5, 29 (1977).

162. B. Crist, J. Polym. Sci., Phys. Ed. 11, 635 (1973).

163. B. Crist and N. Morosoff, J. Polym. Sci., Phys. Ed. 11, 1023 (1973).

164. S.K. Baczek, Ph.D. Dissertation, Polymer Science, University of Massachusetts, Amherst, MA (1977).

165. J.T. Koberstein, Ph.D. Dissertation, Chemical Engineering, University of Massachusetts, Amherst, MA (1979).

166. F.P. Warner, R.S. Stein and W.J. MacKnight, J. Polym. Sci., Phys. Ed. 15, 12 (1977).

167. P. Debye, H.R. Anderson and H. Brumberger, J. Appl. Phys. 28, 679 (1957).

168. R.W. Hendricks, private communication.

169. L.E. Alexander, X-Ray Diffraction Methods in Polymer Science, Wiley-Interscience, N.Y., N.Y. (1969).

170. F.P. Warner, Ph.D. Dissertation, Loughborough University (1975).

171. W. Wenig, F.E. Karasz, and W.J. MacKnight, J. Appl. Phys. 46, 4194 (1975).

172. C.G. Vonk, J. Appl. Cryst. 9, 433 (1976).

173. J.T. Koberstein, B. Morra and R.S. Stein, J. Appl. Cryst. 13, 34 (1980).

174. C. Vonk, J. Appl. Cryst. 6, 81 (1973).

175. W. Ruland, J. Appl. Cryst. 4, 70 (1971).

176. T. Hashimoto, A. Todo, H. Itoi and H. Kawai, Macromol. 10, 377 (1977).

177. W. Wiegand and W. Ruland, Prog. Colloid. Polym. Sci. 66, 355 (1979).

178. W. Ruland, Colloid. Polym. Sci. 255, 417 (1977).

179. R. Bonart and E.H. Müller, J. Macromol. Sci. Phys. B10, 177 (1974).

180. A. Todo, T. Hashimoto, and H. Kawai, J. Appl. Cryst. 11, 558 (1978).

181. R.W. Hendricks, J. Appl. Cryst. 5, 315 (1972).

182. O. Kratky, Makromol. Chem. 35A, 12 (1960).

183. I. Pilz, J. Colloid Interface Sci. 30, 140 (1969).

184. C.G. Vonk, J. Appl. Cryst. 8, 340 (1975).

185. O. Kratky, G. Porod, and Z. Skola, Acta Phys. Austriaca. 13, 76 (1960).

186. J.H. Wendorff and E.W. Fischer, Kolloid Z.Z. Polym. 251, 876 (1973).

187. V. Gerold, J. Appl. Cryst. 11, 376 (1978).

188. C.G. Vonk, J. Appl. Cryst. 4, 340 (1971).

189. M. Wai, unpublished results.

190. H.D. Keith and F.J. Padden, Jr., J. Appl. Phys. 34, 2409 (1963); 35, 1270, 1286 (1964).

191. J.I. Lauritzen, Jr. and J.D. Hoffman, J. Appl. Phys. 44, 4340 (1973).

192. D. Turnbull and J.C. Fisher, J. Chem. Phys. 17, 71 (1949).

193. M.L. Williams, R.F. Landel, and J.D. Ferry, J. Am. Chem. Soc. 77, 3701 (1955).

194. L. Mandelkern, J. Appl. Phys. 26, 443 (1955).

195. L. Mandelkern, Crystallization of Polymers, McGraw-Hill, N.Y. (1964).

196. J. Boon and J.M. Azcue, J. Polym. Sci. A-2, 6, 885, (1968).

197. C.J. Ong and F.P. Price, J. Polym. Sci., Polym. Symp. 63, 59 (1978).

198. D.G. Thomas and L.A.K. Staveley, J. Chem. Soc. 4564 (1952).

199. J.D. Hoffman, SPE Trans. 4, 315 (1964).

200. P.J. Flory, J. Chem. Phys. 17, 223 (1949).

201. W.J. Barnes, W.G. Leutzel and F.P. Price, J. Phys. Chem. 65, 1742 (1961).

202. S. Middleman, Fundamentals of Polymer Processing, McGraw-Hill, Inc., U.S.A. (1977).

203. R. Davies, Cavitation in Real Liquids, Elsevier Pub. Co. Inc., Amsterdam (1964).

204. C.Z. Wagner, Elektrochem. 65, 581 (1961).

205. F.C. Frank, Proc. Roy. Soc. A201, 586 (1950).

206. P.S. Epstein and M.S. Plesset, J. Chem. Phys. 18, 1505 (1950).

207. L.E. Scriven, Chem. Eng. Sci. 10, 1 (1959).

208. M. Cable and D.J. Evan, J. Appl. Phys. 38, 7 (1967).

209. J.L. Duda and J.S. Vrentas, AIChE J. 15, 351 (1969).

210. K.H. Mild, Bul. Math. Biophys. 33, 19 (1971).

211. J. Rudolph, J. Polym. Sci., Polym. Phys. Ed. 17, 1709 (1979).

212. R.B. Bird, W.E. Stewart, E.N. Lightfoot, Transport Phenomena, John Wiley & Sons, Inc., U.S.A. (1960).

213. R.L. Laurence, F. Baginski and L. Berthiaume, private communication.

214. J. Villadsen and M.L. Michelsen, Solution of Differential Equation Models by Polynomial Approximation, Prentice-Hall, Inc., Englewood Cliffs, N.J. (1978).

A P P E N D I X

SOLUTION OF SPHERULITIC DIFFUSION CONTROLLED GROWTH MODEL VIA ORTHOGONAL COLLOCATION

A variety of numerical techniques can be used to solve the system described by equations 112-116. The method described below uses Lagrange interpolating polynomials in an orthogonal collocation technique. This technique is compatible with computer software readily available (214).

The general method is to assume an approximate solution y such that $\tilde{y}(\xi,\tau) \approx y(\xi,\tau)$ where

$$\tilde{y}(\xi,\tau) = \sum_{i=1}^{N+1} y_i(\tau) \cdot l_i(\xi) \qquad (A1)$$

and the $l_i(\xi)$'s are the Lagrange interpolating polynomials having the properties

$$l_i(\xi_k) = \begin{cases} 0 \text{ for } i \neq k \\ 1 \text{ for } i = k \end{cases} \qquad (A2)$$

An in-depth discussion of Lagrange interpolating polynomials can be found in Villadsen and Michelsen (214).

The approximate solution must satisfy equations 112-116. However, since $\tilde{y}$ is an approximation, a residual, $R(\xi)$, will exist which can be defined, using equation 112, as

$$R(\xi) = \frac{\partial \tilde{y}}{\partial \tau} - \xi^4 \frac{\partial^2 y}{\partial \xi^2} + \frac{1}{K_2}(\xi^4 - \xi)\left(\frac{\partial \tilde{y}}{\partial \xi}\bigg|_{\xi=1}\right) \frac{\partial \tilde{y}}{\partial \xi} \tag{A3}$$

One denotes the set of collocation points as $\{\xi_k\}$ for k=1 to N+1 with $\xi_1 = 0$ and $\xi_{N+1} = 1$. If the residuals are restricted to be zero at the collocation points, a system of N+1 ordinary differential equations can be defined using equations A1 and A2 in A3.

$$0 = \dot{y}_k - \xi_k{}^4 \sum_{i=1}^{N+1} y_i(\tau)\ \ddot{l}_i(\xi_k) + \tag{A4}$$

$$\frac{1}{K_2}\ (\xi_k{}^4 - \xi)\left(\sum_{i=1}^{N+1} y_i(\tau)\ \dot{l}_i(\xi_{N+1})\right)\left(\sum_{i=1}^{N+1} y_i(\tau) \cdot \dot{l}_i(\xi_k)\right)$$

$$\text{for } k = 1, \ldots, N+1$$

where the first and second derivatives with respect to τ are represented by the one and two dots, respectively, which are placed over y_k and l_i. If the ξ_k's are known, recursive algorithms can be used to generate the values of $\dot{l}_i(\xi_k)$ and $\ddot{l}_i(\xi_k)$ (214). Thus, one can solve for the unknown parameters $(y_i, \ldots, y_{N+1})$ by numerically integrating equation A4 with respect to τ.

Applying equation A1 to the boundary condition given by equation 115 results in

$$\sum_{i=1}^{N+1} y_i\ \dot{l}_i(\xi_{N+1}) = \frac{-K_2}{\phi}\ \frac{\partial \phi}{\partial \tau} \tag{A5}$$

Solving equation A5 for ϕ, substituting this into equation 113 and realizing that

$$y_b = \left[\sum_{i=1}^{N+1} y_i \, l_i(\xi)\right]_{\xi=1} = y_{N+1} \tag{A6}$$

it can be shown that

$$\frac{\partial \phi}{\partial \tau} = \frac{\mathcal{D}}{R_o (K_2)^2} \left[\sum_{i=1}^{N+1} y_i \dot{l}_i(\xi_{N+1})\right]^2 \frac{1}{f'(y_{N+1})} \tag{A7}$$

The boundary condition of equation 114 gives

$$\xi \to 0, \quad \sum_{i=1}^{N+1} y_i l_i(\xi) \to 0 \tag{A8}$$

Since the l_i's are continuous functions each term of the summation as ξ approaches 0 can be represented by

$$\lim_{\xi \to 0} [y_i \, l_i(\xi)] = y_i \, l_i(0) = 0 \text{ for } i \neq 1 \tag{A9}$$

Since $\xi_1 = 0$ is one of the collocation points,

$$\lim_{\xi \to 0} \left[\sum_{i=1}^{N+1} y_i \, l_i(\xi)\right] = y_1 \tag{A10}$$

but from equation A8,

$$\xi \to 0, \quad y_1 = 0 \tag{A11}$$

thus eliminating y_1 from the state equations. Therefore the problem is reduced to a system of ordinary differential equations given by equation A7 and

$$\dot{Y}_k = \xi^4 \sum_{i=2}^{N+1} Y_i \ddot{l}_i(\xi_k) - \frac{1}{K_2}(\xi^4-\xi)\left(\sum_{i=2}^{N+1} Y_i \dot{l}_i(1)\right)\left(\sum_{i=2} Y_i \dot{l}_i(\xi_k)\right) \tag{A12}$$

subject to the initial conditions

$$\tau = 0, \quad y = 0, \quad \phi = 1 \tag{A13}$$

This can be recast as an initial value problem

$$\dot{\vec{y}} = \vec{F}(\vec{y}) \text{ subject to } \vec{y}(\tau=0) = \vec{y}_0 \tag{A14}$$

where

$$\vec{y} = \begin{bmatrix} y_1 \\ y_2 \\ \vdots \\ y_{N+1} \\ \phi \end{bmatrix} \tag{A15}$$

A semi-implicit integrator can be used to determine the value of $\vec{y}$ for specific values of τ_j,

$$0 = \tau_0 < \tau_1 < \tau_2 \ldots < \tau_j \ldots < \tau_M \tag{A16}$$

In general, the solution at $\vec{y}(\tau_j)$ is used as an initial value for propagating the state equations forward from the state $\vec{y}(\tau_j)$ to $\vec{y}(\tau_{j+1})$, and then through the use of equation A1, the state can be determined anywhere in the medium at any τ_j.